Large-Eddy Simulations of heat exchangers made by additive manufacturing

Serge Meynet

Normandie Université

INSA INSTITUT NATIONAL DES SCIENCES APPLIQUÉES ROUEN NORMANDIE

THÈSE

Pour obtenir le diplôme de doctorat

Spécialité MECANIQUE DES FLUIDES, ENERGETIQUE, THERMIQUE, COMBUSTION, ACOUSTIQUE

Préparée au sein de l'INSA Rouen Normandie

Simulation aux grandes échelles des transferts thermiques dans les échangeurs de chaleur en fabrication additive

Présentée et soutenue par
SERGE MEYNET

Thèse soutenue le 22/06/2023 devant le jury composé de		
M. RÉMI MANCEAU	DIRECTEUR DE RECHERCHE, Université de Pau et des Pays de l'Adour	Rapporteur
M. ARNAUD MURA	DIRECTEUR DE RECHERCHE, Université de Poitiers-ISAE ENSMA	Rapporteur
M. GUILLAUME BALARAC	PROFESSEUR DES UNIVERSITÉS, INP Grenoble	Président du jury
M. ALEXANDRE CARRE	INGENIEUR D'ETUDES, Safran Aero Boosters	Membre
M. STÉPHANE MOREAU	PROFESSEUR, Université de Sherbrooke	Membre
M. VINCENT MOUREAU	CHARGE DE RECHERCHE HDR, Institut national des sciences appliquées de Rouen	Membre Co-encadrant
M. DAMIEN SERRET	DOCTEUR, TEMISTh SAS	Membre
M. ABDELLAH HADJADJ	PROFESSEUR DES UNIVERSITÉS, Institut national des sciences appliquées de Rouen	Directeur de thèse

Thèse dirigée par ABDELLAH HADJADJ (COMPLEXE DE RECHERCHE INTERPROFESSIONNEL EN AEROTHERMOCHIMIE)

ED 591 PSIME

CORIA UMR 6614

La succession de chercheurs est comparable à un seul homme qui apprend indéfiniment.

Blaise Pascal

Plutôt que de maudire les ténèbres, allumons une chandelle, si petite soit-elle.

Confucius

Chaque homme dans sa nuit s'en va vers sa lumière.

Victor Hugo

Résumé

Mots-clés : Echangeurs de chaleur, Fabrication additive, Mécanique des fluides numérique, Rugosité, Simulations aux grandes échelles

Dans l'ingénierie aéronautique et aérospatiale, les échangeurs de chaleur jouent un rôle fondamental. Les progrès récents dans le domaine de la fabrication additive sont une grande opportunité d'innovation pour les échangeurs de chaleur compacts afin d'atteindre de nouvelles performances. La perte de pression et les performances de transfert de chaleur sont les deux principales caractéristiques à optimiser pour assurer l'efficacité de l'échangeur de chaleur.

Cependant, la rugosité importante introduite par la fabrication additive a un impact considérable sur ces performances. En outre, il existe toujours un fossé entre les structures optimisées par le calcul et la réalité industrielle en raison du manque de connaissances fondamentales sur les nouvelles structures de fabrication additive. Par conséquent, les modèles de paroi actuellement utilisés dans les simulations tridimensionnelles stables et instables de mécanique des fluides ne tiennent pas compte de la rugosité typique induite par la fabrication additive.

Le projet H2020 CleanSky2 STREAM était consacré à l'amélioration des performances de la nouvelle génération d'échangeurs de chaleur, en tirant parti de la fabrication additive, des simulations haute-fidélité et de l'optimisation topologique. Dans le cadre de ce projet, l'objectif de ce doctorat était de générer une grande base de données haute-fidélité de simulations à grande échelle à rugosité résolue (RRLES) avec la plateforme de CFD YALES2. Cette base de données était destinée au développement et à l'évaluation de nouveaux modèles de parois en collaboration avec le laboratoire LEGI. Pour atteindre cet objectif, trois étapes ont été nécessaires au préalable.

La première réalisation de cette thèse a été le développement d'un générateur de surfaces rugueuses. Cet outil est capable de générer de multiples surfaces rugueuses imitant celles rencontrées dans la fabrication additive. Parmi les géométries disponibles avec ce générateur, il y a des plans parallèles, des canaux carrés et cylindriques, et des configurations plus industrielles comme des plaques avec des ailettes tubulaires. Les cas d'essai ont mis en évidence de bonnes performances en termes de précision et de temps de calcul.

La deuxième étape a consisté à obtenir des maillages ajustés aux parois. Un générateur de maillage à résolution de rugosité développé au laboratoire CORIA permet de fournir automatiquement un grand nombre de maillages non structurés ajustés aux parois avec un contrôle de la distribution de la taille des cellules du maillage final.

La configuration numérique et la méthodologie pour les RRLES ont été établies et validées. À cette fin, une méthode de recyclage a été développée. Le principe de cette dernière est d'interpoler la vitesse sur un plan éloigné dans le domaine de calcul et d'imposer cette vitesse à l'entrée. Cette méthode permet de réaliser des écoulements périodiques dans les canaux. En outre, un flux de travail entièrement automatisé avec post-traitements intégrés a été mis en place et a permis d'exécuter de nombreuses simulations sur des superordinateurs distants.

Parmi les cas de la base de données, trois configurations ont été particulièrement étudiées afin de mettre en évidence l'impact de la direction d'impression de la fabrication additive sur la topologie de l'écoulement, les profils de vitesse et de température. Des simulations RRLES ont également été menées pour des canaux carrés et cylindriques, ainsi que pour des applications de type industriel telles que des plaques avec des ailettes tubulaires. Enfin, la base de données a été analysée et quelques lois de paroi pour la rugosité ont été proposées.

Les travaux réalisés au cours de cette thèse ont aidé à mieux comprendre l'impact de la rugosité induite par la fabrication additive. Cela a permis de proposer des stratégies de modélisation aux partenaires industriels du projet STREAM et cela ouvre la voie à de nouveaux échangeurs de chaleur efficaces.

Abstract

Keywords: Additive manufacturing, CFD, Heat exchangers, Large-Eddy Simulations, Roughness

In aeronautical and aerospace engineering, heat exchangers have a fundamental role. Recent progress in additive manufacturing is a great opportunity for innovation aiming at compact heat exchangers to reach new performances. Pressure loss and heat transfer performances are the two main characteristics to be optimized for heat exchanger efficiency.

However, the significant roughness introduced by additive manufacturing strongly impacts these performances. In addition, a gap still exists between the computationally optimized structures and the industrial reality due to the lack of fundamental knowledge of the new additive manufacturing structures. Consequently, current wall models used in steady and unsteady three-dimensional Navier-Stokes simulations do not take into account typical roughness induced by additive manufacturing.

The H2020 CleanSky2 STREAM project was dedicated to the performance improvement of the new generation of heat exchangers, taking advantage of additive manufacturing, topological optimization, and high-fidelity simulations. Within this project, this PhD's aim was to generate a large high-fidelity database of roughness-resolved Large-Eddy Simulations (RRLES) with the YALES2 CFD platform. This database was for the development and assessment of novel wall models in collaboration with the LEGI laboratory. To reach this aim, three steps were necessary beforehand.

The first achievement done during this PhD was the development of a rough surfaces generator. This tool is able to generate multiple rough surfaces mimicking those encountered in additive manufacturing. Among available geometries with this generator, there are parallel planes, square and cylindrical channels, and more industrial configurations like plates with tube fins. Test cases have highlighted good performances for accuracy and computational time.

Obtaining body-fitted meshes was the second step. A roughness-resolved mesh generator, developed at the CORIA laboratory, enables to provide automatically a large number of body-fitted unstructured meshes with control of the cell size distribution of the final mesh.

The numerical setup and the methodology for RRLES have been set and validated. For this purpose, a recycling method has been developed. The latter's principle is to interpolate velocity at a distant plane in the computational domain and to impose this velocity at the inlet. This method allows to perform periodic channel flow. In addition, a fully automated workflow with integrated post-processing has been built and has enabled to run numerous simulations on a remote supercomputer.

Among the database's cases, three configurations have been particularly studied in order to highlight the impact of additive manufacturing printing direction on the flow topology, velocity and temperature profiles. RRLES simulations have also been conducted for square and cylindrical

channels, and for industrial-like applications like plates with tube fins. Finally, the database has been analyzed and some rough wall laws have been derived.

The work done during this PhD has led to a better understanding of the impact of roughness induced by additive manufacturing. This led to propose modeling strategies for the industrial partners of the STREAM project and paves the way for the design of new efficient heat exchangers.

Remerciements

C'est une longue et riche aventure qui se termine. De nombreuses personnes m'ont évidemment accompagné sur ce chemin donc je souhaite leur dire merci.

Je tiens tout d'abord à remercier tous les membres du jury d'avoir accepté d'évaluer mon travail de doctorat et pour la discussion très enrichissante lors de ma soutenance, discussion que j'ai appréciée. Je remercie Arnaud Mura et Rémi Manceau pour avoir accepté d'être les rapporteurs de ma thèse. Leurs remarques auront aidé à peaufiner ce manuscrit. Merci au professeur Guillaume Balarac pour avoir accepté de présider mon jury de soutenance et pour les différents échanges que nous avons eu durant mon doctorat. Je remercie également le professeur Stéphane Moreau pour ses remarques et questions avisées sur le sujet. Enfin, merci à Damien Serret et Alexandre Carre pour les échanges que j'ai eus avec eux tout au long de mon doctorat autour des applications industrielles. Ces échanges m'ont permis d'apercevoir et d'appréhender les problématiques rencontrées dans l'industrie. Ainsi, essayer de trouver des solutions concrètes aura été stimulant comme je l'espérais.

Ensuite, je souhaite exprimer ma gratitude envers mon directeur de thèse le professeur Abdellah Hadjadj grâce à qui j'ai progressé sur les plans de la rigueur et de l'excellence scientifique. Sa rigueur ne déteint pas sur son humanisme et par conséquent, chaque échange fût enrichissant à tout point de vue.

Je remercie chaleureusement Vincent Moureau pour son encadrement idéal tant au niveau technique qu'au niveau humain. Je ne pouvais pas espérer un meilleur encadrant et j'ai énormément appris auprès de lui. Les discussions au bureau et les tutos au tableau, par exemple, resteront gravés dans ma mémoire. Un très grand merci également à Ghislain Lartigue et Pierre Bénard pour leur soutien et leur aide au sein de la team YALES2. Je me réjouis de pouvoir continuer à collaborer avec eux trois encore pendant un petit moment dans le cadre d'une nouvelle aventure.

C'est au tour de remercier mes collègues de bureau, enfin plutôt mes amis du Golden Trio. Immense merci donc à Adrien et Pierre (Froggy et Benz pour les intimes) pour tout ce que nous avons pu vivre ensemble et pour le soutien les uns les autres. Peu de mots peuvent décrire tous ces moments passés ensemble. Heureusement, il y en aura d'autres à venir.

Merci également à tous les membres de la team YALES2 du CORIA qui ont permis de rendre cette aventure plus attrayante. Plus largement, je remercie toutes les personnes que j'ai rencontrées au CORIA et pour les différents moments de convivialité. Impossible de citer tout le monde mais chacun se reconnaîtra.

Un énorme merci à Alexis Barge avec lequel j'ai apprécié de collaborer et qui m'aura aidé à aller plus loin dans ces travaux. Je remercie la communauté YALES2 dans son ensemble pour les échanges, particulièrement lors des Extreme CFD workshops. Merci aussi à mes collègues de GDTech France qui ont rendu la période de rédaction de la thèse plus agréable.

Last but not least, je tiens à remercier mes parents et ma famille pour leur soutien sans failles. Merci infiniment à Roch pour son aide si précieuse et sans lequel je ne serai pas arrivé jusqu'ici. Merci aussi à Jacqueline et aux familles Bonnaudet et Guillon. Merci à mes amis et plus particulièrement aux EnsmAmis. Enfin, un immense merci à Blaise pour tous ses conseils toujours pertinents et éclairés.

Contents

Introduction

Context

In aeronautical and aerospace engineering, heat exchangers have a fundamental role. The recent advances in aerospace applications (miniaturization, complexity and integration) make thermal management more challenging than ever. Indeed, for instance, all electronic components are heat-sensitive and display significantly lower performances including failure out of their temperature range. Another role of heat exchangers is cooling oil as heat reduces its viscosity thereby hampering its lubricating and protective properties leading to a faster deterioration of components and the increase of maintenance operations. To this end, more efficient heat exchangers are needed.

Figure 1 – Prototype of an additive-manufactured rocket nozzle featuring internal cooling channels (Extracted from [1])

For reducing weight and volume purposes, topological optimization aims at determining the best repartition of components in a volume under constraints. In the case of heat exchangers, topological optimization is a method of choice that could determine the tube/channel form and their number, leading to a substantial increase in heat transfer efficiency, i.e. enhanced performances while minimizing the occupied volume.

In addition, additive manufacturing paves the way for new designs of critical components (Fig. 1), especially heat exchangers [2]. Recent progress in additive manufacturing is a great opportunity for innovation aiming at Compact Heat Exchangers (CHX) (Fig. 2). Pressure loss and heat transfer performance are the two main aspects to be optimized for heat exchanger efficiency and that are widely investigated. However, the important roughness introduced by additive manufacturing strongly impacts these performances [3]. There is a lack of fundamental knowledge on how these untypical roughness structures modify the heat transfer and the fluid flow, introducing a strong uncertainty between computer design and industrially printed parts.

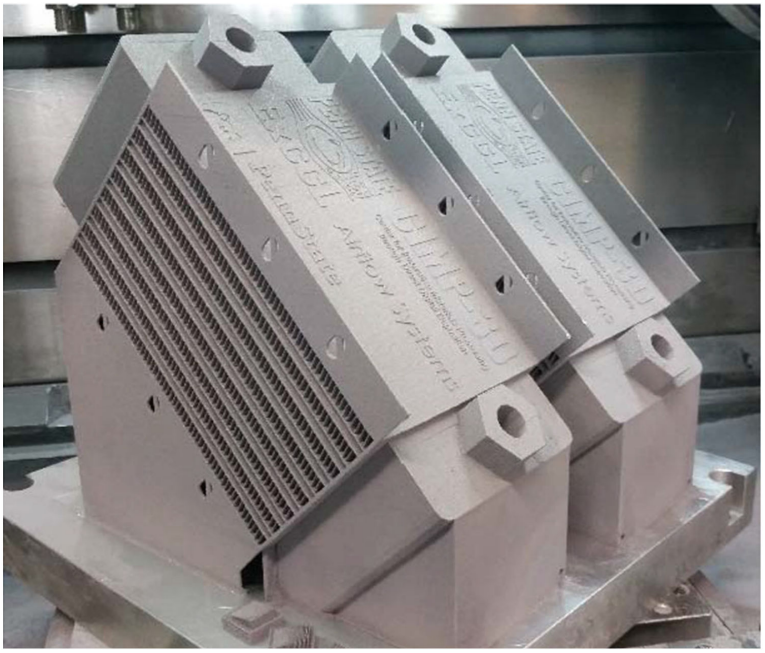

Figure 2 – Two additive-manufactured heat exchangers with external supports attached to the build plate (Extracted from [4])

Thus, simulation-based designs and computational optimization process may lead to inefficient heat exchangers at a real-life level. Variations in pressure losses and heat exchange due to additive manufacturing (AM) innovative geometries and associated roughness must be perfectly known in order to take them into account in the optimization software and, as a consequence, avoid time loss in the conception phase. Without the correct design of such systems, heat pipes are not able to transport enough heat and may function as extremely poor thermal conductors in the systems.

Having any knowledge about flow type, temperature profile and turbulence zones in heat exchangers is a very useful aid for reliable, high efficiency and economical design or optimization. Most of the publications on heat exchanger topological optimization and fluid behavior deals with laminar flow because turbulence generates difficulties, notably owing to the fact to consider the smallest turbulence structures.

Computational Fluid Dynamics (CFD) is a powerful tool for fluid dynamics and thermal design in industrial applications, as well as in academic research activities (Fig. 3). Based on the current capabilities of the main CFD packages suitable for industry (such as FLOTHERM, ICEPAK,

FLUENT and CFX) and the nature of industrial applications, understanding the physics of the processes, introducing adequate simplifications and establishing an appropriate model are essential factors for obtaining reasonable results and correct thermal design.

Controlling better the performance of 3D-printed heat exchangers could therefore be achieved with better rough-wall models. The H2020 CleanSky2 STREAM project is then dedicated to the performance improvement of the new generation of heat exchangers, taking advantage of additive manufacturing and high-fidelity simulations. Within this project, a large high-fidelity database of roughness-resolved Large-Eddy Simulations (RRLES) is expected as an outcome of this PhD.

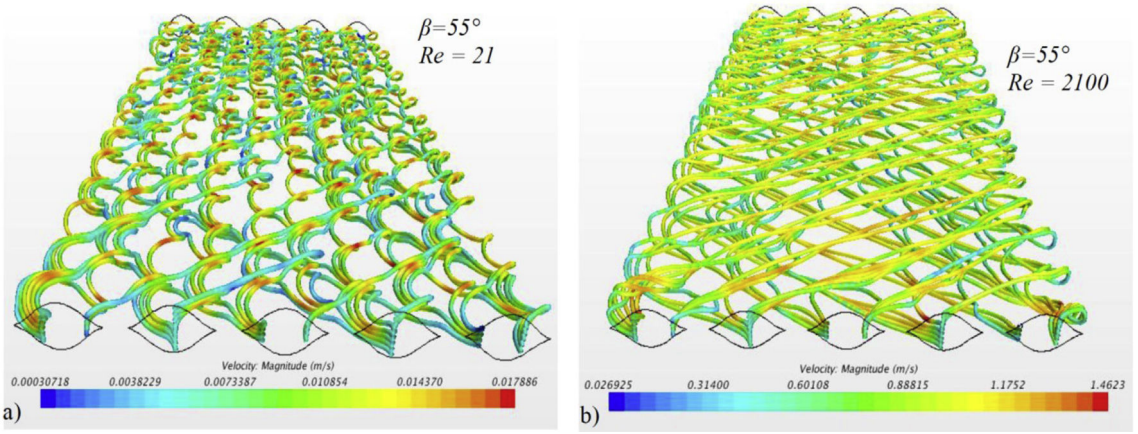

Figure 3 – Example of a CFD simulation for plate heat exchanger. Flow streamlines colored by local flow velocity for two different types of flow structure (Extracted from [5])

Objective of this thesis

This thesis aims to achieve several objectives, including

- Identification of the key physical parameters and the best methodology to model the turbulence, especially in rough additive manufactured parts
- Automatic generation of numerical rough surfaces and meshes
- Building of a parametric Large-Eddy Simulation database of additive-manufactured heat exchangers

The purpose of the database is the improvement of rough-wall modeling based on resolved-rough unsteady simulations. The results will be analyzed in collaboration with the LEGI laboratory in Grenoble to develop new models.

Manuscript content

The manuscript is organized as follows.

- **Chapter 1** addresses classifications of heat exchangers and different manufacturing processes. Additive manufacturing techniques are also categorized, and the principal ones used for heat exchangers are presented. Finally, the roughness's impact from additively manufactured parts is reviewed here.

- **Chapter 2:** The theoretical context of fluid dynamics is presented in this chapter. The first section deals with the numerical modeling of turbulent flows. Standard numerical methods for simulating turbulent flows are presented, focusing on the LES-filtered equations and the closure models. Finally, the second section introduces the YALES2 CFD platform used during this thesis.

- **Chapter 3:** Roughness characterization and its impact on the flow are addressed here. In addition, an extensive literature review is presented about fully resolved rough wall simulations from past studies and the state-of-the-art strategies for roughness modeling.

- **Chapter 4** focuses on an innovative procedure to generate 3D roughness-resolved unstructured and body-fitted meshes with fine control of the cell size distribution and cell quality. This procedure is split into two tools. The first one is a numerical rough surface generator developed during this thesis. Different geometries with prescribed roughness parameters can be created like planar surfaces, cylindrical channels, or plates with tube fins. The second tool is a body-fitted meshes generator, enabling the production of unstructured meshes from rough geometries previously generated.

- **Chapter 5:** Before performing roughness-resolved LES, it is necessary to present and validate the methodology and numerics. In order to run simulations for periodic channels, a recycling method has been developed during this thesis. This method enables to impose a time-varying inlet condition with a velocity interpolated at a given distance within the channel. Numerics are also addressed in this chapter. Three validation cases are finally presented including periodic-channel flow, as well as regular and irregular rough surfaces.

- **Chapter 6** presents developed models representative of the flow obtained in additive manufactured heat exchangers without explicit representation of the surface details in the framework of RANS and LES methods. A Roughness-Resolved Large-Eddy Simulation (RRLES) database of representative channel flows has been built. From database results, derived strategies for turbulence and heat transfer have been developed and assessed.

- **Chapter 7** investigates several heat exchanger configurations featuring a surface condition similar to that of additive manufacturing. The initial configurations presented include square and cylindrical channels, which are commonly observed in experimental additive-manufactured heat exchangers. As seen in Chapter 1, additional surfaces can enhance the heat transfer. Hence, the final case examined in this manuscript is a plate equipped with finned tubes.

Publications

Peer-reviewed journals papers

- Meynet S., Barge A., Moureau V., Balarac, G., Lartigue G. & Hadjadj, A., "Roughness-Resolved LES of Additive Manufacturing-Like Channel Flows", *J. Turbomach.*, 145(8), 081013 (2023)

- Meynet S., Moureau V., Lartigue G. & Hadjadj A., "Automatic Surface and Volume Mesh Generation for Roughness-resolved LES of Additive-Manufacturing Heat Exchangers", *Flow, Turbulence and Combustion*, *Under review*

International conference papers

- Meynet S, Barge A, Moureau V, Balarac G, Lartigue G, & Hadjadj A. "Roughness-Resolved LES of Additive Manufacturing-Like Channel Flows." *Proceedings of the ASME Turbo Expo 2022: Turbomachinery Technical Conference and Exposition*, Rotterdam, Netherlands (June 2022)

- Meynet S., Moureau V., Lartigue G. & Hadjadj A., "Automatic Surface and Volume Mesh Generation for Roughness-resolved LES of Additive-Manufacturing Heat Exchangers", *Proceedings of the 13th International ERCOFTAC symposium on engineering, turbulence, modelling and measurements (ETMM13)*, Rhodes, Greece (September 2021)

CHAPTER 1

Additive manufacturing for heat exchangers

This chapter addresses classifications of heat exchangers and different manufacturing processes. Additive manufacturing techniques are also categorized, and the principal ones used for heat exchangers are presented. Finally, the roughness impact from additively manufactured parts is reviewed here.

Contents

Context

Basically, a heat exchanger (HX) is a device used to transfer thermal energy between two or several fluids or between a solid surface and a fluid. This is a critical component in several energetic and industrial processes such as for power systems generation cooling or for aerospace applications [2]. Although conventional HXs are typically produced in mass using metalworking methods like stamping and brazing for cost-efficiency, in aeronautical engineering, performance may outweigh cost considerations. Indeed their performance regarding heat transfer, pressure losses and

weight can have an impact on the overall efficiency of systems. Due to a wide variety of applications, HXs have to be thus split into different categories.

1.1 Types of heat exchangers

The design of heat exchangers mainly depends on applications, environmental and operating conditions like temperature and pressure for instance. In fact, each type of application requires a specific hierarchy of priorities. For instance, for heat recuperation applications with aggressive chemical fluids, the chemical resistance of manufacturing material is the first criterion. However, for aerospace applications, their manufacturing is driven by three main objectives: increase the thermoaeraulic performance, extend their lifetime, and reduce their volume and weight.

In general, the intended application imposes the geometry, the fabrication process and the material. Aside from the cost, their sizing is a function of several parameters:

- Inlet and outlet conditions (temperature and flow)
- Thermal performance
- Pressure drop
- Volume and weight

1.1.1 Geometry types and fluid phases

There are various criteria that can be used to classify heat exchangers, such as the fluid flow configurations, the type of fluid phases, the geometry types, the heat transfer mechanism, or the compactness. The first categorization outlined in Fig. 1.1 is based on the kind of geometry. HXs are thus divided into four main construction features: tubular, plate-type, with extended surface and regenerators.

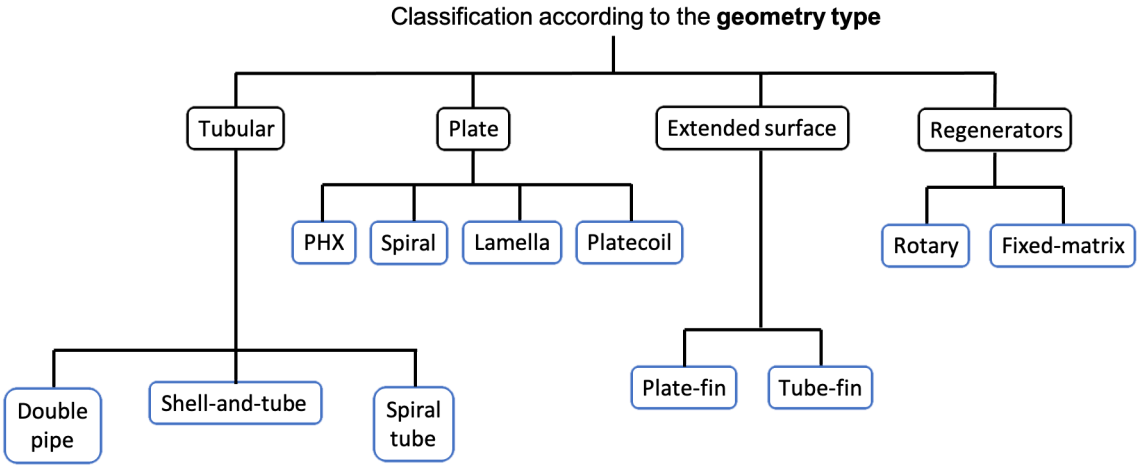

Figure 1.1 – Classification of HX types based on the geometry (adapted from Shah and Sekulić [6])

Tubular

Tubular heat exchangers (HXs) are primarily constructed using circular tubes, although rectangular ducts can also be used. The versatility of design is significant thanks to changing tube diameters, lengths or arrangement. Three sub-categories can be distinguished as double-pipe, shell-and-tube and spiral tube (Fig. 1.2).

The simplest type of HX is a double-pipe. The latter consists typically of concentric pipes in which two fluids pass through. Depending if the application requires the best performance or a constant wall temperature, flow directions can be either counter or parallel.

The principle of shell-and-tube HX relies on a bundle of tubes within a cylindrical shell, and these tubes are parallel to the axis of the shell. In addition, baffles are often implemented in order to modify the fluid flow inside the shell.

Spiral tubes, on the other hand, are composed of one or more coiled tubes arranged within a shell. While heat transfer is enhanced in comparison to straight tubes, cleaning can be difficult to accomplish, making it one of the most significant disadvantages.

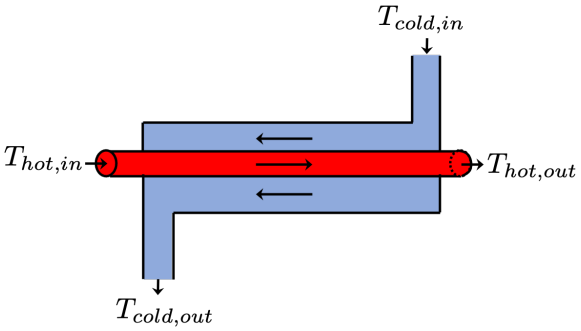

(a) Double-pipe

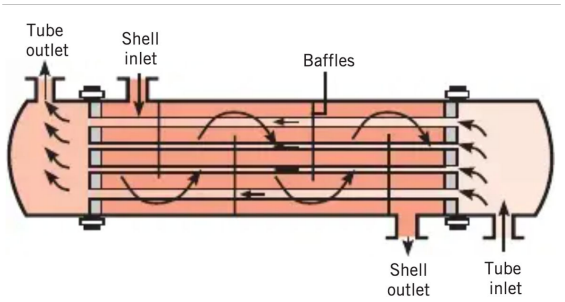

(b) Shell-and-tube (from [7])

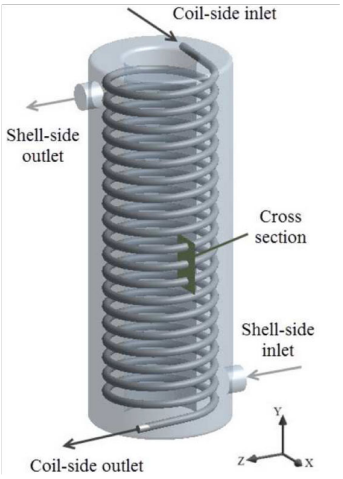

(c) Spiral tube (from [8])

Figure 1.2 – Examples of tubular HX

The scope of this manuscript is limited to the investigation of square and cylindrical tubes. As a result, the primary focus will be on the double-pipe HX.

Plate

As this category's name indicates, these HXs are made of thin smooth plates or have a specific groove shape. They are subdivided into four main configurations (Fig. 1.3).

- Plate HXs (PHX) are traditionally made of several rectangular plates and built with sealing gaskets, by welding or brazing. Although PHX with seals present high thermal effectiveness, allow high design flexibility or ease of cleaning, their use imposes noncorrosive fluids and some leakages can appear with deterioration. This is why PHX can then be welded or brazed. This allows high temperature and high pressure operating conditions. However, the flexibility in designing and cleaning is restrained.
- Spiral plate HXs are composed of two long plates built in spiral and wrapped around a shaft. Consequently, two spiral channels are created. Thus two fluids flow through each channel. The flow rates can be considerably different, and the volume is generally lower compared to shell-and-tube HX but is limited in operating temperature.
- Basically, lamella HX refers to a bunch of flat tubes in a tubular shell. The obtained heat transfer is relatively high and the weight is reduced compared to shell-and-tube HX. Contrariwise, the maximum allowed temperature is limited.
- Panelcoil HX regroups configurations which are either fitting the system in shape and size or put in a tank as flat plate coils. As their shape can be easily designed and as the operating conditions are broad, this kind of HX has many possible applications.

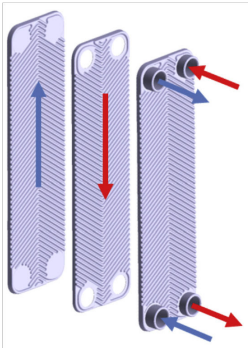

(a) PHX built with gaskets (from [5])

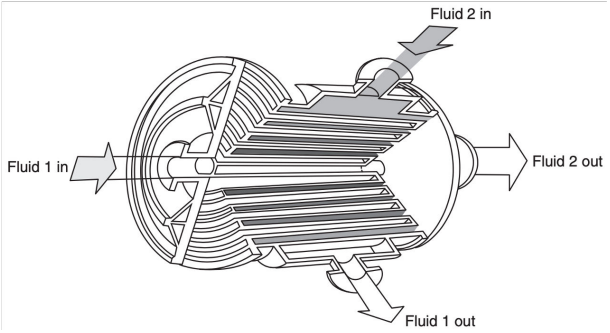

(b) Spiral plate (from [6])

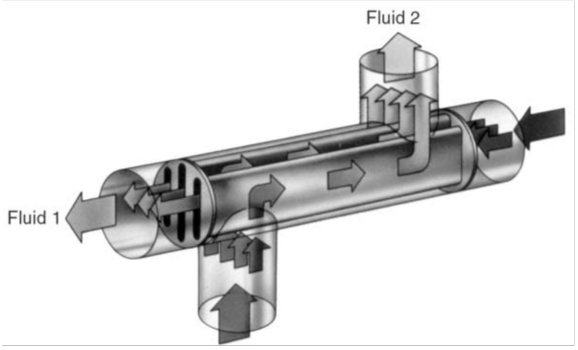

(c) Lamella

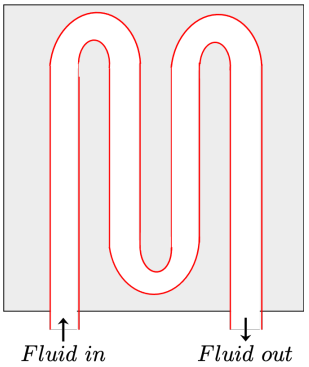

(d) Platecoil

Figure 1.3 – Examples of plate-type HX

The target of this work is initially on PHX as parallel planes configurations are studied here.

Extended surface

In addition to previous configurations, fins are used as extended surfaces in order to increase heat transfer. Fin density can be adjusted according to the requirement of the application. The two

primary types of extended surfaces are plate-fin (Figs. 1.4, 1.5 and 1.6) and tube-fin (Fig. 1.7).

For plate fins, they are integrated between two parallel plates and commonly have triangular or rectangular shapes. Fins can be either plain or interrupted, such as offset strip fins, louver, perforated and pin fins. Moreover, a wavy pattern can also be applied instead of straight fins.

Concerning tube fins, the idea is to transfer the heat by conduction via the wall of tubes. Individually finned tubes or an array of tubes with flat fins can be distinguished.

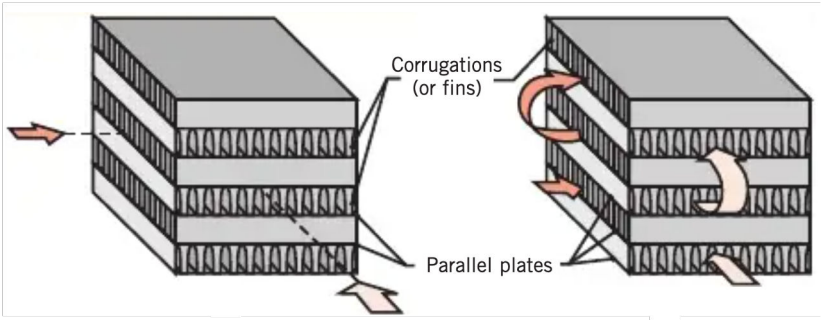

Figure 1.4 – Plate-fin heat exchanger: single pass (left) and multipass (right) (from [9])

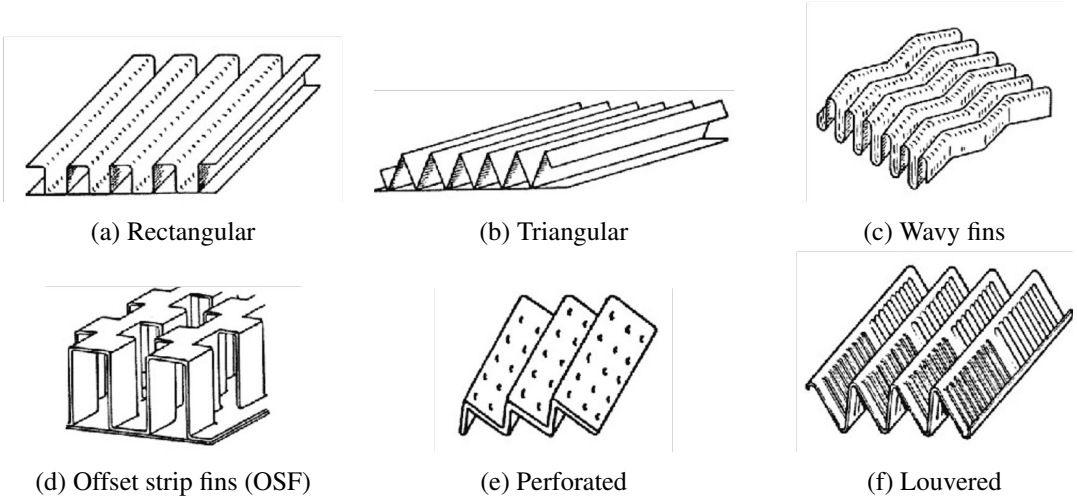

(a) Rectangular (b) Triangular (c) Wavy fins

(d) Offset strip fins (OSF) (e) Perforated (f) Louvered

Figure 1.5 – Different types of plate-fin heat exchangers (from [6])

The manuscript includes an analysis of a finned tube configuration with rough walls that was simulated.

Regenerators

These HXs store heat in a medium and then transfer it to the cold fluid. The medium elements are generally referred to as a matrix and the latter can be rotated periodically or fixed. In the last case, this is the fluid that is streamed cyclically. As regenerative heat exchangers are beyond the scope of this manuscript, no further details will be provided.

1.1.2 Fluid phases

Another classification according to the fluid phases encountered in HX can be established. Cases have been distinguished in Fig. 1.8, and the main HXs used for each case have been indicated.

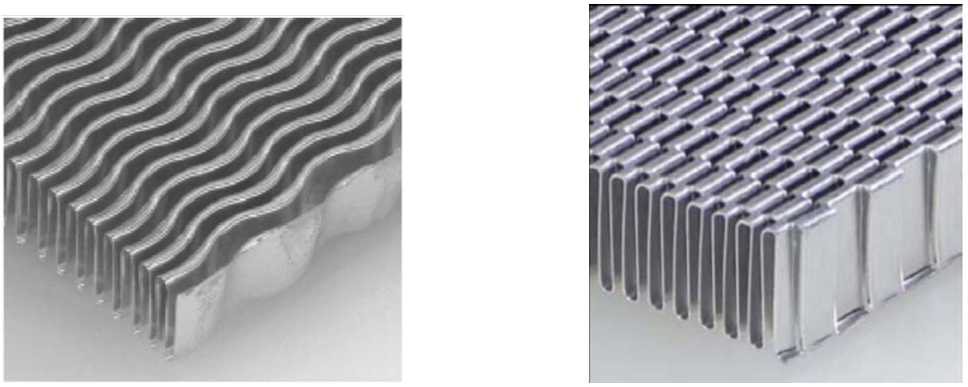

(a) Wavy (b) Offset strip fins

Figure 1.6 – Coupons of plate-type heat exchangers (from [10])

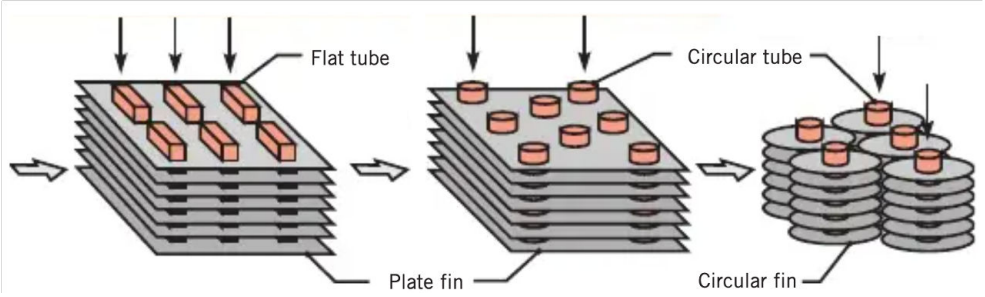

Figure 1.7 – Tube fins heat exchangers (from [9])

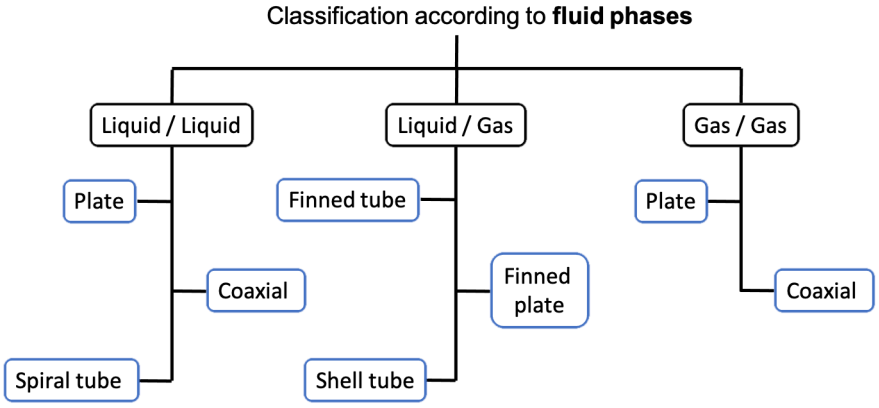

Figure 1.8 – Classification of HX types based on the fluid phases (adapted from Shah and Sekulić [6])

The three different cases are thus analyzed hereafter.

- **Liquid/Liquid:** The heat flux is shared between two or several liquids for heating applications like boilers, heat pumps or solar panels for instance. A phase variation can occur for one of the liquids (evaporation), especially in air conditioning applications. In this type of exchanger, each fluid has the same order of magnitude of thermal resistance. As a consequence, there is no need for a particular design with an extension area. Geometries

frequently used for these applications are coaxial tube, plate and spiral HX.

- **Gas/Gas:** This flow type is mainly used in heat recovery, heating and cooling of fresh air like for the medical field and for dehumidification applications. Like in the liquid/liquid case, fluids have an equivalent thermal resistance and by the following, there is no need to create specific configurations. Moreover, one of the fluids can undergo a phase variation (condensation). The most used geometries for these applications are shell-and-tube and plate HX [6].

- **Gas/Liquid:** This represents the most complex case, as it involves significant differences in thermal resistance between the two fluids. To minimize the size of the heat exchanger, it is necessary to achieve similar thermal conductance on both sides. This requires the use of specific heat exchanger configurations, such as those with extended surfaces or fins, to increase the heat exchange area on the gas side (such as finned tube and finned plate heat exchanger) [6].

1.1.3 Compactness

Contrary to what one might think, this property is not primarily evaluated according to the size of an HX. The latter can be a consequence but not necessarily. The compactness is defined as the ratio β between the exchange surface and the HX's volume.

Depending on the fluid phases, the threshold for a compact HX differs (Fig. 1.9). For a gas-to-liquid HX, this value corresponds to 700 m^2/m^3, and with a liquid-liquid HX, the threshold is equal to 400 m^2/m^3. For comparison purposes, a typical shell-and-tube HX has a surface area density (or compactness) around 100 m^2/m^3. The primary objective of compact heat exchangers (CHX) is to improve their performance by reducing their size and weight.

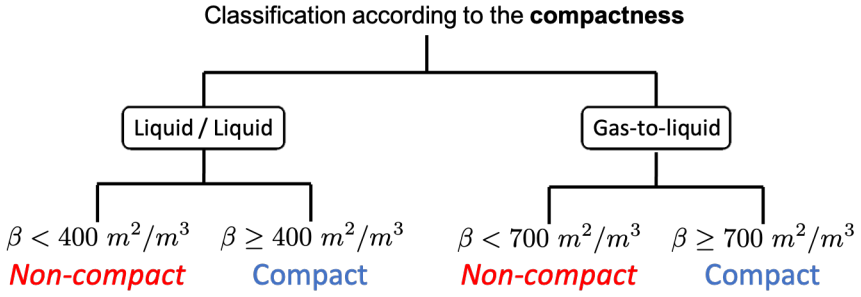

Figure 1.9 – Classification based on compactness (adapted from Shah and Sekulić [6])

1.1.4 Passive and active heat enhancement

As seen above with extended surfaces HXs, various types of heat enhancement can be applied. These techniques are usually limited by increasing the pressure drop, penalizing overall performance. Previous research aimed to determine the optimal balance between heat transfer enhancement and pressure losses. These technologies can be split into two categories: passive techniques and active techniques.

- **Passive techniques:** They are based on the increasing of the convection heat flux coefficient without any external perturbation (mechanic, magnetic,...). The idea is to modify the ge-

ometry of the exchange area by introducing a specific shape in order to generate a secondary flow, such as vortex generators and modified fins (Fig. 1.10).

- **Active techniques:** It consists in introducing an external perturbation in the flow. This energy mainly comes from a mechanical fluctuation, an electromagnetic wave or an external fluid flow.

Figure 1.10 – Several types of passive techniques for heat enhancement [11]

The conventional HXs used in HVAC, heat recovery, and industrial applications typically employ plate, finned tube, and shell-and-tube configurations. The trade-off between heat transfer and pressure drop is often controlled by the compactness and topology of the surfaces. On the other hand, the weight and volume of these HXs are influenced by the manufacturing material and process.

1.2 Manufacturing processes

1.2.1 Traditional manufacturing

The manufacturing of heat exchangers is usually a succession of steps. First, the HX geometry is defined based on the application and the types of operating fluids. The second step consists in determining the geometric parameters suitable to inlet/outlet conditions (temperature, flow and pressure) and performance. Once these parameters are fixed, the manufacturing process has to be selected depending on the desired HX type.

Previously and still nowadays, traditional manufacturing methods for HXs have been employed, such as milling, die-casting, alignment, brazing/welding, or a combination of these processes to mass produce cost-efficient products [12].

- **Plate-type:** They are usually built with gaskets, welded or brazed depending on the leak tightness required [6].
- **Finned-tube:** Fins, which can be plates or modified surfaces (wavy fin or with vortex generators), are attached to the tubes by a tight mechanical fit, tension winding, adhesive bonding, soldering, brazing, welding, or extrusion [6].

- **Finned-plate:** Fins are roll-formed and are attached to the plates by brazing, soldering, adhesive bonding, welding, mechanical fit, or extrusion. They may be used on both sides in gas-to-gas heat exchangers. In gas-liquid applications, fins are generally used only on the gas side; if employed on the liquid side, they are mainly used for structural strength and flow-mixing purposes. They are also sometimes used for pressure containment and rigidity [6].

These traditional techniques allow to produce series of high-quality HXs, although the freedom of design is restrained. In addition, the prediction of overall performances for these HXs is based on correlations and CFD models. The latters yield usually results in minor relative errors (less than 5%). Nevertheless, for rough surfaces, the gap between prediction and measured performance can become considerable.

1.2.2 Additive manufacturing

Additive manufacturing (AM) or 3D printing is known as a simple and quick prototyping technique. This relatively new method is based on depositing construction material layer by layer in order to print a net shape for a 3D piece [13]. The application of AM to the development of a new generation of HX has recently undergone considerable growth. AM potentially facilitates the innovation of more efficient and integrated HX with complex geometries.

Categories and construction process

In concrete terms, AM includes numerous technologies, which are divided into seven main categories.

- **Material extrusion:** Fundamentally, the material is heated and is pushed through a nozzle onto a platform to form a deposited layer.
- **Powder bed fusion (PBF):** A scanning laser or an electron beam is used as the energy source to aggregate powder particles.
- **Material jetting:** Basically, the material is jetted onto a build platform like with an inkjet printer.
- **Binder jetting:** Two materials are required with this kind of technology: powder-based material and generally liquid binder. Here, this is the binder that is jetted onto the platform.
- **Vat Photopolymerisation:** A liquid photopolymer is stored in a vat and light is directed selectively to process the desired layer.
- **Directed energy deposition (DED):** Material in the form of powder or wire is deposited, and in the same time, thermal energy is provided to fuse material.
- **Sheet lamination:** Sheets of material are bounded layer by layer.

Regardless of the AM technology, the HX construction process consists of multiple steps: i) creating a 3D Computer-Aided Design (CAD) file, ii) converting this file into STL format (Standard Tessellated Language) and using a slicing software that decomposes the geometry layer by layer, iii) transferring the STL to the AM machine and manipulating it in order to potentially correct orientation or position, iv) setting up the machine, v) building step, vi) removing parts from the build platform and vii) post-processing like removing building supports or polishing the surface if required.

Pros and cons of additive manufacturing

The major advantage of AM is the ability to build an entire part monolithically (without binding techniques such as welding) by adding successive layers and with complex internal geometries. This feature helps to reduce the weight of HX. Actually, AM allows to modify all shapes and geometric parameters without any need to develop a new tooling or injection mold. This promotes lightweight parts.

In addition, the obtained feature thickness of a layer is dependent on the AM process but it can conceivably be as low as around 50 μm with metal technologies at this time. Such thin thickness favors designing new geometries with increased complexity. Therefore this facilitates new HX having a lower volume and increased performance due to potential complex shapes. This indicates that AM paves the way for further efficient compact HXs.

Cost competitiveness has also been and is still being studied. Indeed, the idea is to determine when AM is cost-effective compared to conventional manufacturing. Another purpose is to identify where cost reductions can be applied during the process. First, the absence of tooling can significantly reduce production costs. Thus AM is generally more cost-effective below a production volume than traditional manufacturing due to an initial cost for the latter. Interestingly, Laureijs *et al.* [14] have shown that for a commercial aviation engine bracket, the additively manufactured part is less expensive when lifetime fuel savings are associated, even for higher production volumes (Fig. 1.11).

Various cost models for AM have been proposed in the past. For instance, Fera *et al.* [15] established such an approach, including the complexity of the part to build. However, due to the breadth of design capabilities offered by AM, those models must be enhanced to better predict cost-effectiveness.

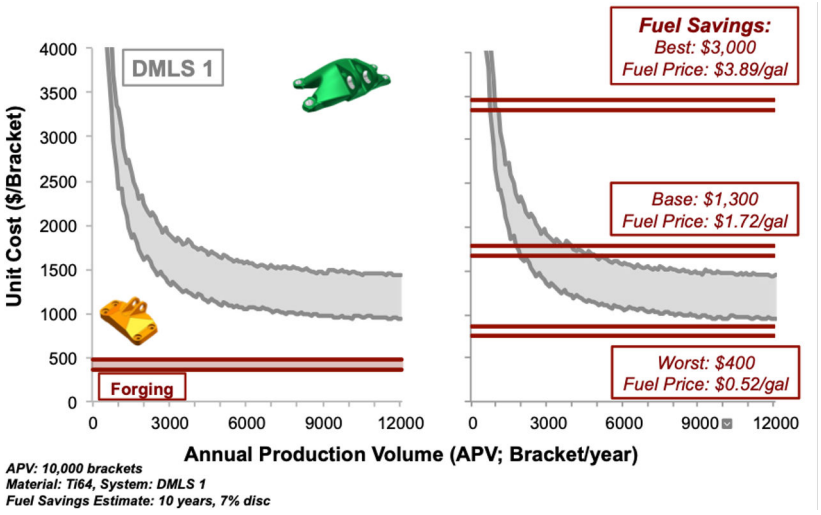

Figure 1.11 – Example of a comparison between costs of additive manufacturing and traditional manufacturing in function of the production volume with different scenari [14]

Nonetheless, these relatively new manufacturing processes have some drawbacks, such as material porosity or a degraded surface condition. For a thermal application, roughness has a double effect. First, some perturbations are created in the boundary layer and they can lead to turbulent flow. The latter tends to increase heat transfer. The second effect is that it penalizes the flow by increasing the pressure drop and by the following pumping and ventilation power. Surface roughness is further analyzed in section 1.4.

The porosity affects performance in two major ways. First, it induces a perturbation in the flow. Second, the porosity modifies the thermo-mechanical properties of the material, such as thermal conductivity and tensile and fatigue strength. For instance, for selective laser melting (SLM), this phenomenon is physically related to shrinkage, gas entrapment during solidification and adhesion of partially molten particles to surfaces between the layers [16, 17, 18]. Wong *et al.* [12] have tested the thermal conductivity of 6061 Aluminum before and after the manufacturing process of heat sink using AM SLM technology. Measurements showed a thermal conductivity of 170 $W.m^{-1}.K^{-1}$ before printing and 70 $W.m^{-1}.K^{-1}$ after the printing. This gap is due to the production of a 90% denser solid. This undesirable effect could contribute to decrease the reliability of HX [19]. The mitigation of this porosity resulting from AM is the object of many actual studies in order to improve the thermomechanical properties of products.

Other issues of AM are the accuracy, repeatability and consistency of prototypes. Accuracy and consistency issues can cause the clogging of tube or channel in HX. Usually, every metallic part fabricated by AM is subject to a post-treatment to polish and remove geometry imperfections that cause undesirable effects. Although in the case of HX, the problem resides in the internal tubing path and microchannel geometries that cannot undergo these post-processes.

Despite several notable drawbacks, the potential applications of additive manufacturing (AM) are virtually unlimited. This has prompted many industrial companies to explore the use of AM in the construction of compact HX and to develop new technologies for reducing the occurrence of defects in the manufacturing process.

1.3 Additive manufacturing processes used for heat exchangers

Among AM technologies, not all of them are suitable for HX in an obvious manner. In general, chosen materials have mainly a high thermal conductivity like metallic materials (aluminum or copper for instance) or ceramic for specific cases that require to ensure a good heat transfer. The involvement of AM in the manufacturing of new types of HXs allows for a wider choice of materials, such as metal ones, ceramic and the use of new kinds of polymers and composites. However, raw materials used in AM are mainly in powder or aggregate form, which normally would affect its thermo-mechanical properties.

For the three principal material categories used for additively manufactured HXs, a description of the principal used technologies is given hereafter.

1.3.1 Processes for metallic parts

Powder bed fusion (PBF)

These technologies are the most widespread to build HX. The powder is coated on the building platform from a reservoir via a roller. Energy stemming from a laser or an electron beam is directed at the material to fuse or melt it for solidifying a layer. The building platform is moved down and the process is repeated until the entire piece is manufactured (Fig. 1.12). Generally, the building process takes place inside an enclosed chamber filled with nitrogen gas to minimize oxidation and degradation of the powdered material. In addition, in order to prevent the warping of the part and to minimize laser power, the building platform and the powder are preheated.

Several similar processes are then widely known like direct metal laser sintering (DMLS), selective laser sintering (SLS) or even electron beam melting (EBM). Different metals have been used for HX in the last fifteen years like aluminum alloys [12, 21, 22], stainless steel, Inconel [23, 24] or titanium alloys like the widespread one Ti-6Al-4V. The latter is indeed one of the key metals for aerospace applications due to its high-temperature stability and corrosion resistance.

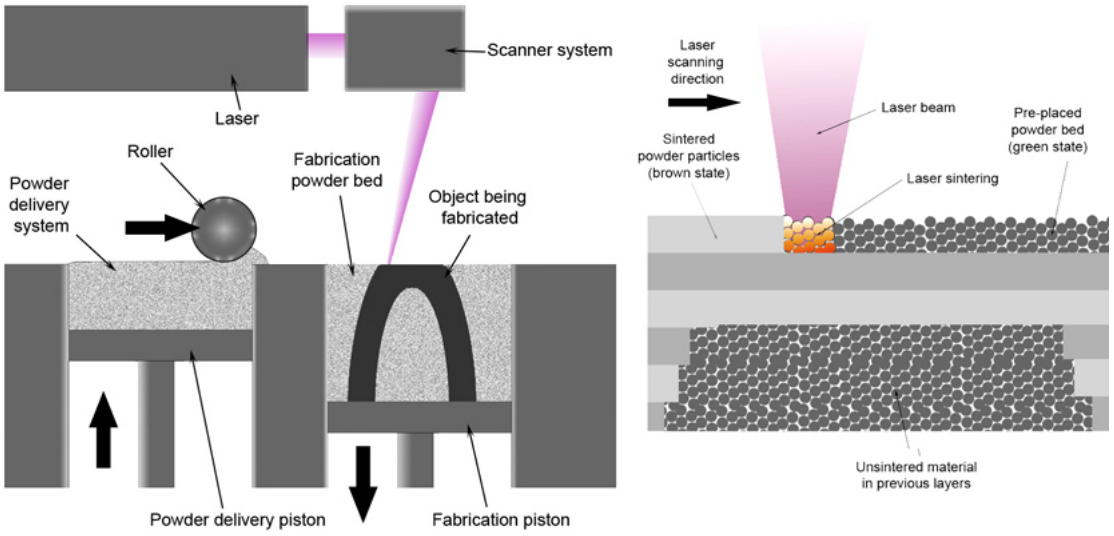

Figure 1.12 – General process of laser powder bed fusion [20]

The development of new alloys is possible thanks to the capabilities of AM technologies and researchers have proposed some.

Cold gas dynamic spray (CGDS)

Some metallic HXs in the literature have been built through this technique [25, 26]. The process is also known as cold spray. The principle consists in depositing the material in the form of solid powder particles on a substrate. This deposition is enabled by the acceleration of the powder particles by a high-pressure carrier gas flowing at supersonic speed [25] (Fig. 1.13). The cold spray has been used to create in majority pin fin HX.

Other metal additive manufacturing methods

Various AM processes can also be found, such as ultrasonic additive manufacturing (UAM). The UAM relies on building a 3D shape through ultrasonic welding of the raw material [28]. Vibrations are transmitted to the metal tape, so an ultrasonic solid-state weld between the tape and base plate is created (Fig. 1.14). An additional subtractive stage can sometimes be necessary to finalize the geometry details. This technique presents an attractive advantage since it allows to use a high thermal conductive material and while obtaining a relatively good surface condition. However, intermittent welding discontinuities can still be found and could cause hermeticity problems.

1.3.2 Polymers

Despite their low thermal conductivity, polymers can be excellent materials for the manufacturing of HX, like polypropylene or polycarbonate. They offer several advantages such as low density, low cost, anticorrosion and antifouling [30]. Nonetheless, the main drawbacks are low structural strength, low thermal conductivity, and poor stability at high temperatures. In order to mitigate the low thermal conductivity, reducing wall thicknesses is a solution. Concerning AM, three categories are the most common for polymer HX.

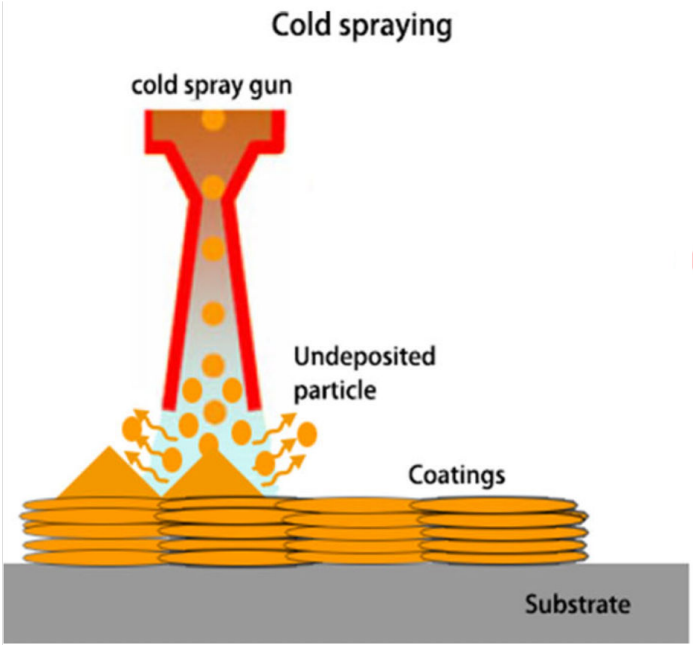

Figure 1.13 – Schematic of the Cold Gas Dynamic Spray process (adapted from Wu *et al.* [27])

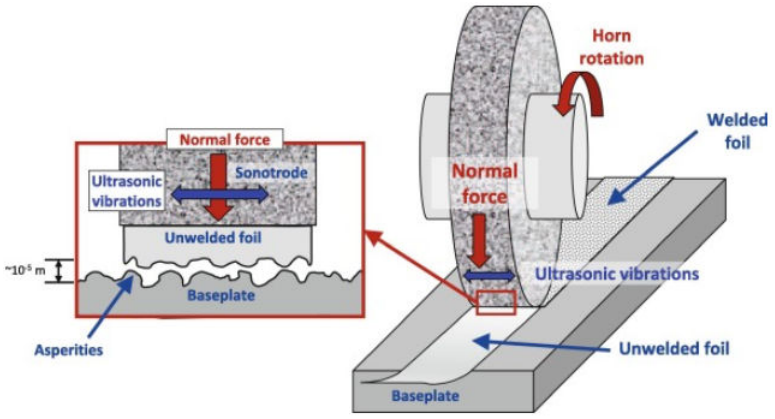

Figure 1.14 – Ultrasonic additive manufacturing process scheme [29]

Vat photopolymerization

The first one is the vat photopolymerization, especially the stereolithography (SLA) method. With a liquid polymer retained in a vat, it consists of photocuring layer by layer by ultraviolet lasers. After each layer is cured, the building platform is moved to cover fresh liquid polymer (Fig. 1.15).

Fused filament fabrication (FFF)

Among fused filament fabrication, fused deposition modeling (FDM) is the most widely known. A thermoplastic filament is heated, pushed through a nozzle and deposited on the build platform (Fig. 1.16). A polymer HX made by FFF was built by Cevallos [32] as a proof of concept (Fig. 1.17). The author encountered porosity issues and special care to the nozzle path has been taken.

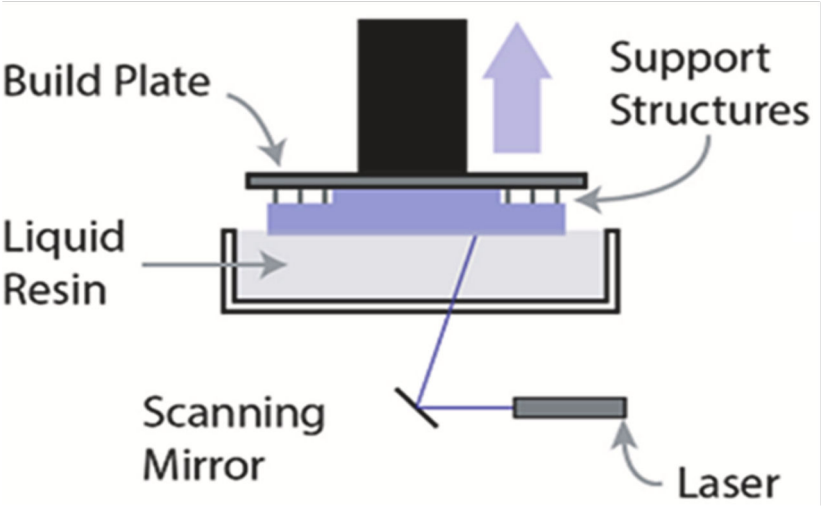

Figure 1.15 – Scheme of the stereolithography (SLA) [31]

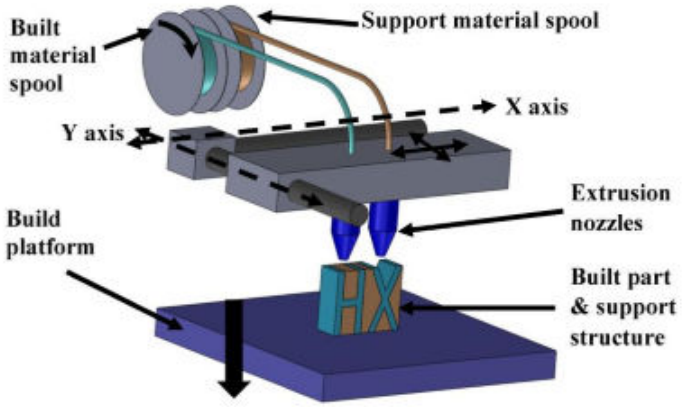

Figure 1.16 – Scheme of the fused filament fabrication (FFF) process [30]

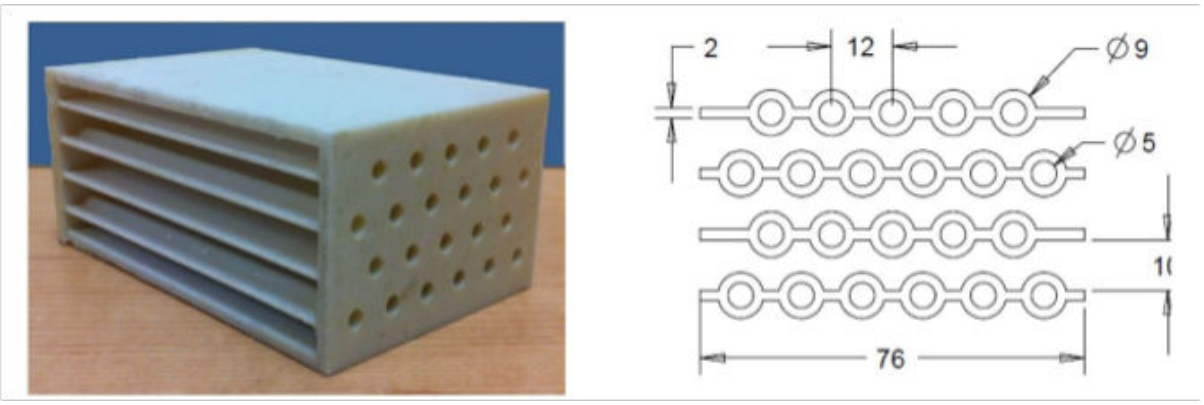

Figure 1.17 – A polymer heat exchanger made by fused filament fabrication (left) and internal cross-section dimensions in mm (right) [32]

Material jetting

The principle is to depose liquid drops of material layer by layer to shape a 3D part. For polymers, the material is often photo or thermally curable (Fig. 1.18).

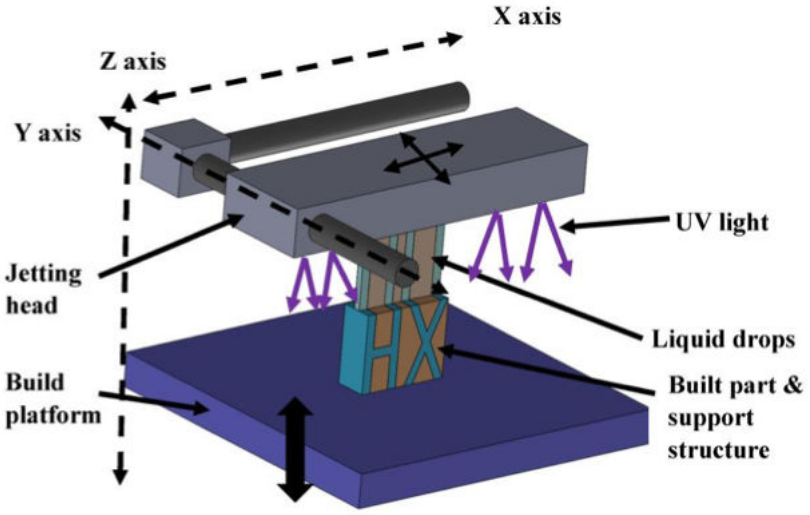

Figure 1.18 – Representation of material jetting apparatus [30]

1.3.3 Ceramics

Ceramic-based AM for HX applications has received less attention compared to metal or polymer-based AM. Nonetheless, ceramics provide a solution for some applications requiring high temperatures or pressures and for some special environments (Fig. 1.19), such as chemically aggressive ones. The design freedom that can boost HX performance can also be applied to ceramic AM. Some technologies have been used, including lithography-based Ceramic Manufacturing (LCM), mold shape deposition [33], and laminated object manufacturing [34].

1.4 Surface condition

On the one hand, roughness is known to enhance heat transfer. For instance, in a simple convective case over a cylinder, roughness enhances the convective heat coefficient by approximately a factor of 2.5 [35]. On the other hand, a poor surface condition can lead to significant limitations such as high pressure losses and a notable gap between real performance and those predicted by current CFD models.

1.4.1 Conventional manufacturing processes

Commercial HXs typically have roughness on the order of 1 μm due to manufacturing processes, and surface finishing techniques may be used for polishing purposes. To further enhance heat exchange, corrugations are often added, as demonstrated by Khan *et al.* [36]. Parametric studies, such as the one conducted by Faizal and Ahmed [37], have also been carried out to determine the optimal configuration for maximizing heat transfer (see Fig. 1.20).

Concerning the roughness itself, Kandlikar *et al.* [38] have conducted an experimental study on the effect of channel roughness inside small diameter tubes. They observed that heat transfer

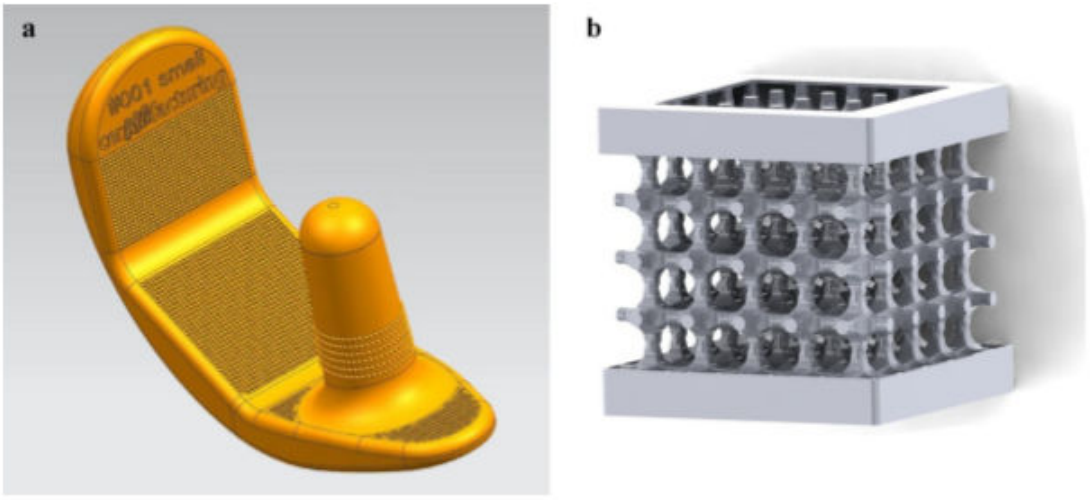

Figure 1.19 – Examples for different implant applications of ceramics: (a) unicondylar knee replacement ; (b) schematic cage for spinal fusion

and pressure drop show a dependence on roughness only for the smallest tube diameter (0.62 mm). Indeed, the ratio between roughness and the diameter is of paramount importance.

Numerous studies have been undertaken about roughness and plate HX (Fig. 1.20). For example, Nilpueng and Wongwises [39] have investigated the impact of plate surface roughness ranging between 1 μm and 3 μm with three different commercial HX. Compared to a smooth surface, the heat transfer coefficient was enhanced between 4 % and 18 %. In addition, the increase was similar for the pressure drop. To sum up, their experimental data have shown that the global performance was increased with a higher roughness for all tested inlet velocities.

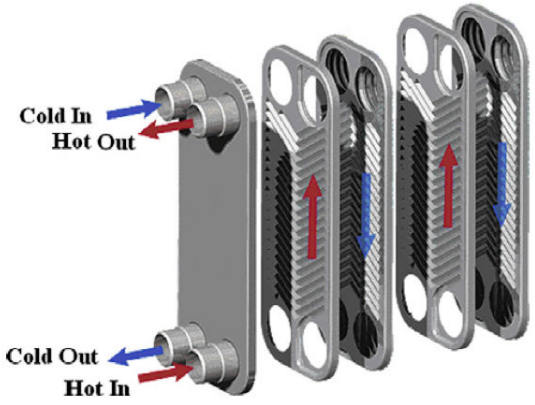

Figure 1.20 – Plate heat exchanger studied by Faizal and Ahmed [37]

1.4.2 Additive manufacturing process

Despite the numerous advantages AM presents for thermal components, the surface condition is degraded compared to traditional manufacturing processes. For instance, the Selective Layer Sintering (SLS) technology produces pieces with roughness between 5 and 35 μm [40]. In a conspic-

uous manner, the roughness is heavily dependent on AM process, materials, printing parameters, build direction and many more parameters. The roughness of HX built by 3D printers is still an active field of research, especially on controlling the surface condition, evaluating its effect on HX performance, and developing numerical models capable of predicting those performances.

One of the first studies investigating the effect of roughness on HX performance was conducted by Ventola *et al.* [22]. They have built via DMLS (direct metal laser sintering) flat and finned heat sinks (Fig. 1.21) for electronics cooling. On average, they found a convective heat transfer enhancement of 63 % for flat surfaces and 35 % for finned ones. They also proposed a correlation for estimating heat transfer of the flow through a DMLS rough channel via the Nusselt number, which represents the ratio between convective and conductive heat transfer. The latter seemed to be in good agreement with their experimental data.

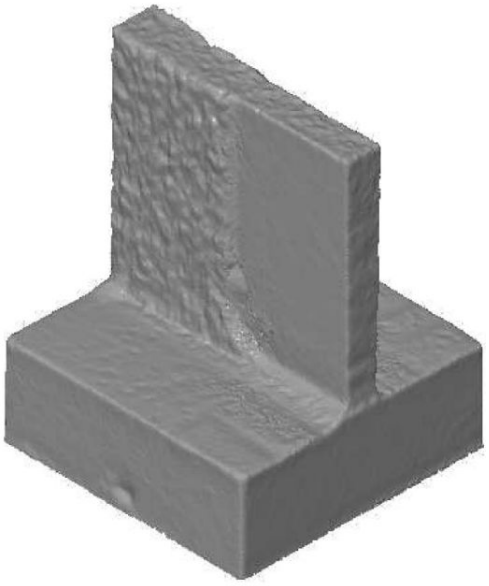

Figure 1.21 – 3D scan of a AM plate fin [22]

Concerning mini-channels HX, Stimpson *et al.* [23] have experimentally investigated the dependence of performance on roughness and hydraulic diameter. The comparison was made between small channels manufactured by DMLS (Direct Metal Laser Sintering) (Fig. 1.22) and the same configuration made by traditional manufacturing. The results showed that increasing the relative roughness led to a decrease in performance in terms of pressure loss, but an increase in thermal performance compared to a conventional heat exchanger. They also compared AM channels to grooved channels and found similar performance.

In the same way but for a different configuration, Bichnevicius *et al.* [41] have scrutinized four compact louvered plate-fin oil coolers. One was conventionally manufactured in aluminum, and the three others were made by selective laser melting (SLM) with the aluminum alloy AlSi10Mg powder. Results underline the fact that the overall performance for this geometry of AM HX are similar to that of the traditional HX. Nevertheless, some performance variations were noticed between the three AM HX, although the same digital model was used for printing.

Leeds *et al.* [42] developed numerically and experimentally a high-performance fin pin HX made with filler polymer using AM. CFD allowed to optimize the geometrical parameters and to predict the overall HX performance. The gap between CFD and experimental results is due to the difference between the designed and printed shape of HX (Fig. 1.23).

For instance, four types of plate-fin HX were compared by Saltzman *et al.* [4] (see Fig. 1.24).

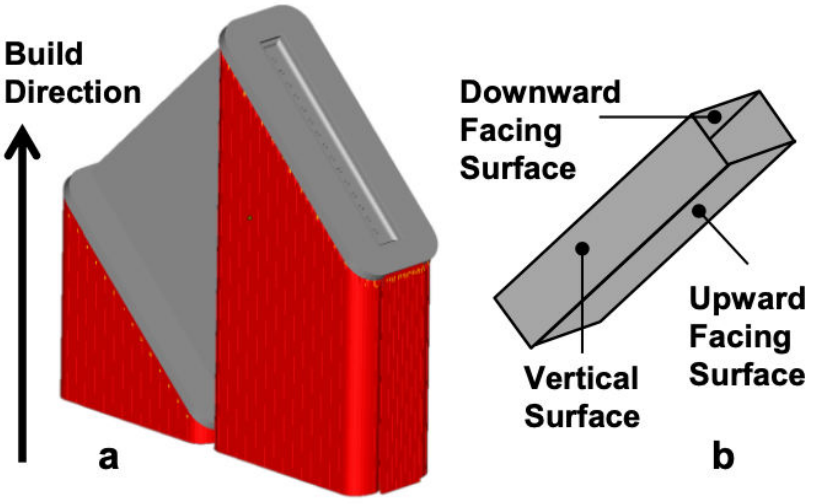

Figure 1.22 – Build orientation of the heat exchanger manufactured by Stimpson *et al.* [23] and channel surfaces denomination

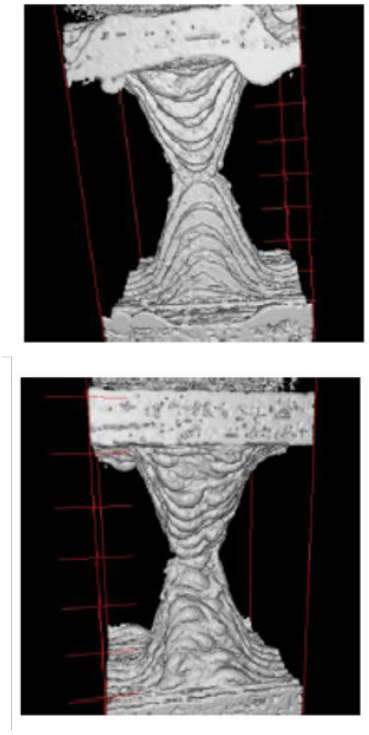

Figure 1.23 – Part of printed heat exchanger by Leeds *et al.* [42]

A traditional aluminum HX was considered as the baseline and the latter was replicated with AM. Enhanced versions of each were also built. For the AM HX, heat transfer was increased by 10 % relative to the baseline but the pressure drop was doubled due to the surface roughness. Vortex generators for the enhanced AM HX slightly improved the heat transfer and friction factor. They have concluded that the design has to be modified compared to the original and to be thought for AM.

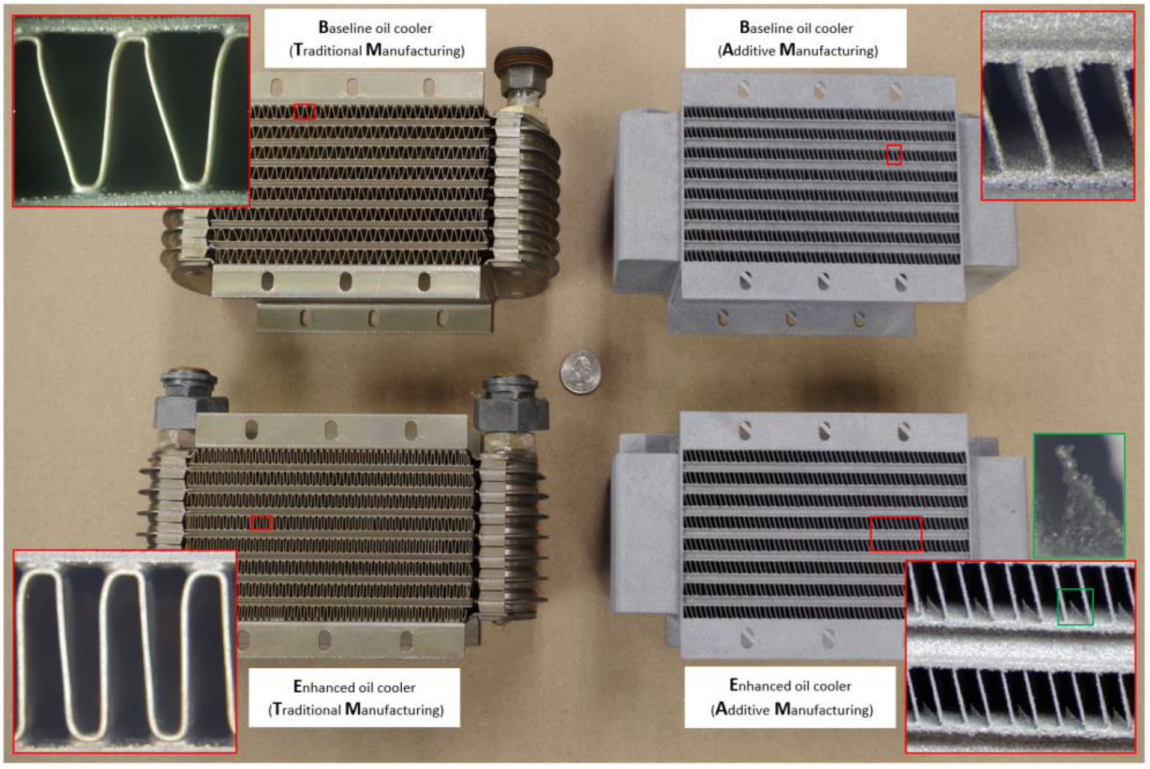

Figure 1.24 – Four heat exchangers tested by Saltzman *et al.* [4]

New possible geometries with AM could then provide the ability to reduce the impact of roughness and by the following pressure losses. One oriented-AM design was proposed by Chekurov *et al.* [43] with a lattice-and-chamber counterflow HX (Fig. 1.25). As it was optimized for AM, obtained performance were excellent and the authors also relied on the intrinsic AM roughness for boosting heat transfer.

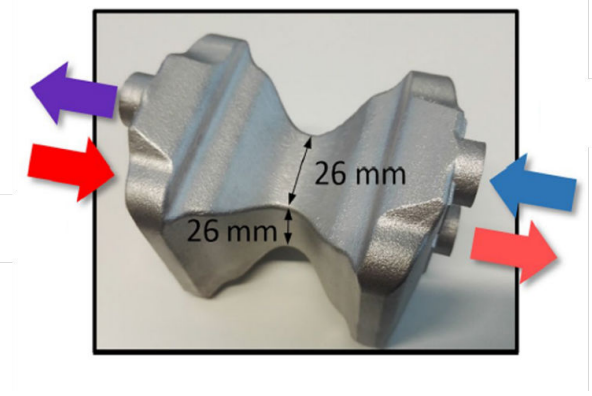

Figure 1.25 – Counter flow heat exchanger by Chekurov *et al.* [43]

Finally, Snyder *et al.* [44] have studied the influence of direct metal laser sintering (DMLS) building direction on the HX performance (Fig. 1.26). Three build directions were tested for cylindrical channels and it appeared that the vertical building direction presented the lowest friction factor. However, similar heat transfer was observed for all tested directions.

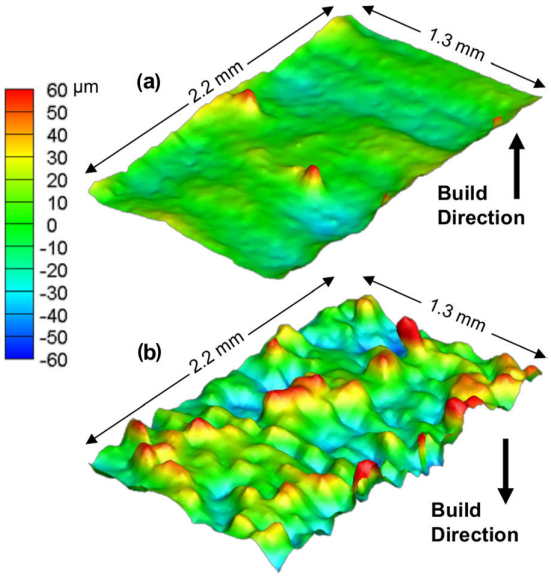

Figure 1.26 – Smooth and roughness HX interfaces [44]

Studies have globally demonstrated a comparable thermal performance with AM or a slight enhancement of heat transfer although the increase of surface roughness. Besides, it should be noted that HX shapes were in the majority designed from slight modifications of conventional configurations. Hence, special AM designs can be proposed for a better improvement of global performance.

1.5 Concluding remarks

Numerous types of heat exchangers exist and some classifications are necessary. One of the latter is based on compactness, which is defined as the ratio between the heat transfer area and the heat exchanger's volume. A compactness discrimination threshold value is used to distinguish between compact and non-compact heat exchangers.

While conventional manufacturing processes are still used, the application of additive manufacturing for heat exchangers has recently gained attention in several research studies and industrial fields. The primary advantages of additive manufacturing include the ability to design complex geometries and achieve high thermal performance in heat exchangers while reducing mass, volume, and cost.

However, additive manufacturing techniques present some limitations, particularly the surface condition. have attempted to assess the impact of roughness on conventional geometrical shapes. Few heat exchanger designs have been proposed until now in order to use the full additive manufacturing potential.

CHAPTER 2

Turbulence modeling and numerical tools

The theoretical background of fluid dynamics is presented in this chapter. The first part deals with the numerical modeling of turbulent flows. Standard numerical methods for simulating turbulent flows are presented, focusing on the Large-Eddy Simulation filtered equations and the closure models. Finally, the second part presents the YALES2 CFD platform used during this thesis and its main features.

Contents

2.1 Numerical modeling for turbulent flows

2.1.1 Navier-Stokes equations

In continuum mechanics, the dynamic of fluid is governed by the Navier-Stokes equations. This set of equations can rigorously be derived from statistical mechanics over control volumes and from fundamental principles such as the mass, the momentum, and the energy conservation equations. The derivation is not trivial and can be found in the literature [45]. Using the conservative form and Einstein's index notation, the mass, the momentum, and the energy conservation equations are expressed hereafter.

- **The continuity or mass-conservation equation**

$$\frac{\partial \rho}{\partial t} + \frac{\partial \rho u_i}{\partial x_i} = 0 \tag{2.1}$$

with ρ the fluid density and u the fluid velocity. In this thesis, the fluid is set to a constant density, and Eq. 2.1 gives the velocity field to be divergence-free:

$$\frac{\partial u_i}{\partial x_i} = 0 \tag{2.2}$$

- **The momentum-conservation equation**

$$\frac{\partial u_j}{\partial t} + u_i \frac{\partial u_j}{\partial x_i} = \frac{1}{\rho} \frac{\partial \sigma_{ij}}{\partial x_i} + f_j \tag{2.3}$$

where f_j denotes volumic forces and σ_{ij} refers to the stress tensor that may be expressed for constant property Newtonian fluids as

$$\sigma_{ij} = -P\delta_{ij} + \tau_{ij} \tag{2.4}$$

with P the pressure, δ_{ij} the Kronecker symbol and τ_{ij} the viscous stress tensor. For a Newtonian fluid, the latter tensor can be expressed in the following manner:

$$\tau_{ij} = \mu \left(\frac{\partial u_i}{\partial x_j} + \frac{\partial u_j}{\partial x_i} \right) - \frac{2}{3} \mu \frac{\partial u_k}{\partial x_k} \delta_{ij} \tag{2.5}$$

where μ is the dynamic viscosity. The divergence-free property leads to:

$$\tau_{ij} = \mu \left(\frac{\partial u_i}{\partial x_j} + \frac{\partial u_j}{\partial x_i} \right) \tag{2.6}$$

$$\frac{\partial \tau_{ij}}{\partial x_i} = \mu \frac{\partial^2 u_j}{\partial x_i \partial x_i} \tag{2.7}$$

The viscous stress tensor is also generally written according to the strain rate tensor S_{ij} with ν the kinematic viscosity:

$$\tau_{ij} = 2\rho\nu S_{ij}, \text{with } S_{ij} = \frac{1}{2} \left(\frac{\partial u_i}{\partial x_j} + \frac{\partial u_j}{\partial x_i} \right) \tag{2.8}$$

Finally, the substitution of the stress tensor into the momentum conservation equation Eq. 2.3 gives for a divergence-free velocity field:

$$\frac{\partial u_j}{\partial t} + u_i \frac{\partial u_j}{\partial x_i} = -\frac{1}{\rho} \frac{\partial P}{\partial x_j} + \nu \frac{\partial^2 u_j}{\partial x_i \partial x_i} + f_j \tag{2.9}$$

- **The energy-conservation equation**

$$\rho\frac{\partial E}{\partial t} + \rho\nabla\cdot(Eu) = -\rho\nabla\cdot(Pu) + \nabla\cdot(\tau\cdot u) - \nabla\cdot q + \dot{Q} \tag{2.10}$$

with E the total energy, which is the sum of the internal energy and the kinetic energy

In the energy-conservation equation, $q = -\lambda\nabla T$ refers to the heat flux depending on the product of the thermal conductivity λ and the temperature gradient according to Fourier's law. Finally, $\dot{Q}$ denotes the volume of the heat source.

The conservation equations system requires a thermodynamic closure. The latter is obtained by an equation of state that relates the thermodynamic parameters of the system. The most common equation of state for characterizing a gas is the perfect gas equation:

$$P = \rho\frac{\mathcal{R}}{W}T \tag{2.11}$$

with $\mathcal{R} = 8.314$ J.mol^{-1}.K^{-1} the universal gas constant and W the mixture molar mass.

2.1.2 Turbulent flows

The notion of turbulent flows was introduced by Reynolds [46], who identified two different states of fluid motion: laminar and turbulent. The laminar flow sees its perturbations damped due to the molecular viscosity while the flow remains "organized". Contrariwise, with increasing velocities, the viscosity is no longer sufficient to dissipate all the perturbations, and various instability mechanisms of non-linear nature will amplify them. The flow evolves then to a turbulent state where its behavior becomes chaotic and intermittent, related to the apparition of an extensive range of temporal scales and spatial structures in the flow. An example of such an instability mechanism is the Kelvin-Helmholtz instability which occurs when there is velocity shear at the interface between two fluids or regions of the same continuous fluid, producing vortical structures.

Yet, turbulent and laminar flows are governed by the same conservation equations. The Navier-Stokes equations can describe both regimes as well as the transition due to their non-linearity behavior. Turbulent flows involve a wide range of spatial and time scales. These flows are characterized by an unsteady nature and disordered flows, and are by definition three-dimensional, unsteady and chaotic phenomena.

Most industrial applications involve turbulent flows, whose properties present various interesting advantages. Among the various uses of turbulence in the industrial domain, some interesting applications may be the reduction of drag force in zones where the flow is detached or the triggering of the mixing of a fluid with multiple components.

The transition from the laminar to the turbulent regime can be quantified by looking at the balance between inertial forces that increase instabilities and viscous forces that absorb and dissipate structures. The dimensionless number introduced by Reynolds represents this balance and is expressed hereafter:

$$Re = \frac{UL}{\nu} \tag{2.12}$$

where U refers to the characteristic velocity of the flow, L to the characteristic length of the configuration, and ν represents the kinematic viscosity of the fluid. Hence, small values characterize laminar flows, while turbulent flows are associated with larger values. The transition between the two regimes takes place around a critical value of the Reynolds number, which depends on the geometry of the domain in which the fluid flows.

The different levels of spatial scales or turbulent structures are associated with different energetic levels. The largest scales, where the most significant structures develop, have a greater energetic level. When large scales transfer the energy of motion to small scales, it is called the energy cascade. This notion of energy cascade was introduced by Richardson [47] and Kolmogorov [48]. The spectrum of turbulent kinetic energy is split into three main zones:

- **Integral zone**: it gathers the flow's largest and most energetic structures. They are associated with the integral scale l_t, defined as the macroscopic scale of the flow. As long as a structure is larger than the characteristic integral length scale, viscous effects will not affect it. The turbulent kinetic energy characterizing this region is defined as:

$$TKE = \frac{1}{2} u_i' u_i' \tag{2.13}$$

  where u_i' is the the fluctuation of the velocity u_i around its mean value $\bar{u}_i$ in the i direction ($u_i = \bar{u}_i + u_i'$).

- **Inertial subrange**: the inertial zone gathers the turbulent structures that are small and unstable enough to be broken into smaller eddies. This range is the beginning of the cascade energy transfer process. According to the Kolmogorov's hypothesis, energy is transferred from the largest eddies to the smallest isotropic ones following a law in $k^{-5/3}$ wavenumbers. Eddies in the inertial range are still large enough not to be subjected to viscous effects. The energy is then transferred between the different turbulent structures without dissipation.

- **Viscous dissipative zone**: the last zone of the cascade contains the smallest turbulent structures of the flow. Here, all the turbulent kinetic energy of the fluid is dissipated in the form of heat. These eddies are characterized by the Kolmogorov scale, whose length and velocity are defined as:

$$l_\eta = \left(\frac{\nu^3}{\epsilon}\right)^{\frac{1}{4}} \text{ and } u_\eta = (\nu\epsilon)^{\frac{1}{4}} \tag{2.14}$$

  where ϵ is the dissipation rate of turbulent kinetic energy that converts this same energy into heat due to the molecular viscosity of the fluid. It should be noted that the Reynolds number associated with the Kolmogorov scale equals one (Eq. 2.15). The viscous dissipation zone is dominated by molecular viscosity ν. The smallest scales of the flow have solely the role of dissipating energy.

$$Re_\eta = \frac{u_\eta l_\eta}{\nu} = 1 \tag{2.15}$$

It is interesting to notice the scale range's dependence on the Reynolds number. The ratio of the smallest to the largest scale evolves with the following similarity to the Reynolds number:

$$\frac{l_\eta}{l_t} \sim Re^{-3/4} \tag{2.16}$$

This ratio suggests that when the Reynolds number increases, the number of scales that transfer or dissipate energy also grows. For a given computational domain, more cells are necessary with a higher Reynolds number value to resolve the whole spectrum of scales.

2.1.3 Vortex identification in turbulent flows

Several criteria are defined in the literature to identify vortices within turbulent flows. They mostly rely on iso-surface of high vorticity [49], pressure iso-surface since the pressure tends to decrease because of the centrifugal force [50], or the eigenvalues of the tensor resulting from a combination of the antisymmetric part and symmetric part of the divergence of the velocity, named as λ_2 [51]. The criterion used in this thesis is based on the velocity gradient tensor proposed by Hunt *et al.* [52]: the Q-criterion, named after the second invariant of this tensor :

$$Q = \frac{1}{2}(\Omega_{ij}\Omega_{ij} - S_{ij}S_{ij}) \tag{2.17}$$

where Ω_{ij} and S_{ij} are respectively, the antisymmetric part and symmetric part of the gradient of the velocity field :

$$\Omega_{ij} = \frac{1}{2}\left(\frac{\partial u_i}{\partial x_j} - \frac{\partial u_j}{\partial x_i}\right) \text{ and } S_{ij} = \frac{1}{2}\left(\frac{\partial u_i}{\partial x_j} + \frac{\partial u_j}{\partial x_i}\right) \tag{2.18}$$

This criterion compares, locally, the rotation rate to the shear rate. The presence of a vortex implies large positive values $Q_{criterion}$ of the Q tensor. Therefore, vortices are defined as regions of positive $Q_{criterion}$, i.e., where the vorticity magnitude is higher than the strain rate, with the additional low-pressure condition. Most of the time, this second condition is assumed to be satisfied if $Q_{criterion} > 0$ [51].

2.1.4 Turbulence modeling approaches

As previously mentioned, the Navier-Stokes equations enable the representation of both laminar and turbulent flow dynamics. The solving of these equations can be achieved thanks to various numerical methods. Direct Numerical Simulation (DNS), Large-Eddy Simulation (LES), and Reynolds-Averaged Navier-Stokes Simulation (RANS) are the three main numerical approaches to perform turbulent flow simulations. A representative overview of the differences between these approaches is given in Fig. 2.1

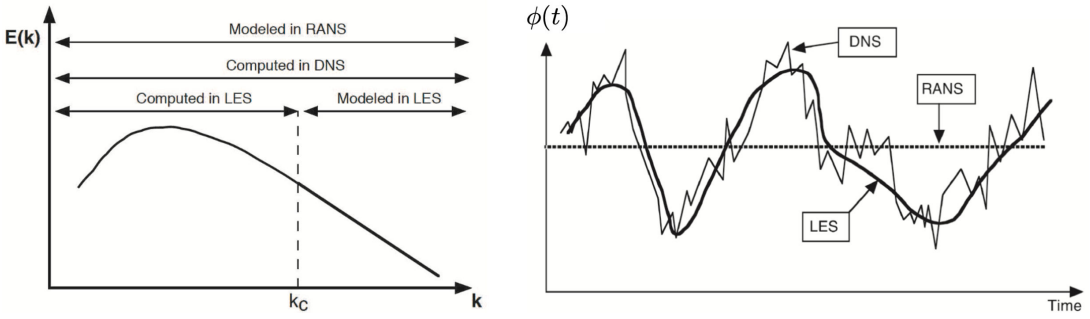

Figure 2.1 – Representation of the resolved and modeled parts of the turbulence scales for the DNS, LES, and RANS approaches in the spectral space (left) and in the physical space (right). (Extracted from [53])

- **Direct Numerical Simulation (DNS)**: it consists in capturing the continuous flow behavior correctly with all the turbulent scales. The discretized form of the Navier-Stokes equations is solved under the assumption that all turbulent structures are well resolved. In that case, no

modeling is necessary, and the only errors are related to the discretized representation of the computational domain. Nevertheless, this approach is extremely costly for highly turbulent flows. Despite recent progress of modern supercomputers, solving all the scales of a high Reynolds number flow is still impossible. Therefore it is generally only possible to perform such simulations for academic studies without limited computational resources. As DNS cannot systematically be applied, other formalisms have to be chosen by adding physical models that avoid resolving all the spatial scales of the turbulence and thus decreasing the computational cost of the simulation.

- **Reynolds-Averaged Navier-Stokes Simulation (RANS)**: the Navier-Stokes equations are solved by applying the Reynolds decomposition. Hence, this formalism enables access only to the static fields. Indeed, this decomposition leads to compute the mean flow field while completely modeling the fluctuating contribution of the flow. Thus, the turbulence has to be entirely modeled. Moreover, because of the nonlinearity of the Navier-Stokes equations, unresolved terms appear in the statistical equations, and then their closures necessitate turbulence models. The RANS approach is attractive for industrial companies since refined meshes are not required and short restitution times are expected.

- **Large-Eddy Simulation (LES)**: in this approach, the largest eddies are resolved while the smallest vortical structures are modeled. This formalism can be seen as a trade-off between the high computational cost of the DNS approach and the entire modeling of turbulent scales in the RANS approach. Indeed, it consists in applying a spatial filtering operator to the Navier-Stokes equations to resolve only the largest scales of the flow. Some criteria aim at estimating the needed resolution of the LES approach [45, 54, 55]. Contrary to the RANS approach, it does not rely on the computation of a mean flow field but instead on a filtered instantaneous field, where the smallest scales have been removed. In that case, unclosed filtered terms, representing the effects of the smallest scales on the largest ones, must be modeled. Finally, LES decreases the computational cost of turbulent flow simulations compared to DNS and can be applied to various complex configurations.

  All simulations performed in this thesis use the LES formalism, which is presented in detail hereafter.

2.1.5 LES filtered-equations

This formalism relies on modeling the dissipative scales of the flow. Therefore it implies the application of a low-pass filter to the Navier-Stokes equations. Applied on a scalar $\phi(\mathbf{x}, t)$, this filtering process consists of a spatial convolution product which is presented in Eq. 2.19.

$$\bar{\phi}(\mathbf{x}, t) = \int_{\mathbb{R}^3} \phi\left(\mathbf{x}', t\right) \mathcal{G}_\Delta\left(\mathbf{x}' - \mathbf{x}\right) \mathrm{d}\mathbf{x}' \tag{2.19}$$

where $\bar{\phi}$ is the filtered quantity and $\mathcal{G}_\Delta$ is the filter associated to the cutoff scale length Δ. Some properties should be satisfied by such homogeneous filters.

- **Normalization for conservation of constants**

$$\bar{\alpha} = \alpha \rightarrow \int_{\mathbb{R}^3} \mathcal{G}_\Delta\left(\mathbf{x}\right) \mathrm{d}\mathbf{x} = 1 \tag{2.20}$$

- **Linearity**

$$\overline{\phi + \psi} = \overline{\phi} + \overline{\psi} \tag{2.21}$$

- **Commutativity for spatial and temporal derivation**

$$\overline{\frac{\partial \phi}{\partial s}} = \frac{\partial \overline{\phi}}{\partial s} \tag{2.22}$$

We can decompose a variable ϕ in a part that is representative of the turbulence scales larger than Δ, noted as $\bar{\phi}$, and a part evolving in the turbulence scales smaller than Δ, noted as $\phi^{'}$, thus giving the following expression:

$$\phi\left(\mathbf{x}, t\right) = \bar{\phi}(\mathbf{x}, t) + \phi^{'}\left(\mathbf{x}, t\right) \tag{2.23}$$

In general, in case the fluid density is variable, we can introduce the notion of the Favre averaging, which is a density-weighted average expressed as:

$$\widetilde{\phi} = \frac{\overline{\rho\phi}}{\bar{\rho}} \tag{2.24}$$

Applying this filtering to the discretized Navier-Stokes equations gives the filtered LES system of equations:

$$\begin{aligned} \frac{\partial \bar{\rho}}{\partial t} + \frac{\partial \bar{\rho}\widetilde{u}_i}{\partial x_i} &= 0 \\ \frac{\partial \bar{\rho}\widetilde{u}_j}{\partial t} + \frac{\partial \bar{\rho}\widetilde{u}_i\widetilde{u}_j}{\partial x_i} &= -\frac{\partial \bar{P}}{\partial x_j} + \frac{\partial \bar{\tau}_{ij}}{\partial x_i} - \frac{\partial}{\partial x_i}\left[\bar{\rho}\left(\widetilde{u_i'u_j'} - \widetilde{u_i'}\widetilde{u_i'}\right)\right] \end{aligned} \tag{2.25}$$

A closure model for the stress tensor $\tau_{ij}^{SGS} = -\bar{\rho}\left(\widetilde{u_i'u_j'} - \widetilde{u_i'}\widetilde{u_i'}\right)$, named the sub-grid stress tensor, is necessary. In LES, the turbulence modeling consists in proposing formulations for the sub-grid stress tensor based on the filtered variables of the above equations.

The sub-grid stress tensor needs to be described by a turbulence model to correctly reproduce the energy transfer from the resolved scales to the non-resolved ones. In this work, only the classical Boussinesq hypothesis [56] is used for the models, which suggests that the sub-grid stress tensor can be formulated like the viscous stress tensor by using a turbulent viscosity $\nu_t = \mu_t/\rho$ such that:

$$\tau_{ij}^{SGS} = \rho\nu_t\left(\frac{\partial \widetilde{u}_i}{\partial x_j} + \frac{\partial \widetilde{u}_j}{\partial x_i}\right) - \frac{2}{3}\rho\nu_t\frac{\partial \widetilde{u}_k}{\partial x_k}\delta_{ij} \tag{2.26}$$

In addition, as demonstrated by Vasilyev *et al.* [57], commutation errors occur due to the filtering. Consequently, care must be taken to ensure that the mesh is of good quality. This explains the efforts made to achieve good meshes, as shown in Chapter 4.

2.1.6 Sub-grid scale modeling

The sub-grid scale turbulence models in LES are formulations of the turbulent viscosity ν_t. In the YALES2 library, a variety of turbulence models is available. Some of the most commonly used are the standard and dynamic Smagorinsky models and the WALE model.

Smagorinsky model

The classical Smagorinsky model [58] is based on the hypothesis of an equilibrium between the creation and the dissipation of kinetic energy at the filter scale Δ. The turbulence here is considered to be a purely dissipative phenomenon, and the formulation of ν_t is:

$$\nu_t = \left(C_{smago}\Delta\right)^2\sqrt{2\widetilde{S}_{ij}\widetilde{S}_{ij}} \tag{2.27}$$

where C_{smago} is the Smagorinsky constant and $\widetilde{S}_{ij}$ is the filtered deformation tensor:

$$\widetilde{S}_{ij} = \frac{1}{2}\left(\frac{\partial \widetilde{u}_i}{\partial x_j} + \frac{\partial \widetilde{u}_j}{\partial x_i}\right) \tag{2.28}$$

The choice of the value for the constant C_{smago} depends on the configuration of interest, but the usual range is between 0.1 and 0.2. However, this model is known to be too dissipative and handles poorly the turbulence near walls.

Germano *et al.* [59] and Lilly [60] suggested to modify the constant C_{smago} locally and in time. The smallest resolved scales deduce the behavior of the sub-grid scales. This requires a second filtering of the resolved velocity with a filter scale $\Delta' > \Delta$. The constant is then determined using the two differently filtered velocity fields. This model is known as the dynamic Smagorinsky model. It is more costly but gives better results for a wide range of applications.

WALE model

The Wall-Adapting Local Eddy-Viscosity (WALE) from Nicoud and Ducros [61] suggests using a turbulent viscosity profile near the walls to better predict the laminar-turbulent transition. The formulation of the turbulent viscosity becomes:

$$\nu_t = (C_{wale}\Delta)^2 \frac{\left(s^d_{ij}s^d_{ij}\right)^{3/2}}{\left(\widetilde{S}_{ij}\widetilde{S}_{ij}\right)^{5/2} + \left(s^d_{ij}s^d_{ij}\right)^{5/4}} \tag{2.29}$$

where C_{wale} is a constant with a recommended value of 0.5 and the tensor s^d_{ij} is written as:

$$s^d_{ij} = \frac{1}{2}\left(\widetilde{h}_{ij} + \widetilde{h}_{ji}\right) - \frac{1}{3}\widetilde{h}_{kk}\delta_{ij} \tag{2.30}$$

with:

$$\widetilde{h}_{ij} = \widetilde{g}_{ik}\widetilde{g}_{kj} \text{ and } \widetilde{g}_{ij} = \frac{\partial \widetilde{u}_i}{\partial x_j} \tag{2.31}$$

This formulation allows the model to consider rotation and strain rate with s^d_{ij}. Thus all turbulent structures are considered for energy dissipation. Also, the turbulent viscosity tends to zero in sheared flows which is the expected behavior near the walls.

2.2 Presentation of YALES2 platform

After having described the theoretical background, this section presents the CFD platform YALES2. A global overview of all the numerical strategies implemented to solve the Navier-Stokes equations on massive meshes is given.

2.2.1 Overview

The numerical simulations presented in this thesis are performed using the finite-volume CFD library YALES2 [62], a low-Mach number Large-Eddy Simulation (LES) and Direct Numerical Simulation (DNS) solver based on unstructured meshes. This library allows having a multi-physics approach to solve the incompressible or low-Mach number Navier-Stokes equations in two and three dimensions. This multi-physical approach arises from the various solvers available in this library, going from non-reactive turbulent flows [63] to two-phase flows [64] and reactive variable density flows [65].

YALES2 enables the management of all types of elements through dual control volumes to integrate transport equations. The control volumes (CV), where the transport equations are integrated, are constructed around the computational grid nodes of the mesh. A schematic representation of a CV is given in Fig. 2.2. The physical variables, such as the velocity and the pressure for example, are also stored on the nodes representing the average value over the CV. At the same time, the fluxes are computed on the control volume's edges. In addition, YALES2 is specifically tailored to solve the incompressible and low-Mach number equations on massively parallel machines with billion-cell meshes.

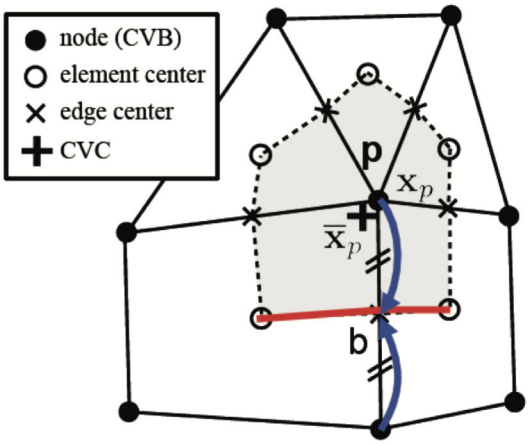

Figure 2.2 – A YALES2 control volume based around a grid node. x_p is the position of the node and $\overline{x}_p$ is the position of the CV barycentre

2.2.2 Main tools and strategies

In LES, fidelity increases with the mesh resolution, the simulated physical time, or by adding complexity to the physics of the flow. Therefore, the steady increase of computational resources supports the development of the CFD field. Here is a list of some of the main tools and strategies developed in the CFD platform YALES2 to perform high-performance computing:

- Low-Mach number approach, for constant and variable-density cases
- Interface tracking for two-phase flows
- Parallel dynamic mesh adaptation and dynamic load balancing
- High-order filtering (HOF)

Not all these strategies are used in this thesis, yet the YALES2 library allows to couple different methodologies easily.

2.2.3 Numerical schemes and operator splitting

The CFD library YALES2 features several numerical schemes for the explicit time advancement of the temporal integration, such as the classical third- and fourth-order Runge-Kutta schemes. In this thesis, only the TFV4A scheme is used. This scheme has been proposed by Kraushaar [66], combines both Runge-Kutta and Lax-Wendroff methods, and is a 4th-order accurate finite-volume method.

Concerning spatial integration, second and fourth-order schemes have been implemented. In this thesis, only the 4th-order spatial scheme is used. Moreover, even if many solvers dedicated to different physical phenomena are implemented into YALES2, only the Incompressible solver (ICS) at constant density has been used during this thesis and is presented hereafter.

To alleviate the constraint of the multiple temporal scales, the YALES2 solver uses an operator splitting method [67] [68]. This method consists in solving each operator (convection, diffusion, etc.) separately with its proper characteristic time-step. The advantage of this method stems from the choice of the time-step used in each iteration taken as the largest characteristic time of the different physical phenomena. Usually, the time step chosen is that of the convection. The diffusion takes multiple sub-steps inside the fluid iteration in order to respect its proper stability condition. However, the operator splitting is susceptible to accumulate numerical errors, known as splitting errors, over time. These errors become larger if the ratio between different characteristic time steps becomes very large.

2.2.4 Double-domain decomposition and parallelism

To solve the incompressible Navier-Stokes equations on unstructured mesh in a massively parallel framework, YALES2 splits its computational domain [62]. Each processor has a part of the domain assigned. The dependency between each sub-domain is considered thanks to communications between processors. These processors exchange information at the interface of each cell group using MPI (Message Passing Interface) instructions. The mesh decomposition must assure an optimal workload repartition between processors. In a purely Eulerian context, the most obvious way is to cut the mesh into sub-domains containing the same number of control volumes. While this decomposition might be trivial for structured meshes, it is not for unstructured meshes. Since YALES2 mainly focuses on unstructured grids, the domain decomposition is handled by external libraries, which are METIS [69] and SCOTCH [70].

In YALES2, this approach is taken a step further to optimize the performances of computations involving a considerable number of processors by using a double-domain decomposition. In this case, the sub-domains created by the first decomposition of the mesh, and attributed to a processor, are further decomposed into multiple groups of computational cells (defined by the grey interfaces in Fig. 2.3). The size of these element groups is determined so that the data contained in them suits the capacities of the processors' cache memory. This double-domain decomposition primarily benefits the optimization of the Poisson solver's performances. In fact, these element groups serve as a coarse mesh used by the two-stage linear solvers like the DPCG [71]. The solver now involves two types of communications: i) external communications between processors at the black interfaces in Fig. 2.3 handled by the MPI communications; ii) internal communications allowing exchanges between the element groups at the grey interfaces in Fig. 2.3, found in a processor. The internal communications are not handled by MPI. In Fig. 2.4, a schematic shows data communication and exchange between element groups, communicators, and boundary conditions.

2.2.5 Incompressible constant density solver (ICS)

The YALES2 CFD platform offers a wide range of different solvers tailored for various physical problems. For aerodynamic studies at low-Mach number flows, like impacting 3D jets or non-reactive flow in closed geometries, the incompressible solver (ICS) is proposed.

The incompressibility hypothesis implies that the density of the fluid remains constant in time and space. This is incorporated into the Navier-Stokes equations used by the incompressible YALES2 solver, and they read as follows:

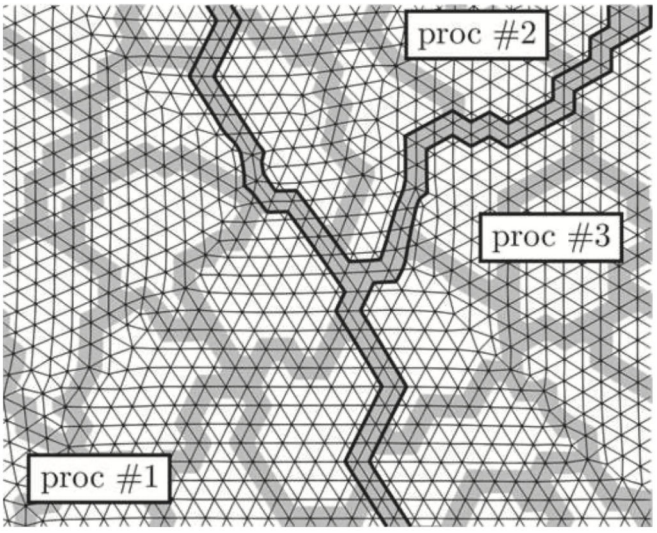

Figure 2.3 – A representation of the double-domain decomposition on a 2D triangular mesh [62]

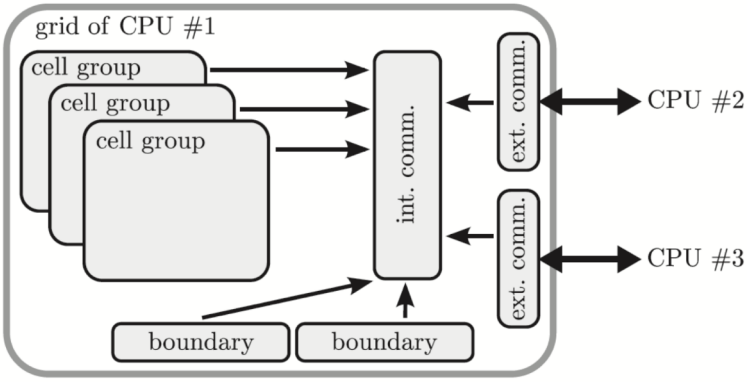

Figure 2.4 – Schematic of the communications when using double-domain decomposition [62]

$$\begin{aligned} \nabla \cdot u &= 0 \\ \frac{\partial u}{\partial t} + \nabla \cdot (u \otimes u) &= -\frac{1}{\rho}\nabla P + \frac{1}{\rho}\nabla \cdot \tau + f \end{aligned} \tag{2.32}$$

where u is the fluid velocity, P the pressure, ρ the constant fluid density, the viscous stress tensor is now written as $\tau = \mu(\nabla u + \nabla u^T)$ with μ the dynamic viscosity and f other volumetric force terms depending on the physics (gravitational force for example). For simplicity, the latter forcing term will be omitted in the demonstration of the following resolution method.

The solving of the Navier-Stokes equations for incompressible flows is based on the projection method proposed by Chorin [67] modified by Kim and Moin [72]. It is noticeable that this formalism resolves the instantaneous velocity field at each time step (associated with integer indices such as n, $n+1$, etc...) when the density, the pressure, and other scalar fields are resolved on staggered time step (associated to non-integer indices such as $n+1/2$, $n+3/2$, etc...). The main stages of this methodology are presented hereafter.

The classical projection method, often used for the simulation of incompressible flows, relies on the Helmholtz-Hodge decomposition under the relatively smooth assumption. At each time

step, the velocity field can be decomposed into an irrotational part and a solenoidal part as

$$u = \Pi_i(u) + \Pi_s(u) \tag{2.33}$$

where $\Pi_i(u)$ refers to the irrotational component and $\Pi_s(u)$ to the solenoidal part of the instantaneous velocity field with respectively the following properties $\nabla \times \Pi_i(u) = 0$ and $\nabla \cdot \Pi_s(u) = 0$. These projection operators are defined as

$$\begin{aligned} \Pi_i &= \nabla \Delta^{-1} \nabla \cdot \\ \Pi_s &= -\nabla \times \Delta^{-1} \nabla \times \end{aligned} \tag{2.34}$$

The operator Δ^{-1} is the inverse of the Laplacian operator. The irrotational component derives from a potential scalar and can thus be written as $\Pi_i(u) = \nabla \phi$. The application of the divergence operator enables to express the previous relation as follows:

$$\nabla \cdot u = \nabla \cdot [\Pi_i(u) + \Pi_s(u)] = \nabla \cdot \Pi_i(u) = \Delta \phi \tag{2.35}$$

Thanks to this decomposition, the velocity balance equation can therefore be solved in two steps:

1. **Prediction step**: A first estimation of the velocity field for the time $n+1$, noted u^*, is obtained by advancing the velocity equation without the contribution of the pressure gradient as it does not contribute to the solenoidal part but to the irrotational part of the velocity field.

$$\frac{u^* - u^n}{\Delta t} = -\nabla \cdot (u^* \otimes u^n) + \frac{1}{\rho} \nabla \cdot \tau^n \tag{2.36}$$

2. **Correction step**: Once the prediction has been made, leading to u^*, the velocity field is corrected by taking into account the pressure gradient:

$$\frac{u^{n+1} - u^*}{\Delta t} = -\frac{1}{\rho} \nabla P^{n+1/2} \tag{2.37}$$

The computation of the corrected velocity, noted here u^{n+1}, necessitates the knowledge of $P^{n+1/2}$, which can be determined by solving the Poisson's equation. This equation can be obtained by taking the divergence operator of the previous equation and integrating the zero divergence constraint for u^{n+1}.

$$\nabla \cdot u^* = \nabla \cdot \Pi_i(u^*) = \frac{\Delta t}{\rho} \Delta P^{n+1/2} \tag{2.38}$$

However, the advancement of the velocity equation that is implemented in the incompressible solver of YALES2 slightly differs [73] from Chorin's approach:

1. **Prediction step**: In that case, the prediction step is done by considering the contribution of the pressure gradient at the time $n - 1/2$ that is generally a relatively good approximation of $P^{n+1/2}$. This approach leads to a better estimation of the predicted velocity u^*, reducing the numerical errors due to the splitting of the temporal advancement.

$$\frac{u^* - u^n}{\Delta t} = -\nabla \cdot (u^* \otimes u^n) - \frac{1}{\rho} \nabla P^{n-1/2} + \frac{1}{\rho} \nabla \cdot \tau^n \tag{2.39}$$

2. **Correction step**: Then, the correction step can therefore be written as

$$\frac{u^{n+1} - u^*}{\Delta t} = -\frac{1}{\rho}\nabla\left(P^{n+1/2} - P^{n-1/2}\right) \tag{2.40}$$

which leads to a Poisson equation of the following form

$$\Delta\left(P^{n+1/2} - P^{n-1/2}\right) = \frac{\rho}{\Delta t}\nabla \cdot u^* \tag{2.41}$$

Finally, solving the Poisson equation is the critical point of the methodology as it necessitates efficient linear solvers to guarantee good performances for massively parallel computations.

The Poisson equation for the pressure presented in the previous section are equations that can be expressed in the form:

$$\Delta\phi = RHS \tag{2.42}$$

In this case, $\phi = P^{n+1/2} - P^{n-1/2}$ and the value of the RHS, the right-hand side, is set from the previous prediction-correction method. This equation deals with solving a linear system in which the discretized values of the pressure field at each computational node in the domain are unknown variables. Therefore, solving this system requires efficient linear solvers as it has to be done for each time step and may represent a predominant part of the CPU cost of the simulation. Indeed, these solvers are based on iterative numerical methods, and a high number of iterations might be necessary to reach a sufficiently accurate estimation of the solution. The number of iterations depends on the algorithms but also the characteristics of the discrete Laplacian operator.

Moreover, each iteration of the linear solver requires some communications between the processors that can represent a non-negligible part of the total simulation time. This proportion can reach 80% if no special considerations are taken into account for the method implementation [71]. Therefore, optimizing the Poisson equation resolution is one of the significant challenges for the simulation of incompressible flows. Finally, several algorithms are available in the CFD code YALES2: the Preconditioned Conjugate Gradient (PCG) [74], the Deflated PCG [75], and also the BiCGSTAB scheme [76].

2.3 Conclusions

This chapter outlined the physics and primary methodologies employed in this thesis. Firstly, it elaborated on the context of turbulent flows and the resolution of the Navier-Stokes equations. Secondly, it introduced the YALES2 CFD platform, from the key tools used in this thesis to the incompressible constant density solver.

CHAPTER 3

Large-Eddy Simulations for rough surfaces: a literature review

Roughness characterization and its impact on the flow are addressed in this chapter. In addition, an extensive literature review is presented about fully resolved rough wall simulations from past studies and the state-of-the-art strategies for roughness modeling.

Contents

3.1 Surface roughness: characteristics and impact

As surface roughness plays an essential role in tribology, this subject has been studied for many decades. The real surface condition can hardly be fully described by a single parameter. Indeed several characteristic parameters are mandatory if a complete surface description is desired.

This section deals with roughness description, which is the first step before addressing the related modeling aspects. Then, the correlation between roughness characteristics and the equivalent sand-grain roughness is also exposed.

3.1.1 Existing parameters

The roughness parameters can have two- (2D) or three-dimensional (3D) shapes. A 2D profile analysis of a surface has been mainly used in engineering applications until recently. However, this kind of analysis is inaccurate with new structures like those encountered in additive manufacturing. This is why a 3D analysis of surfaces is nowadays required to achieve an accurate surface topography.

For 2D analysis, parameters are calculated from a scan line of the surface and are denoted with a capital "R", while 3D roughness parameters are the average of several scan lines and are denoted with a capital "S".

Surface roughness parameters are categorized into three groups: amplitude, spacing, and hybrid. For a complete description of a real surface, almost sixty parameters are required [77, 78]. It is not intended to expose all of them here but only to address the most important ones.

Amplitude parameters

These parameters are used to characterize the vertical deviations of a rough surface (Fig. 3.1). They are predominant for surface topography.

Arithmetic average height

This parameter, commonly denoted R_a, is the most known among the others. In general, quality control is based on this parameter. As the surface average is considered in this manuscript, this parameter will be denoted S_a. Its definition is the average absolute deviation of the roughness irregularities from the mean plane h over the surface.

$$h = \frac{1}{L_x L_y} \int_{L_x} \int_{L_y} h(x,y)\, dxdy \tag{3.1}$$

where $h(x,y)$ is the surface height, L_x and L_y are respectively the streamwise and spanwise lengths. In the following, the mean plane is supposed to be $h = 0$.

The arithmetic average height gives a good estimate of height variations, and it is defined as:

$$S_a = \frac{1}{L_x L_y} \int_{L_x} \int_{L_y} \mid h(x,y) \mid \, dxdy \tag{3.2}$$

Root-mean-square roughness

The variance is given as:

$$\sigma^2 = \frac{1}{L_x L_y} \int_{L_x} \int_{L_y} (h(x,y) - h)^2\, dxdy = S_q^2 - h^2 \tag{3.3}$$

where S_q is the root-mean-square roughness. For the special case where $h = 0$, it implies $S_q = \sigma$.

$$S_q = \sqrt{\frac{1}{L_x L_y} \int_{L_x} \int_{L_y} h(x,y)^2\, dxdy} \tag{3.4}$$

Maximum height

This parameter provides information about estimated and expected maximal roughness. It is sometimes used for some correlations between roughness and the equivalent sand-grain roughness (defined in sub-section 3.1.2).

$$S_t = h_{\,highest\ peak} - h_{\,lowest\ valley} \tag{3.5}$$

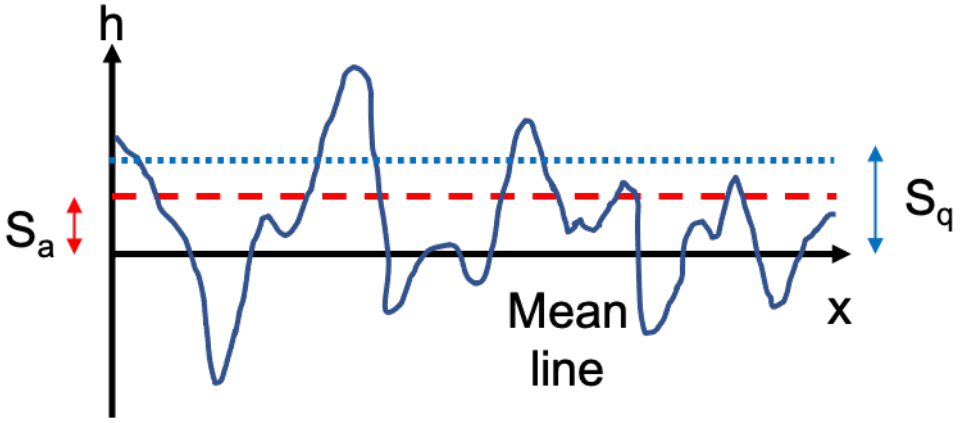

Figure 3.1 – Vizualisation of the arithmetic average height (S_a) and the root-mean-square roughness (S_q)

Skewness

This parameter is used to measure the symmetry of the profile with regard to the mean line (Fig. 3.2). The skewness is sensitive to occasional deep valleys or high peaks. Symmetrical height distribution, *i.e.* with as many peaks as valleys, has zero skewness. It should be noted that profiles with removed peaks or deep scratches have negative skewness, and profiles with valleys filled in or high peaks have positive skewness.

$$Sk = \frac{1}{{S_q}^3 L_x L_y} \int_{L_x} \int_{L_y} h(x,y)^3 \, dxdy \tag{3.6}$$

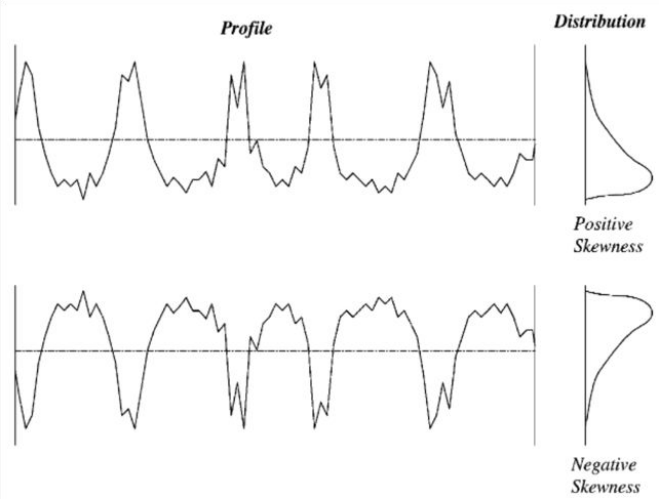

Figure 3.2 – Illustration of positive and negative skewness distributions [77]

Kurtosis

It is the fourth central moment of the profile amplitude probability density function, measured over the assessment length. It describes the sharpness of the probability density of the profile.

$$Ku = \frac{1}{{S_q}^4 L_x L_y} \int_{L_x} \int_{L_y} h(x,y)^4 \, dxdy \tag{3.7}$$

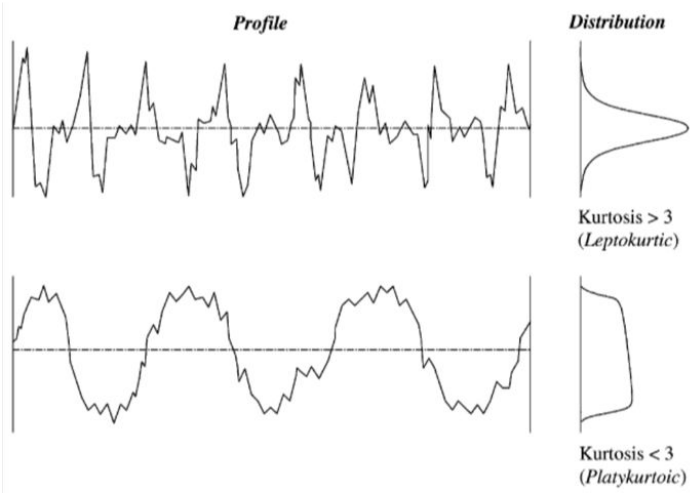

Figure 3.3 – Illustration of kurtosis distribution [77]

If $Ku < 3$, the distribution curve is said to be platykurtic and has relatively few high peaks and low valleys. If, however, $Ku > 3$, the distribution is said to be leptokurtic and has rather many high peaks but low valleys (Fig. 3.3).

Spacing and hybrid parameters

The horizontal characteristics are described with spacing parameters. The number of peaks or the spacing between peaks is as crucial as the average height to achieve a good topography.

The most useful parameter in our case is the mean spacing at the mean line (MS). It is calculated as $MS = \frac{1}{N} \sum_{i=1}^{n} S_i$ with S_i the spacing of adjacent local peaks and N the number of local peaks along the profile (Fig. 3.4).

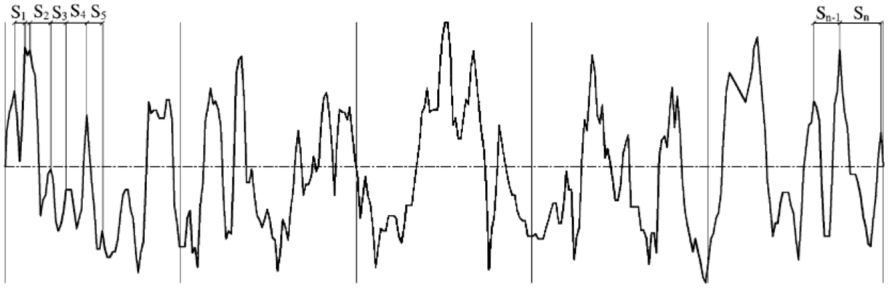

Figure 3.4 – Calculating the mean spacing [77]

The hybrid parameters are a consequence of combining amplitude and spacing properties. They are considered important factors in tribology. The only relevant parameter in our case is the effective slope, which is defined as:

$$ES = \frac{1}{L_x} \int_0^L \mid \frac{dh}{dx} \mid dx \tag{3.8}$$

where L_x is the streamwise length of the surface, and the space derivative is computed locally.

3.1.2 Equivalent sand-grain roughness (ESGR)

The study of turbulent boundary layers over rough surfaces is often based on the method of equivalent sand-grain roughness.

Correlation between the equivalent sand roughness and roughness parameters

A pioneering work was conducted by Nikuradse [79], who measured the pressure drop in pipe flows with walls covered by sand grains. The relative roughness k_s/d is used with k_s the diameter of sand grain cemented to the walls, and d the diameter of the pipe. The value of k_s corresponds to the sand-grain size, which produces the same skin-friction coefficient as the surface of interest in the fully rough regime. This parameter is thus a flow property rather than a physical property. The skin-friction coefficient is defined as:

$$C_f = \frac{2\tau_w}{\rho U_b^2} \tag{3.9}$$

where τ_w is the wall shear stress and U_b the bulk velocity. The experimental data provided by [79] revealed that the skin-friction coefficient C_f depends mainly on an equivalent sand roughness k_s for a sufficiently high Reynolds number regime.

Colebrook *et al.* [80] extended this work by studying the friction factor for industrial pipes. Then, Moody [81] concatenated and consolidated these data into a chart representing the friction factor against the friction Reynolds number for different values of k_s/d (Fig. 3.5). The friction Reynolds number is defined as $Re_\tau = u_\tau k_s/\nu$ with the friction velocity $u_\tau = \sqrt{\tau_w/\rho}$. This is the ratio between inertial and viscous forces through the viscous sublayer thickness.

An equivalent roughness is required for the estimation of a friction factor from the Moody chart. Thus the application of Moody's chart is limited to rough surfaces whose equivalent wall roughness is known *a priori*. However, measurement techniques used for analyzing the surface texture do not provide such parameter due to the definition of k_s. For any surface of interest, a hydraulic experiment is therefore needed to determine k_s.

This is why several studies have focused on finding a general correlation between k_s and physical roughness parameters, particularly with statistical moments of surface elevation.

Schlichting [82] measured k_s for different artificial roughness elements. In the fully turbulent wall region, the velocity profile follows a logarithmic law for smooth and rough surfaces. A new roughness parameter called solidity or roughness density Λ is defined. This is related to S_f/S_p where S_f is the total frontal-projected area of the roughness in the cross-streamwise direction, and S_p is the total plan area of the roughness in the streamwise direction. A relationship exists between the effective slope and the solidity such as $ES = 2\Lambda$. Basically, there are two regimes: the sparse one for which the roughness effect increases with the solidity, and the dense one for which it decreases because of the roughness elements that shelter each other. The value $\Lambda = 0.15$ delimits the two regimes (Fig. 3.6).

A review of roughness parameters for evaluating the equivalent sand roughness was published by Flack and Schultz [84]. They also proposed a correlation based on the root-mean-square and the skewness of roughness. This correlation is only for the fully rough regime (Fig. 3.7), which is related to $ES > 0.35$.

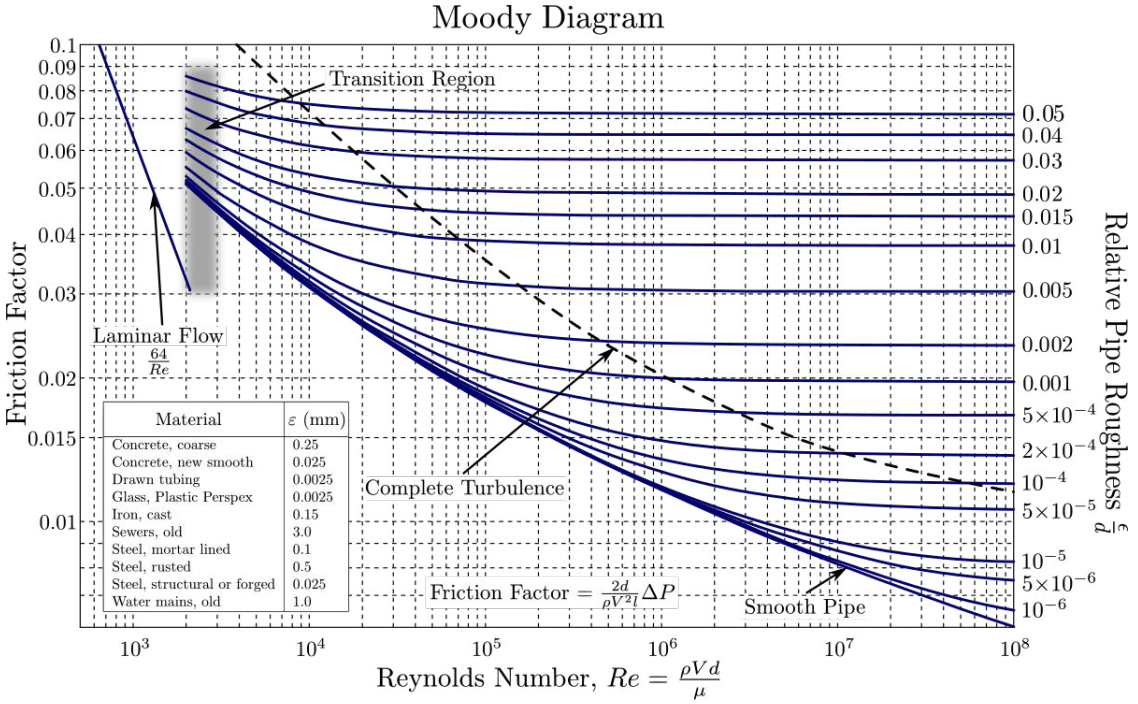

Figure 3.5 – Moody diagram for pipe flows [81] ($\epsilon = k_s$ here)

$$\frac{k_s}{S_q} = 4.43(1 + Sk)^{1.37} \tag{3.10}$$

More recently, Forooghi *et al.* [85] have found that a correlation based on surface height skewness and the effective slope can be used to better predict the ratio k_s/S_t such as:

$$k_s/S_t = 1.07(0.67Sk^2 + 0.93Sk + 1.3)(1 - e^{-3.5ES}) \tag{3.11}$$

Impact of roughness

In fact, the most critical effect of wall roughness on turbulent flows is the downward shift in the mean velocity profile via the roughness velocity function ΔU^+ (as shown in Flack and Schultz [84] for instance).

$$U^+(y^+) = \frac{1}{\kappa}\ln(y^+) + B - \Delta U^+ \tag{3.12}$$

where $\kappa = 0.4$ is the von Karman constant and the value $B = 5.5$ is the log-law constant for a smooth wall.

Equation 3.12 can be re-written as:

$$U^+(y^+) = \frac{1}{\kappa}\ln\left(\frac{y}{k_s}\right) + B - \Delta U^+ + \frac{1}{\kappa}\ln\left(k_s^+\right) \tag{3.13}$$

with $B - \Delta U^+ + \frac{1}{\kappa}\ln\left(k_s^+\right) \approx 8.5$

Many studies aimed to estimate ΔU^+ (Fig. 3.8) to understand the turbulent flow structures over rough walls and to quantify the impacts of the type of roughness.

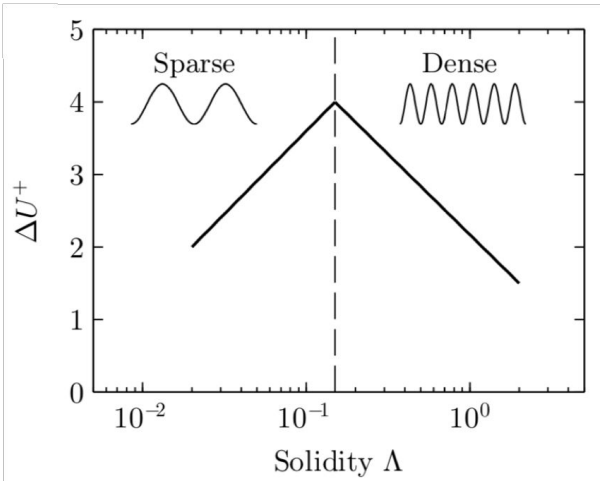

Figure 3.6 – Sketch of roughness velocity function ΔU^+ against solidity Λ [83]

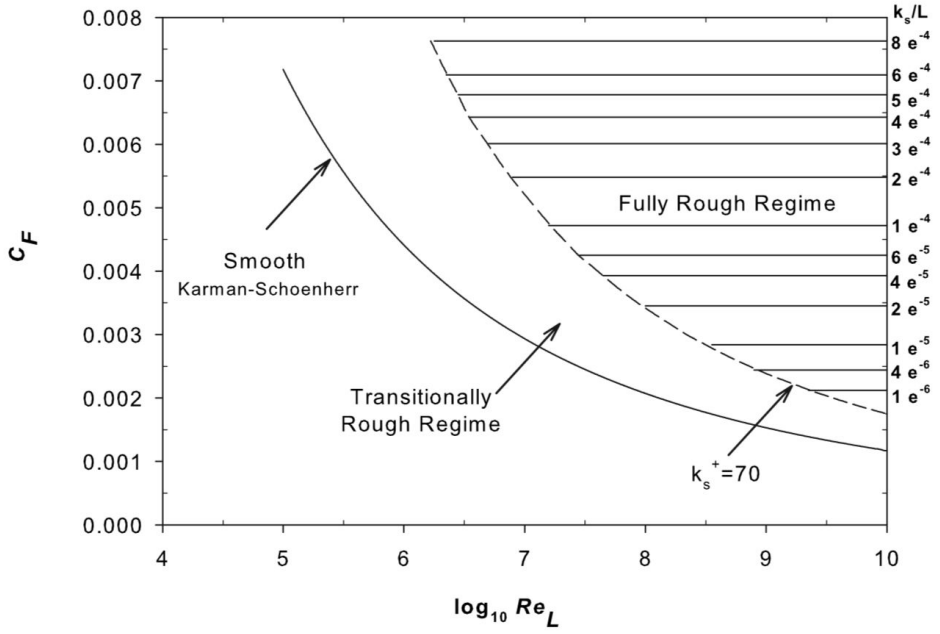

Figure 3.7 – Overall skin-friction coefficient versus Reynolds number [84]

3.2 Roughness-resolved models

Due to difficulties in correctly modeling the flow properties near rough walls, direct numerical simulations (DNS) or Large-Eddy Simulations (LES) with fully resolved rough walls (WRLES) were performed in order to investigate turbulence properties.

3.2.1 Simulations over spanwise extended transverse ribs

Understanding the impact of an isolated rough element on the flow structure is essential, and this is why many researchers studied flows over spanwise ribs [86, 87, 88, 89] (Fig. 3.9). In these studies, similar geometry is used with different initial conditions.

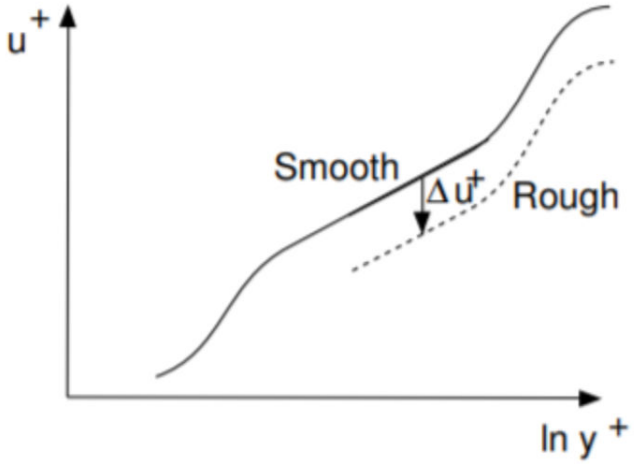

Figure 3.8 – Sketch of velocity profiles over smooth and rough walls plotted in wall-unit variables

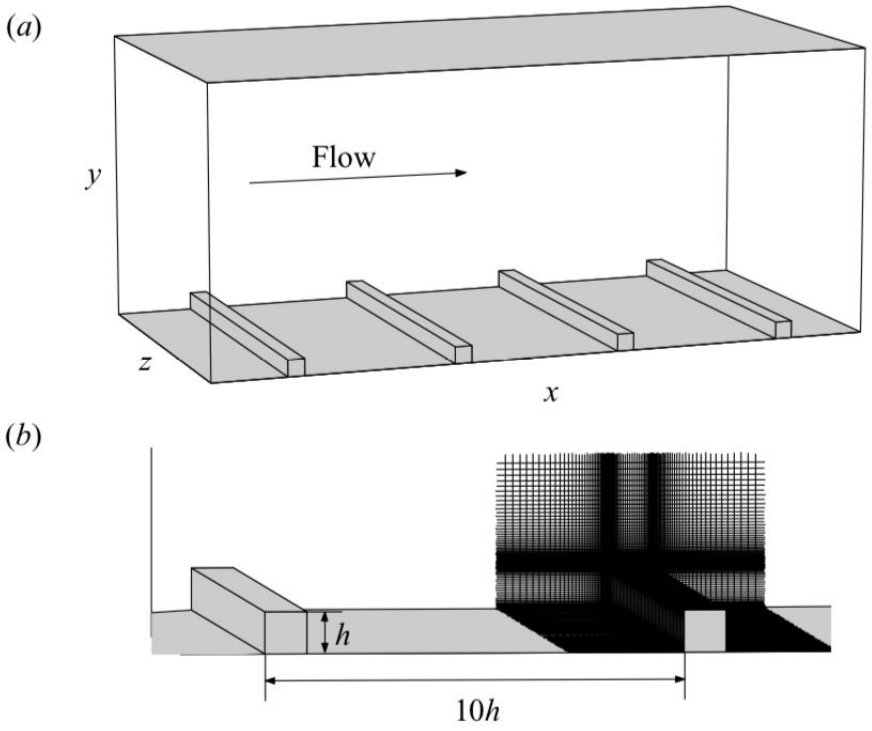

Figure 3.9 – (a) Asymmetric channel geometry of the representative case. (b) Configuration of rib roughness and a subset of the numerical grid (Ikeda and Durbin [88])

As shown in Fig. 3.10a, a reversal flow forms upstream and downstream of the rib caused by boundary-layer separation from the wall. Compared to DNS results, the steady-state RANS shows a different solution, where the primary downstream vortical region is more elongated along the wall and combined into the upstream region ([88]).

The significant effect of the roughness element is to modify the mechanism of turbulent mixing (Fig. 3.11). Strong downwash spanning up to a considerable distance from the wall plays a dominant role in enhancing mixing in the near-wall layer, in place of quasi-streamwise vortices in

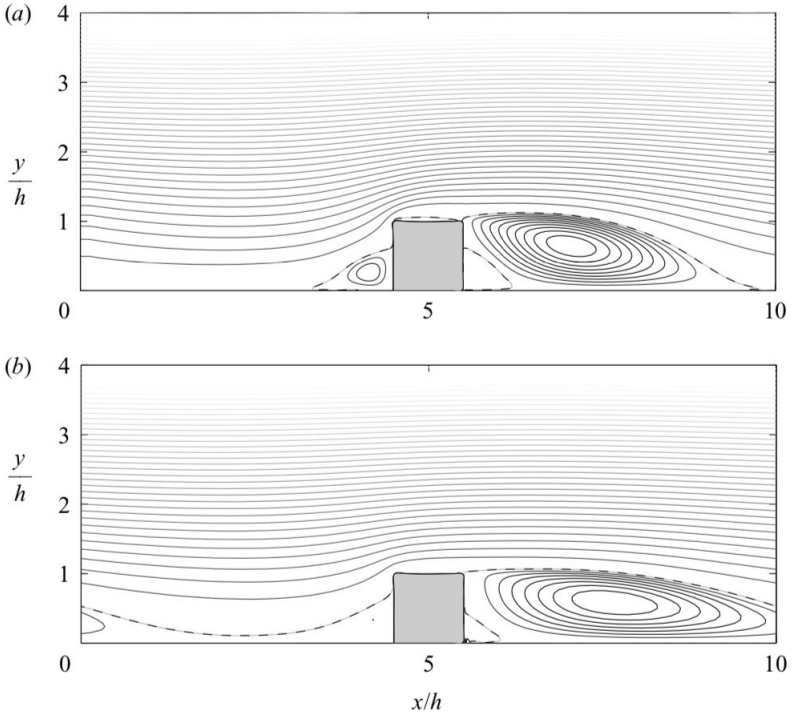

Figure 3.10 – Streamline contours of an averaged field around a square rib (a) DNS ; (b) steady-state RANS. Dashed lines denote zero-velocity streamline [88]

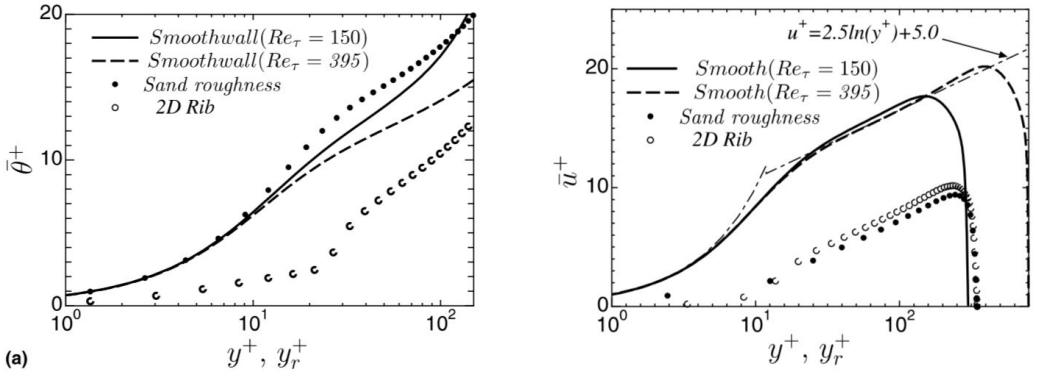

(a) Mean temperature distribution scaled by wall units, θ^+ vs y^+

(b) Mean velocity distribution scaled by wall units, U^+ vs y^+

Figure 3.11 – Mean temperature and velocity profiles in Miyake *et al.* [86]

the buffer layer of the smooth-wall flow (Miyake *et al.* [86]). Although the mean flow and the turbulence statistics are drastically affected by the rods within the roughness sublayer, the elongated streamwise streaky structures can be observed above the rods. Both the height of the roughness elements and the spacing between them are crucial parameters (Ashrafian *et al.* [90]).

The study of Ikeda and Durbin [88] leads to the same conclusions. Transversely mounted rib roughness raises the disarrangement of vortical streaks in both streamwise and wall-normal directions. It induces the non-periodic irregular spanwise vortex shedding, which serves as a source for the turbulent kinetic energy flux towards the wall surface as well as into the bulk flow.

These unsteady vortical motions affect the Reynolds shear stress within and above the roughness, which offsets the pressure gradient in the channel and leads to the reproduction of a log profile. It should also be noticed that the two-dimensional rib roughness, composed of smooth planes, produces three-dimensional unorganized motions of vortices that disturb the viscous sublayer and bears a resemblance to sand-grain roughness. The wall roughness enhances the flow structure's three-dimensionality and reduces near-wall anisotropy (Ikeda and Durbin [88]).

3.2.2 Regular rough surfaces

In order to investigate some turbulent characteristics which could appear with periodic surfaces, DNS studies are performed with regular rough surfaces. Some examples are for instance, Miyake *et al.* [91] ($Re_\tau = 400$), Bhaganagar *et al.* [92] ($Re_\tau = 400$), Orlandi and Leonardi [93] ($Re_\tau = 4200$), Lee *et al.* [94] ($Re_\theta = 300-1300$), Chatzikyriakou *et al.* [95] ($Re_\theta = 180$ and $Re_\theta = 400$), Kuwata and Suga [96] ($Re_\tau = 161$ and $Re_\tau = 223$), MacDonald *et al.* [83] ($Re_\tau = 180$) with $Re_\theta = U_b\theta_{in}/\nu$, θ_{in} being the inlet boundary layer momentum thickness and U_b the free-stream velocity.

Configuration

To mimic real surfaces, sets of geometrical elements are often used to reproduce surface asperities, such as sinusoidal curves, cubes, or hemispheres for instance (see Figs. 3.12, 3.13, 3.14, 3.15, 3.16, and 3.17).

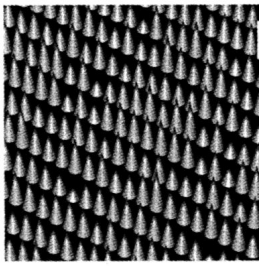

Figure 3.12 – 3D view of roughness element model used in Miyake *et al.* [91]

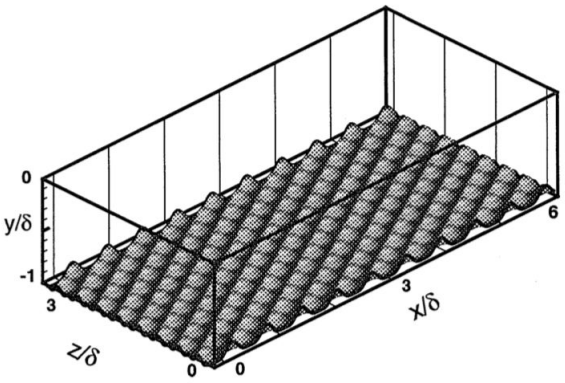

Figure 3.13 – Roughness surface used in Bhaganagar *et al.* [92] for numerical simulations

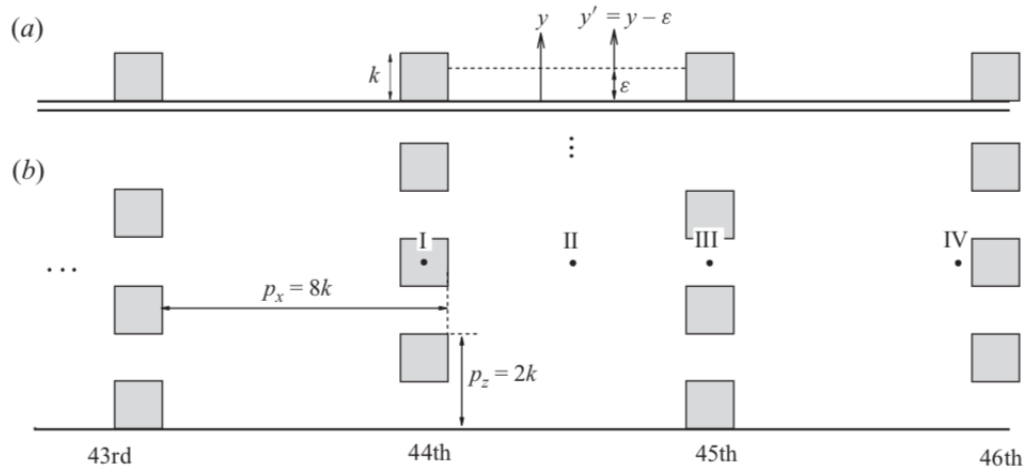

Figure 3.14 – Schematic views of the cube-roughened wall (a) side view (b) top view (Lee *et al.* [94])

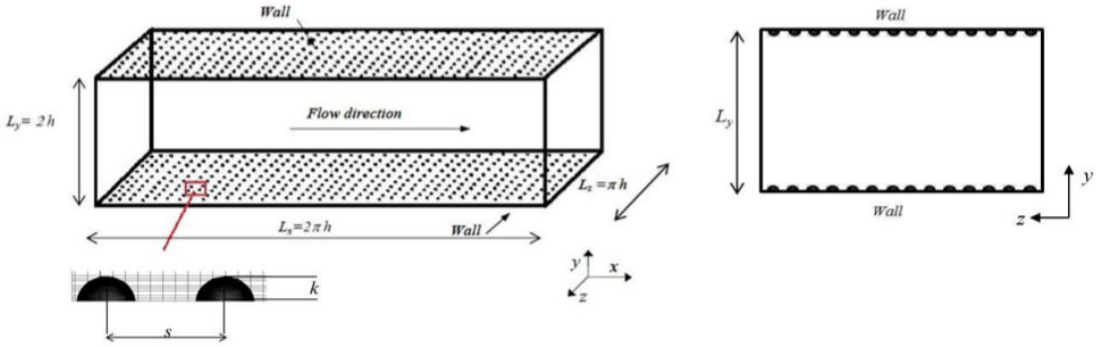

Figure 3.15 – Schematic representation of the computational domain used for roughened-channel flow simulations (Chatzikyriakou *et al.* [95])

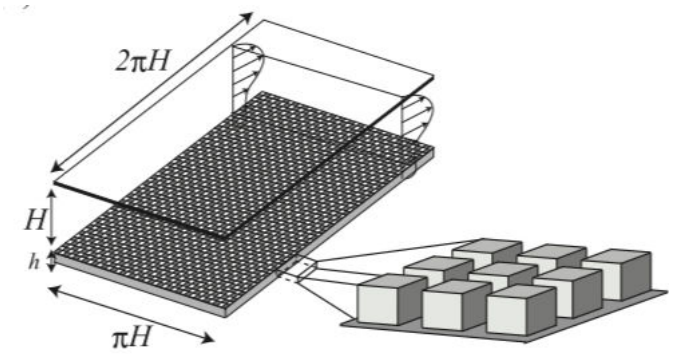

Figure 3.16 – Computational geometry for rough-walled channel flows (Kuwata and Suga [96])

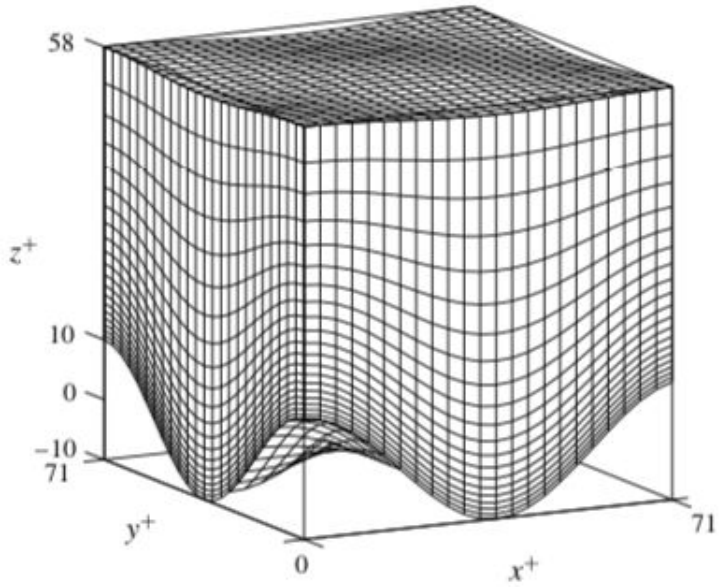

Figure 3.17 – Body-fitted mesh for a single roughness element ($\Lambda = 0.18$), zoom-in on the near-wall region of a channel (MacDonald *et al.* [83])

Results

One of the main conclusions of Bhaganagar *et al.* work [92] is that the streamwise and the spanwise dimensions of roughness elements with a fixed height play a crucial role in determining the influence of the roughness on the outer layer. The normalized spanwise size L_y/H (H being the channel half-height) of the roughness (Tab. 3.1) does not influence the mean velocity statistics but does have a large impact on the velocity fluctuations in the outer layer. This may explain why investigators with different roughness geometries can observe similar log-law shifts ΔU^+ but offer different interpretations of the outer-layer physics based on their observations of higher-order statistics in the outer layer. The velocity fluctuations are altered throughout the boundary layer due to roughness. The vorticity fluctuations, on the other hand, are not significantly altered in the outer layer (Fig. 3.18). Hence, there is an interaction between the inner and the outer layers of the turbulent boundary layer at large scales but not at small scales. ([92]).

Table 3.1 – Case study for varying L_y/H (l_z/δ) with fixed L_x/H = 0.6 (Bhaganagar *et al.* [92])

Cases	l_z/δ
A1	0.5
A2	0.25
A3	0.12
A4	0.08
A5	0.02
A6	0.01

In rough flows, the strong velocity ejections u_2' (wall-normal) promote large fluctuations of u_3' (spanwise), with an increase in flow distortion and a tendency toward isotropy. Whereas in isotropic turbulence, the velocity fluctuations have a random orientation. In rough flows, the surface produces a predominant direction along which the vorticity is aligned (Orlandi and Leonardi [93]).

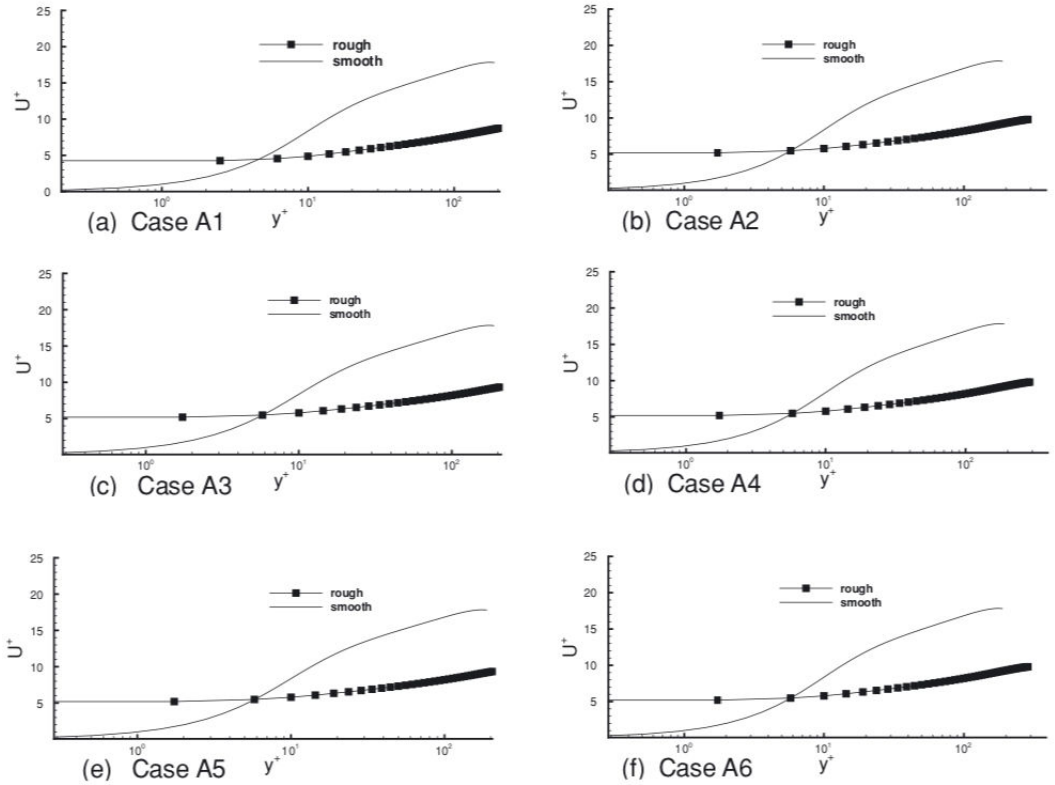

Figure 3.18 – The RMS velocity fluctuations normalized by local u_τ for different values of L_y/H (Bhaganagar *et al.* [92])

The roughness sublayer was estimated to have a depth of approximately $y = 5k$ (k being the roughness height, see Fig. 3.14a), since above the roughness sublayer, the turbulence statistics collapsed well and were found to be spatially homogeneous regardless of their position relative to the cube roughness. In the roughness sublayer, the flow streamlines showed a small recirculation region in front of the cube, and the flow between the cubes was seen to move parallel to the streamwise direction. It was also found that the instantaneous near-wall streaky structures are significantly affected by surface roughness. Consistent results were found with the two-point correlations of the velocity fluctuations, which show that introducing 2-D and 3-D roughness elements onto the smooth wall increases the average streak spacing in the spanwise direction and the diameter of the streamwise vortices. However, wall-normal and spanwise velocity fluctuations did not have extended coherence in the streamwise direction and showed an isotropic behavior over the rough walls. The instantaneous flow fields over the rough walls showed that the spanwise vortices induced by the heads of hairpin-type vortices are frequently observed with uniform-momentum regions beneath them, and these vortical structures are significantly disturbed by the roughness, leading to sudden upward motions (Lee *et al.* [94]).

Overall, the DNS results of Chatzikyriakou *et al.* [95] show a clear separation between the inner wall layer, which is affected by the presence of roughness elements, and the outer layer, which remains relatively unaffected. The roughness element height strongly affects the friction factor and the mean velocity profile. The friction factor increases proportionally to the roughness element height, while the mean velocity profile shifts downward proportionally to the roughness element height. The study reveals that the presence of hemispheres roughness elements promotes locally the instantaneous flow motion in the lateral direction within the wall layer, which was

found to cause a transfer of energy from the streamwise Reynolds stress to the lateral component. The wall-normal stress component remains however unaffected regardless of the roughness height or arrangement. Consequently, the shape of the turbulent kinetic energy profile changes, featuring a lower peak value and forward shift away from the wall as compared to the smooth channel case (Chatzikyriakou *et al.* [95]).

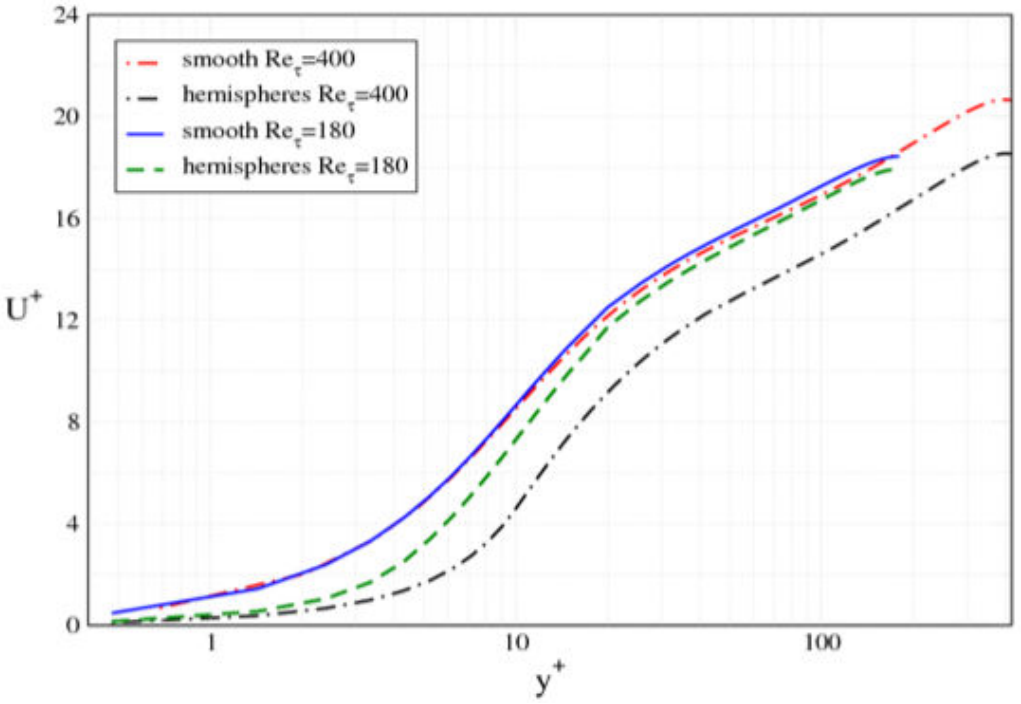

Figure 3.19 – Mean streamwise velocity for cases of smooth surfaces with $Re_\tau = 400$ and Re_τ = 180, rough surfaces with Re_τ = 400 and rough Re_τ = 180 (Chatzikyriakou *et al.* [95])

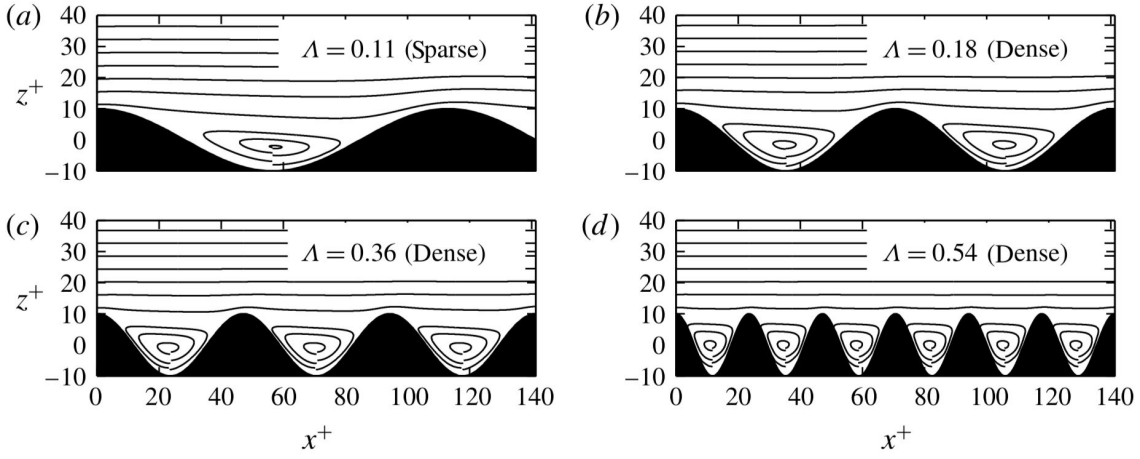

Figure 3.20 – Mean streamline contours in the streamwise and wall-normal planes (MacDonald *et al.* [83])

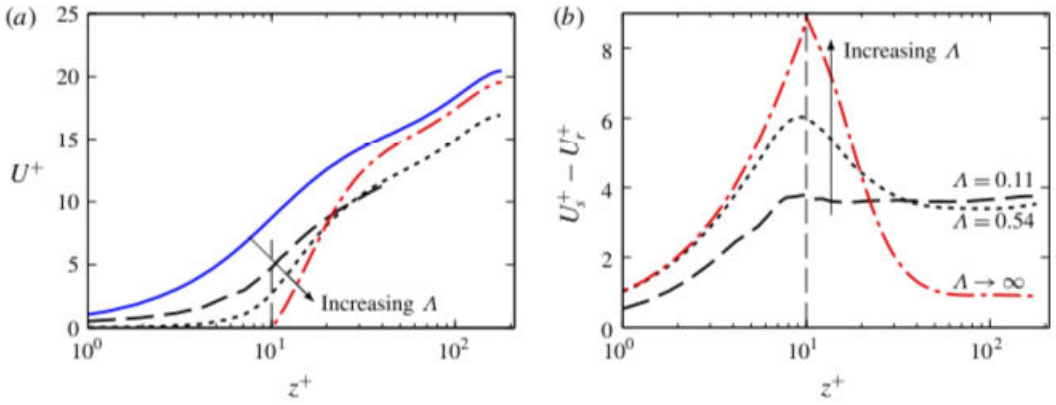

Figure 3.21 – (a) Mean velocity profile (b) Difference between smooth and rough-wall velocities. The blue line depicts smooth wall solution. Red dashed line corresponds to $\Lambda \to \infty$ (MacDonald *et al.* [83])

The dense regime of roughness was found to occur when the solidity is approximately 0.15-0.18. In this regime, the velocity fluctuations within the roughness cavities decreased, although they were not negligible even for the finest simulated case ($\Lambda = 0.54$) (MacDonald *et al.* [83]).

In Fig. 3.20, all streamline contours show an almost identical flow pattern, with similar recirculation regions appearing within the roughness wavelength. Figure 3.21(a) shows that the near-wall streamwise velocity decreases when the solidity increases. As such, the velocity difference between smooth- and rough-wall flows increases with increasing solidity close to the wall (see Fig.3.21(b)). At $z^+ = 10$ for the red line ($\Lambda \to \infty$), $U_r^+ = 0$ thus $U_s^+ - U_r^+ = U_s^+$.

3.2.3 Random roughness

Various numerical simulations were performed over irregularly shaped rough walls, such as those considered in Napoli *et al.* [97], Cardillo *et al.* [98], Busse *et al.* [99], Yuan and Piomelli [100], De Marchis *et al.* [101].

Napoli et al. [97]

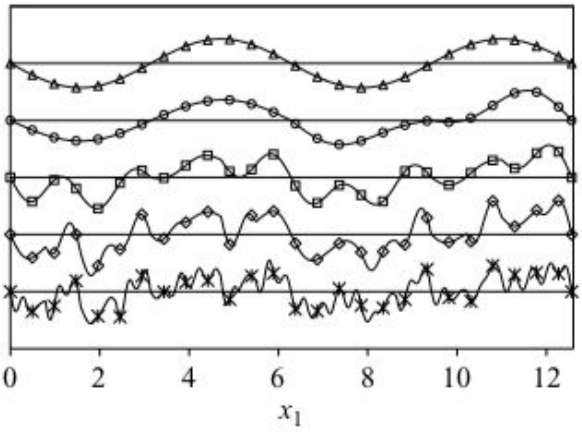

Figure 3.22 – Bottom surface roughness profiles of several cases (Napoli *et al.* [97])

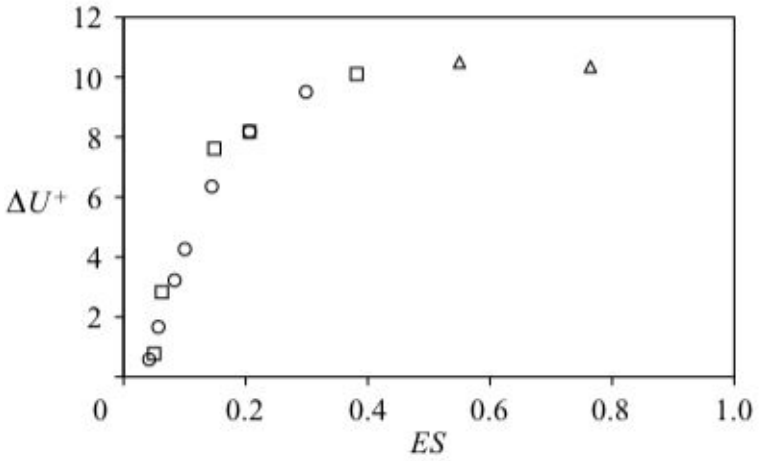

Figure 3.23 – Dependence of the roughness velocity function ΔU^+ on the effective slope of the wall corrugations (Napoli *et al.* [97])

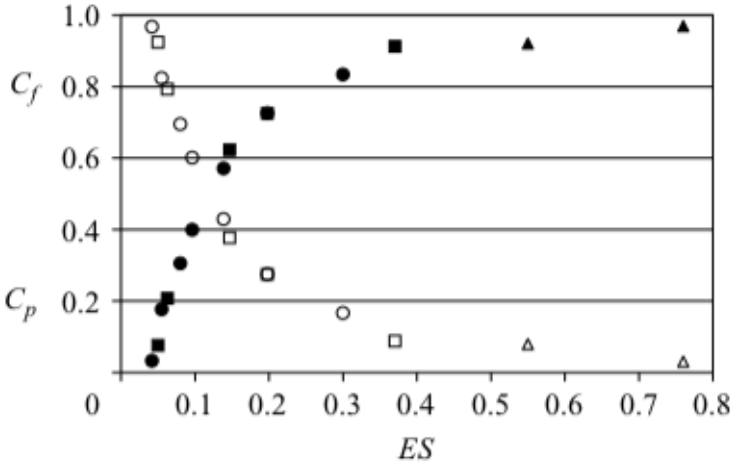

Figure 3.24 – Dependence of the pressure coefficient C_p (filled symbols) and skin-friction coefficient C_f (open symbols) on the effective slope of the wall corrugations (Napoli *et al.* [97])

Quasi-DNS results showed that the ES (Effective Slope) is one of the geometric parameters able to represent the effect of a rough wall on the roughness function (Figs. 3.22, 3.23 and 3.24). The study demonstrates that rough walls constructed in very different ways, characterized by different mean heights and spatial distribution of the roughness corrugations, exhibit very similar behavior if they have similar values of the effective slope.

It was also found that the effective slope determines the relative importance of wall friction and pressure loss.

Cardillo et al. [98] (Figs. 3.25, 3.26 and 3.27)

Comparing the DNS results of a smooth wall with a rough wall one, one can notice a downward shift in the entire mean velocity profiles due to the surface roughness, and the maximum velocity deficit is approximately 4 %. Good agreement is observed between the DNS rough case and the experimental data with some wake region discrepancies due to Reynolds number differences.

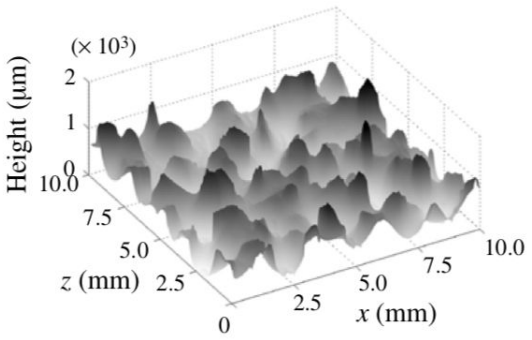

Figure 3.25 – A sample unit of surface roughness topography (Cardillo *et al.* [98])

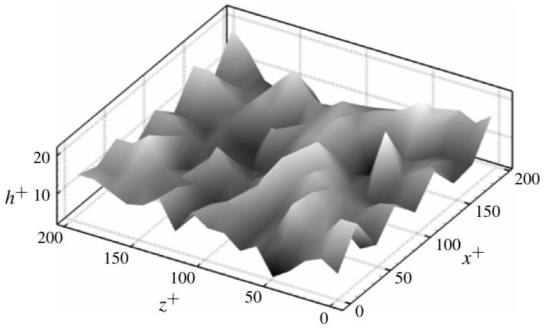

Figure 3.26 – Roughness sample used in simulations. The scaled physical size is 60 mm x 60 mm (Cardillo *et al.* [98])

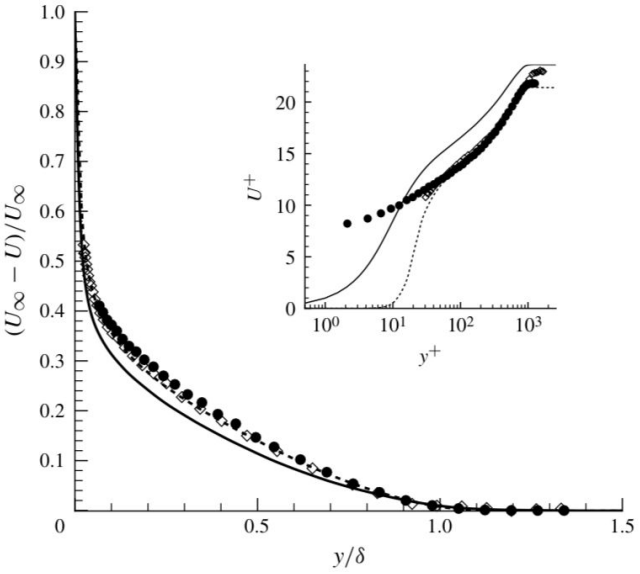

Figure 3.27 – Mean velocity profiles using outer deficit scaling (main) and inner units (inset): dashed-line (Cardillo *et al.* [98] at $Re = 2278$), straight-line (DNS smooth at $Re = 2239$), dots (experimental data at $Re = 2642$) (Cardillo *et al.* [98])

Busse et al. [99]

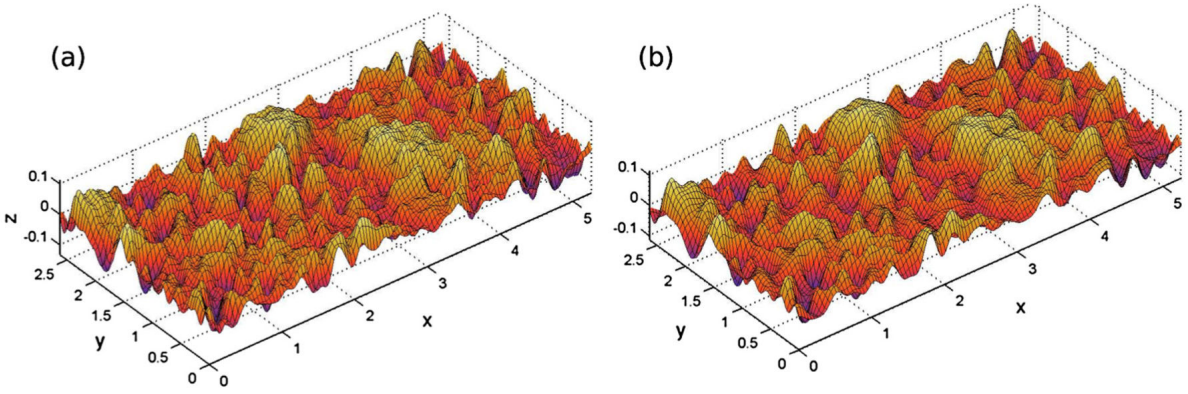

Figure 3.28 – (a) 3D surface data obtained from a graphite sample. (b) The surface data after the filtering step (Busse *et al.* [99])

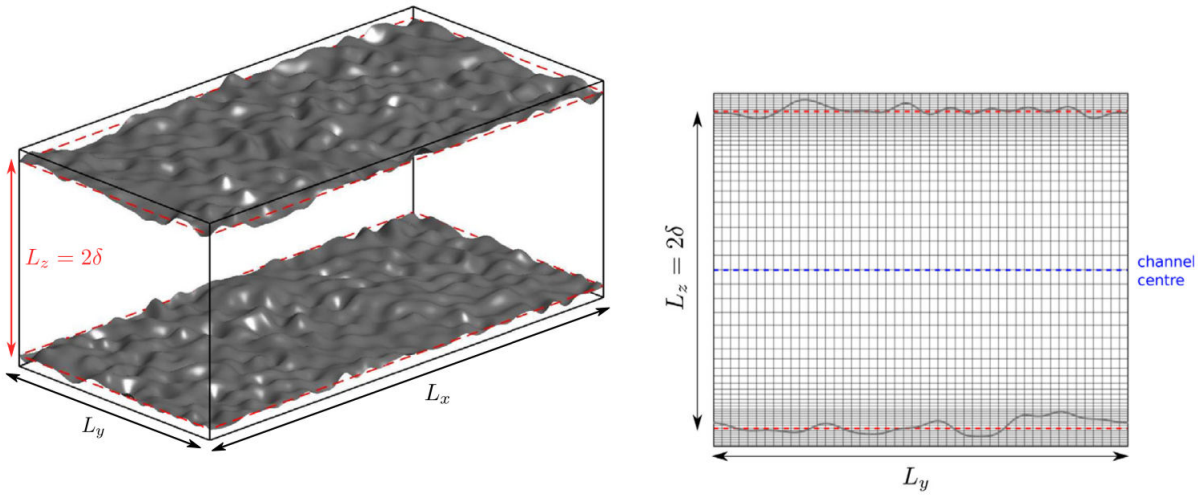

Figure 3.29 – Illustration of the computational domain and the mesh (Busse *et al.* [99])

Before the surface height map can be used as a boundary condition for direct numerical simulations, the surface data needs to be processed. This is related to the following issues. First, the surface scans usually contain a finite amount of measurement noise. Most of the measurement noise typically occurs on small spatial scales and needs to be removed (Fig. 3.28).

Second, for simulations with periodic boundary conditions, a smoothly varying periodic surface is required in Busse *et al.* [99]. If this is not the case, unphysical jumps in the surface would occur at the edges of the computational domain, where periodic boundary conditions are applied. Computational constraints impose the use of periodic boundary conditions (Fig. 3.29). If the periodic boundary conditions were not used in Busse *et al.* [99], a much larger computational domain would be needed for them to ensure independence from the boundary conditions employed at the inlet and the outlet of the domain.

Rough walls are known to break up the near-wall streaks (provided that the roughness effect is strong enough) leading to a more isotropic form of turbulence near the wall. This implies that the streamwise and spanwise grid spacing for rough-wall turbulent flow should be approximately

the same for LES simulations. However, the required resolution also depends on the topography of the rough surface. A higher resolution may be necessary if the latter exhibits features on very small scales.

This is the reason why Busse *et al.* [99] performed a grid dependence study at $Re_\tau = 180$. The results for the mean streamwise velocity profile and the normal Reynolds stresses show a good agreement in the nx576, nx384, and nx288 cases (cf Tab. 3.2) as depicted in Fig. 3.30. Only for the coarsest grids, a significant difference can be observed.

Case	N_x	N_y	Δx^+	Δy^+	$\lambda^{\min}/\Delta x$	$\overline{U}$	ΔU^+
nx192	192	96	4.9	4.9	8	11.3	4.7
nx288	288	144	3.28	3.28	12	11.0	5.0
nx384	384	192	2.5	2.5	16	11.0	5.0
nx576	576	288	1.6	1.6	24	10.9	5.1

Table 3.2 – Parameters values and mean flow statistics for the grid refinement study in Busse *et al.* [99]

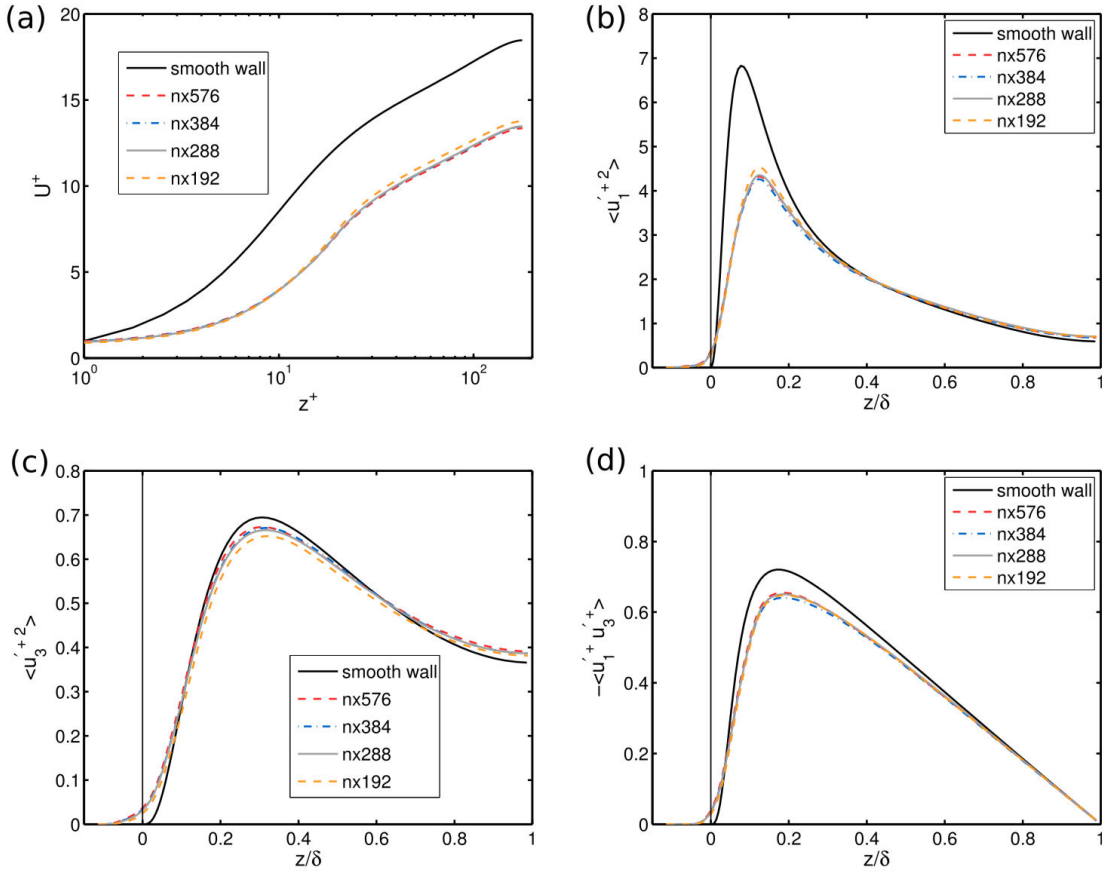

Figure 3.30 – Grid dependence analysis. Mean streamwise velocity profile (a) Reynolds stresses tensor streamwise (b), wall-normal (c) and shear stress (d) (Busse *et al.* [99])

The influence of the small-scale structure of the surface is investigated by varying the cut-off wavelength of the low-pass filter. The maximum retained wavenumber was increased in four steps from $k_c L_x = 8$ to 32 (Fig. 3.31). The most strongly filtered case, 8×4, shows little resemblance to the original surface scan, while the surfaces retaining the highest number of Fourier modes, 32×16 and 24×12 closely resemble the original surface.

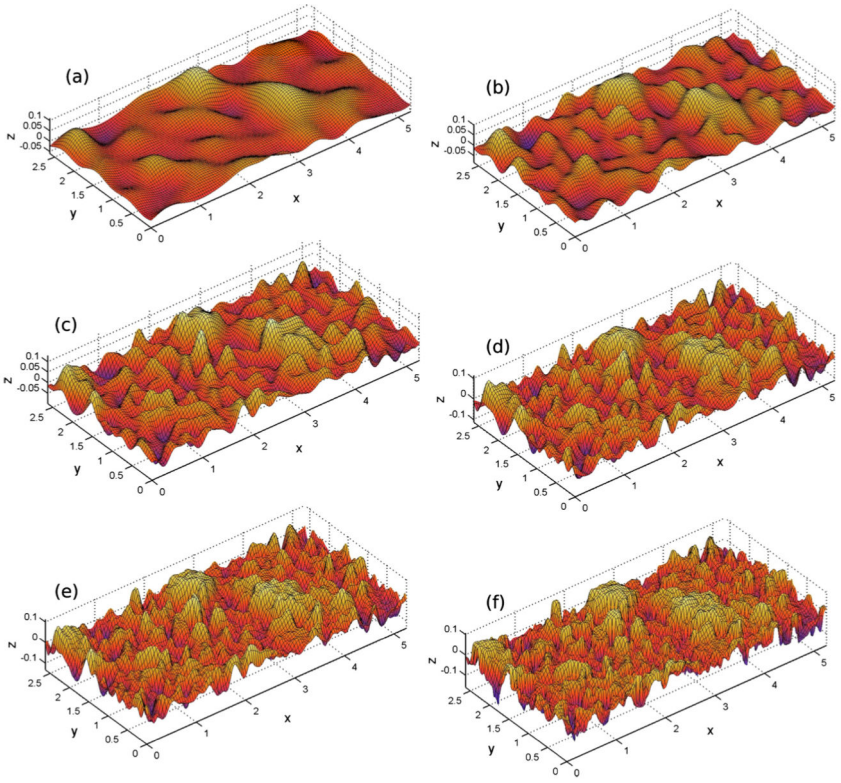

Figure 3.31 – Influence of different levels of filtering on the surface topography. (a)-(e) filtered cases to decrease the level of filtering: (a) 8 x 4, (b) 12 x 6, (c) 18 x 9, (d) 24 x 12, and (e) 32 x 16; (f) unfiltered surface (Busse *et al.* [99])

Parameter	8×4	12×16	18×9	24×12	32×16	Unfiltered
S_a	0.0194	0.0236	0.0273	0.0294	0.0305	0.0318
S_q	0.0256	0.0305	0.0349	0.0373	0.0387	0.0402
$S_{z,5\times5}$	0.0739	0.112	0.149	0.167	0.182	0.196
$S_{z,\max}$	0.170	0.186	0.227	0.228	0.246	0.266
S_{sk}	1.15	0.68	0.46	0.28	0.19	0.08
S_{ku}	4.89	3.52	3.24	2.97	2.93	2.87
L_x^{cor}	0.39	0.30	0.24	0.22	0.22	0.21
L_y^{cor}	0.47	0.41	0.43	0.35	0.30	0.27
S_{sl}	0.48	0.41	0.44	0.36	0.30	0.27
S_{al}	0.38	0.29	0.24	0.22	0.22	0.21
S_{tr}	0.80	0.72	0.54	0.61	0.74	0.75

Table 3.3 – Characteristic parameters for surfaces studied in filter refinement study (Busse *et al.* [99])

In Tab. 3.3, $S_{z,max} = S_t$ (maximum peak-to-valley height), $S_{z,5\times5}$ when the surface is partitioned into 5 x 5 tiles of equal size, S_{sl} the longest correlation length, S_{al} the shortest correlation length, L_x^{corr} the correlation in the streamwise direction, L_y^{corr} the correlation in the spanwise direction and $S_{tr} = S_{al}/S_{sl}$.

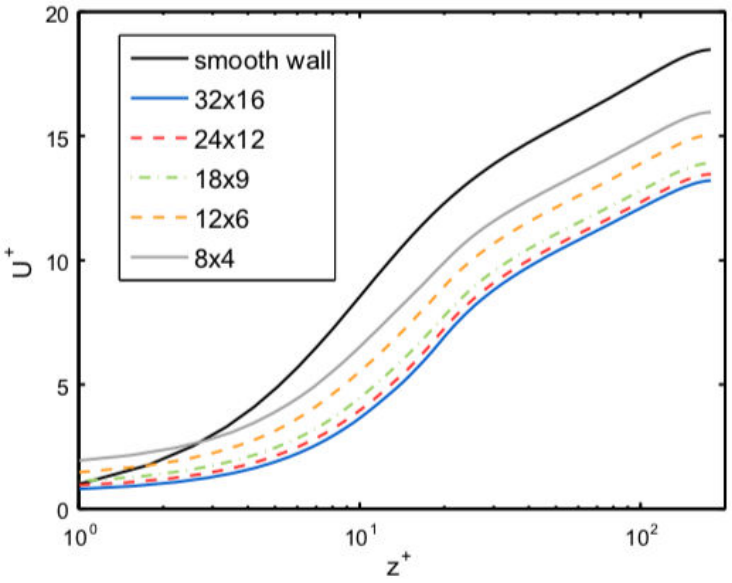

Figure 3.32 – Mean streamwise velocity profile for different degrees of surface filtering (Busse *et al.* [99])

There is a clear dependence of the mean streamwise velocity profile on the level of filtering (Fig. 3.32). A high level of filtering results in a smaller ΔU^+ compared to the least filtered (32×16) case. A substantial amount of filtering also leads to an overall reduction of the roughness height of the surface.

De Marchis et al. [101]

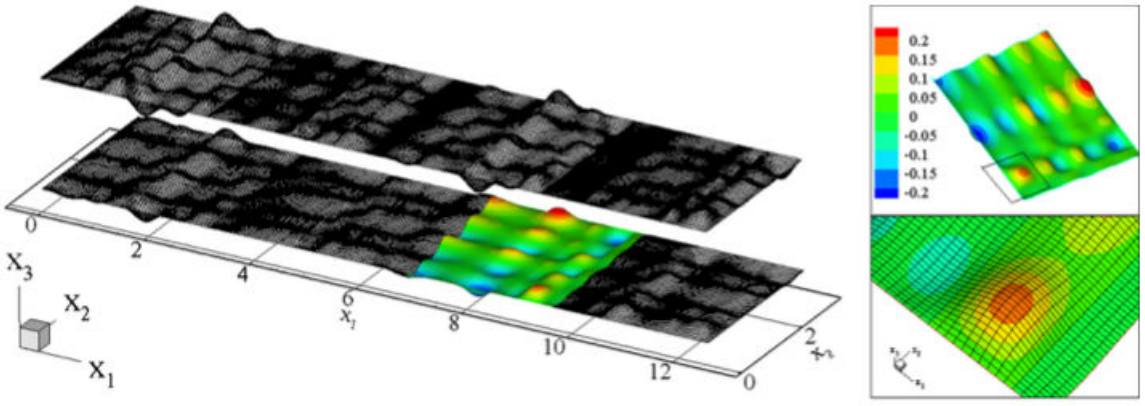

Figure 3.33 – 3D plot with surface irregularities (De Marchis *et al.* [101])

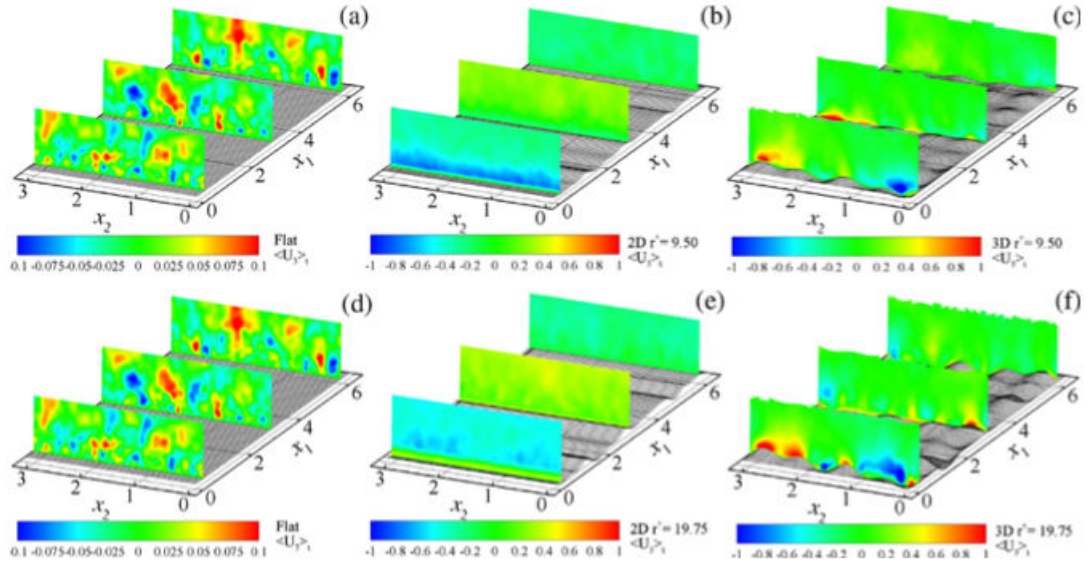

Figure 3.34 – Contour of the wall-normal velocity component along spanwise planes. (a)-(d) smooth walls; (b)-(e) 2D rough walls with different values of roughness; (c)-(f) 3D rough walls with the same roughness in (b)-(e) respectively (De Marchis *et al.* [101])

The analysis, throughout contour plots of the wall-normal and streamwise mean velocity obtained by De Marchis *et al.* [101], indicates that the 2D rough surfaces hide a spanwise heterogeneity of the flow, clearly visible over 3D irregularities (3D roughness depicted in Fig. 3.33). This heterogeneity is reflected in the modification of the turbulence structure (Fig. 3.34). In fact, the results revealed that streaks and wall-normal vortical structures are drastically destroyed in the spanwise direction when 2D rough walls are encountered. In contrast, elongated shapes are preserved over 3D rough geometries with a typical meandering behavior.

3.2.4 Partial conclusions

First, it was shown that ES is one of the geometric parameters suitable for the characterization of the effect of a rough wall. The presence of surface roughness causes an overall thickening of the boundary layer in addition to the modification of the streamwise structures (Cardillo *et al.* [98], Forooghi *et al.* [85]). Yuan and Piomelli [100] found that the critical ES that separates the waviness and roughness regimes can be higher than $ES_{critical} = 0.35$. According to them, this value is higher for realistic surfaces than for artificial random roughness ($ES_{critical} \approx 0.7$).

Second, an analysis of the mean momentum balance enabled the roughness velocity function to be decomposed into two contributions: i) the difference in streamwise velocity at the roughness crest between smooth-wall and rough-wall flows, and ii) the integrated difference in Reynolds shear stress between the two flows. This revealed that the primary reason for the reduction in the roughness velocity function that is seen in the dense regime is the reduction in Reynolds shear stress above the roughness elements, *i.e.* due to the second contribution seen above (MacDonald *et al.* [83]). As solidity increases, it appears that the near-wall cycle is being pushed up away from the roughness. From the peak streamwise turbulence intensity and the energy spectra, the energy peak moves away from the wall for both sparse and dense roughness. Increasing solidity in the sparse regime leads to a reduction in the peak energy, while increasing solidity in the dense regime causes an increase in the peak energy. Compared to the smooth wall, the dense roughness cases

have less turbulent energy in the region immediately above the crest of the roughness.

Finally, the thickness of the layer influenced by roughness is limited up to a couple of times as high as the roughness height. Beyond this layer, the flow is not dependent on the wall condition but rather on the magnitude of the total drag only (Miyake *et al.* [91]).

3.3 Roughness-modeled approaches

Since the simulations of turbulent flows with fully resolved roughness require fine grids for solving small-scale turbulence, DNS or roughness-resolved LES simulations cannot be performed for complex geometries due to the excessively high computational cost. Indeed, the number of computational grid points necessary for DNS and roughness-resolved LES are estimated by Choi and Moin [102] as $N_{DNS} \approx Re_L^{37/14}$ and $N_{RRLES} \approx Re_L^{13/7}$, respectively, with Re_L being the Reynolds number based on turbulent characteristic length.

Hence, there is a clear need to develop WMLES (Wall-modeled LES) models to account for roughness effects. This methodology consists in using a relatively coarse grid near the wall to mimic the dynamic effects in the wall layer through a wall model. The objective of a wall model is to correctly predict the wall-normal tangential velocity gradient (wall-shear stress). The required number of grid points is $N_{WMLES} \approx Re_L$ (Choi and Moin [102]). There are two approaches:

- **Functional strategy**: the idea is to reproduce the roughness function ΔU^+ based on deep knowledge of the physical properties needed to be modeled.
- **Structural strategy**: based on mathematical analysis, this approach aims to reproduce the flow structure via slip-wall conditions as artificial velocity at the wall.

For both strategies, simulations can be performed with either a full LES method or a hybrid RANS/LES formulation, such as Detached Eddy Simulation. In the latter, RANS equations are solved near the wall and interfaced with a LES away from the solid boundary.

3.3.1 Functional strategy

Wall-stress modeling

Numerous researchers have put their effort towards the development of effective models in which the effects of rough boundaries are modeled by wall laws applied to smooth surfaces.

The wall-shear stress needs to be known, and assumptions are made on the shape of the velocity profile. The simplest approximation for the wall-shear stress is algebraically related to the velocity at some distance from the wall. Without pressure gradient effects on the boundary layer, the velocity profile satisfies a logarithmic law (Eq. 5.5).

In order to avoid these assumptions, the thin boundary-layer equations (TBLE) can be considered. This methodology is introduced by Balaras *et al.* [103] (Fig. 3.35).

$$\frac{\partial \overline{u}_i}{\partial t} + \frac{\partial \overline{u}_i\,\overline{u}_j}{\partial x_j} + \frac{1}{\rho}\frac{\partial \overline{P}}{\partial x_i} = \frac{\partial}{\partial y}\left((\nu + \overline{\nu_t})\frac{\partial \overline{u}_i}{\partial y}\right), i = 1, 3 \tag{3.14}$$

$$\overline{u}_i(y = 0) = 0, \overline{u}_i(y^*) = U(y^*) \tag{3.15}$$

The wall-parallel velocities u_1 and u_3 are matched to the LES solution at some distance y^* from the wall, and it is assumed that the pressure is wall-normal independent ($\frac{\partial P}{\partial x_2} = 0$). This distance y^* differs from models but is generally taken as a fraction of the boundary-layer thickness ($y^* \approx 0.1\delta$ to δ).

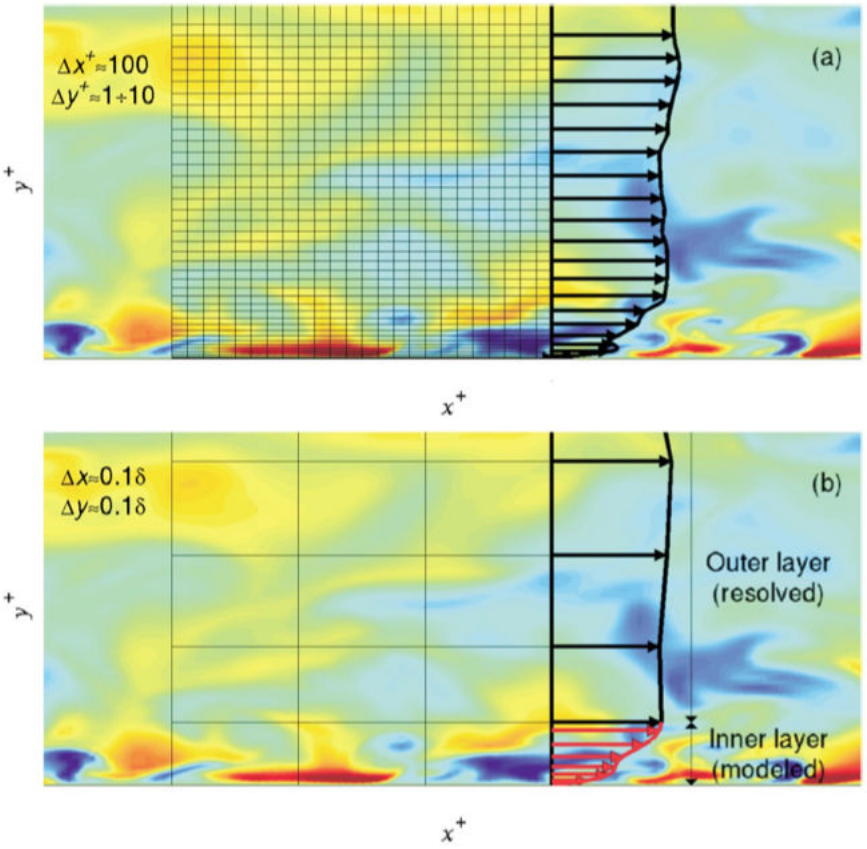

Figure 3.35 – Sketch illustrating the wall-layer modeling strategy. (a) Inner layer resolved (roughness-resolved LES) (b) Inner layer modeled (TBLE) (Piomelli and Balaras [104])

Equilibrium models

A review of models proposed by Piomelli and Balaras [104] shows that all these models neglect the left-hand side of Eq. 3.14, representing unsteadiness, convection, and pressure gradient effects. They assume an equilibrium boundary layer. Balaras *et al.* [103] showed that the predicted wall-shear stress, mean velocities, and turbulence statistics are in excellent agreement with experimental data (cases: plane channel flow, square duct flow, rotating channel flow). The major drawback of this hypothesis is its lack of accuracy in complex configurations (Piomelli and Balaras [104]).

Non-equilibrium models

Therefore non-equilibrium models have been proposed by including the pressure gradient effect. It is shown by Wang and Moin [105] that the results are better with this correction. Taking into account only this effect, equation 3.14 becomes:

$$0 = (\nu + \nu_t)\frac{\partial U}{\partial y} - \frac{1}{\rho}\frac{\partial P}{\partial x}y - \frac{\tau_w}{\rho} \tag{3.16}$$

with U the mean streamwise velocity and τ_w the wall-shear stress defined as $\tau_w = \mu \frac{\partial U}{\partial y} \mid_{y=0}$
It leads to:

$$\frac{\partial U}{\partial y} = \frac{\frac{\partial P}{\partial x}y + \tau_w}{\rho(\nu + \nu_t)} \tag{3.17}$$

Manhart *et al.* [106] proposed an extended inner scaling, which takes into account both the wall-shear stress and the streamwise pressure gradient, for equation 3.16:

$$U^* = \frac{U}{u_{\tau p}}, y^* = \frac{y u_{\tau p}}{\nu} \tag{3.18}$$

where $u_{\tau p} = \sqrt{u_\tau^2 + u_p^2}$ and $u_p = \mid (\mu/\rho^2)\frac{\partial P}{\partial x} \mid^{1/3}$ the velocity based on the streamwise pressure gradient. A parameter α, quantifying which effect is preponderant between wall shear stress or streamwise pressure gradient, can be defined as $\alpha = u_\tau^2/u_{\tau p}^2$ ($\alpha = 0$: zero-shear stress flow; $\alpha = 1$: zero-pressure gradient flow).

Thus equation 3.17 is rewritten as:

$$\frac{\partial U^*}{\partial y^*} = \frac{sign\left(\frac{\partial P}{\partial x}\right)(1-\alpha)^{3/2} y^* + sign(\tau_w) y^*}{1 + \frac{\nu_t}{\nu}} \tag{3.19}$$

The pressure is favorable or adverse in comparing the sign of the wall shear stress and the pressure gradient.

A definition of the eddy viscosity ν_t including non-zero pressure gradient is proposed by Balaras *et al.* [103]:

$$\frac{\nu_t}{\nu} = \kappa y^* \left[\alpha + y^*(1-\alpha)^{3/2}\right]^\beta \left(1 - e^{-y^*/\left(1+A\alpha^3\right)}\right)^2 \tag{3.20}$$

where A and β are two model parameters to be determined through *a priori* tests.

Duprat *et al.* [107] performed LES simulations of a periodic arrangement with hills (Fig. 3.36). They showed good predictions of turbulence statistics.

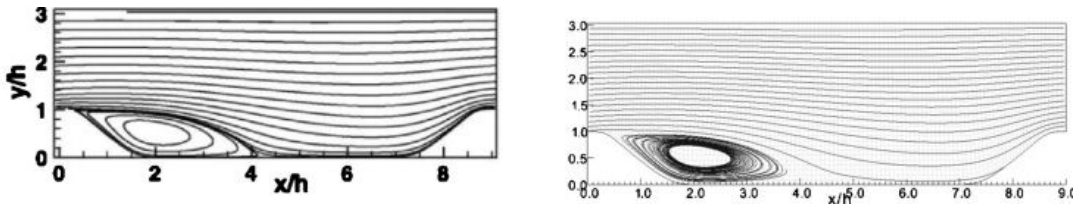

(a) Wall-resolved LES

(b) Simulation using wall-model seen in Duprat *et al.* [107]

Figure 3.36 – Mean streamline contours over a periodic hills surface (Duprat *et al.* [107])

One subtle point with wall-layer models is to find an accurate value of y^*, the interface distance between inner and outer layers. It induces, indeed, some mismatches. One can find more information and details in the review of Bose and Park [108]. Only smooth surfaces are though used for these models so far.

External force term in Navier-Stokes equations

Another way to reproduce roughness effects is to add an external term in Navier-Stokes equations as made by Miyake *et al.* [91], Scotti [109], Breugem *et al.* [110], Busse and Sandham [111], Forooghi *et al.* [112] (2018), and Krumbein *et al.* [113].

Busse and Sandham [111] introduced the Parametric Forcing Approach (PFA), which includes a roughness force term ($-\alpha_i F_i(z, h_i) u_i \mid u_i \mid$) in the right-hand side of the momentum equation:

$$\frac{\partial u_i}{\partial t} + \frac{\partial u_i u_j}{\partial x_j} = \delta_{1i} - \frac{\partial p}{\partial x_i} + \frac{1}{Re_\tau}\frac{\partial^2 u_i}{\partial x_j^2} - \alpha_i F_i(z, h_i) u_i \mid u_i \mid \tag{3.21}$$

Multiple indices do not indicate summation for the roughness force term. The constant mean streamwise pressure gradient ($-\delta_{1i}$) and the fluctuating part ($\frac{\partial p}{\partial x_i}$) are the two components of the pressure gradient.

The extra term contains a roughness density (*roughness factor* α_i), wall-roughness height h_i (which is not explicitly linked to an actual physical height of roughness), and a shape function of distance from a wall $F_i(z, h_i)$ (z corresponds to the distance to the wall). This term is quadratic in the respective local velocity to model form drag effects. However, Forooghi *et al.* [85] highlighted the fact that when the roughness density is high, the form drag is not the only predominant force because the flow is too slow in valleys.

This is why Forooghi *et al.* [112] proposed a modified PFA with a forcing term f_i (Fig. 3.37) which acts parallel to the wall ($f_2 = 0$):

$$\frac{\partial u_i}{\partial t} + \frac{\partial u_i u_j}{\partial x_j} = -\frac{1}{\rho}\frac{\partial P}{\partial x_i} + \nu\frac{\partial^2 u_i}{\partial x_j^2} + f_i \tag{3.22}$$

This forcing term is split into linear and quadratic parts: $f_i = -A(y)u_i - B(y)u_i \mid u_i \mid$. $A(y)$ and $B(y)$ can be expressed as:

$$A(y) = k_K \frac{\nu s(y)^2}{\epsilon(y)^3} \tag{3.23}$$

$$B(y) = c_D \frac{s_f(y)}{2} \tag{3.24}$$

with k_K the Kozney constant (containing the effects of solid shape and fluid flow path), $s(y)$ the total interface area per unit total volume, ϵ the porosity, c_D the drag coefficient and $s_f(y)$ the total projected frontal surface area per unit total volume.

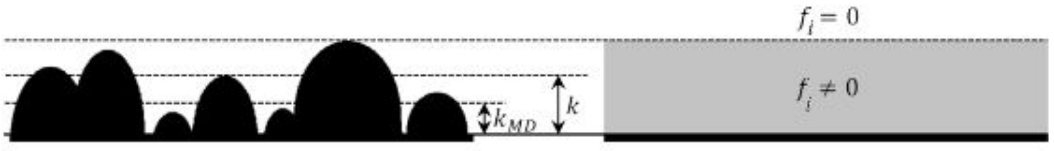

Figure 3.37 – Sketch illustrating the geometry of roughness-resolved DNS; On the right, schematic representation of PFA (Forooghi *et al.* [112] (2018))

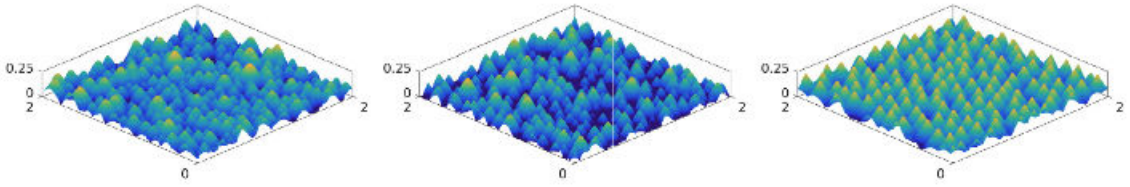

Figure 3.38 – Geometries Ia, II and III used in Forooghi *et al.* [112]

Surfaces used in this study [112] were created with packing roughness elements, the density varying (Fig. 3.38). The modified PFA includes two model constants (Kozney constant k_K and drag coefficient c_D). The obtained results with $c_D = 1.5$ and $k_K = 25$ give an excellent agreement in comparison to DNS results of Forooghi *et al.* [85] (Fig. 3.39).

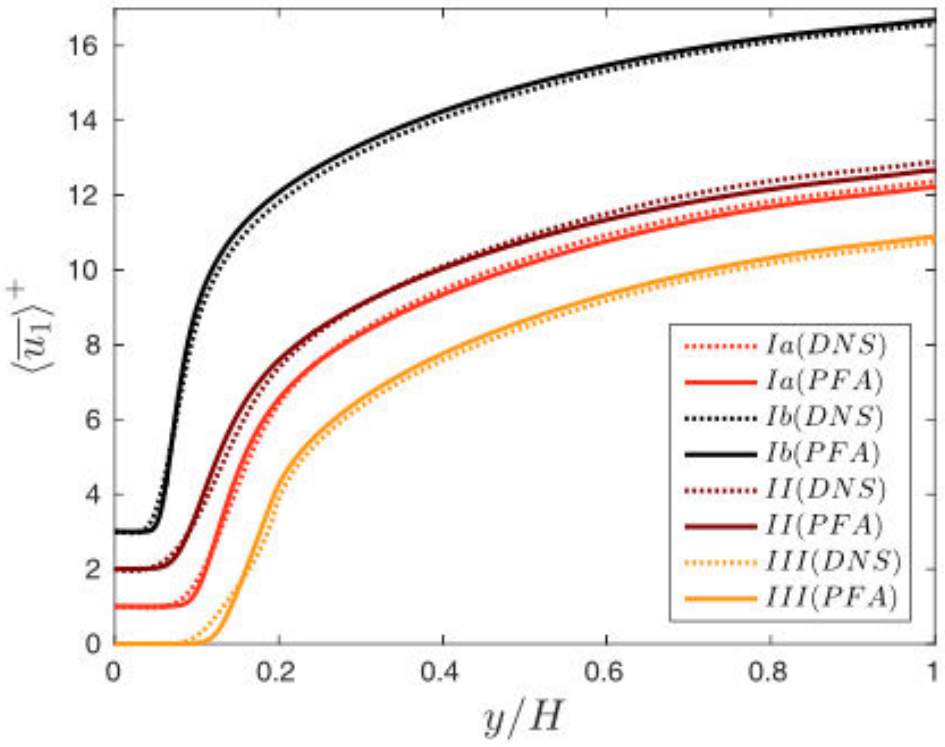

Figure 3.39 – Mean streamwise velocity profiles. Straight line: PFA; dashed lines: DNS (Forooghi *et al.* [112])

Alves Portela and Sandham [114] used PFA in order to test their hybrid method for tackling wall-bounded turbulent flows over rough surfaces. This method is called the stress-blended method (SBM), which consists in performing DNS of the roughness layer and RANS simulations away from the wall. The Reynolds stresses between the two regions are exchanged. Alves Portela and Sandham proved that the SBM gives positive results close to DNS results, even with the PFA.

Partial conclusions

Wall-layer models can yield good agreement with experimental and DNS data for some turbulence statistics. However, they do have some drawbacks related to implementation issues.

First, assumptions on local boundary layer must be made, and even though some results may be accurate, it is uncertain whether they remain valid in other flow regimes.

Second, defining the interface between the inner and outer layers is mandatory for wall-layer models, but it can be challenging, leading to some mismatches.

Third, the computational implementation of some models is hindered by their complexity. Tunable coefficients must be determined by the users to achieve good agreement.

Finally, to the best of the author's knowledge, wall-layer models are only used for smooth surfaces, and rough surfaces are not considered in these models.

3.3.2 Structural approach

An alternative strategy exists by modifying boundary conditions in Navier-Stokes equations instead of relying on boundary-layer approximations.

Control-based strategies

This method computes the wall-parallel shear stresses to obtain a given target velocity profile (obtained from RANS for instance). Based on the SGS model and the discretization near the wall, the wall stress has to be adjusted. The model introduced by Templeton *et al.* [115] is accurate up to $Re_\tau = 20000$ for a channel flow. Wall models must compensate for the numerical and the SGS modeling errors on a coarse grid.

Due to the complexity of their implementation, in addition to the prediction of the target value, this kind of model was not significantly developed.

Slip wall modeling

Principle

Another way is to replace the no-slip boundary condition with prescribed perturbation velocities which reproduce the effects of roughness. Thus the rough boundary is reduced to a parameter in the effective boundary law when solving the Navier-Stokes system in a smooth domain. Perturbation velocities at the wall can be determined as shown by Tuck and Kouzoubov [116], Jäger and Mikelic [117].

Flores and Jiménez [118] applied this method to turbulent channel flows at $Re_\tau \approx 630$ with three different forcings (associated with an equivalent sand roughness).

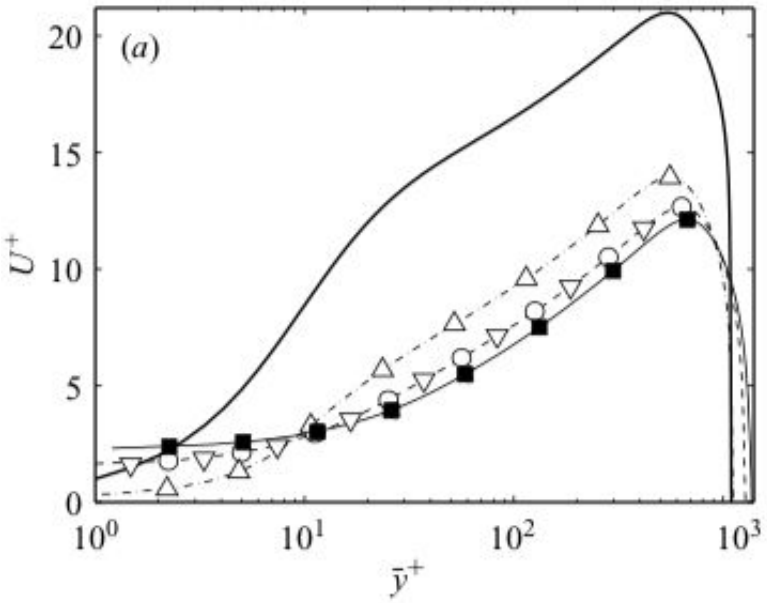

Figure 3.40 – Mean streamwise velocity. Straight line: S0; tip pointing upward triangle: r1; tip pointing downward triangle: r2; square: R3; circle: R2 (Flores and Jiménez [118])

The results obtained in Fig. 3.40 are consistent with those given by Ashrafian *et al.* [90]. Researchers have also demonstrated that the lengths of streaks and quasi-streamwise vortices are shorter. On the other hand, the disturbances enhance the wall-normal and the spanwise velocity fluctuations.

The effect of wall disturbances on the outer flow was also studied. It was found that the height of the layer where the intensity of the forcing of the background turbulence is roughly $6k$, where k is a characteristic length of the forcing. Moreover, the structure and the dynamics of the detached scales of the core region in the present simulations are not affected by the perturbations imposed

on the walls. This underlines the insensitiveness of the detached scales to the boundary condition and its extension to real rough-bounded flows.

Orlandi *et al.* [119] have conducted similar studies by rather means of DNS. They found that rough wall flows reflect mainly the presence of a non-zero wall-normal velocity distribution at the interface between the roughness cavities and the external flow.

Dynamic model

Bose and Moin [120] proposed a slip velocity wall model where the local slip length is calculated dynamically. This approach derives from the application of a low-pass filter to the Navier-Stokes equations:

$$\overline{u}_i(x) = \int G(x', x; \Delta) u_i(x') dx' \tag{3.25}$$

$$\frac{\partial \overline{u}_i}{\partial t} + \frac{\partial \overline{u}_i \overline{u}_j}{\partial x_j} = -\frac{\partial \overline{P}}{\partial x_i} + \frac{1}{Re} \frac{\partial^2 \overline{u}_i}{\partial x_j^2} - \frac{\partial \tau_{ij}}{\partial x_j} \tag{3.26}$$

with G the filter kernel and Δ the spatially varying filter width. The differential filter used in this study has a Germano-like form:

$$\overline{\Phi} - \frac{\partial}{\partial x_k} \left[l_p \frac{\partial \overline{\Phi}}{\partial x_k} \right] = \Phi \tag{3.27}$$

where $\overline{\Phi}$ is the filtered scalar and l_p corresponds to the spatial variation of the filter width. The filter kernel can be expressed in 1D as:

$$G(x', x) = \frac{1}{4\pi l_p} \frac{\exp\left(\frac{-|x'-x|}{\sqrt{l_p}} \right)}{\mid x' - x \mid} \tag{3.28}$$

A singularity constraint $l_p = 0$ is imposed on boundaries. Evaluating equation 3.27 at the wall and with this constraint, it becomes:

$$\overline{u}_i - \frac{\partial l_p}{\partial x_k} \frac{\partial \overline{u}_i}{\partial x_k} = u_i \mid_w \tag{3.29}$$

They then choose a smooth and no-slip wall ($u_i \mid_w = 0$) and apply local coordinates to the equation 3.29. This yields the equation 3.30 with n the local wall-normal direction ($\frac{\partial l_p}{\partial x_k} = 0$ in both tangential directions to the wall).

$$\overline{u}_i - \frac{\partial l_p}{\partial n} \frac{\partial \overline{u}_i}{\partial n} = 0 \tag{3.30}$$

The gradient $\frac{\partial l_p}{\partial n}$ is a length scale. Conventionally, it is written $\frac{\partial l_p}{\partial n} = C\overline{\Delta}_w$.

$$\overline{u}_i - C\overline{\Delta}_w \frac{\partial \overline{u}_i}{\partial n} = 0 \tag{3.31}$$

Equation 3.31 is known as Robin boundary condition. If $C\overline{\Delta}_w = 0$ at the wall for a wall-modeled LES, $\overline{\Delta}_w$ is too large to capture turbulent structures within the inner layer. This is why it is mandatory to impose a non-vanishing length scale. This induces slip velocity at the wall in addition to local transpiration (penetration velocity).

Re_τ	Δx^+	Δy^+	Δz^+	$\frac{\Delta x}{\delta}$	$\frac{\Delta y}{\delta}$	$\frac{\Delta z}{\delta}$
395	26	10	15			
2000	133	50	75	0.066	0.025	0.038
10^4	666	250	375			

Table 3.4 – LES resolution of the turbulent channel flow test case (Bose and Moin [120])

The dynamic computation of the slip length is exposed in the paper. In addition, one of the considered test cases is a turbulent channel flow at three different Reynolds numbers: $Re_\tau = 395, 2000$ and 10000.

The mesh resolution seen in Tab. 3.4 is insufficient to resolve turbulent structures near the wall. Mean streamwise velocity profiles are drawn for the three cases (cf Fig. 3.41).

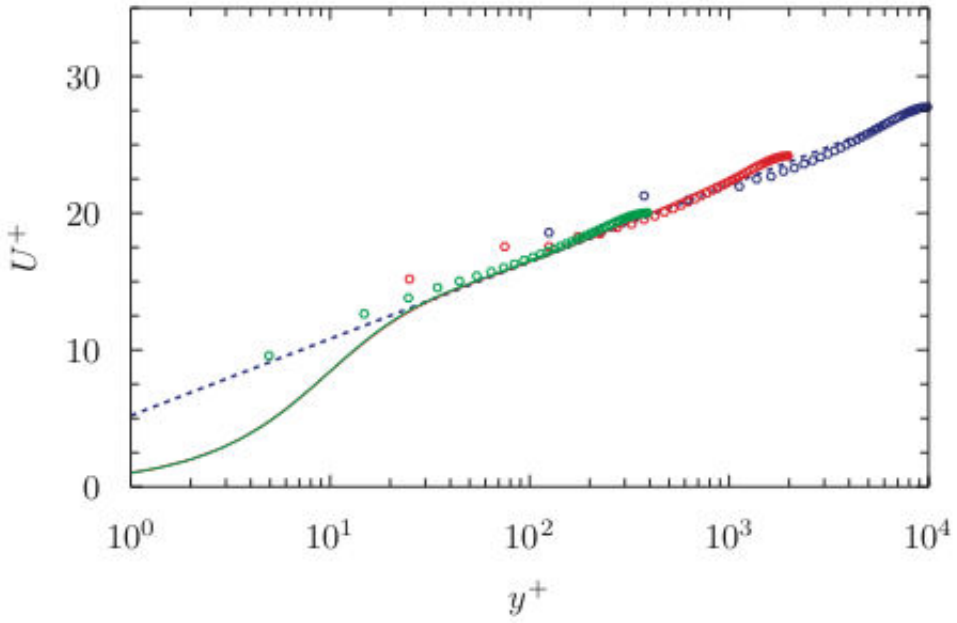

Figure 3.41 – Mean streamwise velocity profiles. Dots: LES results (green: $Re_\tau = 395$, red: $Re_\tau = 2000$, blue: $Re_\tau = 10000$); solid lines: DNS results; dashed line: log-law profile (Bose and Moin [120])

The results are in good agreement with the DNS data or the standard log-law profile in the outer layer. With the slip velocity, results deviate from DNS when approaching the wall. In addition, the results show that the slip velocity increases with the Reynolds number. Thus, fewer inner-layer structures are resolved. The log-law layer mismatch is avoided with this model and suggests the dynamic slip length procedure is robust.

A significant advantage is that the model does not require assumptions on the boundary layer and *a priori* coefficients. However, tests were made only with smooth surfaces. This is why this model has to be validated for rough surfaces.

Plane-averaging theory

More recently, Kuwata and Kawaguchi [121] proposed a model based on a plane averaging theory (Fig. 3.42). The idea is to define a representative elementary plane (REP) parallel to the rough wall and to model the plane-averaged drag force term, which appears in the averaged Navier-Stokes equations. The additional term is decomposed into linear and quadratic parts.

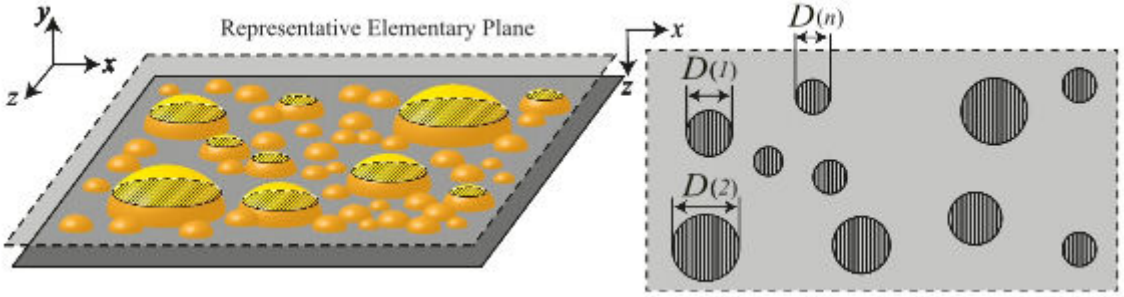

Figure 3.42 – Schematic representation of the REP principle (Kuwata and Kawaguchi [121])

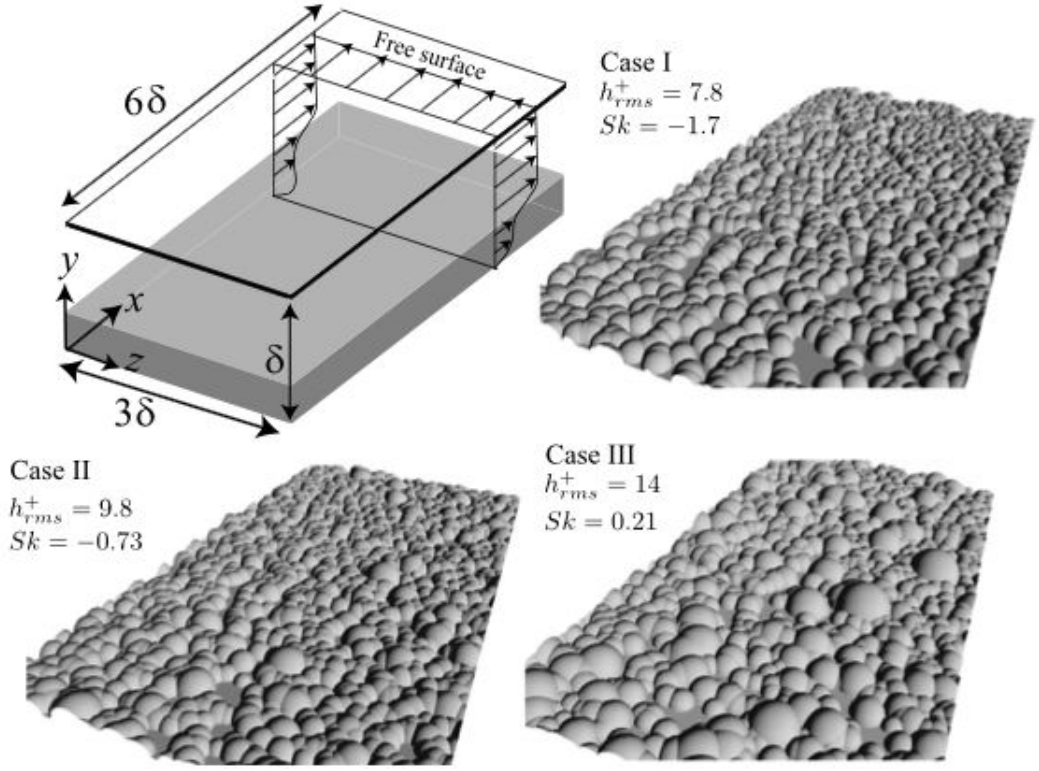

Figure 3.43 – Configurations used by Kuwata and Kawaguchi [121]

The obtained results by Kuwata and Kawaguchi [121] are comparable to the DNS data in terms of mean velocity and Reynolds stress profiles (Figs. 3.43 and 3.44). Nevertheless, near the rough wall, there is a disturbed velocity that contributes to the dissipation of the turbulent kinetic energy, which is not taken into account by the model of Kuwata and Kawaguchi [121].

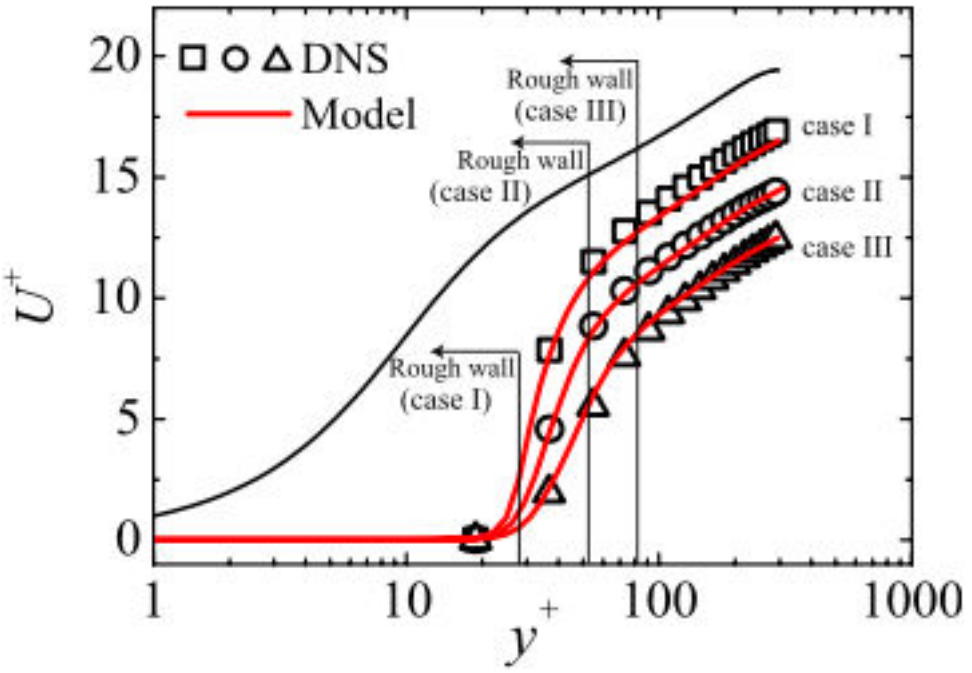

Figure 3.44 – Results obtained by Kuwata and Kawaguchi [121])

3.3.3 Models in commercial CFD software

Most of the commercial CFD codes use the same approach for the modeling of rough surfaces ([122]), assuming that the roughness effect preserves the logarithmic law with a certain shift as shown in Fig. 3.45.

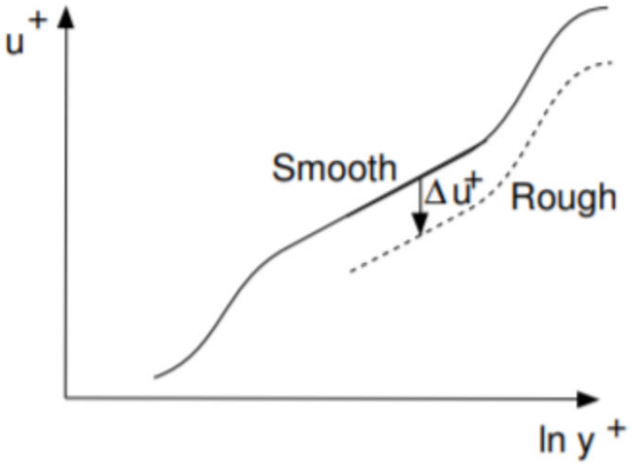

Figure 3.45 – Velocity profiles over smooth and rough walls plotted in wall-unit variables

These corrections are modeled as follows:

$$U^+(y^+) = \frac{1}{\kappa} \ln\left(\frac{y^+}{k_s^+}\right) + B \tag{3.32}$$

with B given as in Eq. 3.33.

$$B = \begin{cases} 5.5 + \frac{1}{\kappa}\ln k_s^+ & 1 \leq k_s^+ \leq 3.5 \\ 6.59 + 1.52\ln k_s^+ & 3.5 \leq k_s^+ \leq 7 \\ 9.58 & 7 \leq k_s^+ \leq 14 \\ 11.5 - 0.7\ln k_s^+ & 14 \leq k_s^+ \leq 68 \\ 8.48 & 68 \leq k_s^+ \end{cases} \tag{3.33}$$

The velocity shift ΔU^+ can be calculated as a function of y^+ and k_s^+ using the expression of Grigson:

$$\Delta U^+ = \frac{1}{\kappa}\ln\left(1 + \frac{k_s^+}{e^{3.25\kappa}}\right) \tag{3.34}$$

This correction generally consists of superposing an additive effect on the wall to reproduce the same pressure effect and increasing the eddy viscosity at the wall. Moreover, the Reynolds analogy is not available for the rough surface. Thus another correction will be applied for the thermal problems. This modification relies on the turbulent Prandtl number such as:

$$Pr_t = Pr_{t\infty} + \Delta Pr_t \tag{3.35}$$

where $Pr_{t\infty}$ is the standard turbulent Prandtl number set equal to 0.9.

The thermal correction ΔPr_t should be limited by a certain extent from the wall. An exponential decay involving the mean roughness height R_a has been introduced to account for the turbulent diffusion and the wetted surface effects, S_{corr}. The final correction of Chedevergne and Aupoix [122] leads to:

$$\Delta Pr_t = Fe^{-\frac{y}{R_a}} \tag{3.36}$$

$$F = A(\Delta U^+)^2 + B\Delta U^+ \tag{3.37}$$

$$A = (0.0155 - 0.0035S_{corr})(1 - e^{-12(S_{corr}-1)}) \tag{3.38}$$

$$B = -0.08 + 0.25e^{-10(S_{corr}-1)} \tag{3.39}$$

$$\Delta U^+ = \Delta U^+(k_s^+) \tag{3.40}$$

This model is used in the software *Ansys Fluent* to account for the effect of rough surfaces with heat transfer. For simplicity, the model is summarized using three key parameters, including B, k_s^+ and C_s as:

$$B = \begin{cases} 0 & \text{for } k_s^+ \leq 2.25\text{, hydrodynamically smooth} \\ \frac{1}{\kappa}\ln\left[\frac{k_s^+ - 2.25}{87.75} + C_s k_s^+\right] sin(\beta) & \text{for } 2.25 \leq k_s^+ \leq 90\text{, transitional regime} \\ \frac{1}{\kappa}\ln(1 + C_s k_s^+) & \text{for } 90 \leq k_s^+\text{, fully rough regime} \end{cases} \tag{3.41}$$

where $\beta = 0.4258(\ln k_s^+ - 0.811)$

In general, two parameters can be used to reproduce the effect of wall roughness. The first one is the roughness height k_s and the second one is the roughness constant C_s. The default roughness constant is $C_s = 0.5$.

It has to be noted that it is not physically meaningful to have a mesh size such that the wall-adjacent cell is smaller than the roughness height. For better results with this software, it is recommended to set the distance from the wall to the centroid of the wall-adjacent cell greater than k_s.

3.4 Concluding remarks

This chapter provides a comprehensive review of previous and current research on roughness characterization and its impact on turbulence modeling of wall flows. The primary goal of such modeling is to accurately predict the roughness velocity function ΔU^+ for scaling the velocity profile and the corresponding skin friction distribution.

Several DNS studies available in the literature have been discussed, including those on transverse ribs, various regular rough surfaces, and anisotropic surfaces. These studies provide reasonable estimates of turbulent statistics, flow structures, and boundary layer characteristics for different roughness densities and surface isotropy.

Two primary strategies exist for surface roughness modeling: the functional and the structural approaches. While the functional approach provides good results under certain boundary layer assumptions, the structural method does not require such assumptions but requires modifications to boundary conditions. However, they are generally not applied for rough surfaces, except for the Kuwata and Kawaguchi model [121]. The chapter also covers commercial CFD software models that take roughness into account.

CHAPTER 4

Automatic surface roughness and body-fitted meshes generation

This chapter presents a novel approach to creating 3D roughness-resolved unstructured and body-fitted meshes, allowing for precise control over cell size distribution and quality. The process consists of two tools: a numerical rough surface generator, developed as part of this thesis, which can produce various geometries with specified roughness parameters, such as planar surfaces, cylindrical channels, or plates with tube fins. The second tool is a body-fitted mesh generator, which can create unstructured meshes from the rough geometries previously generated.

Contents

4.1 Intrinsic challenges

An efficient strategy to study the impact of different roughness topologies on turbulence and heat transfer within compact heat exchangers (CHX) is to numerically and accurately generate a large number of rough surfaces. Several ways have been exposed in past studies. First, the pioneering work of Patir [123] has relied on the linear transformation of data sets for generating Gaussian surfaces. Autoregressive moving average and autoregressive time series methods have been introduced and exploited for rough surface generation [124, 125]. Hu and Tonder [126] have then developed a procedure based on Fourier transformation via 2D digital filters. Bakolas [127] and, more recently, Francisco and Brunetière [128] have enhanced this last method by compensating

for the intrinsic limitations. A faster method from Patir's procedure was enhanced by Manesh *et al.* [129] with a non-linear conjugate gradient algorithm, which also reduces memory requirements. Finally, some methods using the fractal function are reported [130, 131]. However, they are not convenient because the fractal dimension is seldom measured for surface topography.

Numerically generated surfaces that match statistically with real surfaces produced via AM are required. Several articles have attempted to establish the surface topography characteristics [132, 133, 134]. They bring out difficulties in providing accurate roughness parameters owing to the fact that many AM process parameters impact roughness. Some particularities are though outlined, like non-Gaussian anisotropic surfaces and higher roughness than conventional manufacturing processes. Consequently, the surface generator has to mimic these properties.

Concerning mesh generation, a large number of studies have been dedicated to this topic for several years. Nonetheless, automatically generating numerous unstructured and conformal meshes from CAD geometries with a robust algorithm is challenging. Geuzaine and Remacle [135] have created Gmsh, a 3D finite element mesh generator. However, for roughness-resolved LES cases, meshes of more than tens of millions of cells are required. In addition, they have to be rapidly generated. Therefore different mesh generation algorithms are necessary. An approach for hybrid meshes, including prismatic layers, was proposed by Ito and Nakahashi [136]. Once again, this type of mesh seems although unsuitable for automatic mesh generation. Thus, creating an inherently parallel body-fitted mesh generator for rough surfaces is needed.

This chapter focuses on an innovative procedure to generate 3D roughness-resolved unstructured and body-fitted meshes with fine control of the cell size distribution and cell quality. It is organized in the following way. The numerical method for generating rough surfaces is exposed in section 2, and the body-fitted mesh generator is the focus of section 3.

4.2 Rough-surface generator (RSG)

4.2.1 Surface roughness global characteristics

For the development of new turbulence models that take into account real surface characterization, such as those currently encountered in additive manufacturing, a numerical method to generate such rough surfaces is required. As described in Chapter 3, surface roughness parameters that characterize the height moments of a surface are categorized into three groups: amplitude, spacing, and hybrid. For a complete description of a real surface, nearly sixty parameters are needed. This large amount of parameters is prohibitive for including all parameters in the RSG. As a reminder, the predominant roughness parameters commonly used in the literature are the arithmetic average height denoted S_a, the root-mean-square height S_q, skewness Sk, kurtosis Ku and the roughness density (Λ) or the effective slope ES [77]. The arithmetic average height is the most known among the parameters and is usually used to control the roughness of manufactured parts. This is defined as the average absolute deviation of the roughness irregularities compared to the mean roughness height, which is assumed to be zero throughout this manuscript. The root-mean-square height S_q is also another important parameter that is more difficult to measure. Here, streamwise, spanwise, and crosswise directions are respectively along the x, y, and z axes. Thereby $z(x, y)$ represents the height of the surface in function of x and y coordinates.

$$S_a = \frac{1}{L_x L_y} \int_{L_x} \int_{L_y} \mid z(x, y) \mid \, dxdy \tag{4.1}$$

$$S_q = \sqrt{\frac{1}{L_x L_y} \int_{L_x} \int_{L_y} z(x, y)^2 \, dxdy} \tag{4.2}$$

For reminder purposes, while skewness quantifies the asymmetry of the surface's probability density function (PDF), kurtosis describes its sharpness. Surfaces with high peaks or deep valleys correspond to respective positive or negative skewness. If $Ku < 3$, the distribution curve is said to be platykurtic and has relatively few sharp peaks. On the contrary, if $Ku > 3$, the distribution is said to be leptokurtic, and many sharp peaks are located on the surface. The case $Ku = 3$ corresponds to a Gaussian PDF. Additional information is also needed about the spatial properties of the surface in the wall-tangential space directions. Studies have underlined the predominance of the effective slope in predicting roughness effects, defined as the average of the slope of the roughness along the streamwise direction [97, 101]:

$$ES = \frac{1}{L_x L_y} \int_{L_x} \int_{L_y} \left| \frac{\partial z(x,y)}{\partial x} \right| dxdy \tag{4.3}$$

4.2.2 Roughness in additive manufacturing

In additive manufacturing, several factors have an impact on the surface topography, such as the thickness of printed layers, the angle of the surface compared to the horizontal build bed, powder's particle size distribution for power bed methods or the laser power and scan speed for Selective Laser Melting (SLM), the material used and many more. For the targeted applications in this work, surface finishing is not considered as such a procedure can create leakages in CHX. Several studies proposed artifacts for testing machines, topography measurement tools and quantifying surface texture [132, 133, 134]. Depending on the printing inclination angle, the value of roughness parameters varies. Furthermore, for one specific angle, there are differences between upward and downward faces. A staircase effect can also appear, contributing to a more rough surface. Even if the skewness and kurtosis factors belong to areal parameters within ISO 25178-2 norm [78], their values are both not consistently exposed in articles. A wide range of AM process parameters has an impact on the surface topography. This has impelled some researchers to predict roughness using machine learning approaches like in Li *et al.* [137].

Nevertheless, one key point is that surfaces produced with AM are likely non-Gaussian and anisotropic. Due to the layer-by-layer nature of AM process, patterns of peaks or valleys called welding tracks can usually be distinguished. Slags also appear on the surface due to powder particles or material that are not correctly melted [133].

4.2.3 Numerical method

The chosen method for numerically generating rough surfaces relies mainly on the algorithm described by Hu and Tonder [126] and with improvements from Bakolas [127]. They have developed a random surface generation approach based on Fourier analysis, filtering, and Johnson translator system [138]. The proposed algorithm has also been developed for possibly ensuring periodic boundaries.

For clarity, the method is split into four main steps, which are illustrated in Fig. 4.1. All the key points and details of each step are described hereafter.

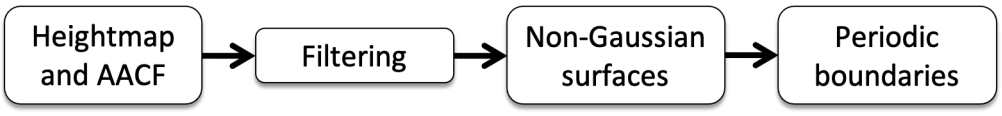

Figure 4.1 – Main steps of the roughness surface generator.

4.2.3.1 Heightmap and areal autocorrelation function

Since rough surfaces can be described by height and spatial characteristics, two statistical functions are sufficient to obtain a given surface: the elevation distribution PDF and the areal autocorrelation function (AACF). The latter allows thereby to provide information about the spacing of the surface heights. It is defined as:

$$AACF(\tau_x, \tau_y) = E[z(x, y)\ z(x + \tau_x, y + \tau_y)] \tag{4.4}$$

with E the expectation value of the product between height elevation at two different locations. This definition introduces two correlation lengths, τ_x and τ_y, respectively along the x-axis (streamwise) and the y-axis (spanwise). In a certain manner, the latter can be assimilated to the bump width in the corresponding direction. For isotropic surfaces, these lengths are equal but their values differ when the roughness is anisotropic.

Considering the patterns observed in additive manufacturing, anisotropic surfaces have to be considered in this work. The AACF incorporated in the RSG is the following:

$$AACF(\tau_x, \tau_y) = S_q^2 \exp\left(-\left[\left(\frac{x}{\tau_x}\right)^2 + \left(\frac{y}{\tau_y}\right)^2\right]^{\frac{1}{2}}\right) \tag{4.5}$$

4.2.3.2 Filtering and Fourier analysis

The considered procedure is based on the 2D digital filtering technique exposed by Hu and Tonder [126]. Such filter is a system transforming an initial $(N+n, M+m)$ matrix η into an output N x M matrix z. The matrix η contains uncorrelated random numbers $\eta(i, j)$ having a Gaussian distribution. With *finite impulse response* (FIR) filters, the transformation is written as the following convolution:

$$z(i, j) = \sum_{k=1}^{n} \sum_{l=1}^{m} h(k, l)\ \eta(i + k, j + l) \tag{4.6}$$

where the filter coefficients $h(k, l)$ have to be determined from the prescribed AACF. For this purpose, the Fourier transformation of the equation (4.6) yields:

$$Z(w_x, w_y) = H(w_x, w_y)\ A(w_x, w_y) \tag{4.7}$$

with Z and A the Fourier transforms of z and η respectively. The Wiener–Khinchin theorem relates the transfer function H to the power spectral densities (PSD) of η and z, correspondingly S_η and S_z. This relationship is given in Eq. 4.8.

$$S_z(w_x, w_y) = \mid H(w_x, w_y) \mid^2\ S_\eta(w_x, w_y) \tag{4.8}$$

As the numbers $\eta(i, j)$ have a Gaussian distribution and are uncorrelated, the PSD S_η is equal to a constant value. Here, the distribution is normal. Hence the constant value equals one. Furthermore, the PSD S_z corresponds to the Fourier transform of the expected AACF. An inverse fast Fourier transform (FFT) applied on H yields, therefore, the filter coefficients h as shown in Eq. 4.9.

$$h = FFT^{-1}(H) = FFT^{-1}\left(\sqrt{\mid FFT(AACF) \mid}\right) \tag{4.9}$$

4.2.3.3 Non-Gaussian surfaces

For non-Gaussian surfaces, values of the skewness and the kurtosis are changed through the filtering process. Thereby, another transformation step applied to the sequence η is necessary beforehand to provide a new sequence η'. The skewness $Sk_{\eta'}$ and kurtosis $Ku_{\eta'}$ of η' can be obtained via Eq. 4.10 and 4.11.

The transformation step is performed through a so-called Johnson translator system [138]. Desired modified skewness $Sk_{\eta'}$ and kurtosis $Ku_{\eta'}$ are then set as input and the sequence η' is the output. In order to generate the latter, parameters of this system can be calculated with methods developed by Hill *et al.* [139] and Tuenter [140]. Finally, a convolution between filter coefficients h and this new sequence η' yields desired S_q, Sk, Ku and AACF for the output surface z.

$$Sk_{\eta'} = \frac{Sk\,(\sum_{i=1}^{q}\theta_i^2)^{\frac{3}{2}}}{\sum_{i=1}^{q}\theta_i^3} \tag{4.10}$$

$$Ku_{\eta'} = \frac{Ku\,(\sum_{i=1}^{q}\theta_i^2)^2 - 6\sum_{i=1}^{q-1}\sum_{j=i+1}^{q}\theta_i^2\theta_j^2}{\sum_{i=1}^{q}\theta_i^4} \tag{4.11}$$

with Sk and Ku the desired skewness and kurtosis for the final surface z and with

$$\theta_i = h(k,l);\ k = 0,\ldots,n-1;\ l = 0,\ldots,m-1;\ q = km + l \tag{4.12}$$

4.2.3.4 Implementation of periodic boundaries

A procedure for ensuring periodic boundaries with continuous slope has been integrated into the RSG. A specific algorithm for this purpose can be optionally activated and is exposed in Fig. 4.2.

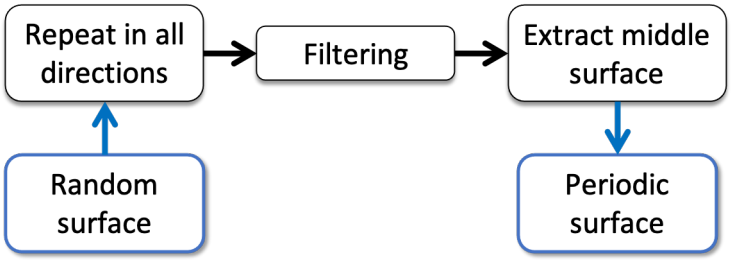

Figure 4.2 – Procedure for obtaining periodic boundaries.

First, the desired planar surface is repeated in x- and y-directions. Then a 2D Savitzky-Golay filter [141] is applied on the global surface, which ensures the periodicity with continuous slope. Indeed this kind of filter is widely known in signal processing for smoothing data. Finally, the middle surface is extracted and becomes the output surface of the generator. This procedure is highly effective and convenient for some applications like periodic channels. The result is illustrated in Fig. 4.3

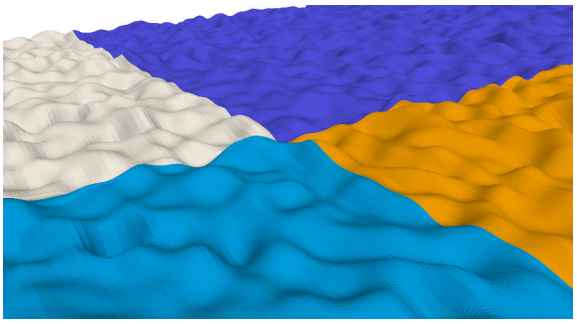

Figure 4.3 – Repeated surfaces in x- and y-directions with periodic boundaries junctions.

4.2.3.5 Complete algorithm

Since each main step has been detailed, the algorithm is entirely given hereafter.

Algorithm 1 Rough surface generator (RSG)

1: **Input**: Height $\rightarrow S_q$, Sk, Ku ; Spacing $\rightarrow \tau_x$, τ_y
2: Computation of the filter coefficients h (Eq. 4.9)
3: Computation of modified skewness $Sk_{\eta'}$ and modified kurtosis $Ku_{\eta'}$
4: **while** $\left| \frac{Sk_z - Sk}{Sk} \right| \geq \pm 5\%$ and $\left| \frac{Ku_z - Ku}{Ku} \right| \geq \pm 5\%$ **do**
5: Generation of a Gaussian surface η
6: Use of Johnson translator system $\rightarrow$ modified non-Gaussian sequence $\eta^{'}$
7: Filtering process
8: **end while**
9: Periodic boundaries if selected
10: Final surface with prescribed S_q, Sk, Ku, τ_x and $\tau_y \rightarrow$ STL file

The first step is to determine roughness characteristics for the desired surface: S_{q_z}, Sk_z, Ku_z, $AACF$ and correlation lengths. For simplifications, the mean height plane is fixed at $z = 0$. An additional option can be selected to apply a rotation on the AACF for having roughness patterns oriented at a given angle (**Step 1**). Then, the 2D digital filter coefficients $h(k, l)$ are calculated from the AACF with Eq. 4.9 (**Step 2**).

Modified skewness $Sk_{\eta'}$ and kurtosis $Ku_{\eta'}$ are later obtained through Eqs. 4.10 and 4.11 (**Step 3**). The Johnson translator system is utilized to transform the Gaussian data set η into the non-Gaussian sequence η' (**Steps 4-6**) with prescribed skewness $Sk_{\eta'}$ and kurtosis $Ku_{\eta'}$.

The rough surface z is then generated (**Step 7**) as seen in the Eq. (4.6) with η replaced by the data set η'. A threshold of $\pm 5\%$ on the relative error for skewness and kurtosis is used in order to ensure that the values of these parameters are close to the desired results (**Steps 4-8**). If the target is not reached, a new set of random numbers η is generated, and the algorithm is restarted. Eventually, if periodic boundaries are chosen by the user, they can be prescribed as seen in the sub-section above (**Step 9**). The output surface is a triangulated surface provided as an STL file (Standard Tessellation Language). Additionally to the algorithm Alg. 1, the complete flowchart of the RSG is presented in Fig 4.4.

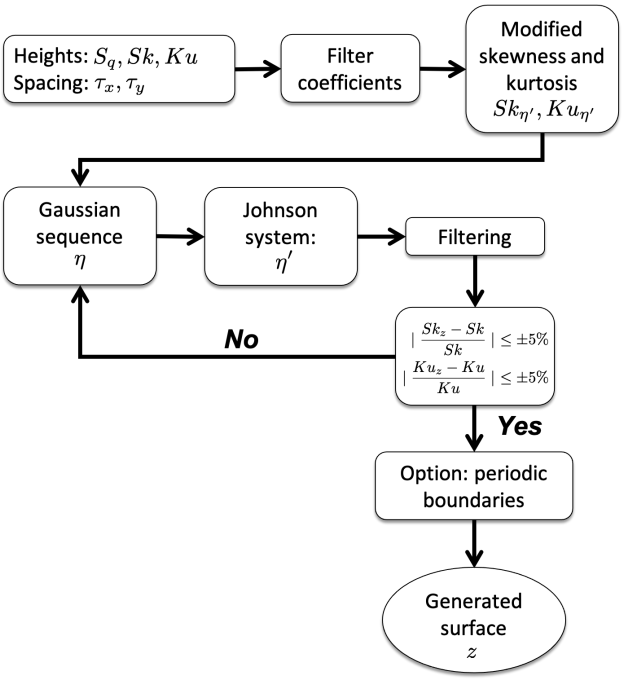

Figure 4.4 – Flowchart of the RSG.

4.2.4 Results

4.2.4.1 Generated surfaces and geometries

The first application of the RSG is the generation of rough planes. However, the RSG has been successfully used for periodic and non-periodic planar surfaces, parallel planes, square and cylindrical channels through surface parametrization and mapping. Furthermore, unmelted particles and slags are present on the surface topography in AM. Thus, an option has been incorporated to enable this AM surface particularity. Some industrial configurations can also be built, like channels containing tube fins. Examples of these geometries are shown in Fig. 4.5.

Besides geometrical aspects and roughness parameters values, one has to notice that correlation lengths are of paramount importance on the effective slope. Indeed, the flow direction is taken into account, and modifying values of correlation lengths change the topography as illustrated in Fig. 4.6. For these examples, the domain size is $8H$ x $3H$ x $2H$ with $H = 1\ mm$. For both geometries, standard deviation, skewness, and kurtosis are respectively set to $S_q = 30\ \mu m$, $Sk = 0.1$, and $Ku = 4.0$. The only difference is a modification of correlation lengths τ_x and τ_y in the AACF.

4.2.4.2 Performance and limitations

In the surface generation process, many Gaussian series have to be generated until the transformed data set matches the required statistical parameters. Then, as high precision is required on the generated surface properties, a lot of series are necessary. It is justified by the fact that the latter are supposed to be uncorrelated infinite series. Besides, as the process relies on generated random numbers, reproducing a data set is impossible. If a particular surface, among all those generated, gives satisfactory results, there is no savable parameter in order to reproduce it with high fidelity. This is why we have introduced a threshold on the relative error for skewness and kurtosis, which is set to $\pm 5\%$. Implicitly, this procedure requires that the length and the width of the surface in

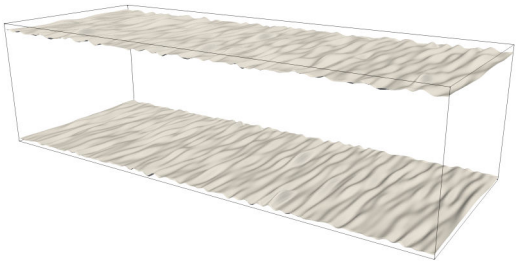

(a) Parallel rough planes

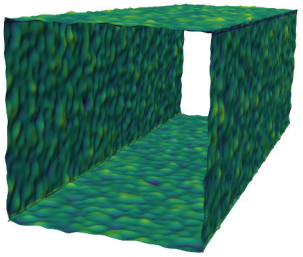

(b) Square rough channel

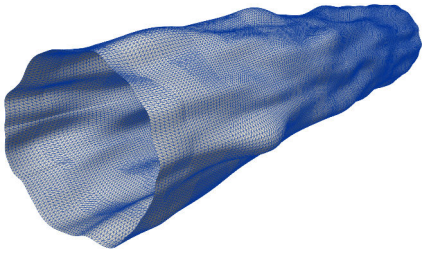

(c) Cylindrical channel with surface mesh

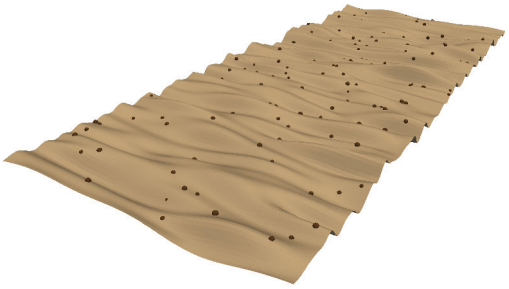

(d) Rough plane with unmelted particles

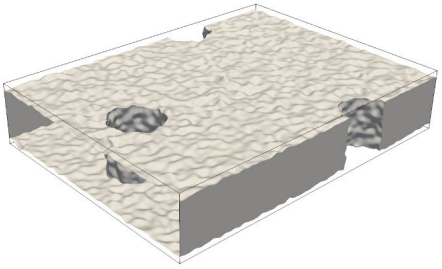

(e) Plates with tube fins

Figure 4.5 – Examples of geometries generated with the RSG.

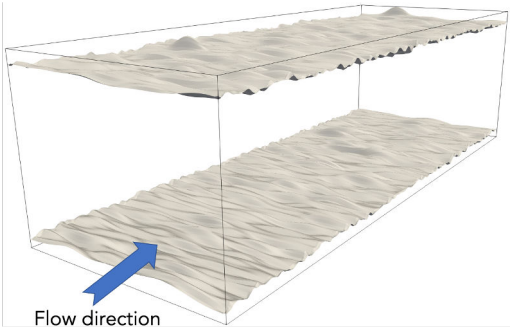

(a) $ES = 0.46$

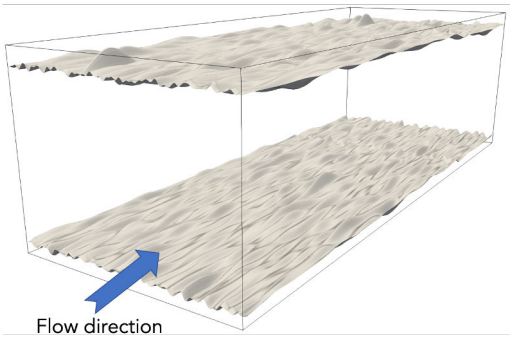

(b) $ES = 0.09$

Figure 4.6 – Parallel planes with same roughness parameters except for correlation lengths: (a) $\tau_x = 50\ \mu m$, $\tau_y = 500\ \mu m$ (b) $\tau_x = 500\ \mu m$, $\tau_y = 50\ \mu m$.

x- and y-directions are sufficient to contain several correlation lengths. Otherwise, the surface statistics would not be correct.

To test the RSG, several planar surfaces were generated with different roughness parameters and correlation lengths values. The spacing along the x-axis and y-axis is 2 μm, and the AACF

used is written in Eq. 4.5. In addition, some results on the performance of the generation process are presented in Tab. 4.1. The correlation lengths chosen for these tests are τ_x = 100 μm, τ_y = 100 μm. Generated surfaces of the different cases are shown in Fig. 4.7. Concerning the CPU cost, it is negligible in comparison to the meshing cost.

	Parameters	Input	Output	Error(%)
Case 1	Sk	0.100	0.097	3.00
	Ku	4.00	3.99	0.25
Case 2	Sk	0.400	0.402	0.5
	Ku	4.00	4.07	1.75
Case 3	Sk	0.400	0.399	0.25
	Ku	7.00	7.05	0.71

Table 4.1 – Performance tests on skewness and kurtosis.

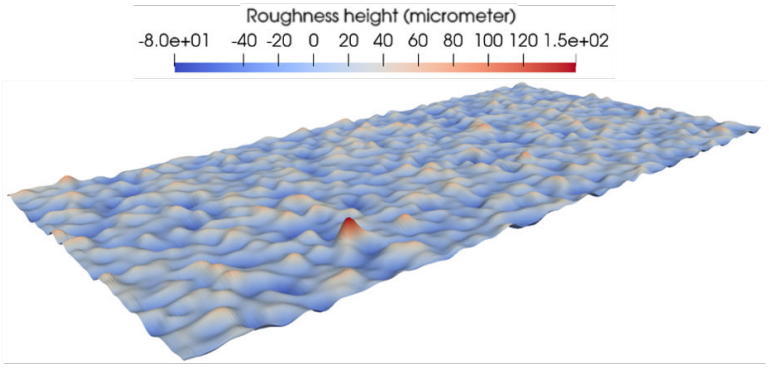

(a) Case 1: $Sk = 0.1$, $Ku = 4.0$

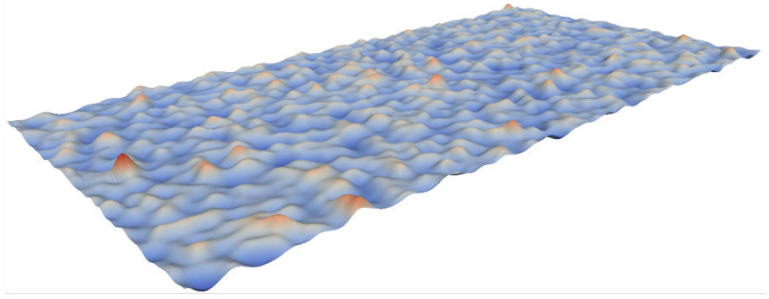

(b) Case 2: $Sk = 0.4$, $Ku = 4.0$

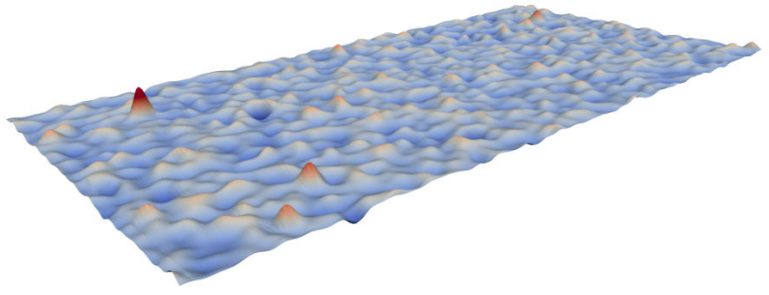

(c) Case 3: $Sk = 0.4$, $Ku = 7.0$

Figure 4.7 – Rough surfaces with different skewness and kurtosis for performance assessment (same scale for all figures).

4.3 Roughness-Resolved mesh generator (RRMG)

This section focuses on the principle of the roughness-resolved mesh generator, the algorithmic details, and its performance.

4.3.1 Objective

Once the STL surface is generated from the RSG, meshing is a critical step for predictive roughness-resolved LES. The challenge lies in the strict control of both the mesh cell size and its quality. The cell size is important in LES as it gives the cut-off between the resolved and modeled scales. The cell-size gradient is also essential as it may lead to space commutation errors in LES or local mesh quality issues. Finally, the mesh quality, often measured through the cell skewness, has to be good enough to avoid introducing numerical errors in the finite-volume schemes. Thereby a fully-automatic and well-controlled procedure for generating roughness-resolved meshes is needed. The idea is that both the fluid and solid domains must be discretized with body-fitted tetrahedral-based meshes with a controlled resolution at the wall.

4.3.2 Method

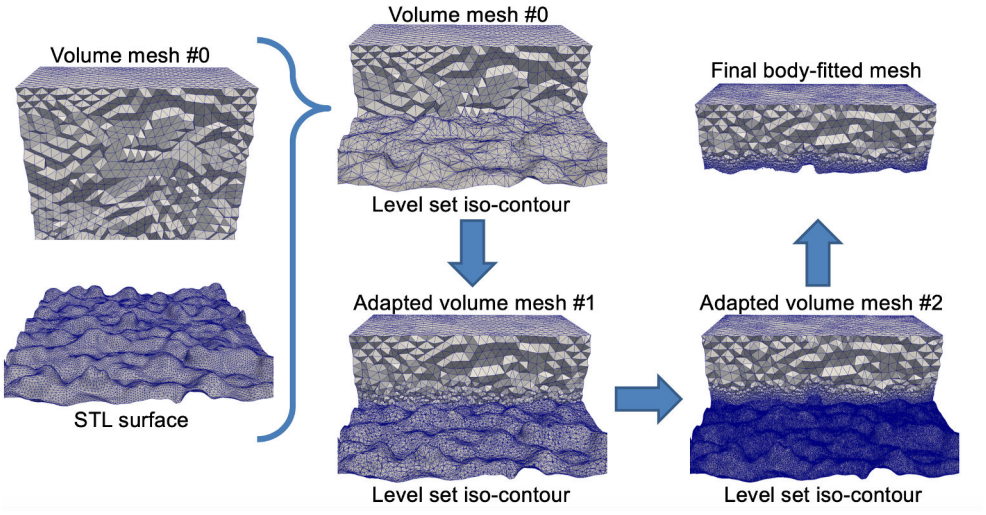

Figure 4.8 – General principle of the RRMG.

The RRMG, whose method is exposed in Fig. 4.8, is a volume-based mesh generator. It is not strictly a mesh generator as it requires a coarse input mesh that will be modified and cut to obtain the final mesh. The RRMG is based on many features available in the YALES2 code. It relies heavily on the parallel volume and surface mesh adaptation developed jointly by CORIA, INRIA, LEGI, and SAFRAN TECH. This adaptation provides fine control of the cell size and its gradient over the volume and at the rough surface. However, the mesh adaptation requires to know where to adapt the mesh in the coarse initial mesh, i.e., where the roughness-resolved boundary is located. To this aim, many other features of YALES2 are used: handling of partitioned triangle sets, level set creation and displacement, computation of geometric distance to a level set or triangles in parallel on unstructured grids. All these features participate in the process which is exposed hereafter. Given one or several STL files, one has to prescribe a desired cell size per STL. One or several interior points have to be specified to distinguish between the interior and the exterior of the surface (fluid or solid).

4.3.3 Numerical procedure of the RRMG

4.3.3.1 Global procedure

In order to get the final mesh of good quality, the procedure is indeed split into several steps. These are summarized in Fig. 4.9, from reading STLs to the mesh.

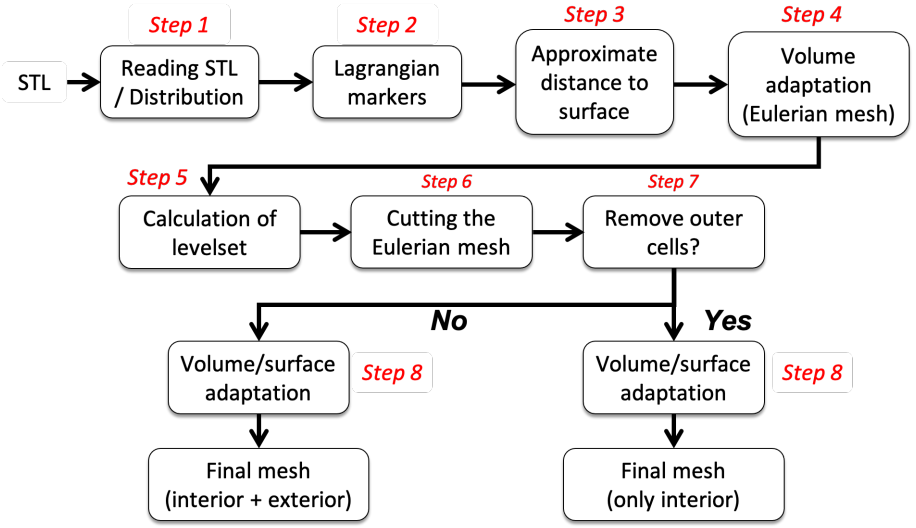

Figure 4.9 – Procedure for the RRMG.

Given the STL and the desired cell size, the user is also allowed to keep both exterior and interior domains or only the interior one. For clarity, each step is explained hereafter.

4.3.3.2 Step 1: Reading of the STL surface and distribution on processors

The first step of the process is the reading of the STL files and a first isotropic adaptation step in order to get enough triangles to perform the distribution onto the processors. The isotropic STL file adaptation is performed in the code with calls to the MMGS adaptation library [142]. Then, the STL is colored with the METIS library [69] and distributed. Each group of triangles is represented as a master sub-surface on one processor and several slaves or ghost surfaces on the other processors, which also have a bounding box that crosses one of the sub-surfaces. From the initial surface generated with the RSG illustrated in Fig. 4.10a, the distribution and the refinement are represented in Fig. 4.10b and 4.10c. This distribution mechanism is essential to get good performance on a large number of processors.

4.3.3.3 Step 2: Generation of Lagrangian markers from the surface

Once the STL file is read, refined, and distributed on the processors, Lagrangian particles are created at the triangle barycenter and at the nodes of the master surfaces, as shown in Fig. 4.11. Lagrangian particle tracking is a feature available in many CFD codes. This type of algorithm is based on the tracking of many point particles carrying many data: position, speed, and forces. Here, Lagrangian particles carry some data, such as the original triangle node coordinates and the desired cell size, but they are easier to handle than triangles. These particles are relocated on the grid to find out which cell they belong to, and they can then be used to compute an approximate distance, i.e., the minimum distance of a node of the mesh to the particles or an exact distance based on the projection of the node onto the triangles carried by the Lagrangian particles.

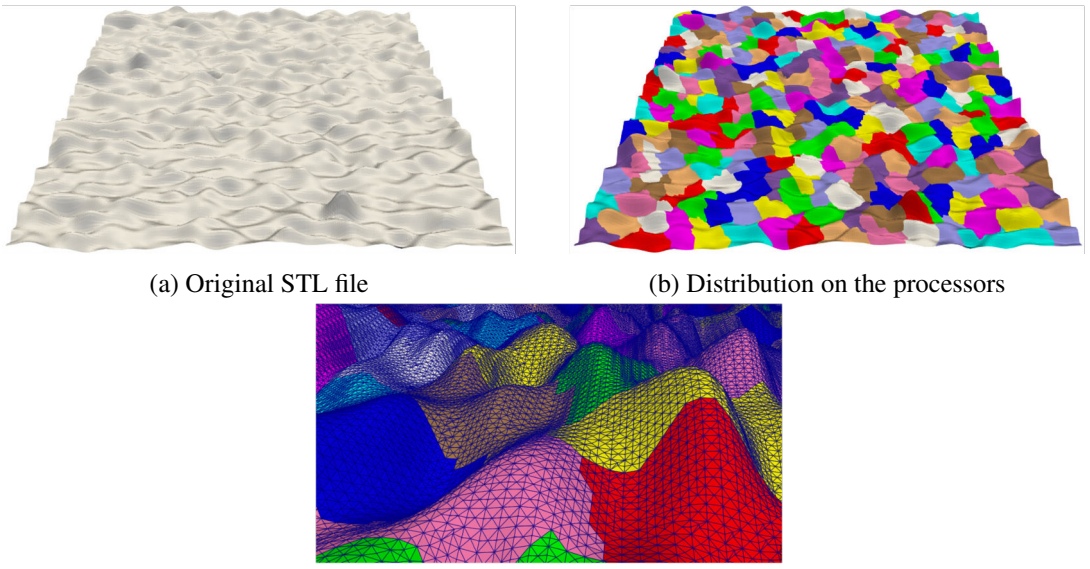

(a) Original STL file

(b) Distribution on the processors

(c) Refinement of the surface

Figure 4.10 – Step 1 of the RRMG.

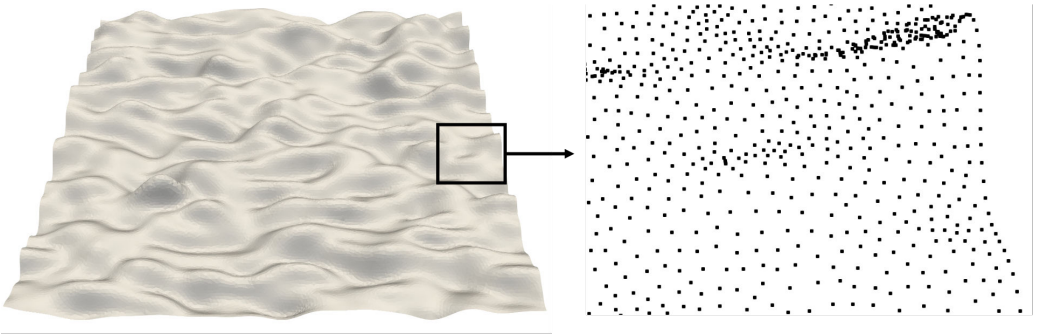

Figure 4.11 – Step 2: Generation of Lagrangian particles. On the left, the rough surface from the RSG containing around 58 000 cells. Approximately the same number of Lagrangian particles are then generated, hence about 240 x 240 particles as the surface is square. On the right, a zoom-in of the surface on the particles.

4.3.3.4 Step 3: Computation of approximate distance to surface

After the particles are relocated on the volume mesh, the approximate distance of each node of the volume mesh to the surface is computed.

4.3.3.5 Step 4: Volume adaptation of the Eulerian mesh

Since the distance to the STL is calculated at each node, the cells in the vicinity of the surface can be refined by defining a specific metric field. This metric field is smaller at the surface location and has to respect a maximum cell size gradient condition (Fig. 4.12). In order to keep a good quality of the volume mesh, several successive steps are performed. In the final step, the metric at the surface is equal to the desired cell size.

The number of steps can be adjusted depending on the ratio between the cell size of the initial mesh and the final desired cell size at the surface. For the moment, the interior and the exterior

of the final flow domain are not distinguishable, and the cells close to the surface do not coincide with it.

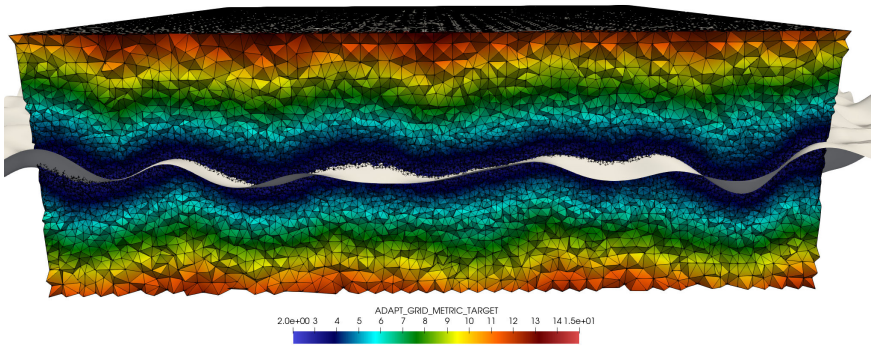

Figure 4.12 – Step 4: Refinement of the volume. The metric field target with the rough surface from the RSG. Minimum value near the surface for getting the prescribed cell size. Maximum cell size gradient must be respected hence the metric field.

4.3.3.6 Step 5: Calculation of a level set function from interior points and markers

To ultimately get a body-fitted mesh, the surface has to be materialized in the unstructured mesh. For this purpose, an implicit representation of the surface is created thanks to a distance-based level set method. In this method, a signed distance function is generated such that the surface is the zero iso-contour of this level set. Building a distance function, which is positive on both sides of the surface, is trivial. However, building a signed-distance function is more challenging (Fig. 4.13). The chosen algorithm here is based on a level set displacement, which can be seen as a wrapping method. The algorithm is the following:

- a geometric distance to the Lagrangian particles is computed in a narrow band around the surface: $d(x) = |x - x_p|$ where x and x_p are the coordinates of the node and the projected node, respectively. This parallel algorithm is based on a fast-marching method from Janodet *et al.* [143]. The idea is to build the list of the closest Lagrangian particles to the surface at each node. The distance is then obtained by projecting the node position onto the triangles represented by the Lagrangian particles.
- the desired cell size Δx is subtracted from the geometric distance creating a small negative distance region around the surface: $d_{\text{displ}}(x) = d(x) - \Delta x$. This step creates two zero iso-contours of the level set around the surface at $d(x) = \Delta x$.
- from the interior points and based on the volume mesh connectivity, the interior domain up to the first level set is flagged and kept. The remaining domain is assigned a negative distance. At the end of this sub-step, only one level set remains.
- The remaining level set is displaced back by adding the desired cell size: $d_{\text{final}}(x) = d_{\text{displ}}(x) + \Delta x$.

While this methodology gives an approximate description of the surface on the volume mesh, the errors have been assessed, and they are small and of the order of a fraction of the desired cell size. The great benefit of using a level set is that it automatically corrects some topology issues from the STL files, such as small gaps. Since the algorithm is distance-based, no topological properties are needed for the STL files.

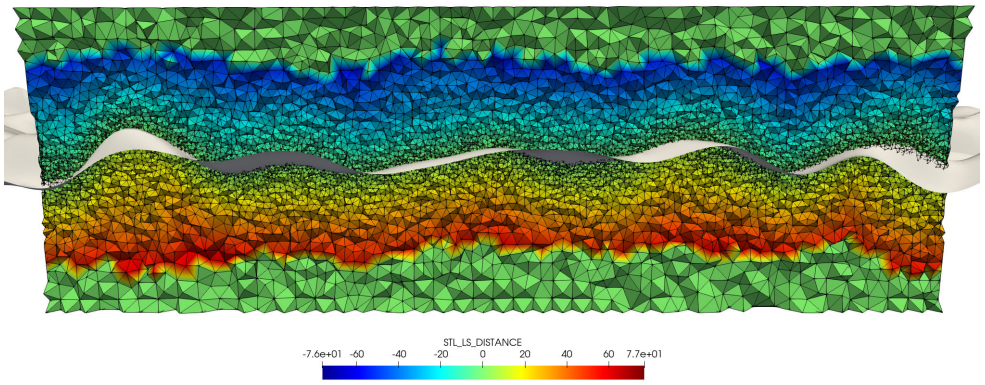

Figure 4.13 – Step 5: Signed distance.

4.3.3.7 Step 6: Cutting of the Eulerian mesh

Once the signed-distance level set function is built, the Eulerian mesh is cut, i.e., all the edges, faces, and cells crossed by the level set function are tessellated to transform the implicit surface into an explicitly meshed surface (Fig. 4.16).

In a tetrahedron, the cutting algorithm must consider the number of edges crossed by the level set. This leads to distinguish 16 cases illustrated in Fig. 4.14 and Fig. 4.15. Then, to have a fully parallel algorithm, a global index of the nodes has to be considered for having compatible faces between two cut elements that share a parallel interface.

4.3.3.8 Step 7: Removal of the outer cells

After the cut, the outer cells that are already flagged can be removed from the volume mesh. This step requires to rebuild some connectivity in parallel and to distribute the grid again onto the processors to keep good performance.

4.3.3.9 Step 8: Volume/surface adaptation of the interior Eulerian grid

The mesh that undergoes the preceding steps is of good quality inside the volume but of very poor quality at the surface as the mesh cut generates tiny edges and potentially highly skewed elements. Then, parallel volume and surface adaptation is performed with the MMG library to recover a correct mesh. The final mesh is represented in Fig. 4.17.

4.3.4 Assessment of final mesh

The final mesh obtained at the end of the whole generation process and illustrated in Fig. 4.17 is assessed in this section. To this aim, the skewness distribution and the cell-size distribution based on the cell volume are given in Fig. 4.18a and 4.18b. To minimize the truncation errors of the finite-volume schemes of YALES2, it is necessary that a mesh contains cells whose maximum skewness is below 0.8.

The obtained skewness distribution shows that the number of cells with high skewness is very limited, and the distribution is centered around 0.25. The cell-size distribution is also representative of what is prescribed. A large number of cells have the prescribed cell size at the interface, and the cell size grows fast to the size in the original grid.

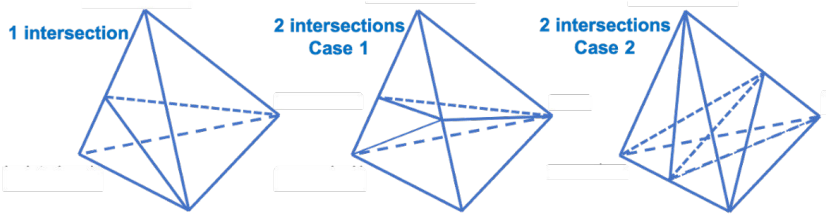

(a) One and two intersections cases

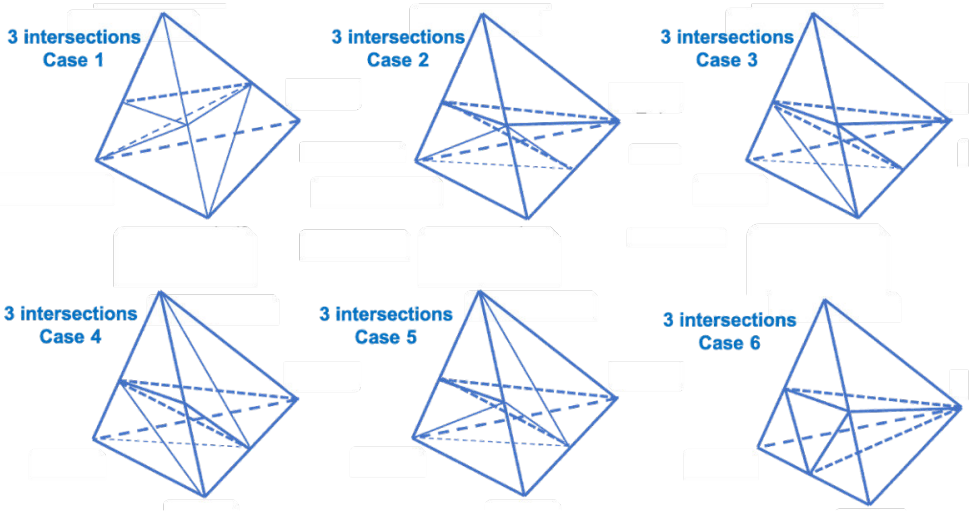

(b) Three intersections cases

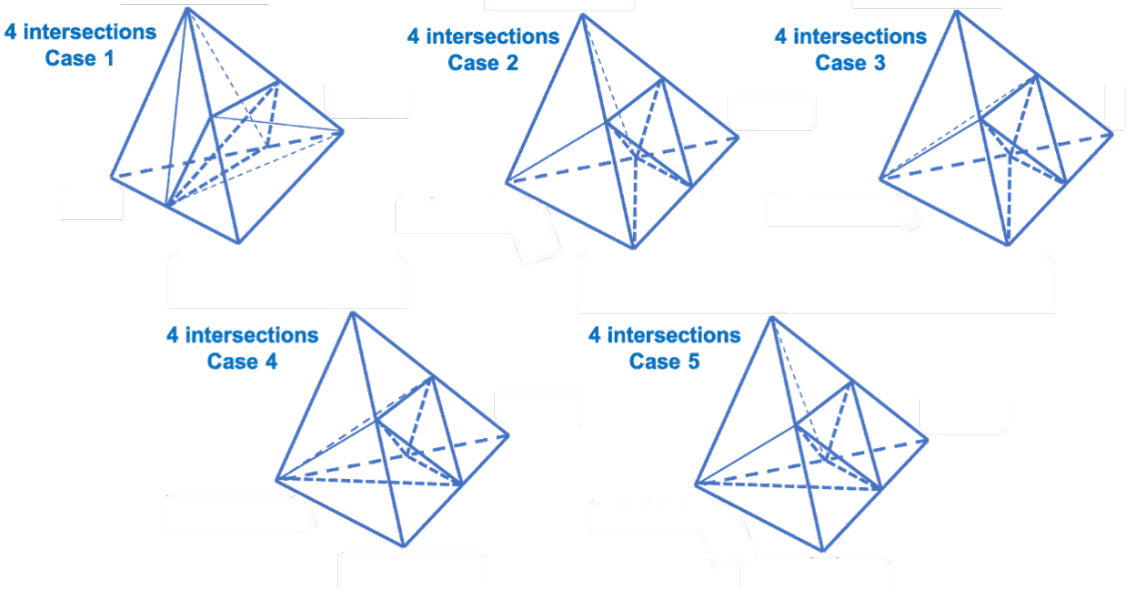

(c) Four intersections cases

Figure 4.14 – Tessellation algorithm: from one to four intersections cases (step 6).

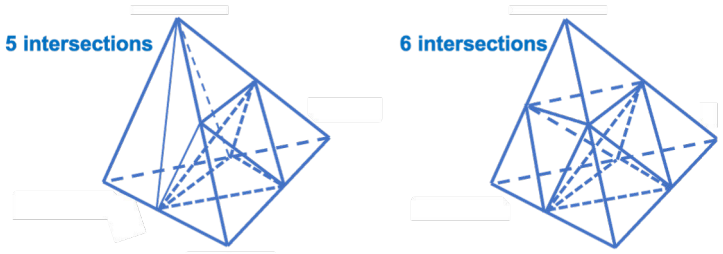

Figure 4.15 – Tessellation algorithm, five and six intersections cases (step 6).

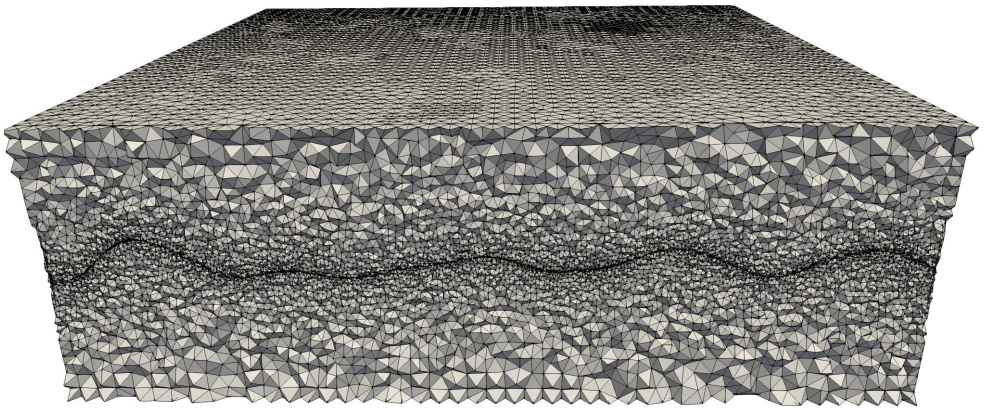

Figure 4.16 – Step 6: Cutting of the mesh.

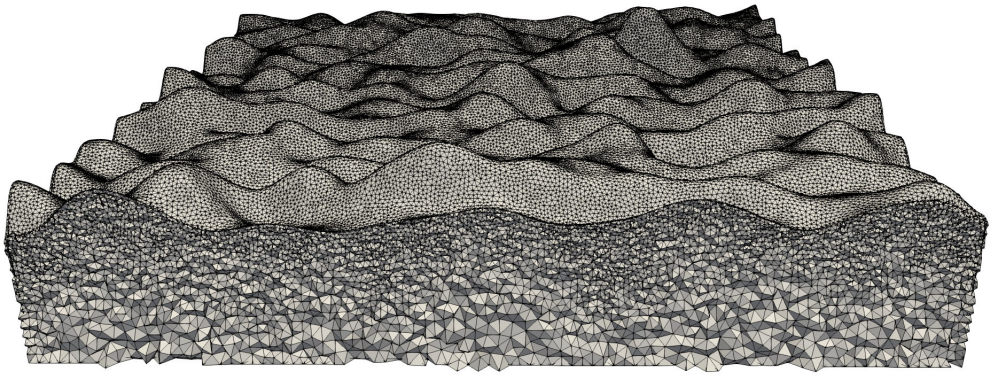

Figure 4.17 – Final mesh after surface/volume adaptation.

4.4 Conclusions

This chapter provides a comprehensive description of the surface and mesh generators and their capabilities. These generators are necessary to automatically produce body-fitted meshes with resolved roughness and user-defined parameters.

The rough surface generator (RSG), which was developed as part of this thesis, can generate various types of roughness and geometries in the STL format based on roughness parameters. An option for periodic boundaries with continuous slope is also available.

The roughness-resolved mesh generator (RRMG) is fully automated and allows control of the wall cell size. It discretizes both the fluid and the solid domains, resulting in good quality tetrahedral-based meshes. With both these tools, roughness-resolved Large-Eddy Simulations can be performed.

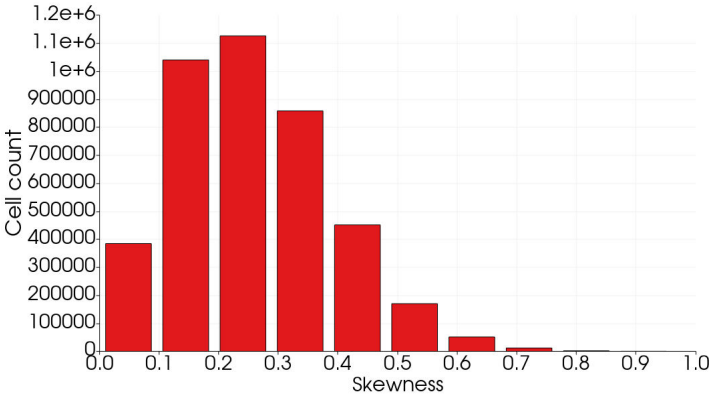

(a) Skewness distribution. In this case, nearly all cells have a skewness below 0.8, indicating a good mesh quality.

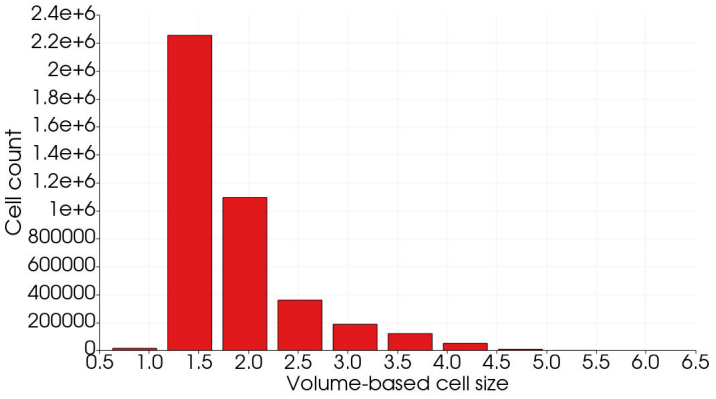

(b) Cell size based on the volume $V^{1/3}$. For this case, the target is at $1.9\ mm$.

Figure 4.18 – Final mesh quality.

CHAPTER 5

Roughness-resolved Large-Eddy Simulation: methodology and validation

Before performing roughness-resolved LES, the methodology and numerics must be set and validated. In order to run simulations for periodic channels, a recycling method has been developed during this thesis. This method enables to impose a time-varying inlet with a velocity interpolated at a distant plane in the channel. Numerics are also addressed in this chapter. Three validation cases are finally presented: periodic-channel flow, regular and irregular rough surfaces.

Contents

5.1 Numerical setup

5.1.1 Methodology, boundary conditions

The automatic generation of fully periodic channels is very challenging, and ensuring periodic meshes is complex for unstructured grids. The periodicity is though necessary to reach statistical convergence of the flow. Instead of imposing strict periodic boundary conditions in the streamwise and spanwise directions, a Lagrangian recycling method has been developed [144]. This method does not require to add a body force as a source term in the Navier-Stokes momentum equation to compensate for the wall friction. This approach can also be used as a precursor in spatially developing boundary layers by increasing L_{out}. The idea behind this recycling method is simply to use a time-varying inlet boundary condition with a velocity coming from a distant plane in the channel. This 3-step recycling process is based on passive Lagrangian particles as illustrated in

Fig. 5.1. A flow rate is imposed at the inlet and for optimizing performances, the recycling is done every N time step, $N > 1$. A linear interpolation in time is performed between two recycled planes. No rescaling is applied on the velocity profile as such profile is unknown a priori. Thus, contrary to what is proposed in Xiao *et al.* [145] for instance, no target or corrections on the velocity field are applied as input of this method. In this article, we select $N = 20$ as it gives the better compromise between performances and velocity interpolation errors.

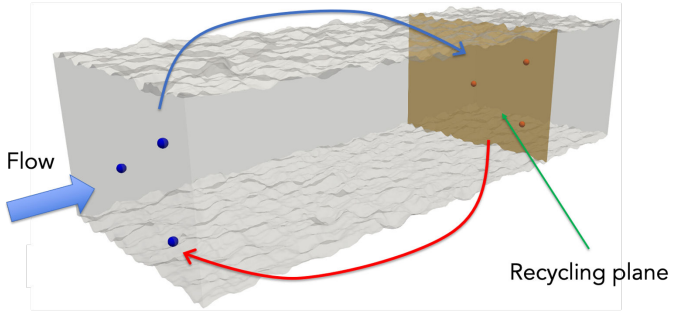

Figure 5.1 – General principle of the developed recycling method

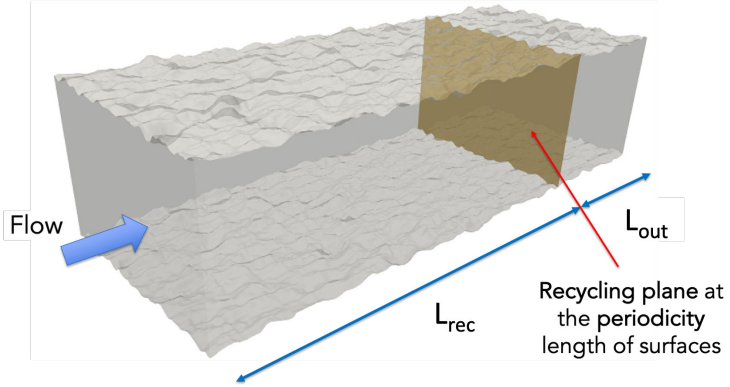

Figure 5.2 – Computational domain split into two areas: the recycling and the buffer zones

The complete process is described here:

1. Lagrangian particles are created at the inlet of the grid (blue spheres in Fig. 5.1) and are translated to the recycling plane.

2. The target field at the recycling plane, velocity for instance, is interpolated for translated particles (red spheres in Fig. 5.1)

3. This is the relocation step: particles are transferred at the inlet, and the field at this location is updated.

The computational domain is then defined with a recycling zone and a buffer area to avoid any influence of the outlet boundary treatment on the recycled velocity (Fig. 5.2). Thus the location of the recycling plane is primordial and should be set at a given distance from the outlet within the domain. For two parallel planes, this distance was found to be at least equal to the length between both planes, and in our cases, the latter corresponds to $2H$ (H being the half-height of the channel). Indeed, perturbations of the velocity field due to the outlet boundary condition may be recycled and injected at the inlet if L_{out} is below this threshold.

In order to decrease interpolation margin errors between the inlet and the recycling plane, both locations should be equivalent at the wall. The generated rough surface and conformal mesh both respect this periodicity condition only in terms of wall topology. A no-slip wall boundary condition is applied on rough planes, and the other sides in the spanwise direction are considered as slip walls. This methodology is also applied in the smooth configuration.

5.1.2 Numerics and models

Incompressible flow simulations are considered in this manuscript. The chosen target bulk Reynolds number range is the fully developed turbulent flow. The fluid kinematic viscosity is set to $\nu = 1.517\ 10^{-5}\ m^2/s$, and the maximal CFL number used is equal to 0.8. The WALE subgrid-scale model is retained as it is widely used for LES of boundary layer flows [61]. A fourth-order central finite-volume scheme is used, and the four-step fourth-order scheme TFV4A is applied for velocity and scalar transport prediction [66].

From STL generation to post-processing, all calculation steps are integrated into a workflow tool. This allows to manage automatically series of runs on a distant super-computer.

5.2 Simulation analysis

This section details the different tools used for the subsequent analysis of the RRLES.

5.2.1 Non-dimensional velocity and temperature

For scaling velocity and temperature profiles, a calculated effective distance introduced by Kuwata & Kawaguchi [146] is used. Indeed, due to irregularities of the surface height, this kind of distance is not straightforward to determine, as in a smooth-wall case. The effective distance is defined in Eq. 5.1 with h_w the minimal height of the surface. The variable φ corresponds to the x-y plane porosity, which is the ratio between the x-y plane surface occupied by the fluid and the total x-y plane area.

$$h_e = \int_{h_w}^{h} \varphi \, dh \tag{5.1}$$

Computation of the friction velocity u_τ (Eq. 5.2) is based on the difference between average pressure at the inlet and at the recycling plane as exposed in Fig. 5.3. The shear Reynolds number is then calculated as $Re_\tau = \frac{u_\tau H}{\nu}$. and the quantity h_e^+ is defined as $h_e^+ = \frac{h_e u_\tau}{\nu}$.

$$u_\tau = \sqrt{H \frac{\langle p_i \rangle - \langle p_r \rangle}{\rho L}} \tag{5.2}$$

Concerning the friction factor, the Fanning definition $f = 2\left(\frac{u_\tau}{U_b}\right)^2$ is used with U_b the bulk velocity. All these quantities are monitored at each iteration in the LES simulation.

For the analysis of heat transfer, a normalized passive temperature $\bar{Z}$ is used. This latter can be defined as $\bar{Z} = \frac{\bar{T}-T_p}{T_\infty - T_p}$ with T_p the temperature imposed at a wall and T_∞ the bulk temperature. This scalar is considered passive and this hypothesis is valid if the temperature difference has no significant impact on the density, which is assumed here. This is why the temperature can be replaced by this dimensionless scalar. The equation for this scalar is the following:

$$\frac{\partial \bar{Z}}{\partial t} + \nabla \cdot (\bar{u}\bar{Z}) = \nabla \cdot (D_z \nabla \bar{Z}) \tag{5.3}$$

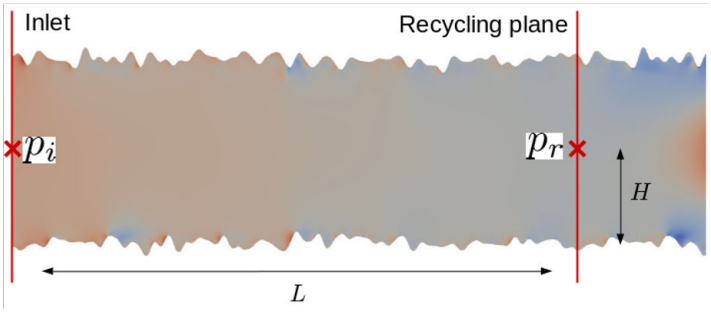

Figure 5.3 – Principle of the calculation of the friction velocity

Thus, $\bar{Z} = 1$ is imposed at the upper wall and $\bar{Z} = 0$ everywhere including the bottom wall. The laminar Prandtl number Pr of this scalar is set to $Pr = 0.71$, and the turbulent Prandtl number is equal to unity. The diffusivity D_z includes the molecular and turbulent diffusivities.

5.2.2 Budget equations

Different turbulence budget equations have been computed, dumped, and stored. This is the case for the mean kinetic equation (Eq. 5.4). Quantities denoted with the bracket $\langle\rangle$ symbol are time-averaged, and u' corresponds to the fluctuating velocity component within the Reynolds decomposition. The quantity ν_t refers to the turbulent viscosity, which is modeled through the WALE model.

$$\begin{aligned}
&\underbrace{\frac{1}{2}\frac{\partial \langle\widetilde{u}_i\rangle\langle\widetilde{u}_i\rangle\langle\widetilde{u}_j\rangle}{\partial x_j}}_{1} + \underbrace{\frac{\partial \langle\widetilde{u}_j\rangle\langle\widetilde{p}\rangle}{\partial x_j}}_{2} \\
&+ \underbrace{\frac{\partial \langle\widetilde{u}_i\rangle \left\langle\tau_{ij}^{SGS}\right\rangle}{\partial x_j}}_{3} - \underbrace{2\frac{\partial \langle\widetilde{u}_i\rangle \left\langle\nu\widetilde{S}_{ij}\right\rangle}{\partial x_j}}_{8} + \underbrace{\frac{\partial \langle\widetilde{u}_i\rangle \langle u_i' u_j'\rangle}{\partial x_j}}_{4} \\
&= \underbrace{\left\langle\widetilde{S}_{ij}\right\rangle \left\langle\tau_{ij}^{SGS}\right\rangle}_{5} + \underbrace{\left\langle\widetilde{S}_{ij}\right\rangle \langle u_i' u_j'\rangle}_{6} - \underbrace{2\left\langle\widetilde{S}_{ij}\right\rangle \left\langle\nu\widetilde{S}_{ij}\right\rangle}_{7}
\end{aligned} \tag{5.4}$$

with $\tau_{ij}^{SGS} = -2\nu_t\widetilde{S}_{ij}$ and $\widetilde{S}_{ij} = \frac{1}{2}\left(\frac{\partial\widetilde{u}_i}{\partial x_j} + \frac{\partial\widetilde{u}_j}{\partial x_i}\right)$.

5.3 Validation

The recycling methodology and numerics are first validated. Thus, three cases are studied. The first one is a periodic-channel flow. An open channel including packed hemispheres and an irregular rough surface are respectively the second and the third validation cases.

5.3.1 Comparison to periodic-channel flow

We validate our numerical methods by reproducing the classical $Re_\tau = 180$ pressure-gradient driven periodic smooth channel flow DNS test case from [147] (referred to as KMM hereafter). The geometry is $L_x = 4\pi H$, $L_y = 2\pi H$, $L_h = 2H$ with the same RRLES direction denomination

and the dimensionless mesh resolution is $\Delta_x^+ = 8.6,\ \Delta_y^+ = 8,\ \Delta_h^+ = [0.38, 5.3]$. A first test (T1) is done with the periodic condition methodology, and a second one (T2) uses the recycling boundary condition. For the latter, we set the recycling plane at a distance $2H$ above the outlet in the longitudinal direction, and the input flow rate is chosen to impose the same bulk velocity measured in [147]. Results are summarized in Fig. 5.4. Good agreement between tests and references shows that our numerical schemes and recycling boundary conditions are appropriate for infinite periodic channel flow simulations.

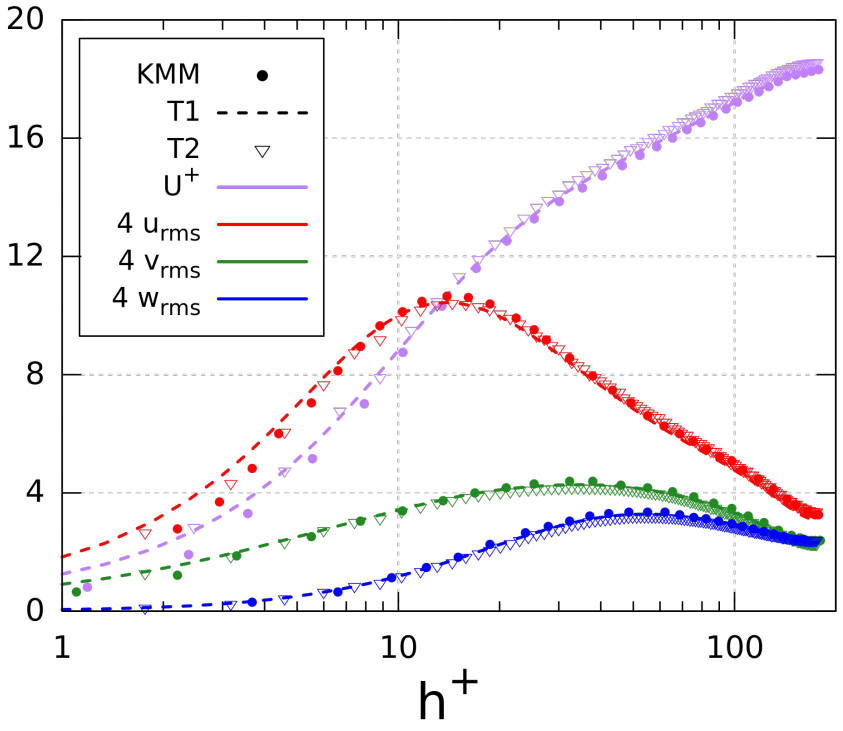

Figure 5.4 – Mean velocity and fluctuation profiles in the channel flow test case

5.3.2 Regular rough surface: packed hemispheres

In a more pragmatical way, Chatzikyriakou *et al.* [95] performed a detailed LES and DNS simulations campaign to study the impact of hemispheres as rough elements on fully developed turbulent flows (cf Fig. 5.5). They have tested different configurations for two shear Reynolds ($Re_\tau = 180$ and $Re_\tau = 400$). The idea behind this kind of geometry is linked to subcooled boiling heat transfer applications where potential hemispherical bubbles are attached to the heated wall. They expose a clear separation between the inner wall layer and the outer layer. The friction factor increases proportionally to the roughness element height, while the mean velocity profile presents a downward shift proportionally to the roughness element height. Their study also reveals that these roughness elements promote locally the instantaneous flow motion in the lateral direction in the wall layer.

For Large-Eddy Simulations (LES), the chosen test case is a channel with two planar surfaces at the bottom and the top, including hemispheres. There are two main objectives with this kind of geometry. The first one is to be able to compare with the roughness model of *ANSYS Fluent* software. A second reason is to validate the methodology and to compare results with a reference paper. Indeed, Chatzikyriakou *et al.* [95] performed calculations with hemispheres as rough elements.

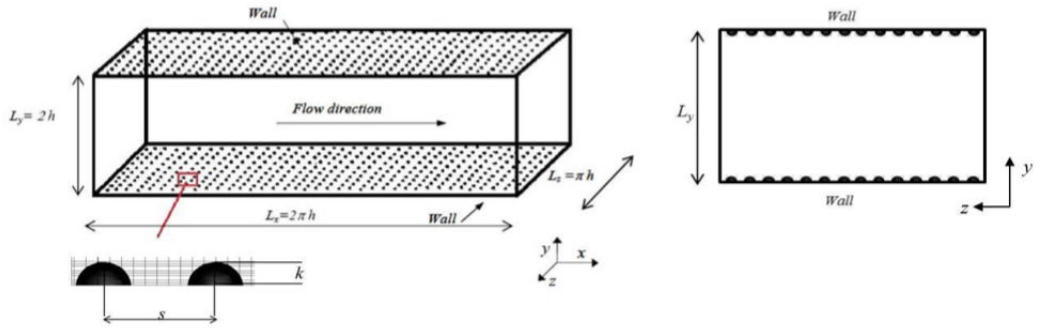

Figure 5.5 – Schematic representation of the computational domain used for roughened-channel flow simulations (Chatzikyriakou *et al.* [95])

In order to achieve these goals, two configurations with different hemispheres' radii and spacing between them are investigated. The latter is defined as the distance between the extremities of two hemispheres and is described in Fig. 5.6. To confront LES results with RANS ones, studying the flow above a sufficiently rough surface is interesting. This is why the radius is set to 50 μm. In addition, to fit with the *ANSYS Fluent* model for rough surfaces, hemispheres should be side by side. However, the mesh could be too heavy; thus, a spacing of 50 μm is also selected to minimize the computational cost. For the second configuration, illustrated in Fig. 5.7, parameters are the same as those used in Chatzikyriakou *et al.* [95]. Values are reported in Tab. 5.1. The parameter H corresponds to the half-height channel, and the equivalent S_a is the surface value of the roughness height. Finally, it should be noted that $L_x \approx 2.5\,\pi H$, $L_y \approx \pi H$ and $L_z = 2H$. Theoretically, this ensures to capture all turbulence streaks.

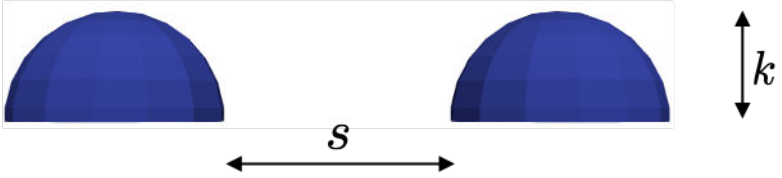

Figure 5.6 – Notation for radius k of hemispheres and the spacing s

Working hypotheses

In each case, incompressible flow simulations are performed. The shear Reynolds number is defined as $Re_\tau = \frac{u_\tau h}{\nu}$ with h the half channel height. The chosen target Reynolds number range is the fully developed turbulent flow. This is why the Reynolds number for both configurations is above 6000.

Comparison with RANS results: configuration 1

The purpose of this configuration is to compare with RANS results and more specifically to compare the friction factor value. Therefore the surface is relatively rough, and the first objective is to get a body-fitted mesh.

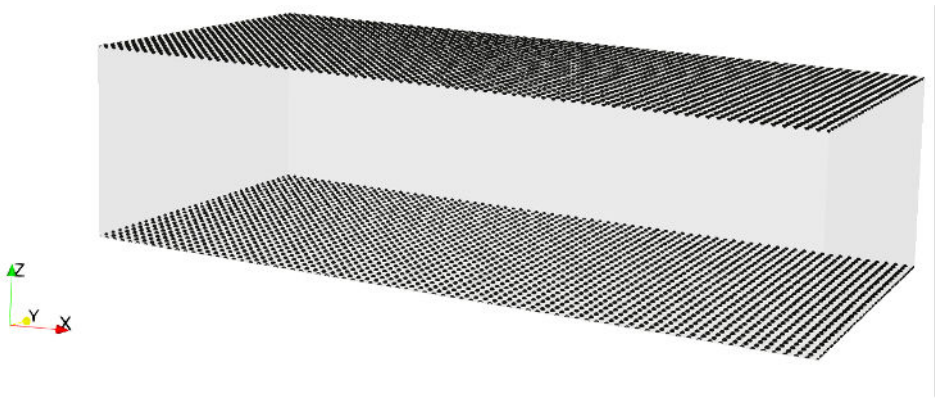

Figure 5.7 – Computational domain for configuration 2

Parameters	Configuration 1	Configuration 2
k	$50.0\ \mu m$	$12.5\ \mu m$
s	$50.0\ \mu m$	$25.0\ \mu m$
$L_x, L_y, L_z\ (mm)$	$5.1; 2.4; 1.5$	$3.9; 1.6; 1.0$
$H\ (mm)$	0.75	0.5
Equivalent $S_a\ (\mu m)$	16.9	5.79

Table 5.1 – Configurations for LES test cases

Meshing

A balance between a sufficient number of elements and a relatively light mesh has to be achieved. In addition, the meshing process has to keep the topology intact. This task is challenging due to hemispheres and the intersection between these rough elements and a planar surface.

Due to a diameter of hemispheres which equals $50\ \mu m$, an imposed $7\ \mu m$ cell size on the surface is selected. A cartesian grid is also used, hence a maximum cell size. The refinement ratio h_{grad} equals 0.1. This latter denotes that the size of the next cell into the domain is 10% higher than the previous cell. All values are reported in Tab. 5.2. With these characteristics, the number of elements rises to 55 million for the final mesh (Fig. 5.8).

Results

As seen in Chapter 3, the wall roughness has an impact on the turbulent flow and induces a downward shift in the law of the wall:

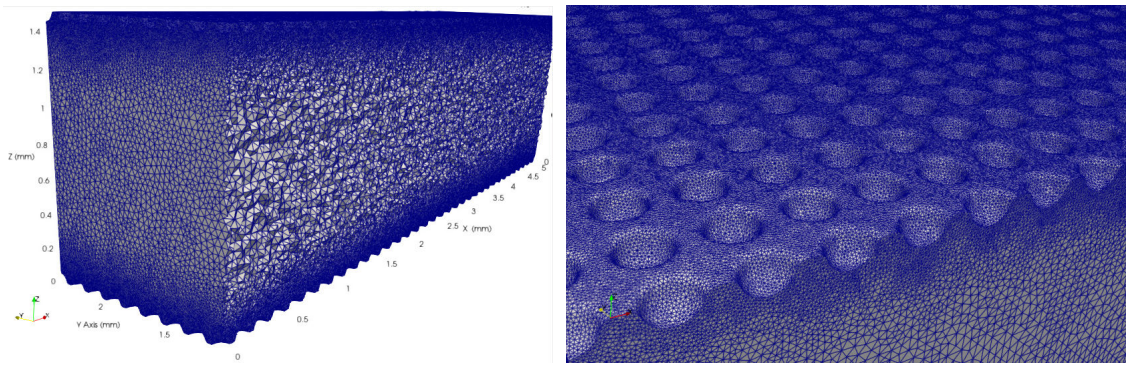

(a) Global mesh (b) Zoom-in on hemispheres

Figure 5.8 – Mesh of the configuration 1

Parameters	Values
$L_x, L_y, L_z\ (mm)$	$5.1; 2.4; 1.5$
N_x, N_y, N_z	$125\ ;\ 120\ ;\ 50$
Cell size on STL	$7\ \mu m$
h_{grad}	0.1
Number of elements	$55\ M$

Table 5.2 – Mesh characteristics of configuration 1

$$U^+(z^+) = \frac{1}{\kappa}\ln(z^+) + B - \Delta U^+ \tag{5.5}$$

where U^+ is the velocity normalized by the shear velocity $u_\tau = \sqrt{\frac{\tau_w}{\rho}}$, z^+ is the normalized length scale defined by $z^+ = \frac{zu_\tau}{\nu}$, $\kappa = 0.4$ is the von Karman constant and the value $B = 5.5$ is the log-law constant for a smooth wall. The so-called roughness function ΔU^+ corresponds to the shift of the mean velocity profile compared to a smooth wall.

The shear Reynolds number is given as $Re_\tau = \frac{hu_\tau}{\nu}$ with h the half channel height as already mentioned. The friction factor used in this study is the Fanning one and is defined, with U_b the bulk velocity, as:

$$f = \frac{2\tau_w}{\rho U_b^2} = 2\left(\frac{u_\tau}{U_b}\right)^2 \tag{5.6}$$

One key point is to determine the shear velocity. Once this quantity is calculated, velocity profiles can be plotted, and there is actually the opportunity to calculate the friction factor. A first method could be to estimate the shear stress τ_w. However, an accurate estimate appears to be problematic due to roughness. This is why we decide to calculate u_τ from the pressure gradient. Indeed, a relationship between these two quantities exists (cf Eq 5.7), and the pressure gradient is determined at the center of the channel along the streamwise axis inside the recycling domain.

$$u_\tau = \sqrt{-H\ \nabla(P/\rho)} \tag{5.7}$$

Finally, target results for this case can be calculated and are reported in Tab. 5.3.

Parameters	Values
Re	8240
$u_\tau\ (m/s)$	19.54
Re_τ	966
$S_a/2H = S_a/D$	$1.12\ 10^{-2}$
Friction factor	$2.94\ 10^{-2}$

Table 5.3 – Results of configuration 1

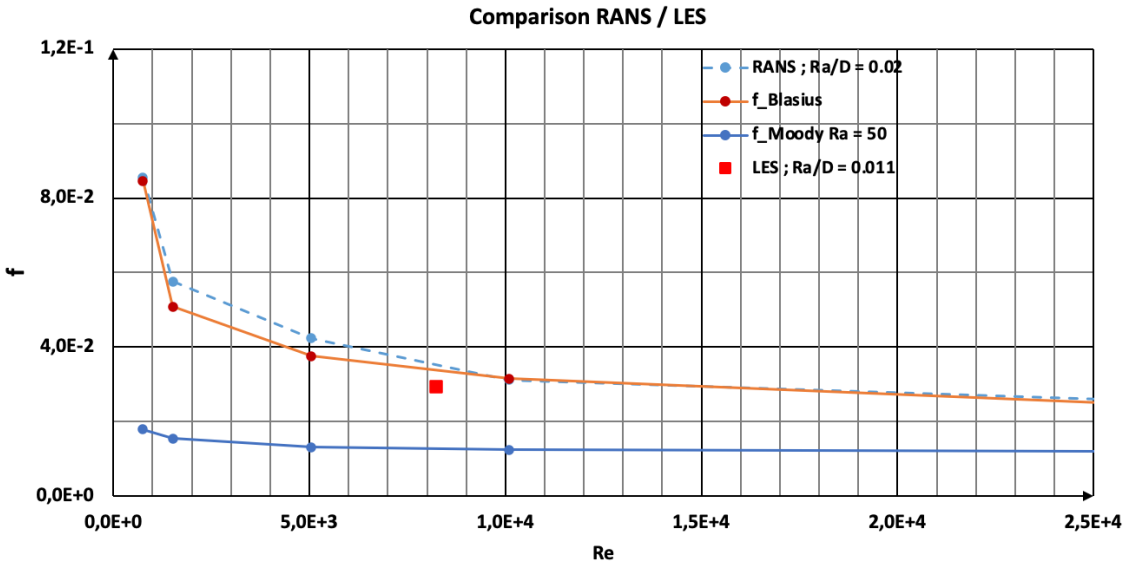

Figure 5.9 – Comparison between RANS and LES results on the friction factor for the configuration 1; RANS: $S_a/D = 0.02$ and LES: $S_a/D = 0.0112$

RANS simulations with $S_a = 50\ \mu m$ ($S_a/D = 0.02$) were performed by TEMISTh. Figure 5.9 presents results for the friction factor, and the Moody correlation was divided by 4 in order to correspond to the Fanning definition. LES result is slightly lower than RANS ones, but this is expected due to a higher relative roughness for the RANS case. This confirms that both RANS and LES methodologies are coherent. The friction factor obtained with Blasius correlation yields a coefficient $f_{Blasius} = 3.32\ 10^{-2}$ at the Reynolds number $Re = 8240$. The relative error between the latter and the obtained coefficient with LES is 11.5%; therefore, this is additional evidence of a good methodology. It should also be observed that the experimental Moody correlation is twice lower than other results and seems irrelevant here.

Comparison with the reference paper Chatzikyriakou *et al.* [95]: configuration 2

As written above, we want to compare our results to those obtained in Chatzikyriakou *et al.* [95]. The chosen case is $s/k = 2$ and $Re_\tau = 400$. However, the reference paper exposes only outcomes on the turbulence effect and yields no result in terms of thermal performance. We will present the temperature profile though no comparison is possible with this article.

Meshing

A turning point for this mesh is to get an average z^+ close to 5. This induces to perform LES case with sufficient accuracy near walls in order to get the velocity profile. No DNS calculations have

to be conducted here so there are fewer constraints for the mesh.

For this configuration, the diameter of hemispheres equals 25 μm, and an imposed 5 μm cell size on the surface is chosen (Fig. 5.10). The refinement ratio h_{grad} is unchanged and is equal to 0.1 (Tab. 5.4). The obtained averaged z^+ in the recycling domain is approximately 3.2: around $z^+ \approx 0.5$ at the planar wall and $z^+ \approx 3.2$ at the top of hemispheres (Fig. 5.11). The recycling plane is located at the position $x = 2.9\ mm$, and it can be underlined that the highest z^+ values ($z^+ > 5$) are in the buffer zone thus, there is no impact on our profiles.

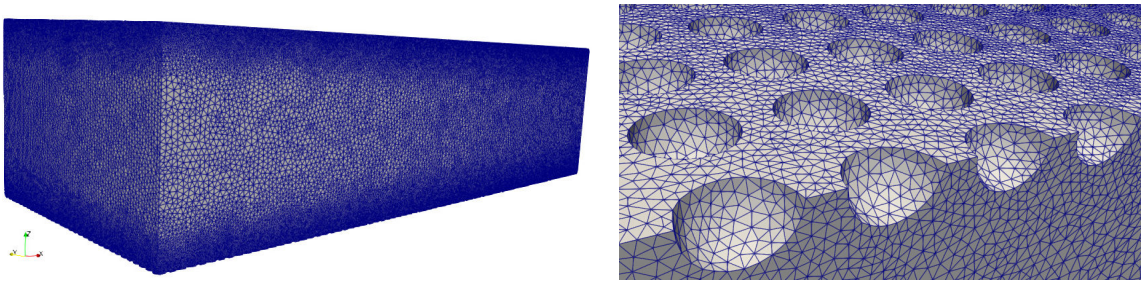

(a) Global mesh (b) Zoom-in on hemispheres

Figure 5.10 – Mesh of the configuration 2

Parameters	**Values**
$L_x, L_y, L_z\ (mm)$	3.9; 1.6; 1.0
N_x, N_y, N_z	195 ; 80 ; 100
Cell size on STL	5 μm
h_{grad}	0.1
Number of elements	54 M

Table 5.4 – Mesh characteristics of configuration 2

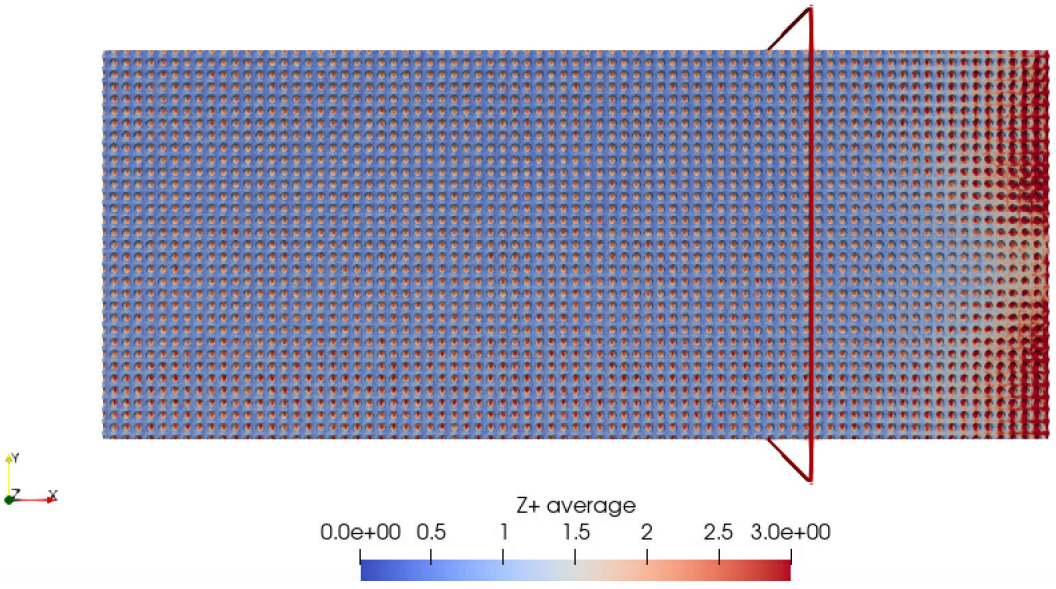

Figure 5.11 – Field of z^+ on the top surface. The red plane symbolizes the recycling plane

Results

As the shear Reynolds number is imposed ($Re_\tau = 400$), we need to calculate the bulk velocity to set the correct flow rate. For this purpose, the taken friction factor is the same as in Chatzikyriakou *et al.* [95]: $f_{chosen} = 0.033$. Their friction coefficient definition is Darcy's this time. Therefore we deduced the bulk velocity:

$$f = 2\left(\frac{u_\tau}{U_b}\right)^2 \; ; \; U_b = \frac{u_\tau}{\sqrt{f_{chosen}/2}} \tag{5.8}$$

Parameters	Values
Re_τ	400
$u_{\tau_{chosen}}\ (m/s)$	12.1
f_{chosen}	0.033
Re	6226
$u_{\tau_{calc}}\ (m/s)$	14.9
$Re_{\tau_{calc}}\ (m/s)$	491
f_{calc}	0.049

Table 5.5 – Global results of configuration 2

We recalculate the shear velocity $u_{\tau_{calc}}$ from the equation Eq. 5.7 and the latter is slightly higher than imposed (Tab. 5.5). This implies that we expect the downward shift of the velocity profile to be slightly higher than in the reference paper.

Then, we can check qualitatively velocity and give an overview with an instantaneous velocity field (cf Fig. 5.12). One can see the influence of the rough elements on the flow and also some recirculation zones. In comparison with Chatzikyriakou *et al.* [95] instantaneous velocity in Fig. 5.13, fields seem to be equivalent and appear to present similarities.

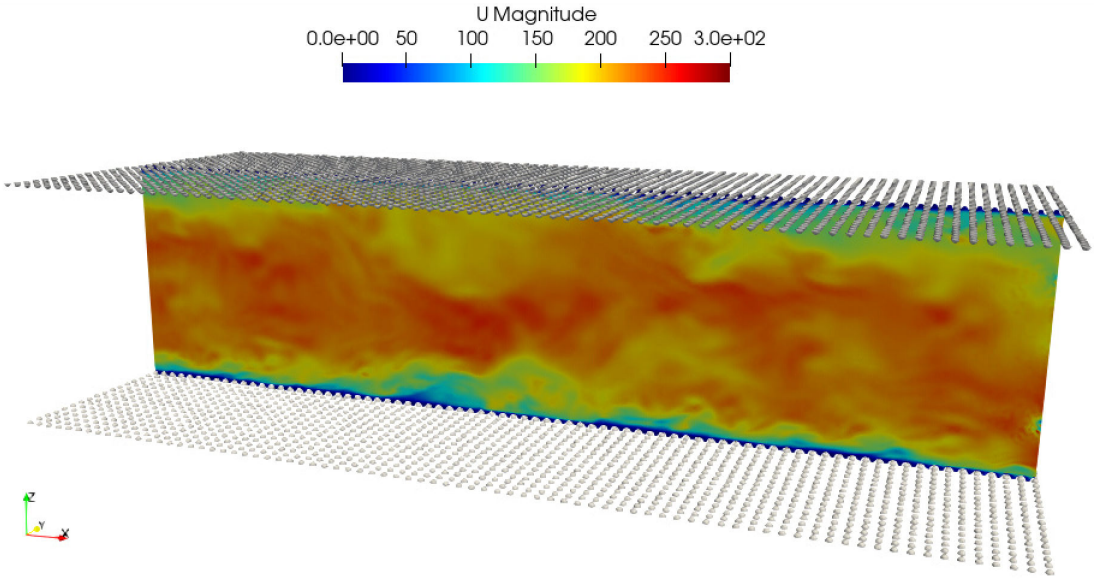

Figure 5.12 – Instantaneous velocity field at the center of the channel from our LES

The streamwise mean velocity profiles against wall units are exposed in Fig. 5.14. As expected, the downward shift is higher for our result than in the reference paper due to a larger friction factor.

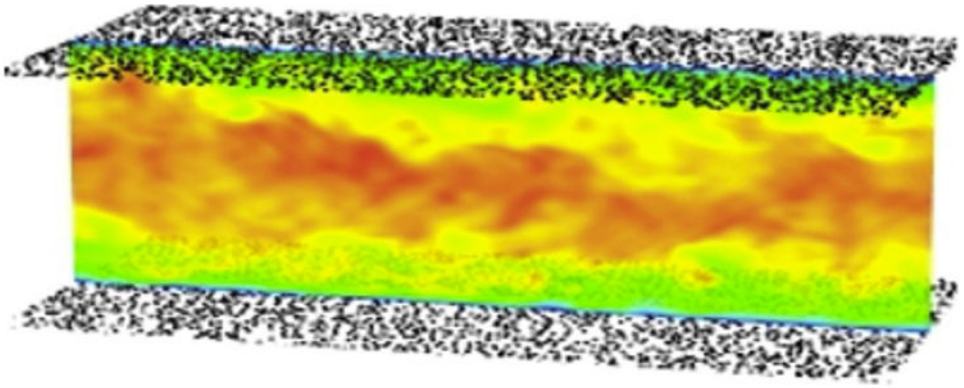

Figure 5.13 – Instantaneous velocity field from Chatzikyriakou *et al.* [95]

For $z^+ < 3$, the slight difference between LES and DNS of [95] can be explained by the fact that $z^+ \approx 3$ corresponds to our minimum value of z^+ at the top of hemispheres. On our global profile, we can see then the impact of the roughness elements and a higher friction coefficient. Therefore, the tendency of the velocity profile is retrieved in comparison with the reference paper.

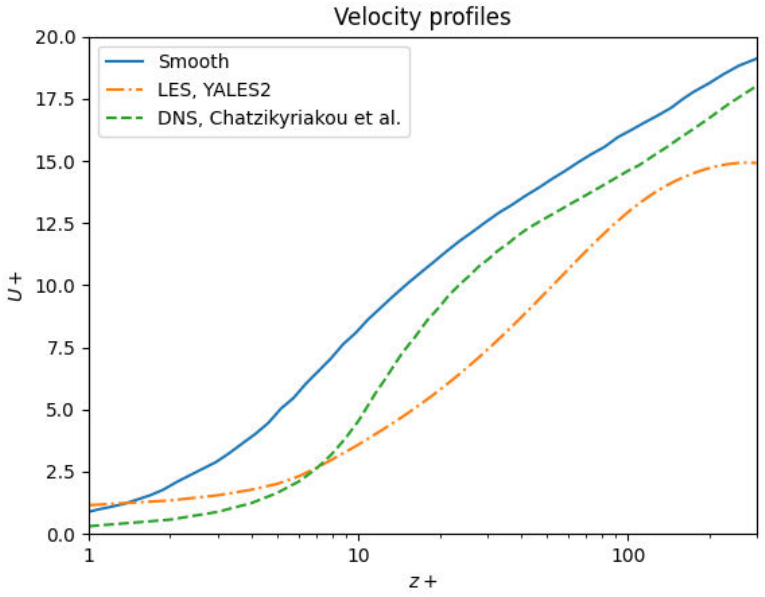

Figure 5.14 – Velocity profiles: LES simulation with YALES2 (dash-dot line), DNS result from Chatzikyriakou *et al.* [95] (dashed line), smooth wall channel

Temperature profile

With the objective to study thermal performances, we have already integrated a normalized passive temperature, as already mentioned. Although no comparison is possible with this configuration, a given temperature profile is expected. Thus an overview of this scalar profile is interesting for upcoming simulations.

As a reminder, the scalar Z is equal to 1 everywhere except at the bottom wall. With this temperature gradient, we look forward to have the profile of temperature as seen in Fig. 5.15 from Toki *et al.* [148].

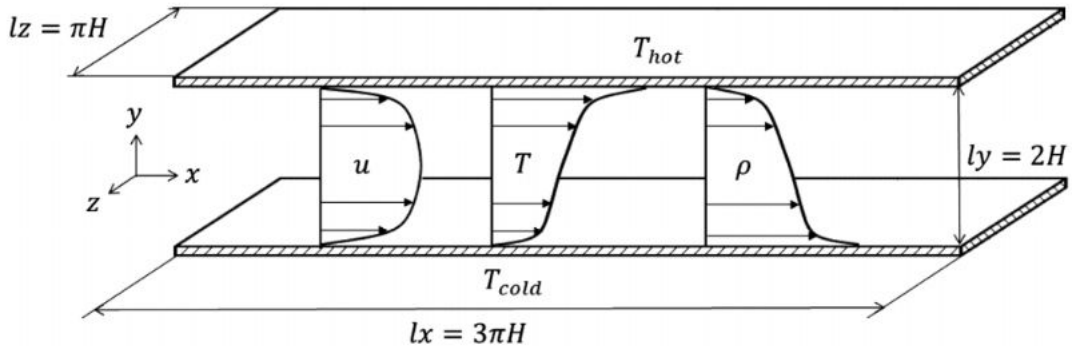

Figure 5.15 – Expected velocity and temperature profiles in a turbulent channel with a temperature gradient, scheme from [148]

The profile obtained with this simulation is presented in Fig. 5.16. Results are similar to what was expected. The influence of hemispheres could explain the slight bump near the bottom wall.

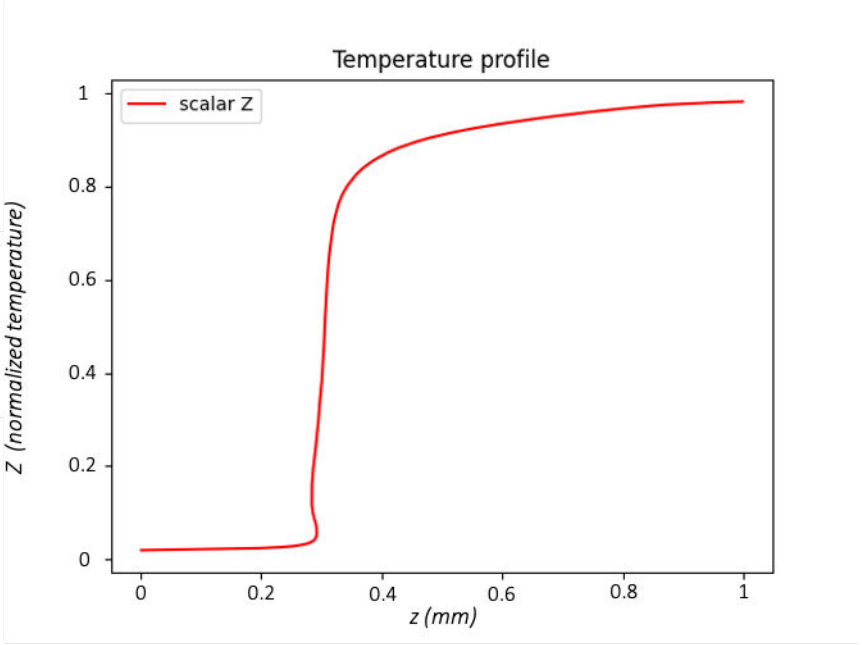

Figure 5.16 – Temperature profile obtained with the scalar $\bar{Z}$ for the configuration 2

Partial conclusions

Simulations with two configurations have been performed in order to validate the methodology and to compare results with RANS simulations. For the first configuration, obtained friction factor is in good agreement with the ones obtained with RANS and some correlations.

About the second configuration, the objective was to compare outcomes with a reference paper. The conclusion is that our LES is consistent with this article but illustrates the difficulty in reproducing these results. Besides, the temperature profile is consistent with the theoretical result.

5.3.3 Irregular rough surface

More challenging cases must be tested to evaluate the methodology concerning additive manufacturing surfaces. For this purpose, the capability of the methodology is assessed on two cases consisting of parallel planes with different effective slopes: $ES = 0.24$ and $ES = 0.72$ (Figs. 5.17 and 5.18). They correspond to canonical cases targeted for an LES database. The mesh properties are summarized in Tab. 5.6, and performance are given in Tab. 5.7.

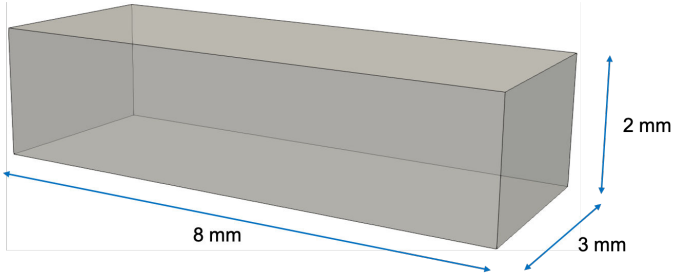

Figure 5.17 – Dimensions of the computational domain for RRLES.

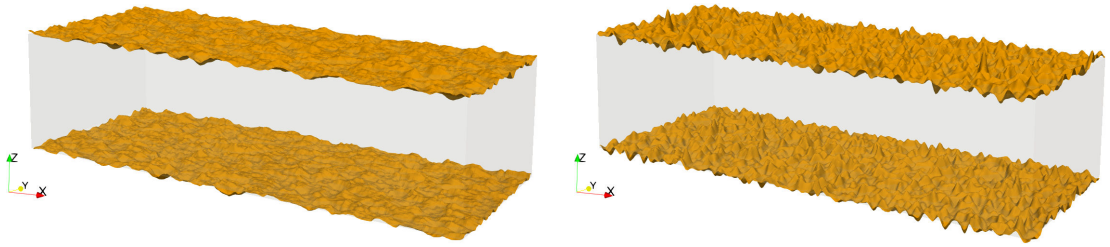

(a) $ES = 0.24$ (b) $ES = 0.72$

Figure 5.18 – Two cases of parallel planes geometries.

Parameters	Values
L_x, L_y, L_z (mm)	$8.0; 3.0; 2.0$
Initial N_x, N_y, N_z	400 ; 150 ; 100
Cell size on STL	10 μm
Max cell size gradient	0.1

Table 5.6 – Mesh properties.

From these meshes, roughness-resolved LES are then performed. The flow is assumed incompressible, the fluid kinematic viscosity is set to $\nu = 1.517\ 10^{-5}\ m^2/s$ (air at 300 K), and the maximal CFL number used is equal to 0.8. The turbulence model is the WALE sub-grid scale model [61]. The chosen value for the present case is $Re_\tau = 700$. With these parameters, the maximum non-dimensional wall distance of the first point in the flow y^+ is less than 5.

The temperature is modeled with a normalized passive temperature $\bar{Z} = \frac{\bar{T}-T_p}{T_\infty - T_p}$, with T_p temperature imposed at the wall and T_∞ the bulk temperature. The temperature can be replaced

	ES	Cells	CPUs	CPU hours	RAM /CPU
Case 1	0.24	82M	560	930h	1205Mb
Case 2	0.72	67M	280	812h	1690Mb

Table 5.7 – Meshing performance.

by this scalar if the temperature difference has no incidence on the density, and this assumption is made here. $\bar{Z} = 1$ is imposed at the upper rough wall, whereas $\bar{Z} = 0$ is set at the bottom wall.

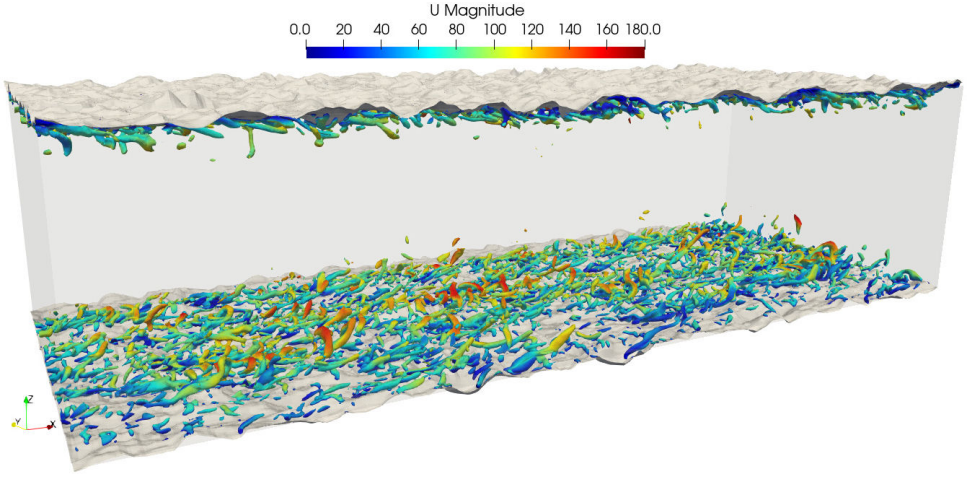

Figure 5.19 – Q-criterion iso-contours in the RRLES ($ES = 0.24$ case).

Q-criterion iso-contours are shown in Fig. 5.19 for the case $ES = 0.24$ to illustrate the vortical structures at the wall vicinity. It should be noticed that this isotropic roughness breaks streaks and promotes faster onset of turbulence.

For more quantitative results, mean velocity and temperature profiles are plotted in Fig. 5.20 and Fig. 5.21 respectively. For the velocity, this is a double-averaged profile in space (streamwise and spanwise directions) and in time. In addition, for scaling this profile, the non-dimensional effective distance $h_e^+ = \frac{h_e u_\tau}{\nu}$ is used. The definition given by Kuwata and Kawaguchi [146] is shown in Eq. 5.9 with h_w the minimal height of the surface and φ the ratio between the x-y plane area occupied by the fluid and the total x-y plane area.

$$h_e = \int_{h_w}^{h} \varphi \, dh \tag{5.9}$$

About the temperature profile, the height h is averaged in space, and the mean height has been fixed at $h = 0.0\ mm$ and at $h = 2.0\ mm$ for rough planes. Hence negative heights and some greater than $2.0\ mm$ on the graph's x-axis in Fig. 5.21.

As expected, increasing the effective slope leads to a downward shift of the velocity profile. Moreover, the temperature gradient is higher for $ES = 0.72$ than for $ES = 0.24$ near the rough walls.

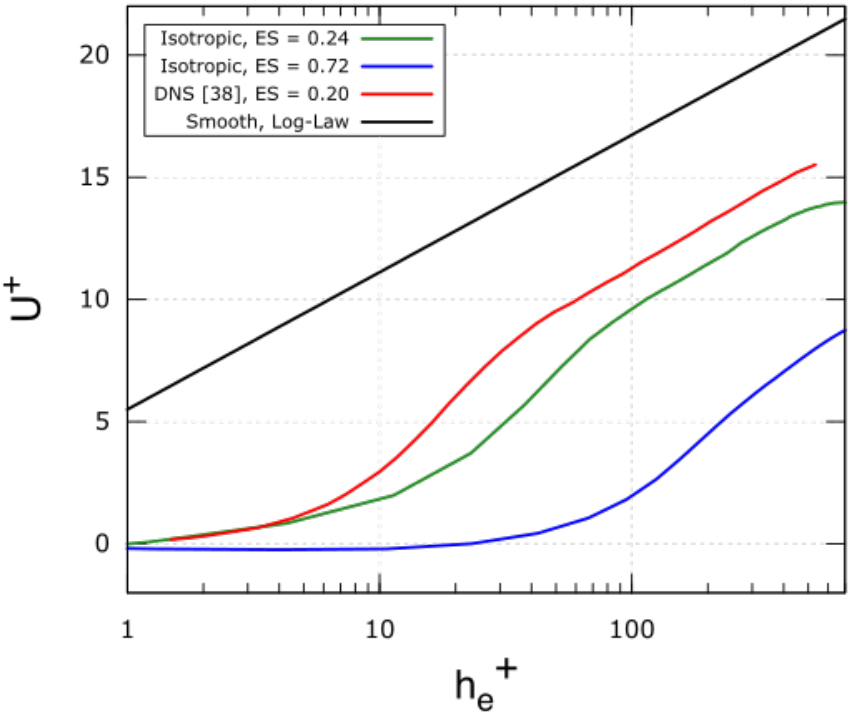

Figure 5.20 – Mean velocity profiles of RRLES cases $ES = 0.24$ and $ES = 0.72$ at $Re_\tau = 700$, DNS from Kuwata and Nagura [149] for $ES = 0.20$ at $Re_\tau = 600$.

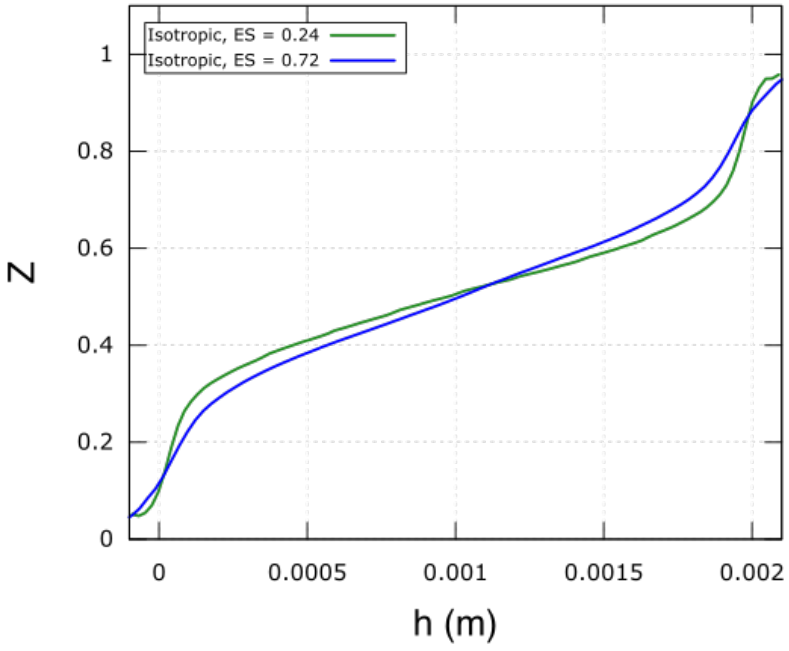

Figure 5.21 – Mean normalized passive temperature profiles of cases $ES = 0.24$ and $ES = 0.72$ at $Re_\tau = 700$.

To highlight the latter point, instantaneous passive scalar fields at the center of channels are exposed in Fig. 5.22. More temperature fluctuations are observed for the $ES = 0.72$ case, which induces this near-wall higher gradient.

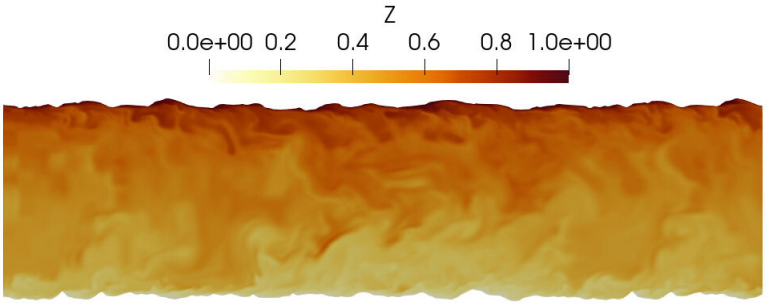

(a) $ES = 0.24$

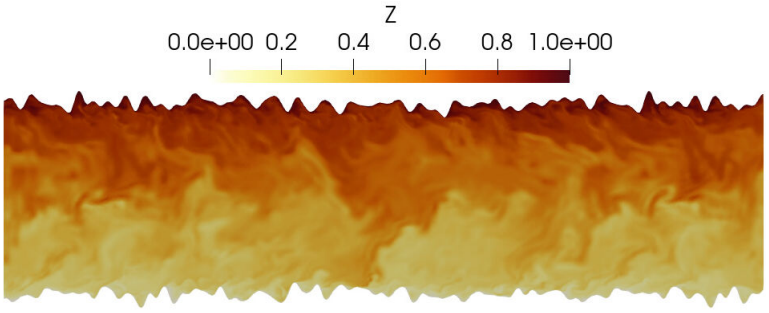

(b) $ES = 0.72$

Figure 5.22 – Instantaneous passive scalar fields after $t = 1\ ms$.

5.4 Conclusions

Numerics used in this thesis and a developed recycling method have been presented. The latter enables to set a time-varying inlet and to perform periodic channel simulations.

Three different cases have been studied for the methodology's validation purpose. The first one is a periodic smooth channel, and good agreement between tests and references has been found. The recycling boundary condition is then appropriate to perform infinite channel flow simulations.

Simulations with two configurations of packed hemispheres have been performed. For the first configuration, obtained friction factor is in good agreement with the ones obtained with RANS and some empirical correlations. About the second configuration, our LES is coherent with the reference article.

The last presented test case is an irregular rough surface. Results have been shown to be consistent with the literature even if the comparison with literature results obtained with different methods is difficult.

These cases demonstrate that the developed tools allow to conduct roughness-resolved Large-Eddy Simulations properly. Consequently, this paves the way for a database of RRLES from which derived models could be proposed for additive-manufacturing heat exchangers.

CHAPTER 6

Towards roughness modeling strategies

The objective of this chapter is to present developed models representative of the flow obtained in additive-manufactured heat exchangers without explicit representation of the surface details in the framework of RANS and LES methods. A Roughness-Resolved Large-Eddy Simulation (RRLES) database of representative channel flows has been built. From database results, derived strategies for turbulence and heat transfer have been developed and assessed.

Contents

6.1 Preliminary study: impact of roughness anisotropy

As seen in Chapter 1, surface roughness generated with additive manufacturing can be substantially larger than with traditional manufacturing techniques. Surface states of metal additive-manufactured test samples analyzed in several studies have indeed underlined this key point [150, 133, 151, 152, 153, 154]. Moreover, the wall roughness is not isotropic in space and varies according to the main direction of printing [151, 152]. Some patterns called welding tracks can appear on the surface [133]. This typical roughness has a significant impact on the performances in terms of pressure drop and heat transfer capacity [150, 153, 154]. Hence, the following study evaluates the roughness anisotropy's influence in order to better choose the parameters of the RRLES database.

6.1.1 Numerical setup

In this sub-section, chosen configurations and methodology are addressed. In order to ensure periodic channels, recycling conditions are applied on velocity and temperature.

Configurations and meshes

First of all, rough surface (RSG) and body-fitted unstructured mesh (RRMG) generators have been used [155] (cf Chapter 4). As a reminder, the former creates triangulated surfaces stored in the STL format used by the latter to compute level set functions. The level set functions are then employed to refine an existing 3D unstructured mesh and to create a conforming body-fitted mesh with controlled cell size, quality and size gradation. The resulting meshes are suitable for performing RRLES with higher-order finite-volume schemes.

Roughness-resolved LES (RRLES) are conducted for periodic channels of size $8H$ x $3H$ x $2H$ in the streamwise (x), spanwise (y) and crosswise (h) directions with H the half height of the channel which is equal to $1.0\ mm$. This domain size was confirmed to be sufficient to have a negligible impact on the periodic recycling on the wall friction [146]. In addition, the half-height was selected in order to be close to hydraulic diameters and channel heights encountered for some AM experiments as the L-2x-In case in Stimpson *et al.* [156].

Concerning the chosen configurations, three different cases representing two printing directions plus a streamwise and spanwise isotropic case have been selected for analysis (Fig. 6.1). A smooth channel is also considered as a reference. Roughness parameters that are targeted in this article are the root-mean-square height (S_q), the height distribution skewness (Sk) and kurtosis (Ku) and the effective slope (ES). While the surface height distributions are the same in the three cases, the effective slope differs due to the different space auto-correlation functions.

In addition to the printing direction, the idea is to generate surfaces that mimic roughness height distribution encountered in additive manufacturing. A broad range of roughness parameters values can be found in the literature even though there are differences between upward- and downward-facing surfaces [150, 133, 151, 152, 153, 154]. For this purpose, values of the latter for S_q, Sk and Ku are set respectively to $20\ \mu m$, around 0.2 and 4.0. Final values are exposed in Tab. 6.1 and probability density functions of height are plotted in Fig. 6.2 for the three geometries.

With the RRMG, conforming body-fitted meshes are obtained from these geometries. A balance on the element count has to be reached to sufficiently resolve the flow while minimizing the cost. In addition, the meshing process has to keep the topology intact. The mesh generation process starts from a cartesian grid which is tessellated and adapted numerous times.

The initial numbers of elements in each direction (N_x, N_y, N_h) for the cartesian grid are fixed in order to initially get isotropic cells of $20\ \mu m$. The cell size gradient is equal to 0.1 and the cell size on the rough surface is set to $\Delta y_w = 7\ \mu m$. The final number of mesh elements for RRLES is about 130 million cells.

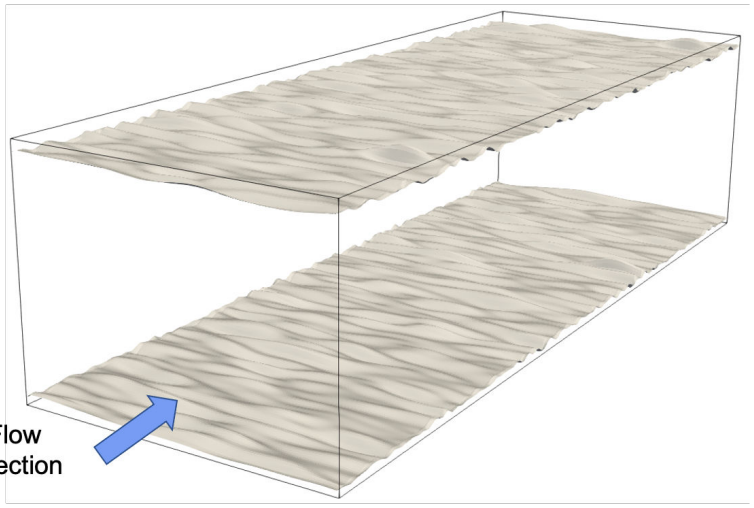

(a) Perpendicular printing direction to the flow ($ES = 0.29$)

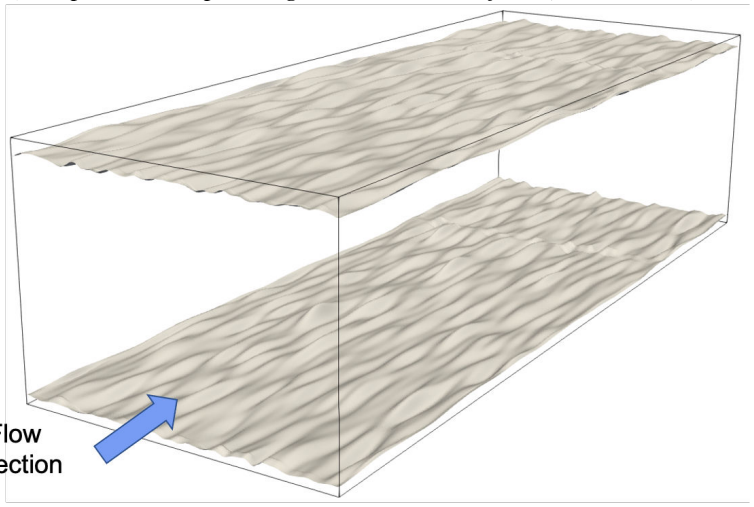

(b) Parallel printing direction to the flow ($ES = 0.06$)

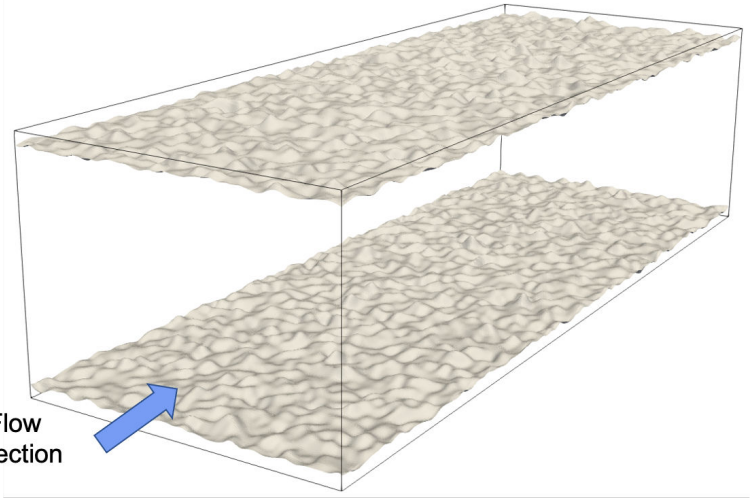

(c) Isotropic roughness case ($ES = 0.24$)

Figure 6.1 – Geometry of considered configurations

	ES	$S_a\ (\mu m)$	$S_q\ (\mu m)$	$S_h\ (\mu m)$	Sk	Ku
Front	0.29	15.6	20.0	187	0.21	3.92
Parallel	0.06	15.6	20.0	181	0.21	4.01
Isotropic	0.24	15.6	20.0	216	0.21	3.90

Table 6.1 – Roughness parameters of chosen geometries

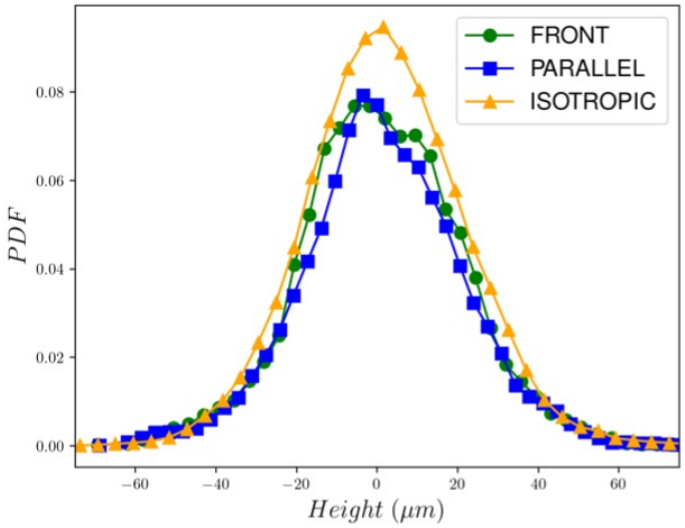

Figure 6.2 – Probability density function of height for the three cases

All characteristics and performances of the meshing process are summarized in tables Tab. 6.2 and Tab. 6.3. The mesh for the smooth case is a stretched cartesian grid with the dimensionless wall grid spacing of $\Delta_x^+ = 13.7, \Delta_y^+ = 5.5, \Delta_h^+ = [0.5, 7.3]$ in accordance with operating conditions.

For each configuration, the mesh size is fixed for all the tested Reynolds numbers. The mesh resolution for the present study is discussed hereafter. It must be noted that the dimensionless roughness $S_a/\Delta y_w$ is only larger than two, which may seem insufficient for the wall resolution. However, with body-fitted grids, this latter has to be sufficient for capturing the wall roughness (curvature and position as illustrated in Fig. 6.3) and the wall-normal velocity gradient.

Parameters	**Values**
$L_x, L_y, L_z\ (mm)$	8.0; 3.0; 2.0
Initial N_x, N_y, N_z	400 ; 150 ; 100
Cell size on STL	7 μm
Max cell size gradient	0.1

Table 6.2 – Meshing characteristics

We now discuss the RRLES mesh size used in the manuscript. Figure 6.4 compares the results obtained from the $Re = 17\,000$ isotropic configuration with a fine mesh (denoted M2, the cell size of 7 μm) and those obtained with a coarser mesh (M1) whose cell size is 10 μm. It is seen that no significant differences may be observed between the two simulations, both on velocity first- and second-order moments. This suggests that results will probably be weakly improved with a mesh finer than M2 for the analyzed moments.

	ES	Cells	CPUs	CPU hours	RAM /CPU
Front	0.29	130.1M	1024	4096h	294Mb
Parallel	0.06	129.7M	1024	4198h	292Mb
Isotropic	0.24	122.9M	1024	5307h	279Mb

Table 6.3 – Meshing performances

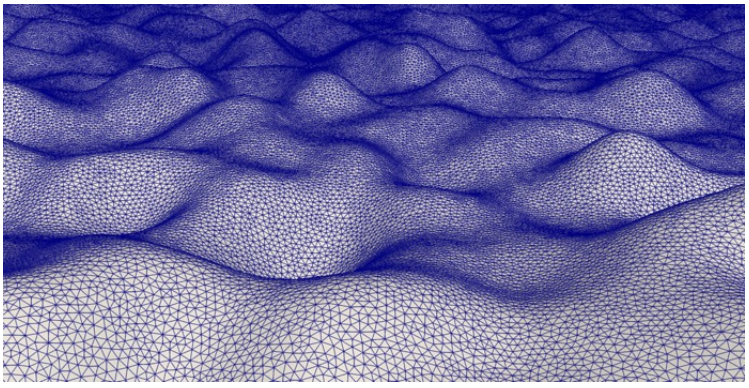

Figure 6.3 – Zoom-in of the mesh on the upper surface for isotropic case ($ES = 0.24$)

Thus, we consider that the dimensionless wall normal resolution y^+ obtained with the mesh M2 for this case is a satisfactory reference. Due to the surface alternating of peaks and valleys, making the wall-normal mean velocity gradient to vary in space, it is more relevant to observe the statistical distribution of the wall resolution than its mean value alone to evaluate the mesh quality. Fig. 6.5 shows the probability density function of y^+ obtained for the considered Reynolds numbers. Obviously, the distributions for the two lowest Reynolds numbers are satisfactory. On the other hand, the distribution for $Re = 25\ 000$ is larger than our limit. Nevertheless, it is similar to the one obtained for $Re = 17\ 000$ with M1. According to these results, we can consider that M2 is adequate for the simulations performed in this manuscript.

Statistics and performance

For collecting statistics, each RRLES is split into two steps. The initialization step is performed during a given transient time, and then statistics are accumulated. For each step, the durations are summarized in Tab. 6.4. For the second step, the dimensionless time t^+ defined by $t^+ = \frac{tu_\tau}{H}$ is around 20 on average. Interestingly, due to inhomogeneities of the surface, the time to establish a fully-developed turbulent channel flow is reduced compared to smooth cases.

RRLES CPU costs are presented in Tab. 6.5. For clarity, the CPU hours are averaged over all Reynolds numbers cases for each configuration.

Numerics and models

Working hypotheses

In each case, incompressible flow simulations are performed. The chosen target bulk Reynolds number range is the fully developed turbulent flow. This is why, RRLES are performed at $Re = 5\ 000$, $Re = 8\ 000$, $Re = 17\ 000$ and $Re = 25\ 000$. The fluid kinematic viscosity is set to $\nu = 1.517 \times 10^{-5}\ m^2/s$ and the maximal CFL number used is equal to 0.8. The WALE subgrid-

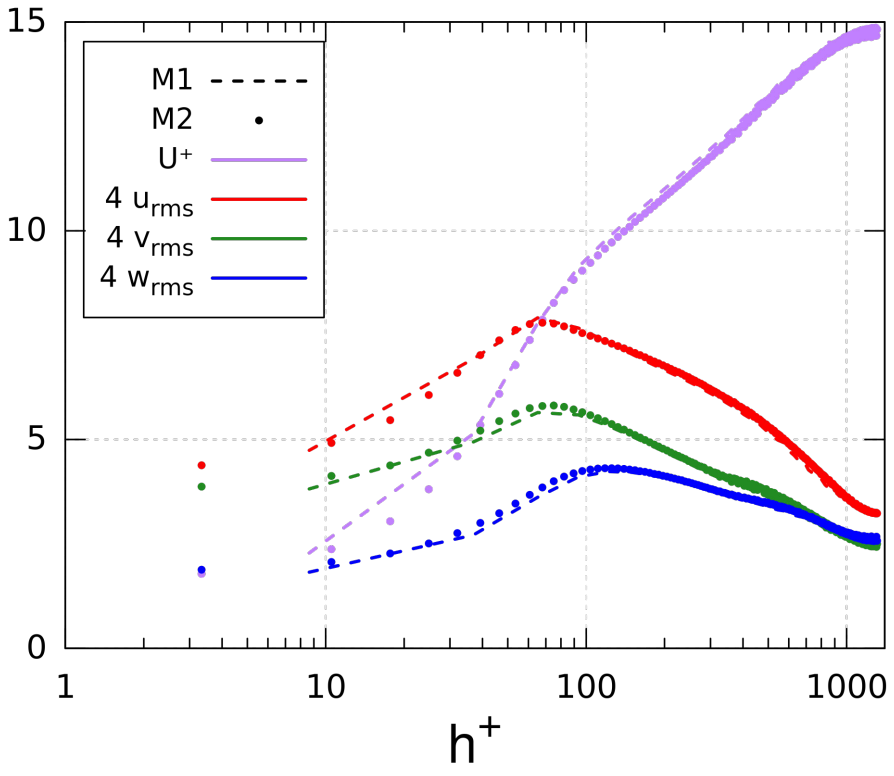

Figure 6.4 – Mean velocity and fluctuation profiles for different meshes from RRLES isotropic case, $Re = 17000$

Re	Init [ms]	Init Nbr. of FTT [-]	Stats [ms]	Stats Nbr. of FTT [-]
5000	0.7	8.8	4.0	50.6
8000	0.5	10.7	2.4	51.2
17 000	0.3	12.7	1.2	51.0
25 000	0.02	12.7	0.8	50.7

Table 6.4 – Time accumulation for statistics (nbr. of FTT: number of flow-through time)

	ES	Cells	CPUs	CPU hours
Front	0.29	130.1M	560	32 800h
Parallel	0.06	129.7M	560	18 500h
Isotropic	0.24	122.9M	560	32 500h

Table 6.5 – RRLES performances

scale model is retained as it is widely used for LES of boundary layer flows [61]. A fourth-order central finite-volume scheme is used, and the four-step fourth-order scheme TFV4A is applied for velocity and scalar transport prediction [66].

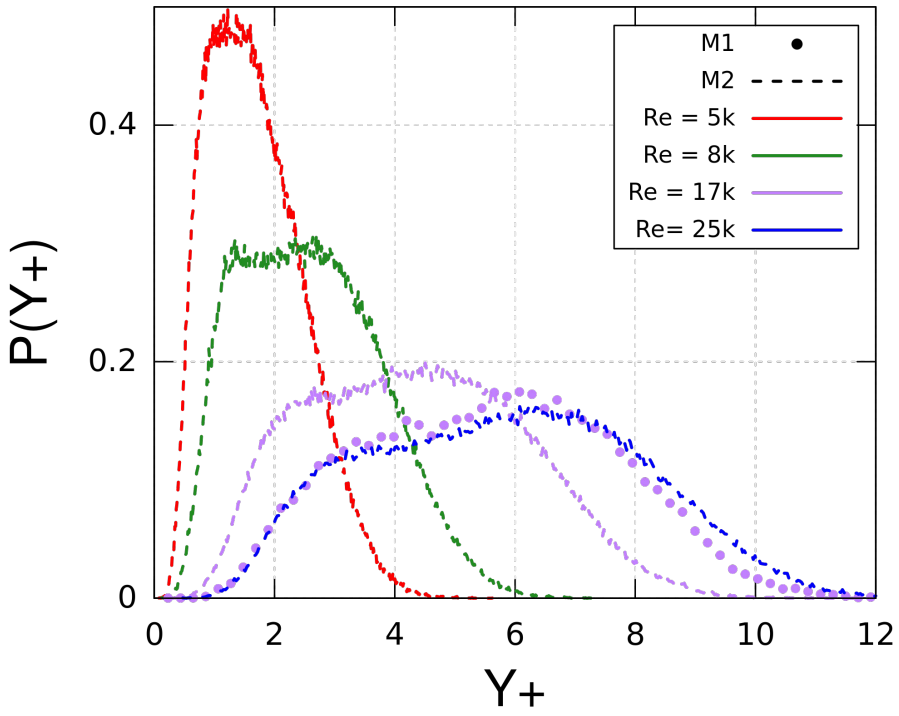

Figure 6.5 – Dimensionless mean wall resolution PDF from RRLES isotropic cases

6.1.2 Results and discussion

In this sub-section, the wall-unit velocity and temperature profiles as well as the momentum and kinetic energy balance equations described in the previous section are analyzed. This analysis should provide a better understanding of the impact of the wall roughness on the flow, especially the effective slope parameter.

Impact on turbulence

A first qualitative analysis can be done by visualizing the vortices generated over the rough surface. The same Q-criterion iso-contours are plotted for the three different cases in Fig. 6.6 at a Reynolds number of 8 000. At first glance, it is clearly noticed that the parallel case promotes elongated vortices in the flow direction, while the two other cases also feature small vortices trapped between valleys. These trapped vortices are more coherent in the front case due to the orthogonal wavy pattern of the wall. Even if the roughness height distribution is the same, important differences are visually perceptible.

Mean streamwise velocity profiles are plotted in Fig. 6.7 for the three cases at Reynolds numbers of 8 000 and 17 000 as well as the smooth wall configuration. The impact of ES is clearly visible as the velocity profile is shifted downward with increasing ES. Differences are also noticeable between isotropic and anisotropic surfaces. Indeed, if the ES in the isotropic case is lower than the front configuration, the mean velocity near the wall has a steeper increase for the isotropic case. These results indicate that the orientation of the wall roughness has a non-linear impact on the mean velocity in the channel. Moreover, increasing the Reynolds number tends to shift downward the profile in the log-law region as expected.

Concerning the fluctuating velocity, streamwise and spanwise components are plotted for

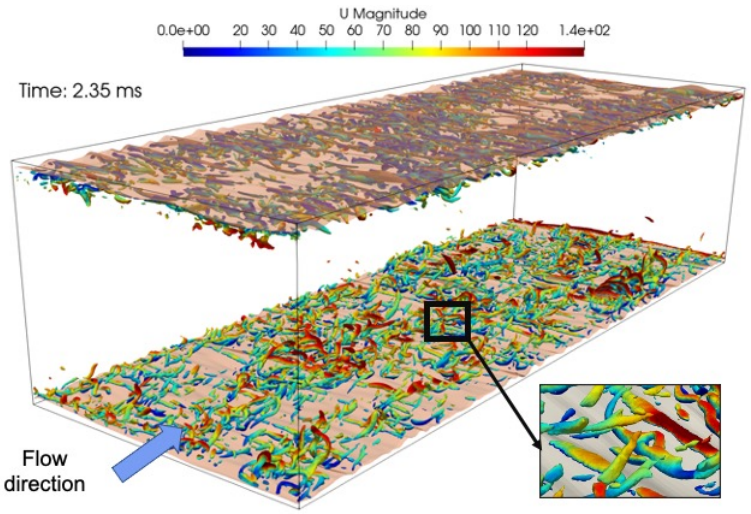

(a) Front case ($ES = 0.29$)

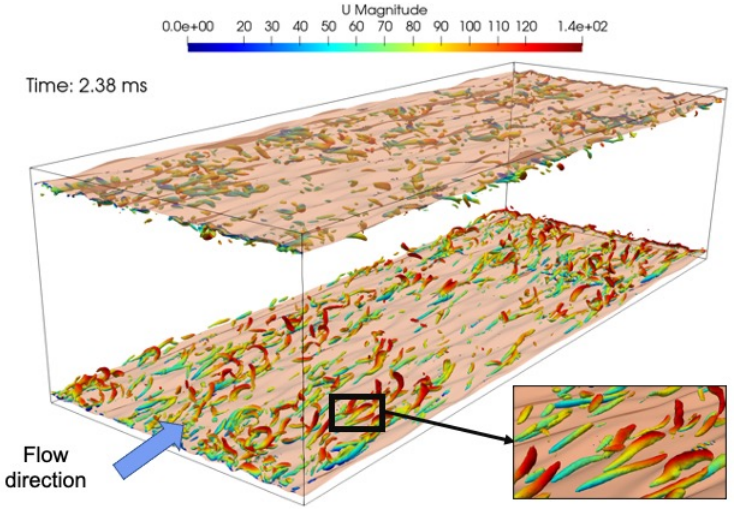

(b) Parallel case ($ES = 0.06$)

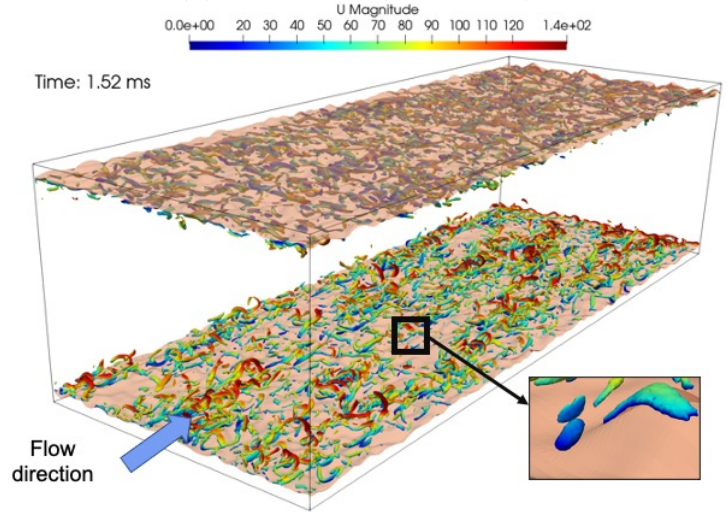

(c) Isotropic case ($ES = 0.24$)

Figure 6.6 – Q-criterion iso-contour colorized by velocity at $Re = 8000$

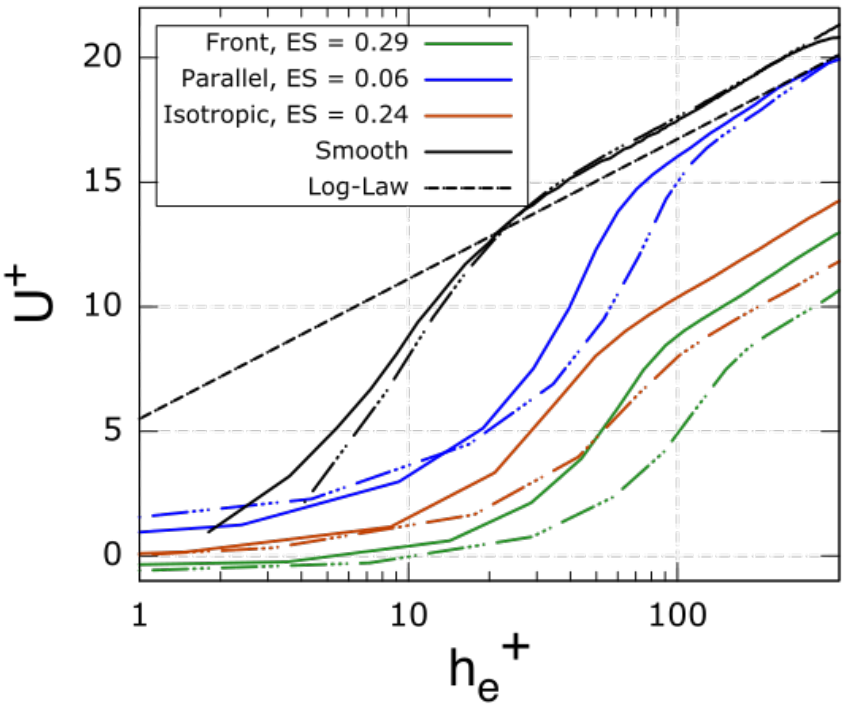

Figure 6.7 – Velocity profiles ($Re = 8\,000$ continuous line, $Re = 17\,000$ dashed line)

Reynolds numbers $Re = 8\,000$ and $Re = 17\,000$ in Fig. 6.8 and 6.9, respectively. For the streamwise fluctuating velocity u_{rms}, and considering the two anisotropic cases, the ES has an impact on the maximum value, and this latter is shifted to the flow stream when changing the roughness direction. This peak is also less pronounced for higher ES values. As for the mean velocity, the isotropic case has a slightly different behavior and while its ES value is in between the two anisotropic cases, the u_{rms} profile is not in between the two of the anisotropic cases confirming the non-linear behavior of the rough wall with ES.

For spanwise velocity fluctuations, the maximum of the profile is less affected by the geometry but its location follows the same trend as the streamwise fluctuations. Increasing the Reynolds number to 17 000 tends to shift the peaks to the channel center, to reduce the sharpness of the peaks for both velocity fluctuations and to slightly increase the maximum value of peaks for spanwise fluctuations.

The reduction of the anisotropy of the velocity fluctuations observed in each case compared to the smooth configuration is consistent with previous studies [157, 158]. It has been shown that this is caused by the redistribution of the mean roughness wake kinetic energy into turbulence, generating additional normal and spanwise stresses[159]. The streamwise turbulence is also mainly converted into wake energy as the streaks are destroyed by the roughness elements. Increasing the Reynolds number contributes to intensify this phenomenon.

The presence of the wake is slightly visible on the mean velocity profiles when they become negative in the near-wall region for the isotropic and front cases. The mean kinetic energy balance plotted in Fig. 6.10 (cf Eq. 5.4 for each budget term) shows that this region is dominated by the work of the pressure drag (term 2) against the flow direction. Those observations are no more valid for the parallel case since the surface topology does not create significant re-circulation zones, letting the viscous drag (terms 7 and 8) to be dominant. Thus, the decrease of the turbulence anisotropy and the pressure loss are less pronounced in this case.

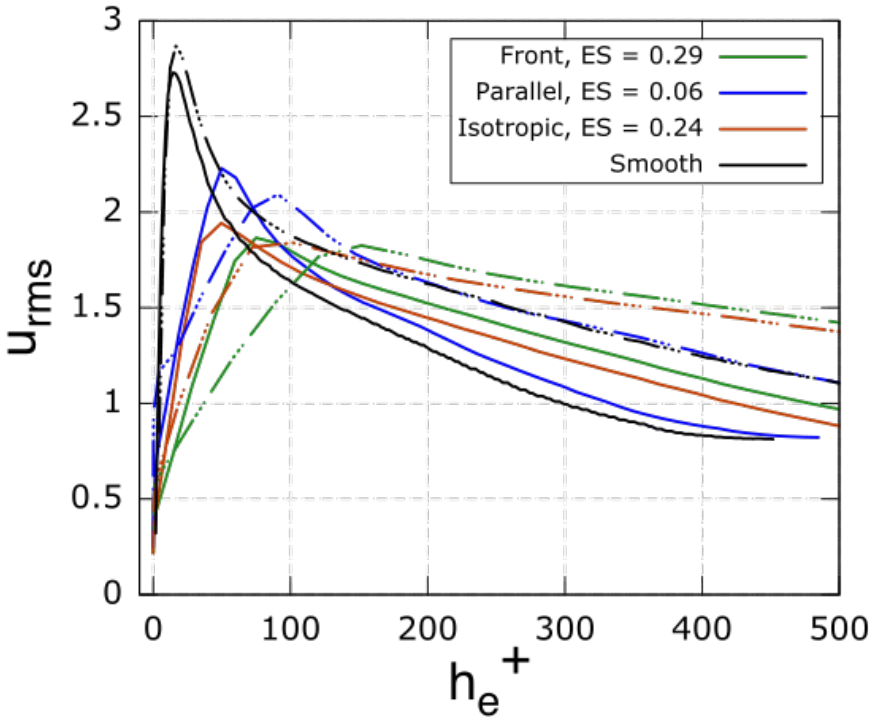

Figure 6.8 – Fluctuation of streamwise velocity ($Re = 8\,000$ continuous line, $Re = 17\,000$ dashed line)

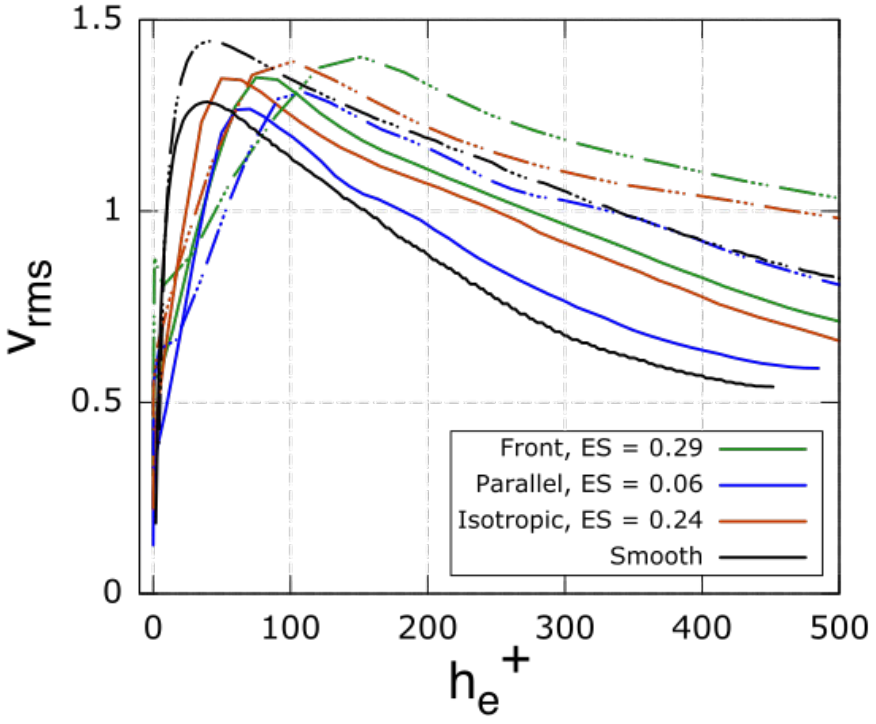

Figure 6.9 – Fluctuation of spanwise velocity ($Re = 8\,000$ continuous line, $Re = 17\,000$ dashed line)

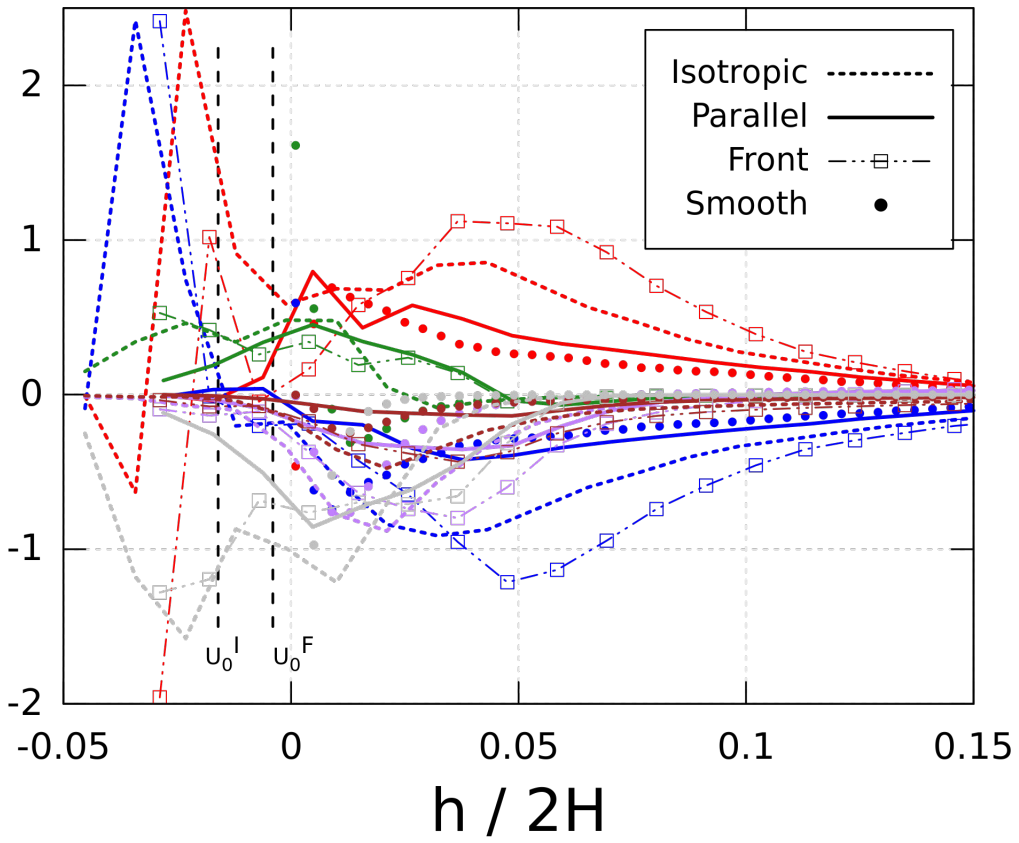

Figure 6.10 – Mean kinetic budget terms for $Re = 8000$ normalized by u_τ^4/ν from smooth case. 1: —, 2: —, 4: —, 6: —, -7: —, 8: —. U_0^I, U_0^F refer to mean velocity cross-zero scales for isotropic and front cases.

For each Reynolds number and all roughness types, the roughness velocity function ΔU^+ is studied. The latter is evaluated at $h_e^+ = 100$ and compared to the boundary-layer log law. Results are summarized in Tab. 6.6. The first remark is that ΔU^+ is amplified with a higher Reynolds number. Values are mainly higher in the front case except at $Re = 25\ 000$, where the isotropic case has a larger value. These results point out that the additive manufacturing direction has a strong impact on the mean velocity profile, although roughness height distributions are the same.

ΔU^+	Re 5 000	Re 8 000	Re 17 000	Re 25 000
Front	5.90	7.84	11.1	13.9
Parallel	0.41	0.69	1.34	2.89
Isotropic	3.10	5.48	10.2	15.0

Table 6.6 – Roughness function values evolution

Concerning the effect of the effective slope on pressure loss, the friction factor is investigated. The Colebrook correlation [80] (Eq. 6.1) is taken as a reference in order to compare friction factor values obtained in the current RRLES database to the Moody diagram. The definition used in

this correlation is Darcy's one and the relationship between Darcy and Fanning friction factors is $f_{Darcy} = 4f$. Therefore, in Fig. 6.11, friction factors from the Colebrook equation are divided by a factor of 4 for getting comparative results. Two relative roughness S_a/D_h values ($S_a/D_h = 10^{-2}$ and $S_a/D_h = 5.10^{-3}$) for the Colebrook formula are plotted as the relative roughness of the present cases is intermediate: $S_a/D_h = 7.8\ 10^{-3}$.

$$\frac{1}{\sqrt{f_{Darcy}}} = -2\log\left(\frac{S_a}{3.7D_h} + \frac{2.51}{Re\sqrt{f_{Darcy}}}\right) \tag{6.1}$$

As expected, for each Reynolds number, the friction factor is higher with increasing ES. For the front and isotropic cases, values are above the Colebrook correlation ones and tend to increase slightly with the Reynolds number. However, the trend for parallel case is reversed: the curve is below Colebrook expectations and decreases. There is a clear distinction in the friction factor behavior when varying the printing direction. Therefore this correlation is inadequate for describing the tendency and evaluating a priori the friction factor. It also highlights again the need for better correlations for this type of roughness.

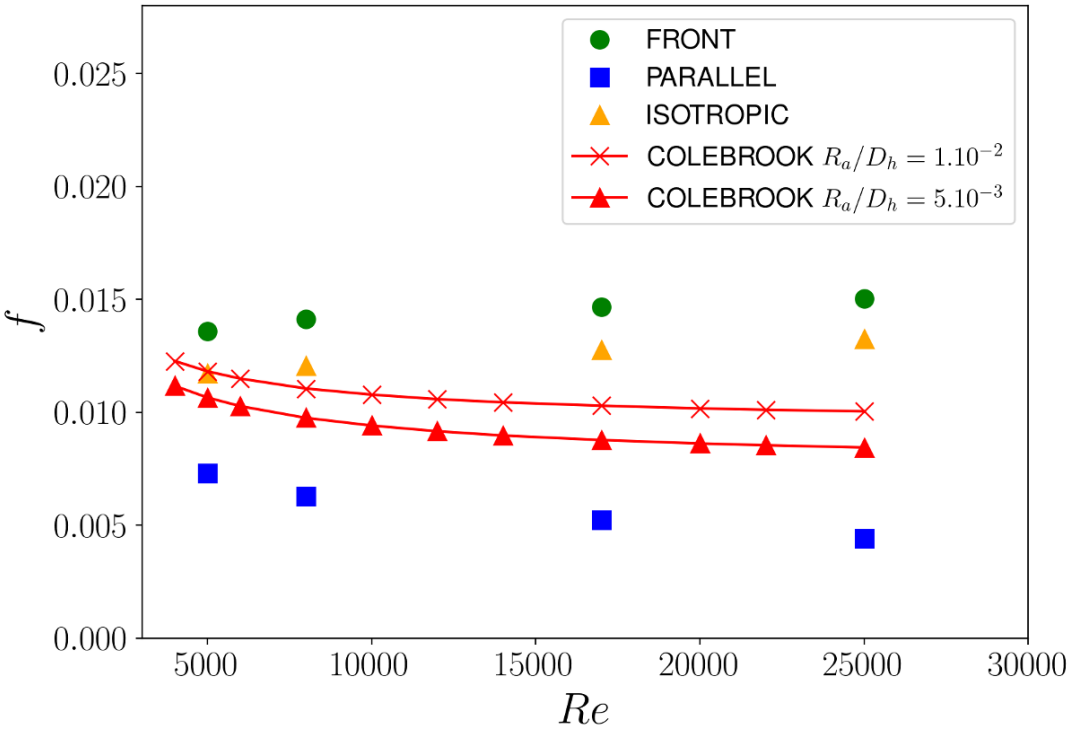

Figure 6.11 – Friction factor values at different Reynolds numbers for each case

Impact on temperature

The roughness influence on heat transfer is also studied with this RRLES database. Indeed, modifications to the turbulent boundary layer induced by the roughness inhomogeneities can modify the temperature boundary layer and potentially the mean temperature field. As explained above, a normalized passive temperature $\bar{Z}$ is transported and averaged. Instantaneous $\bar{Z}$ field for the three rough cases are illustrated in Fig. 6.12. This figure shows that the temperature fluctuations observed close to the wall have wavelengths similar to those of the wall roughness. This is particularly visible in the front and isotropic cases. In the parallel case, the chosen cut cannot represent

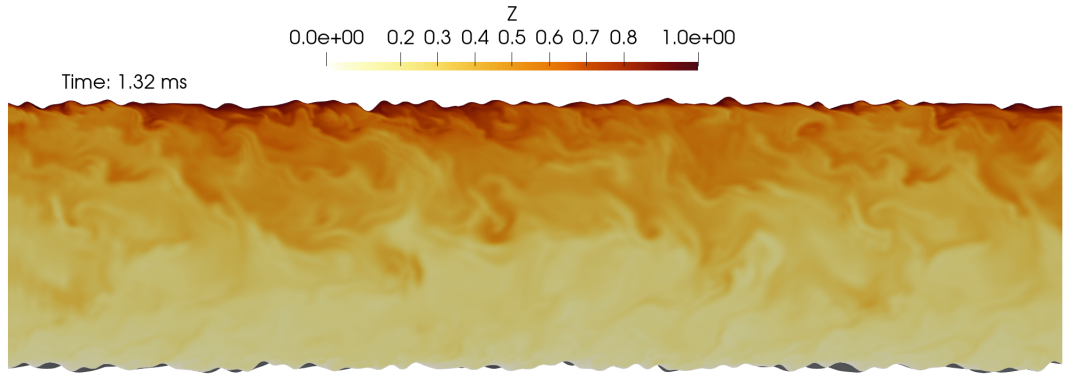

(a) Front case ($ES = 0.29$)

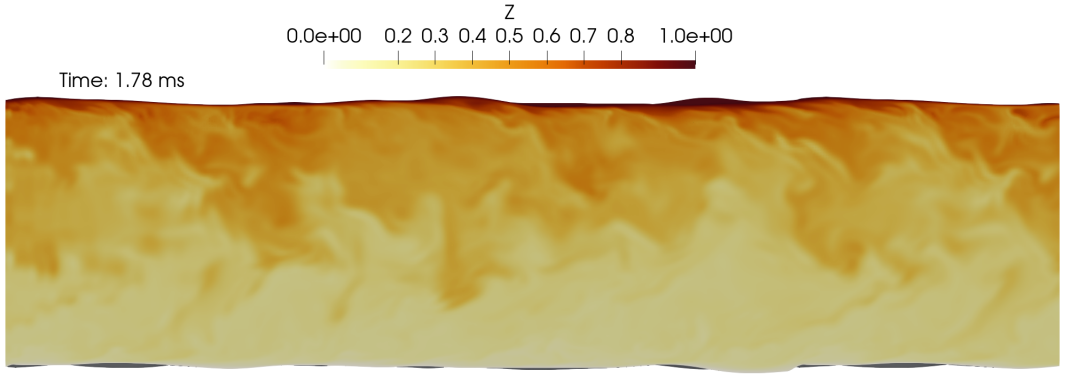

(b) Parallel case ($ES = 0.06$)

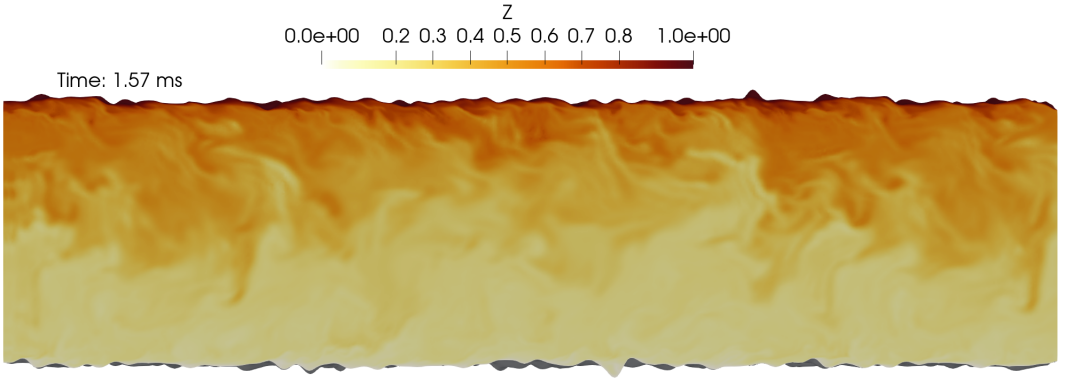

(c) Isotropic case ($ES = 0.24$)

Figure 6.12 – Instantaneous normalized temperature field at $Re = 8\ 000$

the wall roughness as the roughness features are rather aligned with the cut plane. As a result, fewer short wavelengths are visible in this cut close to the wall.

In order to quantify if temperature transport by turbulence is enhanced by wall roughness or not, mean temperature profiles are plotted for two different Reynolds numbers in Fig. 6.13. At $Re = 8\ 000$ (Fig. 6.13a), the temperature transport in the boundary layer is enhanced by wall roughness as the mean temperature gradient increases towards a constant value in the whole channel height. The three rough cases have a slightly different behavior close to the wall. The isotropic case seems to be the configuration closest to the smooth case. For the two anisotropic cases, coherent structures in the roughness valleys seem to slightly increase the temperature wall gradient and thus the wall heat transfer.

For $Re = 17\ 000$, the conclusions are different and more intuitive. Indeed, the parallel rough-

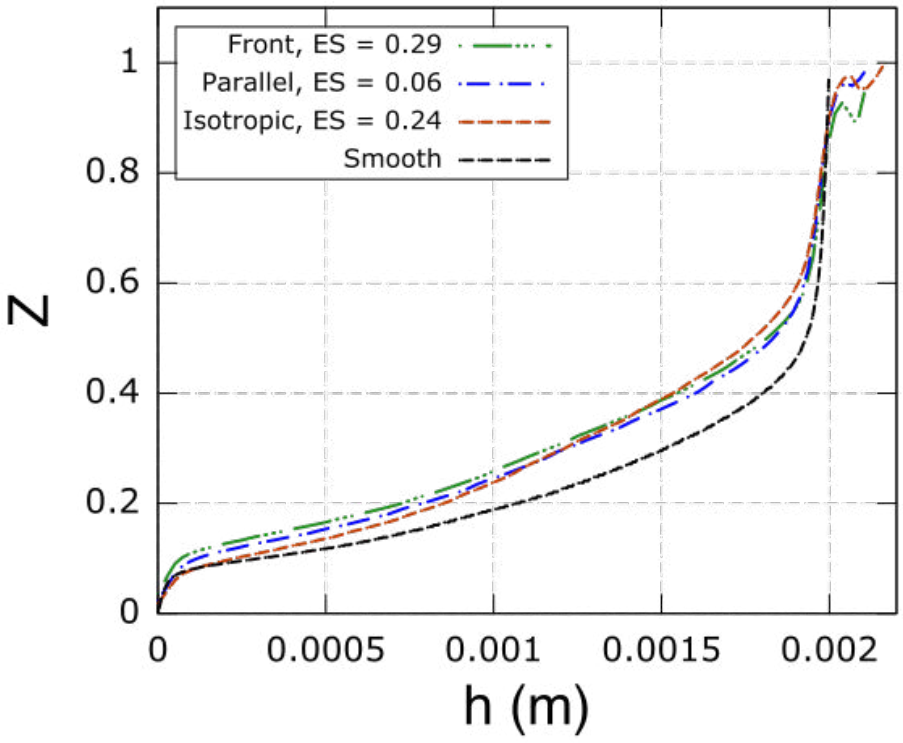

(a) $Re = 8\,000$

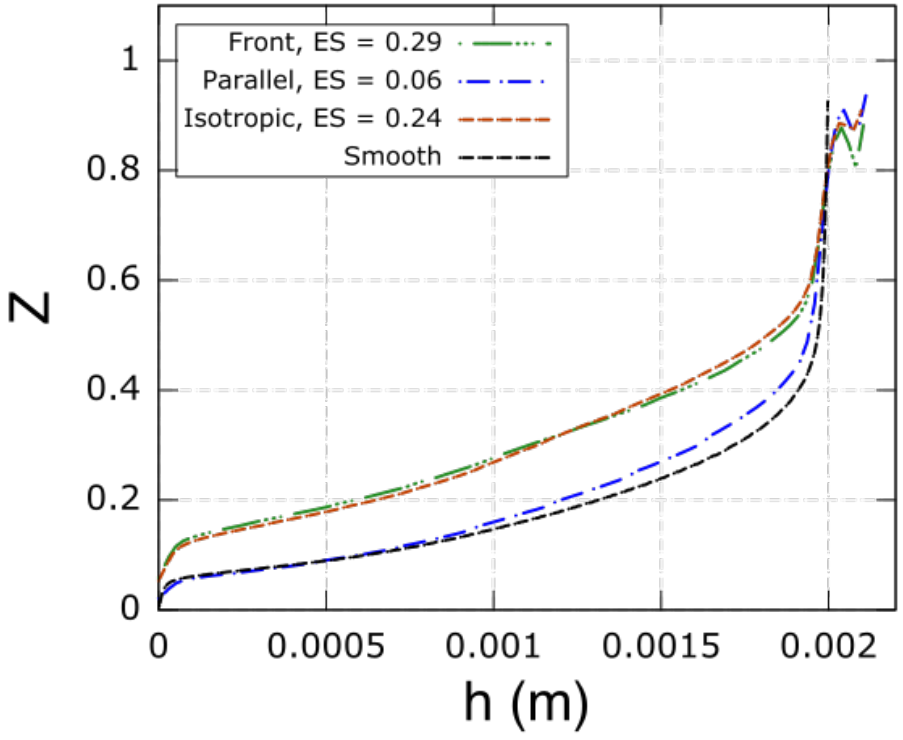

(b) $Re = 17\,000$

Figure 6.13 – Dimensionless mean temperature profiles

ness and smooth cases have almost the same temperature profiles as expected due to the alignment of the roughness elements with the flow. The front and isotropic cases also have the same temperature profile with a clear shift toward the constant gradient imaginary profile. In these cases, the wall roughness promotes temperature transport by turbulence. For this higher Reynolds case, the dependence of the wall heat transfer with the effective slope is better recovered. Again, the different non-linear behaviors of the temperature with both the effective slope and the Reynolds number illustrate the challenge of finding a Nusselt number correlation for rough walls.

6.1.3 Partial conclusions

This part presents roughness-resolved Large-Eddy Simulations that are representative of the flow obtained in additive-manufactured heat exchangers. The most challenging task in the building of this database is the generation of representative rough surfaces and conformal unstructured meshes. Three different configurations of parallel rough plane channels with the same roughness height distribution but different effective slopes have been chosen and modeled. The impact of the effective slope parameter, which is directly linked to the alignment of the wall roughness with the flow, has a strong impact on the flow topology, velocity and temperature profiles, as expected. In these cases, the existing empirical correlations find their limits and new correlations are needed.

6.2 RRLES generated database

The main objective of this part is to develop models in the framework of RANS and LES methods that reproduce the effects of the typical additive manufacturing (AM) roughness without explicit representation of the surface details. To this end, the creation of a Roughness-Resolved Large Eddy Simulation (RRLES) database of representative channel flows emerges as a worthwhile process. Chapter 4 and Chapter 5 presented the development of tools that enabled the achievement of this objective. The results obtained from the database will be utilized to propose different modeling strategies.

6.2.1 Configurations

The rough surface and body-fitted generators are used to perform RRLES. The idea is to generate surfaces that mimic roughness height distribution encountered in AM. Roughness parameters that are targeted in this aim are the root-mean-square height (S_q), the height distribution skewness (Sk) and kurtosis (Ku) and the effective slope (ES). We then define several sets of surfaces whose rough properties cover typical values encountered in AM.

In addition to the above-mentioned roughness parameters, the typical AM roughness can be linked to the printing direction via the effective slope as seen in the previous section. Thus, the two anisotropic cases representing two printing directions parallel and perpendicular to the flow direction are part of the database. The rough properties of the other cases are isotropic. A smooth surface is also considered as a reference. The different sets are summarized in tables 6.7-6.10. Furthermore, some geometries of the database are illustrated in Fig. 6.14. The influence of the effective slope is visually noticeable on these geometries.

6.2.2 Presentation of results

Simulations are conducted for periodic channels of size $8H$ x $3H$ x $2H$ in the streamwise (x_1), spanwise (x_2) and normal (x_3 or h) directions with H the half height of the channel. This parameter is selected in order to be close to hydraulic diameters and channel heights encountered for some AM experiments. Mean surface height is 0 and $2H$ for the lower and upper walls, respectively.

Case	$S_q/H(\%)$	Sk	Ku	$ES(\%)$	Orientation
S00	0	0.0	0	00	smooth
S11	2	0.2	4	17	isotropic
S12	2	0.2	4	20	isotropic
S13	2	0.2	4	27	isotropic
S14	2	0.2	4	30	isotropic
S15	2	0.2	4	32	isotropic

Table 6.7 – Surface set I

Case	$S_q/H(\%)$	Sk	Ku	$ES(\%)$	Orientation
S21	2	-0.2	4	17	isotropic
S22	2	-0.2	4	20	isotropic
S23	2	-0.2	4	27	isotropic
S24	2	-0.2	4	30	isotropic
S25	2	-0.2	4	32	isotropic

Table 6.8 – Surface set II

Case	$S_q/H(\%)$	Sk	Ku	$ES(\%)$	Orientation
S31	5	0.2	4	24	isotropic
S32	5	0.2	4	30	isotropic
S33	5	0.2	4	41	isotropic
S34	5	0.2	4	50	isotropic

Table 6.9 – Surface set III

Case	$S_q/H(\%)$	Sk	Ku	$ES(\%)$	Orientation
S41	2	0.2	4	24	isotropic
S42	2	0.2	4	28	perpendicular
S43	2	0.2	4	6	parallel

Table 6.10 – Surface set IV

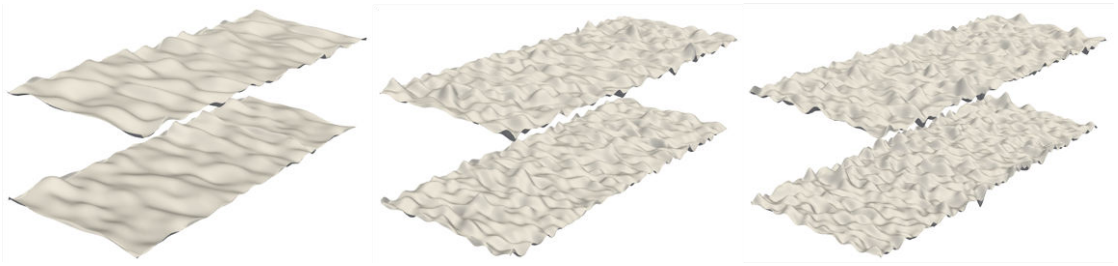

(a) S31 case *(b) S33 case* *(c) S34 case*

Figure 6.14 – Geometry of some cases of the database

The chosen target bulk Reynolds number range is the fully developed turbulent flow. This is

why, RRLES are performed at $Re = 5\,000$, $Re = 8\,000$, $Re = 17\,000$ and $Re = 25\,000$. The considered Reynolds numbers and surfaces make the RRLES flows to cover both transitionally and fully rough regimes.

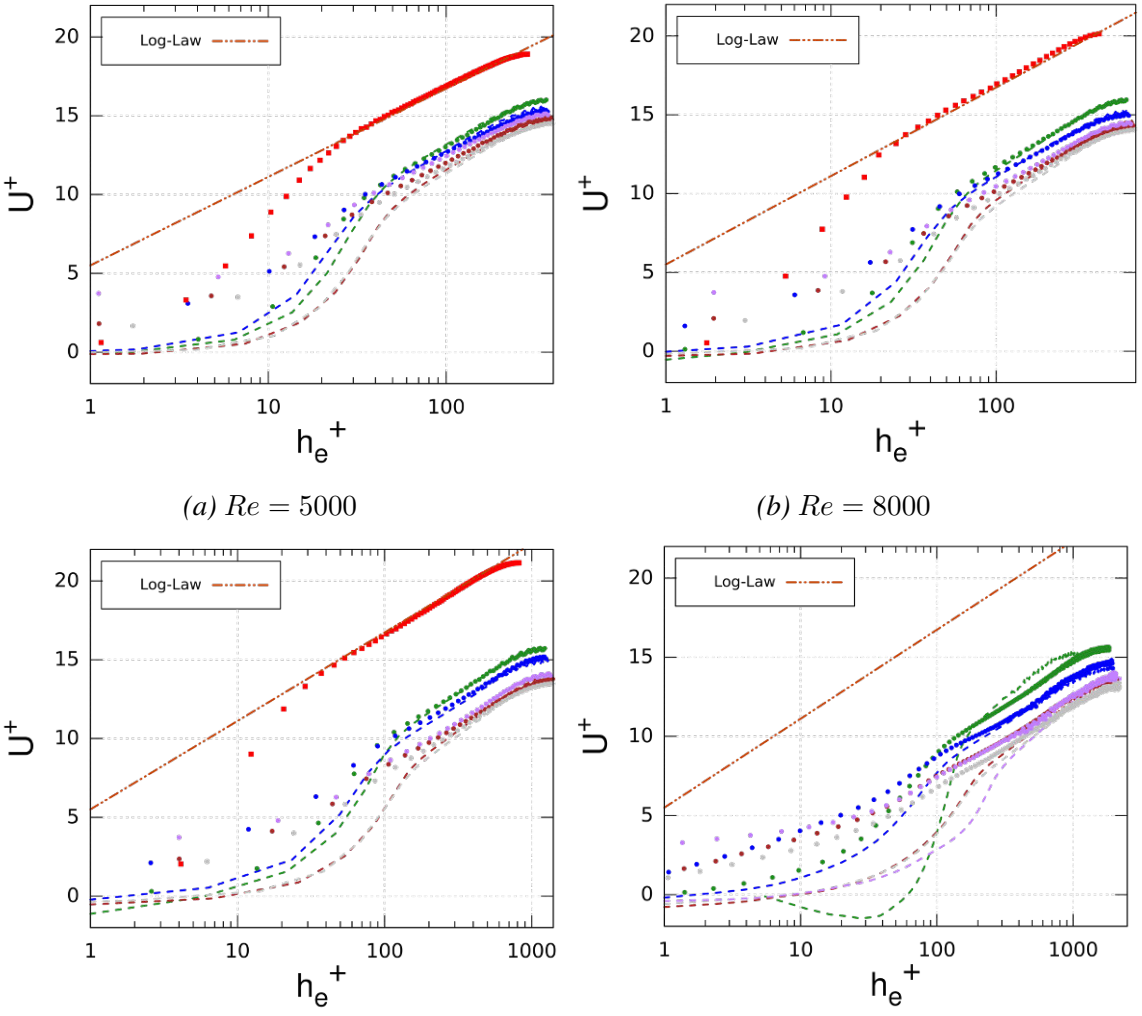

(a) $Re = 5000$ *(b)* $Re = 8000$

(c) $Re = 17000$ *(d)* $Re = 25000$

Figure 6.15 – Velocity profiles for sets I (points) and II (dashed lines). $S11$ and $S21$:— (Green), $S12$ and $S22$:— (Blue), $S13$ and $S23$:— (Brown), $S14$ and $S24$:(Gray)—, $S15$ and $S25$:— (Purple). Smooth case: red points

Regarding velocity profiles, the results are presented in Figs. 6.15 and 6.16. First of all, similar results are retrieved as highlighted in sub-section 6.1.2. The effective slope tends to increase the downward shift of the velocity profile and this tendency is accentuated by increasing the Reynolds number.

Second, the skewness seems to have an effect on these profiles. Indeed, the roughness function ΔU^+ is more significative for Set II than for Set I. As a negative skewness corresponds to more pronounced valleys, this result seems logical. In Fig. 6.16, one can notice that increasing the Reynolds number reduces the gap between the cases of $ES = 0.41$ (S33) and $ES = 0.5$ (S34).

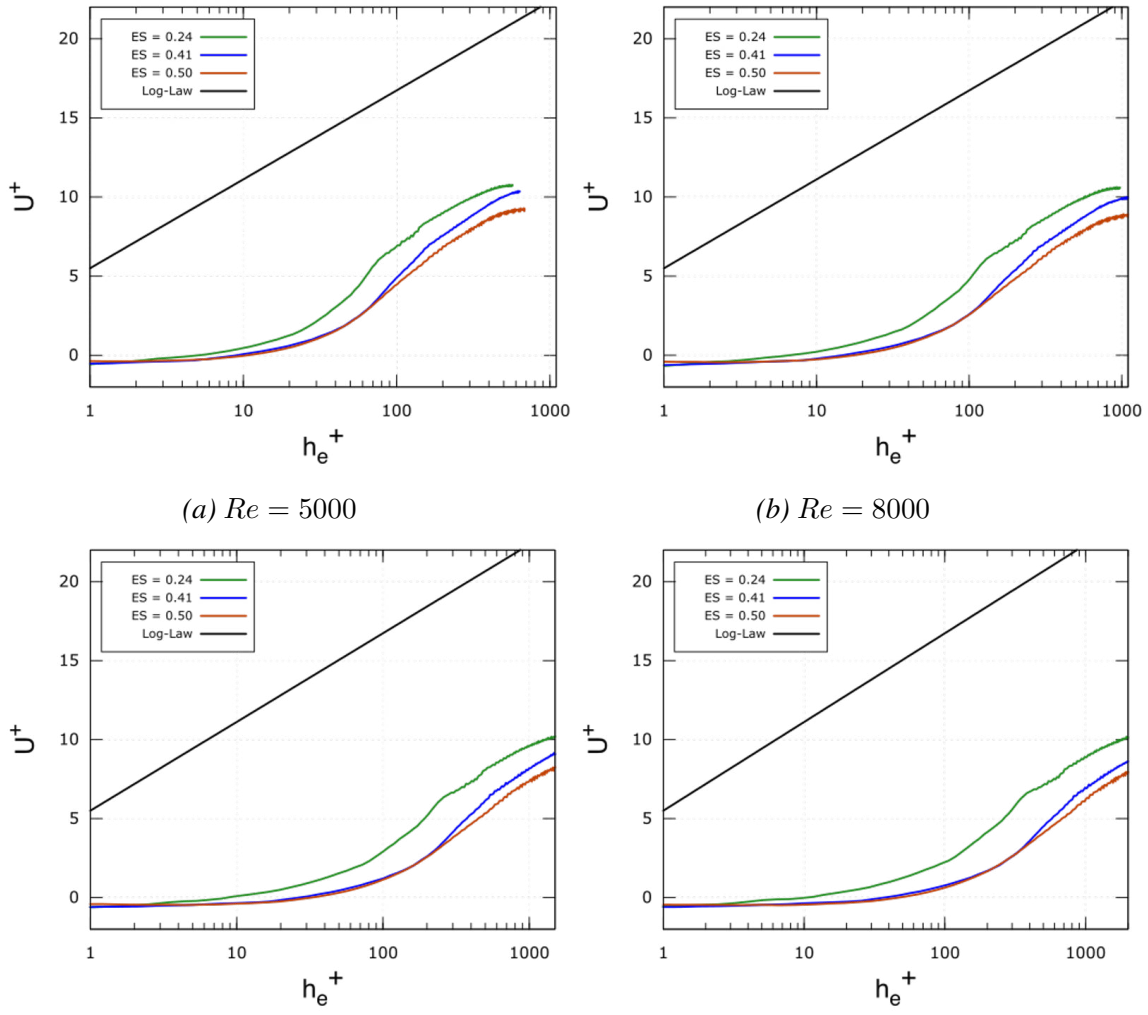

(a) $Re = 5000$ *(b)* $Re = 8000$

(c) $Re = 17000$ *(d)* $Re = 25000$

Figure 6.16 – Velocity profiles for set III. Green: S31, Blue: S33, Red: S34

Results concerning the friction factor are given in Fig. 6.17 for sets I and II and in Tab. 6.11 for set III. The highest effective slope cases for sets I and II ($ES = 32\%$) show a slightly lower value. This suggests that the threshold value of $ES = 30\%$, distinguishing the sparse and the dense regimes for the roughness function ΔU^+ (cf section 3.1.2), seems to be retrieved.

Contrarily, this is not the case for set III. The difference lies in the relative roughness S_q/H which is higher for set III. It should be noted that a higher relative roughness could induce blockage effects as the roughness is likely to be an obstacle. Therefore, this should indicate that the threshold value could be larger for these cases.

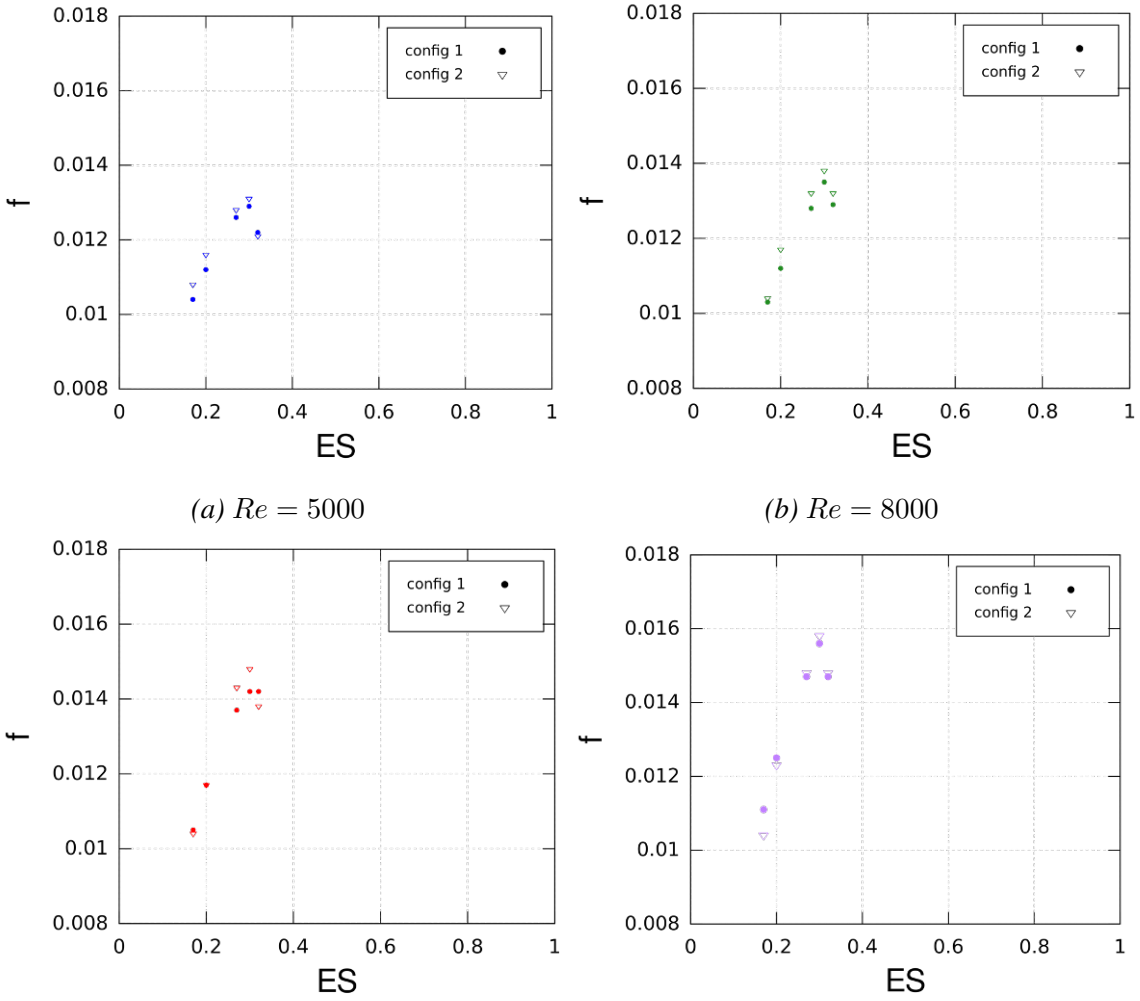

(a) $Re = 5000$ *(b)* $Re = 8000$

(c) $Re = 17000$ *(d)* $Re = 25000$

Figure 6.17 – Friction factor values. Dot: Set I, Triangle: Set II

Case	S31	S32	S33	S34
$ES(\%)$	24	30	41	50
$Re = 5k$	2.44×10^{-2}	2.76×10^{-2}	2.99×10^{-2}	3.60×10^{-2}
$Re = 8k$	2.50×10^{-2}	2.92×10^{-2}	3.16×10^{-2}	3.82×10^{-2}
$Re = 17k$	2.53×10^{-2}	2.98×10^{-2}	3.34×10^{-2}	4.04×10^{-2}
$Re = 25k$	2.47×10^{-2}	3.11×10^{-2}	3.50×10^{-2}	4.11×10^{-2}

Table 6.11 – Friction factor values for set III

6.3 Modeling approaches for turbulence

From database results, derived strategies have been developed in close collaboration with Alexis Barge from the LEGI laboratory (Grenoble). Regarding turbulence, these strategies may be separated into three categories.

The first category stays in line with standard approaches. In this kind of model, the mean wall stress is estimated through a modified smooth law of the wall. The modification of the law of

the wall follows empirical correlations obtained from experimental data and roughness-resolved simulations. The work to enrich the empirical correlations with the database results is presented in sub-section 6.3.1.

The second modeling category fits in the framework of the boundary layer theory. Recent advancements have been proposed in the literature for this kind of model. We discuss the adaptation of those approaches to our cases in sub-section 6.3.2.

The last category employs stochastic tools to reproduce the wall stress statistical behavior. This is detailed in sub-section 6.3.3.

6.3.1 Functional modeling

Hereafter, we compare the database results with correlations yielded in the literature.

Equivalent sand-grain roughness correlations

One of the main effects of the wall roughness is the reduction of the mean velocity in the streamwise direction. This reduction may be written with the modified log-law of the wall:

$$U^+ = \frac{1}{\kappa}\ln(h^+) + 5.5 - \Delta U^+ \tag{6.2}$$

with $\kappa = 0.41$ the von Kármán constant and superscript $+$ indicate wall-units. The velocity defect term ΔU^+ is known as the roughness function [160]. The aim of correlative methods is to empirically estimate the roughness function and use Eq. (6.2) to evaluate the shear stress at the wall. The most popular approach is based on the equivalent sand grain roughness (ESGR) k_s^+, i.e., a packed layer of spheres of diameter k_s with the same performances as the actual surface. Once the ESGR is known, the roughness function is evaluated with the following correlations:

$$\Delta U^+ = \frac{1}{\kappa}\ln\left[\frac{k_s^+ - 2.25}{87.75} + C_s k_s^+\right] \times \sin\Big(0.4258(\ln k_s^+ - 0.811)\Big) \tag{6.3}$$

for the transitional rough regime ($2.25 < k_s^+ \leq 90$), with $C_s = 0.5$ the roughness constant, and

$$\Delta U^+ = \frac{1}{\kappa}\ln(1 + C_s k_s^+) \tag{6.4}$$

for the fully rough regime ($k_s^+ > 90$). For the hydro-dynamically smooth regime ($k_s^+ \leq 2.25$), the roughness function is set to zero ($\Delta U^+ = 0$). This method is used to perform the RANS simulations generally with the *ANSYS Fluent* software.

The main difficulty is to estimate the ESGR. The diverse variety of existing correlations for the ESGR (see [161]) demonstrates that there is no universal roughness function valid for all types of roughness. Uncertainty in the estimate of k_s^+ may be then significant, especially if the roughness type has not been well studied. Thus, the roughness constant C_s can be modified in accordance with the type of given roughness. Unfortunately, a clear guideline for choosing C_s for arbitrary types of roughness (such as AM roughness) is not available.

Our objective here is to build a table that provides the right values of C_s for the typical AM roughness at our concern to improve the performances of the RANS simulations done by the STREAM project's industrial partners. To this end, we first evaluate the ESGR for our cases with a correlation supposed to be the most adapted to our database (here Boyle and Stripf [162]). Then, we measure the ΔU^+ value from the RRLES. The value of C_s is finally reconstructed with Eqs. (6.3)-(6.4). Results are summarized in Tab. 6.12. The value of C_s for other cases should be interpolated from this table.

Re_b		5000		8000		17000		25000	
Case	k_s	k_s^+	C_s	k_s^+	C_s	k_s^+	C_s	k_s^+	C_s
S11	1.03e-4	36.6	0.312	61.85	0.232	124.6	0.156	186.03	0.124
S12	1.03e-4	37.4	0.331	63.62	0.245	129.0	0.164	196.47	0.129
S13	1.02e-4	39.4	0.365	67.79	0.269	139.3	0.179	213.35	0.141
S14	1.03e-4	40.5	0.377	70.33	0.276	145.9	0.182	220.53	0.144
S15	1.03e-4	39.7	0.391	68.36	0.288	143.5	0.189	214.55	0.151
S21	6.88e-5	24.4	0.392	41.23	0.291	83.1	0.196	124.01	0.156
S22	6.88e-5	25.1	0.414	42.77	0.306	86.7	0.205	132.08	0.162
S23	6.88e-5	26.5	0.457	45.57	0.337	93.6	0.224	143.42	0.176
S24	6.88e-5	26.9	0.474	46.89	0.345	97.3	0.230	147.02	0.182
S25	6.88e-5	26.5	0.492	45.57	0.362	95.7	0.238	143.03	0.189
S31	2.56e-4	138.2	0.171	235.81	0.127	472.8	0.085	695.4	0.068
S32	2.56e-4	145.4	0.183	251.12	0.134	508.4	0.090	769.0	0.071
S33	2.56e-4	150.9	0.205	262.04	0.150	536.9	0.099	818.2	0.079
S34	2.56e-4	167.3	0.211	290.86	0.154	596.4	0.103	896.6	0.082
S41	1.03e-4	32.8	0.385	56.20	0.284	116.3	0.188	174.2	0.149
S42	1.03e-4	34.9	0.385	60.21	0.292	122.6	0.195	183.4	0.156
S43	1.03e-4	26.6	0.237	41.81	0.184	77.6	0.130	105.8	0.108

Table 6.12 – Equivalent sand grain roughness k_s, value of k_s^+ and re-constructed value of C_s for the database cases.

Geometrical correlations

The main drawback of k_s^+ is that it is not a physical parameter of the roughness topography. Thus, many efforts have been made in the literature to find correlations between ΔU^+ and the parameters of the representative surface listed in section 6.2. The observed data pointed out that ES and S_q have the better correlation. With the aim of finding a universal correlation based on geometrical parameters, De Marchis *et al.* [163] compiled data from several studies and proposed the following correlation:

$$\Delta U^+ = \frac{1}{\kappa}\ln(ES \times S_q^+) + 3.5 \tag{6.5}$$

The comparison between the roughness function measured in the database and Eq. 6.5 is shown in Fig. 6.18. It is seen that our results fit the correlation pretty well except for cases from Set III.

The value of S_q for those cases is relatively high in front of the half-height of the channel and may be responsible for blockage effects. These effects are not considered in current correlations but can be important in additive-manufactured heat exchangers. This leads to an over-prediction of the pressure loss and an increase in the velocity defect. Indeed, the shift of the results compared with Eq. 6.5 appears to be similar between the different cases. The tendency is also maintained.

The deviation of the results for a low value of the product $ES \cdot S_q^+$ is similar to the one observed in De Marchis *et al.* [163]. Also, those cases correspond to the surface $S43$ and have the particularity to be the only ones whose wall stress is dominated by viscous effects [164]. We conclude here that the correlations based on geometrical parameters available in the literature may be used as they are to model AM roughness with a modified law of the wall.

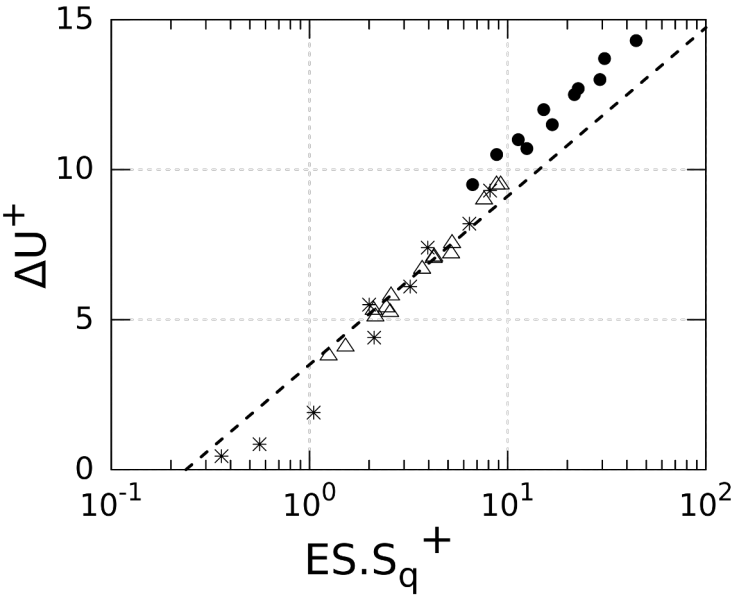

Figure 6.18 – Velocity defect ΔU^+ as function of geometrical parameter $(ES \cdot S_q^+)$ for the database cases compared with the roughness function (Eq. 6.5) shown by the dashed line. Set I: $\triangle$, Set III: $\bullet$, Set IV: $*$. Results for set II are identical to set I.

6.3.2 Boundary layer modeling

This sub-section focuses on the current boundary layer based wall modeling strategies proposed in the literature. Our motivation here is to adapt the recent advancements to the numerical framework of our RANS and LES methodologies.

Roughness adapted TBLE

Wall stress models based on boundary layer approximation have now become common approaches in the context of wall-modeled LES. Those methods consist in assuming that the filtered velocity is equivalent to the averaged velocity close to the wall. In this configuration, a simplified averaged set of partial equations derived from the Navier-Stokes equations, named thin boundary-layer equations (TBLE), can be considered. Considering a stationary flow and equilibrium between the pressure gradient and the convective terms, simplified TBLE are written as follows:

$$\frac{d}{dh}\left[(\nu + \nu_t)\frac{d\tilde{u}}{dh}\right] = 0 \tag{6.6}$$

with $\tilde{u}$ the wall tangential velocity. Equation (6.6) may be regarded as a steady RANS solution for the mean velocity field in the near-wall region. Thus, the turbulent eddy viscosity ν_t is modeled by a RANS-type model, such as the mixing-length model with wall damping. This equation is solved on an embedded near-wall mesh (see Fig. 6.19), which refinement is affordable due to the TBLE simplicity.

The model steps are the following: (i) the LES tangential velocities are interpolated on the TBLE grid points at some distance from the wall $h = h_{wm}$, (ii) the TBLE is solved with a RANS solver and a no-slip condition at $h = 0$, (iii) the wall stress evaluated on the second grid is applied as a Von Neumann condition to close the LES equations. Communication location and overlapping of the two grids are sensitive parameters discussed in Bose *et al.* [165].

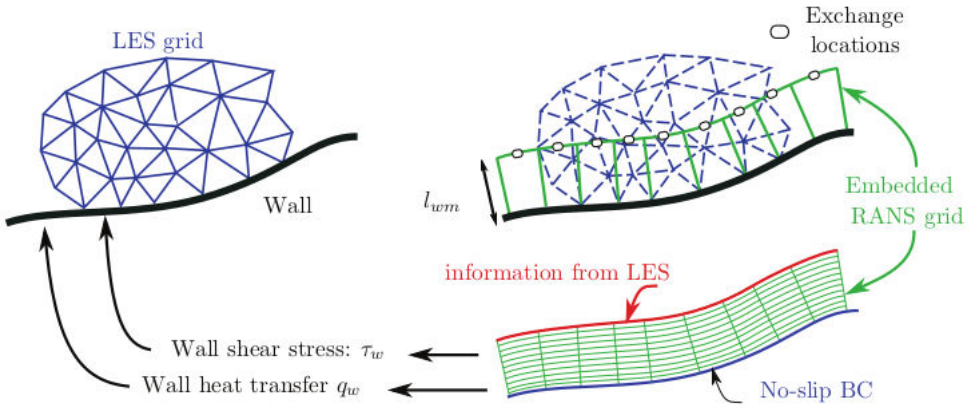

Figure 6.19 – Overlapping of LES grid and TBLE grid at the wall. Image taken from Park and Moin [166].

Recently, Olmeda *et al.* [167] proposed an extension of this approach for rough wall turbulence. The idea is to modify the upper boundary conditions of the wall model such that the calculated wall stress corresponds to a flow with the same LES conditions and a rough wall. By writing

$$\tilde{u}_{TBLE}(h_{wm}) = \tilde{u}_{LES}(h_{wm}) + u_\tau \Delta U^+ \tag{6.7}$$

at the communication grid point, it is possible to trick the wall model to solve a flow with a higher wall stress than the one corresponding to a smooth wall. This formulation needs a roughness function to know the mean velocity defect ΔU^+. Different functions are available in the literature [163, 161] in addition to our RRLES database and can be chosen in accordance with the considered cases.

Duprat wall law

Another TBLE approach available in the literature is proposed by Duprat *et al.*[168] in which the streamwise pressure gradient is not neglected. In this study, it is assumed that the TBLE can be integrated analytically in the wall-normal direction, leading to

$$\frac{\partial \tilde{u}}{\partial h} = \frac{h\dfrac{\partial P}{\partial x_1} + \tau_{w,1}}{\rho(\nu + \nu_t)} \tag{6.8}$$

with $\tau_{w,1} = \rho\nu \left.\partial\tilde{u}/\partial h\right|_{h=0}$. This formulation has the advantage of not relying on a second near-wall grid to solve the TBLE. Non dimensional velocity $U^+ = \tilde{u}/u_{\tau p}$ and length $h^+ = \frac{h u_{\tau p}}{\nu}$ are introduced with a combined velocity $u_{\tau p} = \sqrt{u_\tau^2 + u_p^2}$ using the friction velocity u_τ and an additional velocity based on the streamwise pressure gradient $u_p = \left|(\mu/\rho^2)(\partial P/\partial x)\right|^{1/3}$. Moreover, a parameter $\alpha = u_\tau^2/u_{\tau p}^2$ comprised between 0 and 1 can be used to quantify the preponderant effect between shear stress and streamwise pressure. From Eq. 6.8 and nondimensional scaling, the following formula can be obtained:

$$\frac{\partial U^+}{\partial h^+} = \frac{\text{sign}\left(\partial P/\partial x_1\right)(1-\alpha)^{3/2} h^+ \text{sign}(\tau_{w,1})\alpha}{\left(1+\dfrac{\nu_t}{\nu}\right)} \tag{6.9}$$

with the eddy viscosity modeled by

$$\frac{\nu_t}{\nu} = \kappa h^+ \left[\alpha + h^+(1-\alpha)^{3/2}\right]^{0.78} \left(1 - e^{-h^+/(1+17\alpha^3)}\right)^2 \tag{6.10}$$

It should be noted that imposing $\alpha = 1$ leads to obtain the solution of Eq. 6.6 with the same procedure. Numerically, the instantaneous tangential velocity $\tilde{u}_{LES}$, wall distance h and pressure gradient $\partial P/\partial x_1$ are computed at the center of the wall grid cell. An iterative process is then used to identify the value of α (or u_τ if $\alpha = 1$) that satisfies Eqs. 6.9 and 6.10. For ease of computation, the iterative process for α is pre-calculated with a tabulation technique described in Maheu *et al.* [169].

LES

In the framework of roughness LES modeling, we plan to extend the Duprat wall law with the procedure described by Olmeda *et al.* [167]. The modifications are straightforward and consist in modifying the cell-centered velocity $\tilde{u}_{LES}$ in the same manner as previously done in Eq. 6.7 before solving Eqs. 6.9 and 6.10.

RANS

Since the TBLE theoretical framework is close to the RANS formulation, we can consider that the Duprat wall law with imposed $\alpha = 1$ (i.e., standard log-law of the wall) can be used with a RANS solver. Here, the RANS computed mean tangential velocity is used for the TBLE model instead of the instantaneous LES velocity. As previously described, the tangential velocity should be modified in accordance with Eq. 6.7.

6.3.3 Stochastic modeling strategy

This subsection presents an original modeling strategy in the framework of Large-Eddy Simulation, developed in close collaboration with Alexis Barge from the LEGI laboratory (Grenoble). The motivation is to take advantage of the instantaneous LES process to stochastically reproduce the rough wall stress statistical behavior and apply it to a flat wall. The statistical analysis of the wall stress from the database results is performed to identify the scenario to be reproduced by the model and is discussed in the first part. The stochastic modeling strategy is then presented.

Statistical analysis

Usually, both for smooth and rough walls, the wall stress vector considered of interest for modeling is the resulting one oriented in the direction of the mean tangential flow $\tau_{w,1}$. In the following, we study the total wall stress vector defined as:

$$\tau_{w,i} = \frac{\nu}{\rho}\left.\frac{\partial \tilde{u}_i}{\partial n_j}\right|_w + p \cdot n_i|_w \tag{6.11}$$

with $n_i|_w$ the wall normal vector. The first term represents the viscous stress and the second term is the pressure. We consider the wall stress statistics accumulated for all surface grid

points at the statistically stationary state. Here, the angled brackets $\langle\rangle$ denote the average over the surface. Figure 6.20 shows the probability density function (PDF) of the wall stress vector components and its norm $|\tau_w| = (\tau_{w,i}\tau_{w,i})^{1/2}$ for the rough surface $S13$. The results for the other rough surfaces and Reynolds number are nearly identical and are not shown here for conciseness purpose. We can see that all distributions exhibit large stretched tails. This means that the flow over the rough surface may experience rare but strong events of momentum loss. It is also to be noticed that the ratio of the wall stress norm to its root mean square (the subscript rms) $\xi = |\tau_w|/|\tau_w|_{rms}, |\tau_w|_{rms} = \langle|\tau_w|^2\rangle^{1/2}$ corresponds to the log-normal distribution:

$$LN(\xi,\mu,\sigma^2) = \frac{1}{\xi\sigma^2\sqrt{2\pi}}\exp\left(-\frac{(\ln\xi-\mu)^2}{2\sigma^2}\right) \tag{6.12}$$

with the presumed mean $\mu = -\ln 2/2$ and standard deviation $\sigma^2 = \ln 2$. From the expression for the moments of the log-normal distribution $m_k = \exp(k\mu + k^2\sigma^2/2)$, as shown in Zamansky *et al.* [170], the values of μ and σ correspond to the fact that $\langle|\tau_w|^{1/2}\rangle = \langle|\tau_w|\rangle^{1/2}$. The comparison with the PDF of $|\tau_w|$ for pure viscous stress (smooth wall) shows that these conclusions only hold for a rough wall.

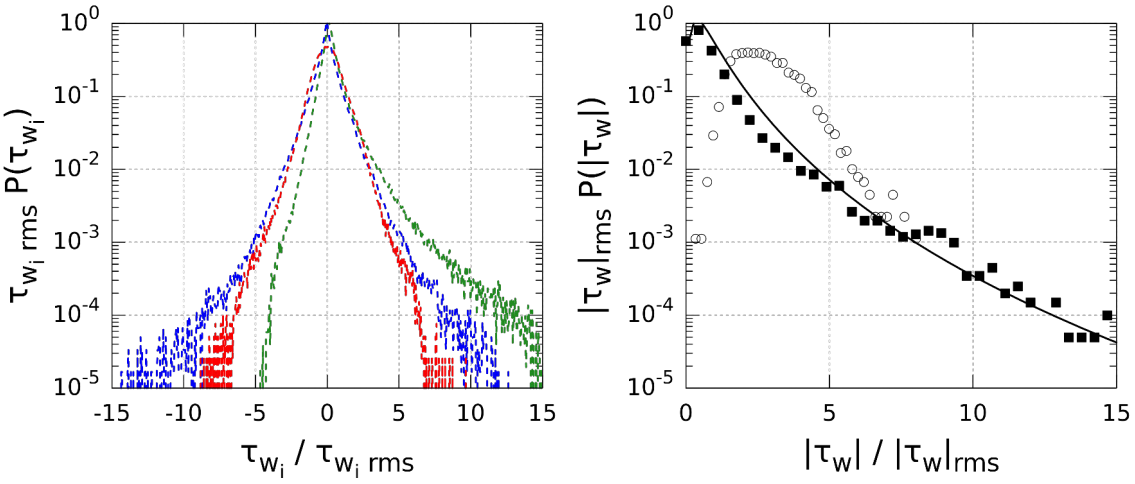

Figure 6.20 – (a) PDFs of the wall stress vector components ($i = 1$:- - -,$i = 2$:- - -,$i = 3$:- - -) for surface $S13$ at $Re_b = 8000$. (b) PDFs of the wall stress norm for $S00$ (○) and $S13$ (■) at $Re_b = 8000$ compared to the log-normal distribution (—) with the following parameters: $\mu = -\ln 2/2$, $\sigma = \ln 2$. PDFs are standardized by $\tau_{w_{rms}} = \langle\tau_w^2\rangle^{1/2}$.

At this point, we highlight that the distributions of the total wall stress intensity and its components are universal for our cases. The momentum loss for a given case corresponds to the value of the streamwise component of the wall stress vector. The momentum loss between the different surfaces should be then characterized by the mean value of the total wall stress intensity $\langle|\tau_w|\rangle$. As mentioned in sub-section 6.3.1, this component mostly depends on ES and S_q. One can expect that this is also true for the norm of the total wall stress. Figure 6.21 shows values of $\langle|\tau_w|\rangle$ for the different cases of this study.

Curiously, $\langle|\tau_w|\rangle$ is quite stable if S_q is fixed and does not change much with ES. On the other hand, the effect of the ES on the momentum loss can be seen in the mean value of the streamwise wall stress component. Surface $S43$ shows an exception to this behavior. Such a low value of ES makes the viscous drag to be largely dominant in the wall stress contribution [164], which is not the case with the other surfaces. Typical values of ES encountered in AM are usually greater and

this kind of regime is not well represented in our database. More RRLES with low ES values would have been performed for further analysis. Those tendencies are maintained with the other Reynolds numbers (not shown here).

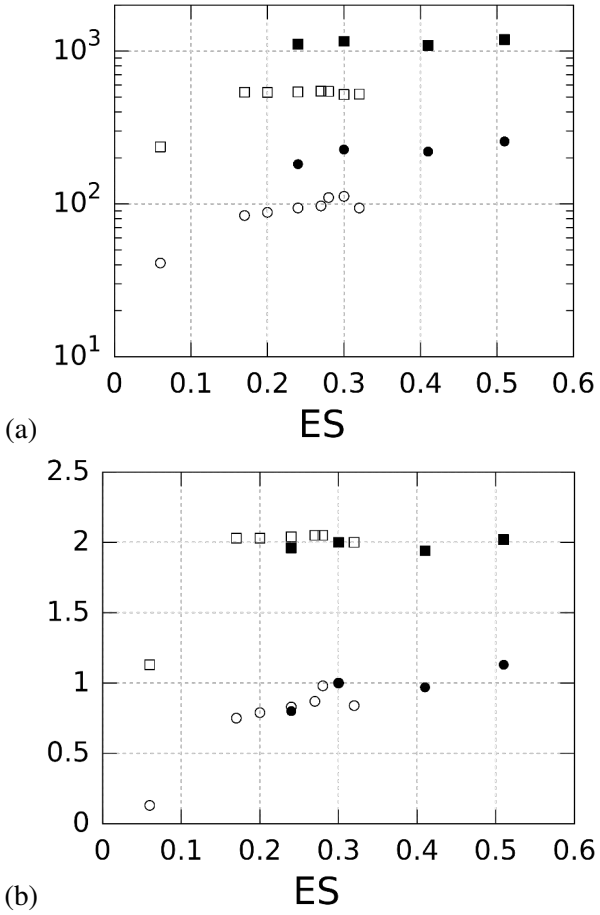

Figure 6.21 – (a) Mean values of the norm (□,■) and streamwise component (○,●) of the wall stress vector as a function of the surfaces ES for $Re_b = 8000$ (open symbols: $S_q/H = 0.02$, filled symbols: $S_q/H = 0.05$). (b) The same figure normalized by results from surfaces $S14$ and $S32$ for cases with $S_q/H = 0.02$ and $S_q/H = 0.05$, respectively.

We suggest that the wall stress mean intensity is mainly related to the mean roughness height deviation, while the ES acts on the distribution of the vector norm over its components, at least for a sufficiently high value of ES (around 0.2). Even though this observation is valid for the wall stress components' mean values, it is not straightforward to hold the same conclusion for the global behavior of the wall stress vector. Indeed, the variations of the rough surface and the recirculation zones vary the distribution of the wall stress norm along the directions with the local surface characteristics.

The study of the distributions of the wall stress unit vector components appears then to be relevant. Those are plotted in Figs. 6.22b-d.

It is seen that the most probable orientation for the direction vector is aligned in the direction of the mean flow. The spanwise and normal components do not show significant changes in their preferential orientation between the different cases. The normal component exhibits two main opposite values because both the upper and lower walls are taken into account in the PDF calculation.

Conversely, the peak of probability for the streamwise component is dependent on the considered surface and gets more importance with an increase in roughness level.

Remarkably, the value of e_1 that corresponds to this peak is close to the considered surface ES. Case $S43$ still shows an exception. We can also notice that due to the re-circulation zones activity, the deviation of all distributions becomes larger as the ES increases. Finally, for the surfaces that share the same ES, the distributions are almost identical, independently of other roughness parameters such as mean roughness height deviation or perpendicular anisotropy.

From these observations, we can conclude that the ES mainly controls the wall stress direction vector. As for the wall stress norm, the results do not change with the Reynolds number.

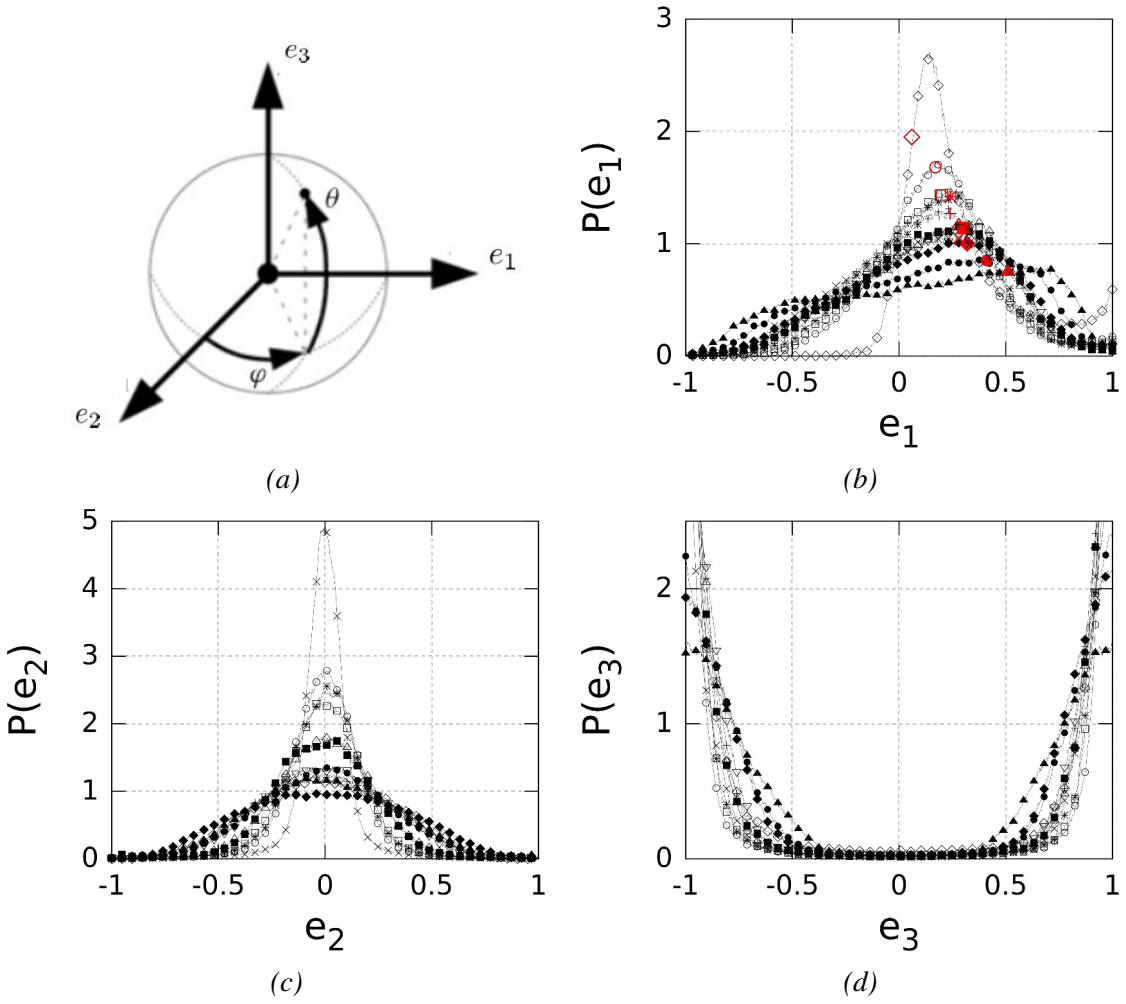

Figure 6.22 – (a) Definition of the angles and wall stress orientation vector components. (b) Streamwise orientation component distributions for the different surfaces at $Re_b = 8000$ (S11: ∘, S12: □, S13: △, S14: ▽, S15: ♦, S31: ∗, S32: ■, S33: •, S34: ▲, S41: +, S42: ×, S43: ⋄). Red points indicate the ES value of corresponding surfaces. Results for Set II are identical to Set I. (c)-(d) Same for spanwise and normal components.

A last interesting observation from the results is that the log-normality of the wall stress norm is maintained for different latitude θ and longitude φ angles (defined in Fig. 6.22a) of the vector direction. In Fig. 6.23, the distributions of $|\tau_w|$ for different values of θ and φ follow fairly well the unconditional PDF. We conclude that the amplitude and the direction of the rough wall stress vector are two independent variables.

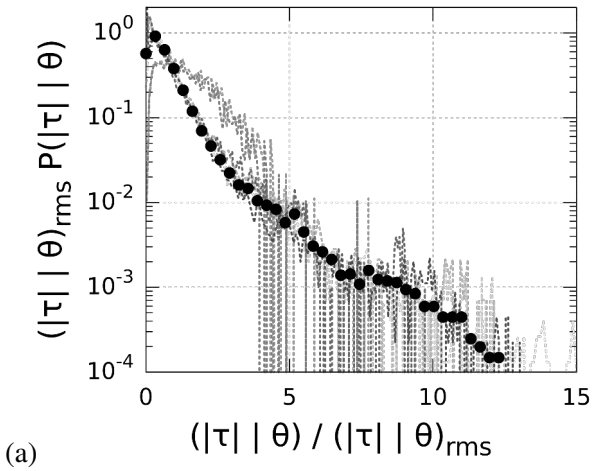

(a)

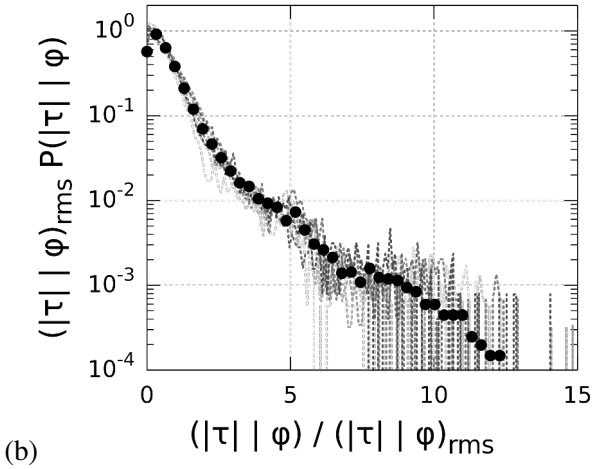

(b)

Figure 6.23 – (a) Distribution of the wall stress norm conditioned to different values of the angle θ ($\cdots$ from light to dark grey: $\theta = -3\pi/8, -\pi/4, -\pi/8, 0, \pi/8, \pi/4, 3\pi/8$) and compared with the unconditioned distribution (•). (b) Same for the angle φ (from $-3\pi/4$ to $3\pi/4$).

6.3.4 Stochastic rough modeled LES

Reproduction of the wall stress

The modeled wall stress is introduced as a product of two independent stochastic variables, the wall stress norm $|\tau_w|$ and the *i*-th component of the unit directional vector e_i:

$$\tau_{w,i} = |\tau_w| \cdot e_i \tag{6.13}$$

For the wall stress norm, we consider the log-normal Ornstein-Uhlenbeck stochastic process:

$$d|\tau_w| = -|\tau_w| \left(\ln \frac{|\tau_w|}{\langle |\tau_w| \rangle} - \frac{\sigma^2}{2} \right) \frac{dt}{T_w} + |\tau_w| \left(\frac{2\sigma^2}{T_w} \right)^{1/2} dW(t) \tag{6.14}$$

with $\sigma^2 = \ln(2)$ the standard deviation and $\langle |\tau_w| \rangle$ the mean value of the wall stress norm that is supposed to be preliminarily known. $dW(t)$ is the increment of a Brownian process ($\langle dW \rangle = 0, \langle dW^2 \rangle = dt$) and $T_w = L^*/u_\tau$ is the relaxation time. We somehow link the latter to the typical

size of re-circulation zones turbulent structures with L^* the correlation length of the surface height in the mean flow direction.

The unit vector of the wall stress direction evolves in time according to the Ornstein-Uhlenbeck process on the unit sphere. This process is governed by the stochastic equation written for the components of this vector [171]:

$$de_i = -e_i^* \frac{dt}{T_w} + \sqrt{D_j}\epsilon_{ijk} dW_j \circ e_k, \langle dW_i dW_j \rangle = \delta_{ij} dt \tag{6.15}$$

The first term represents the relaxation to the presumed direction with the specified components e_i^* and typical relaxation time T_w defined above. We consider E_i a coordinate system with E_1 tangent to the surface and oriented in the mean flow direction, E_3 is normal to the surface and E_2 satisfies orthogonality. According to the analysis in the previous section, the presumed direction E_i^* in this system is defined in the following manner: E_1^* is equal to the surface ES value, $E_2^* = 0$ and E_3^* is chosen to obtain $E_i^* E_i^* = 1$. Finally, e_i^* are the components of E_i^* expressed in the global coordinate system.

The second term represents the Ito form of the diffusion process on the unit sphere re-written in the form of the Stratonovich calculus (denoted by $\circ$). Here, δ_{ij} is the Kronecker delta, $W_j = (1, 2, 3)$ represents independent components of a Brownian vector process and ϵ_{ijk} is the Levi-Civita symbol. D_j is a vector of diffusion coefficients for each component.

As seen in the previous section, the deviation of the unit vector components only depends on the surface ES. From this consideration, D_j is arbitrarily set to correspond to the expected component distribution shapes for a considered surface. We repeat this operation for the different ES available in the database to build an empirical table that should return the right diffusion coefficients from the rough surface properties. Equation 6.15 preserves the norm $e_i(t)e_i(t) = 1$ at any instant, if initially $e_i(0)e_i(0) = 1$. Time integration is performed with the midpoint scheme as in Sabelnikov *et al.* [171].

Von Neumann condition with transpiration

In addition to the stochastic modeling, we modify the numerical treatment at the wall boundary. Imposing the wall flux through a Von Neumann condition implies that the wall velocity may be different than the real wall velocity. Since the wall is not a porous media, the normal component of the wall velocity must be suppressed to avoid mass flow through the wall.

However, if we consider the real rough geometry, the flat wall covers planar zones that are normally filled with fluid or solid. Moreover, it has been shown in Orlandi *et al.* [172] that the characteristics of rough wall turbulence reflect the presence of a non-zero wall-normal velocity disturbance at the interface of rough walls. Thus, we consider here that the local transpiration (non-zero penetrating velocity) induced by the modeled wall stress represents physical events and should be allowed. The wall's normal component of the velocity is then no more suppressed but corrected in the following manner to keep global zero mean mass flow through the wall:

$$u_i^w = u_i^w - \left(\langle u_j^w \rangle \cdot n_{w,j} \right) n_{w,i} \tag{6.16}$$

where u_i^w is the velocity at the wall. Equations 6.13 - 6.16 constitute the present stochastic rough modeled LES.

Calibration

In the previously described models, the mean wall stress norm $\langle |\tau_w| \rangle$ and rough surface properties are mandatory parameters to calibrate the stochastic processes. The latter are expected to be known

beforehand. On the other hand, acquisition of the mean wall stress norm is not straightforward since theoretical works usually focus on the mean stress oriented in the flow direction $\langle\tau_{w,1}\rangle = \langle|\tau_w|\rangle e_1$. We consider here two different strategies to estimate *a priori* the value of $\langle|\tau_w|\rangle$. The first method is to use interpolated results from our database or other empirical data.

The second option is to use the correlations available in the literature and the modified law of the wall to estimate $\langle\tau_{w,1}\rangle$. Knowing that the component of the wall stress unit vector in the flow direction should relax to the surface ES value, Eq. 6.13 leads to $\langle|\tau_w|\rangle = \langle\tau_{w,1}\rangle/\langle e_1^*\rangle$. The well-calibrated stochastic processes described above are applied at each grid point of the wall surface. It should be pointed out here that every process on grid points tends to have the same mean values but random fluctuations are not correlated in space. With this method, the complete wall stress behavior on the boundary is reproduced, including pressure efforts in the wall-normal direction.

6.3.5 Validation of the models

Hereafter, we present the assessment of the proposed models. Rough-Modeled LES (RMLES) are conducted to reproduce the cases of the Roughness-Resolved LES (RRLES) database. Methodologies and geometries are the same as those described in section 6.2. The models used for evaluation are the Duprat wall law [168] adapted to the rough wall (TBLE) and the stochastic model presented in section 6.3.3 (denoted hereafter as to SRLES). We used the correlation from De Marchis *et al.* [163] to calibrate the TBLE approach. Values of $\langle|\tau_w|\rangle$ needed for the stochastic model are directly taken from the database. Following the strategies stated in sub-section *Calibration* just above, we add a few cases in which $\langle|\tau_w|\rangle$ is computed from the value of $\langle\tau_{w,1}\rangle$ obtained with the TBLE model. Those are named Duprat-SRLES.

For better clarity of the results, only the simulations for bulk Reynolds numbers $Re_b = 8000$ and $Re_b = 17000$ are presented. Those two are indeed sufficient to cover both transitionally and fully rough regimes with considered surfaces. LES are performed on a Cartesian mesh whose size is chosen to be in the typical range encountered in wall-modeled LES. Mesh resolutions expressed in wall units for the modeled cases are summarized in Tab. 6.13.

Re_b	8000			17000		
Case	Δ_x^+	Δ_y^+	Δ_z^+	Δ_x^+	Δ_y^+	Δ_z^+
S11-S15 ; S41-S42	37	18	14	77	39	29
S21-S25	37	18	14	77	39	29
S31-S34	54	28	20	101	35	56
S43	23	12	9	40	21	15

Table 6.13 – RMLES mesh resolution as a function of the different sets.

We first observe the model's capacity to estimate the channel pressure loss. Friction factor $f = 2\left(u_\tau/U_b\right)^2$ obtained with the RMLES are compared with RRLES in Fig. 6.24. Basically, this factor f informs on the capacity of the models to predict the mean value of the wall stress since U_b is imposed and $u_\tau = \sqrt{\tau_{w,1}/\rho}$. The main difference between sets I and II is the value of the roughness height skewness Sk. This parameter is not taken into account for the model's calibration. Thus, results for surfaces from sets I and II are identical.

It is seen that the results for Set I and IV are satisfyingly close to the references for both Reynolds numbers. The differences between the modeling approaches are also not significant. On the other hand, the prediction of the friction factor for Set III is over-estimated with the SRLES and under-estimated with the TBLE. The presence of the blockage effects in the Set III cases may explain this difference. Those effects are contained in the parameter $\langle|\tau_w|\rangle$ taken from RRLES, but we cannot be sure that they are well treated in the stochastic scenario. For the TBLE, they are not

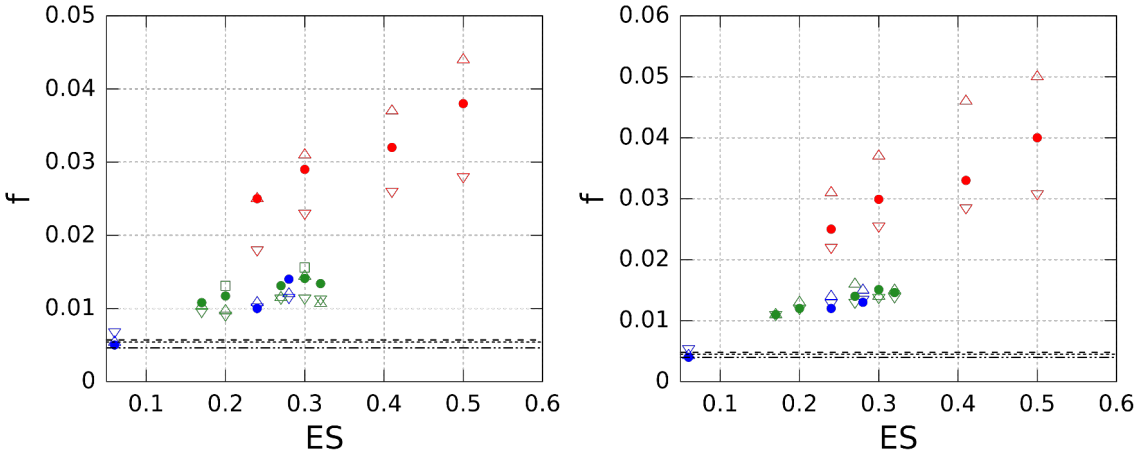

(a) *(b)*

Figure 6.24 – (a) Comparison of the friction factor in the $Re_b = 8000$ channel flow between RRLES (•), TBLE (▽), SRLES (△) and Duprat-SRLES (□) for cases of Set I (—), Set III (—) and Set IV (—). Lines denote the friction factor in the smooth channel for the wall-resolved LES (− − −), Duprat wall modeled LES (· · ·) and no-slip coarse LES (− · · −). (b) Same for $Re_b = 17000$.

even taken into account. Nevertheless, the order of magnitude and the trend are in accordance with the RRLES. The results are also compared with the friction factor obtained in the smooth channel with different LES methods. The significant difference between the smooth and rough channels results shows the necessity of using a rough model to evaluate the head loss due to the presence of the rough surface.

A good prediction of the mean wall stress does not guarantee that the turbulence dynamics inside the channel are well reproduced. To evaluate this feature, we perform new simulations in which the exact $\langle \tau_{w,1} \rangle$ extracted from the RRLES is imposed at the boundary condition (MLES for Mean wall stress LES). Then, we compute the mean velocity profiles inside the channel. Comparison of the velocity profiles between the different methods for $Re_b = 8000$ and $Re_b = 17000$ is shown in Fig. 6.25 and 6.26.

As expected, we can notice that the use of the mean value of the wall stress alone leads to an overestimate of the mean velocity profile. One can argue that imposing $\langle \tau_{w,1} \rangle$ alone is irrelevant because the mean wall stress is not homogeneous in space due to surface irregularities. Nevertheless, imposing the mapped RRLES mean wall stress gives the same results.

More than the mean values for the wall stress should be then taken into account to predict the mean velocity profile. A weakness of this approach is that the wall stress is not connected to the flow. Conversely, the TBLE approach is connected to the flow since the wall tangential velocity is an input to the model. The results obtained with this model are indeed closer to the references.

The SRLES is neither not connected to the flow and also relies on a priori known mean values. On the other hand, the heart of the model is to reproduce the global wall stress behavior; the reasons of this behavior are not need to be known. Moreover, the wall stress evolves over time, and the stochastic scenario reproduces the strong events observed in the analysis. These features of the model may be seen in the results that reproduce well the mean velocity profiles of the RRLES. The error for the case $S41$ is more critical since the stochastic scenario has been constructed with hypotheses that are not valid for low ES.

The combination of the qualities of TBLE and SRLES models may be seen in the Duprat-SRLES results that also fit well with the references.

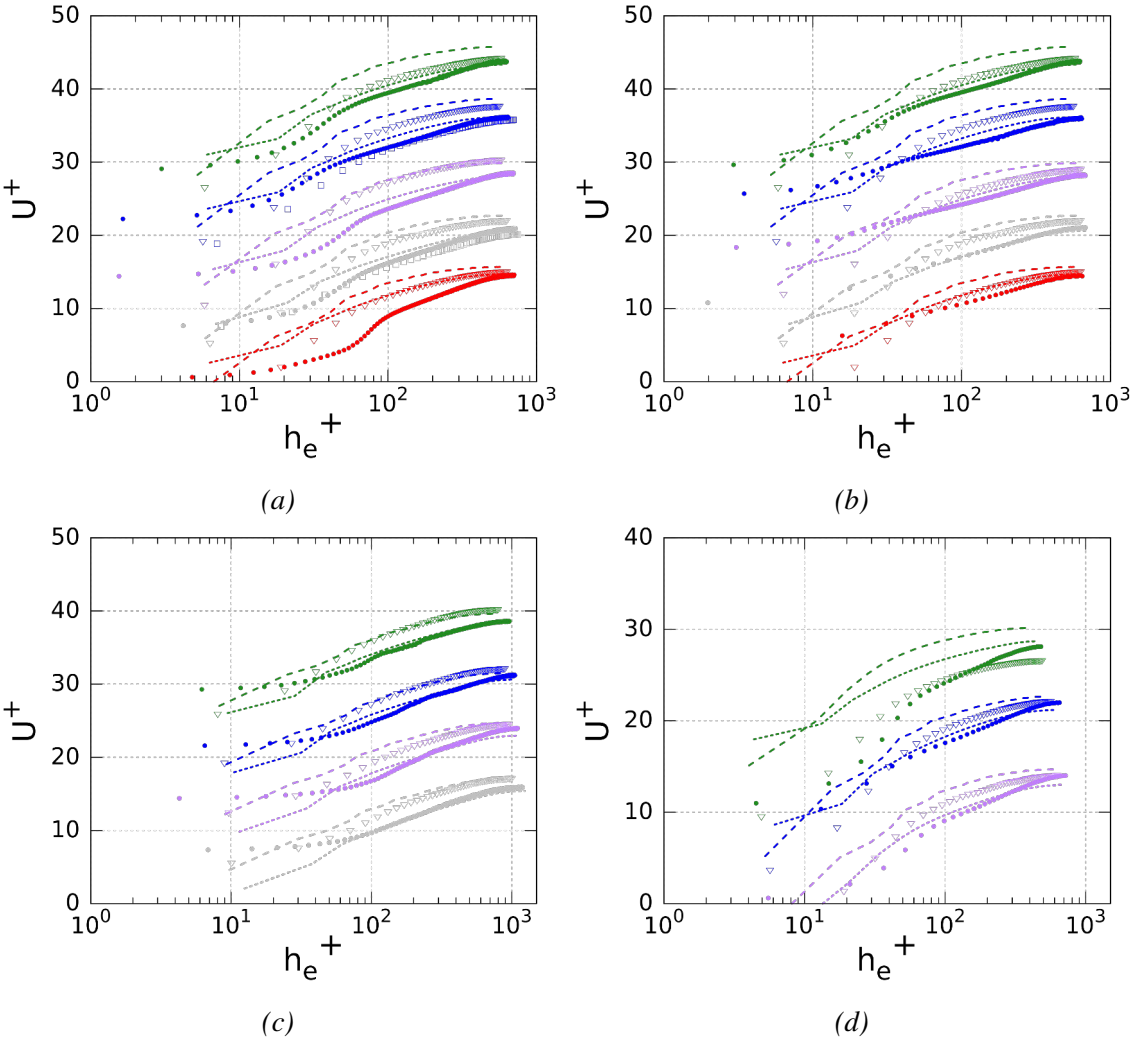

Figure 6.25 – (a) Comparison of the mean velocity profiles in the $Re_b = 8000$ channel flow between RRLES (•), MLES (– – –), TBLE (▽), SRLES (- - -) and Duprat-SRLES (□) for cases of Set I ($S11$:—,$S12$:—,$S13$:—,$S14$:—,$S15$:—). See [155] for the definition of h_e^+. Profiles are shifted up for better visibility. (b) Same for Set II ($S21$:—,$S22$:—,$S23$:—,$S24$:—,$S25$:—). (c) Same for Set III ($S31$:—,$S32$:—,$S33$:—,$S34$:—). (d) Same for Set IV ($S41$:—,$S42$:—,$S43$:—).

As explained earlier, results for set I and II are identical due to the model's formulation.

6.3.6 Partial conclusion

This section has exposed the assessment of the presented LES models. Models have been tested by reproducing representative cases from the RRLES database. Three modeling strategies have been considered for assessment. The first one imposes the exact mean wall stress taken from the RRLES database at the wall. The second model evaluates the wall stress in the framework of TBLE approaches with the Duprat wall law. The last model adds stochastic fluctuations to the wall stress assessed with the two first approaches.

In a first time, the capacity of the models to reproduce the value of the friction factor has been evaluated. All models have shown satisfying performances.

In a second time, we have compared the velocity profiles inside the channel with the references.

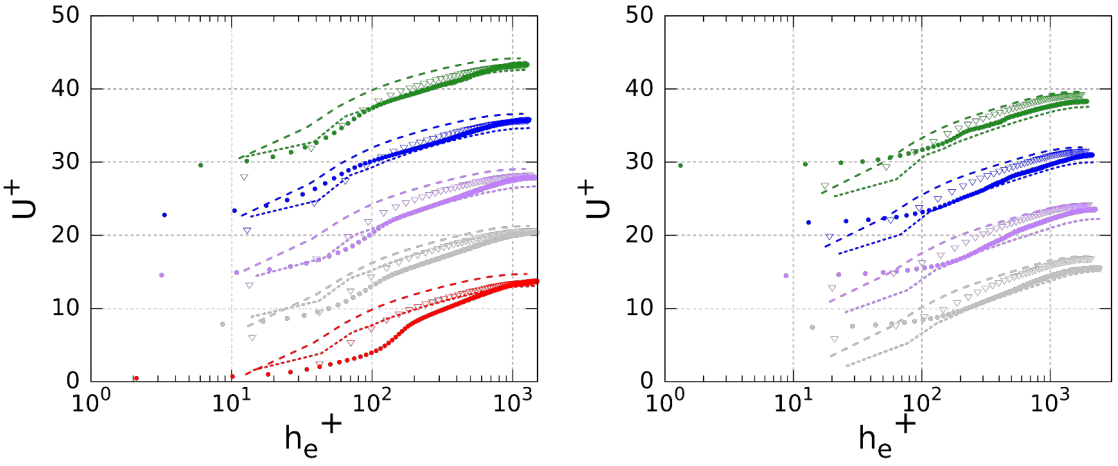

(a) *(b)*

Figure 6.26 – (a) Comparison of the mean velocity profiles in the $Re_b = 17000$ channel flow between RRLES (•), MLES (– – –), TBLE (▽) and SRLES (- - -) for cases of Set I ($S11$:—,$S12$:—,$S13$:—,$S14$:—,$S15$:—). Profiles are shifted up for better visibility. (b) Same for Set III ($S31$:—,$S32$:—,$S33$:—,$S34$:—).

We showed that the use of the mean value of the wall stress alone is not enough to reproduce the mean velocity behavior inside the channel. The results are better predicted if the modeled wall stress is connected to the flow, like in the TBLE approach. Adding stochastic fluctuations led to significant improvements in predicting the mean velocity profiles for both methods.

The combination of the TBLE method with the stochastic model appears to be promising. However, only a few cases have been conducted with this approach. Extension of the assessment for this strategy to the other cases would have been of interest for future works.

Another perspective of this study would be to evaluate the models on other basic cases, such as pipe flows or square channels.

6.4 Modeling strategies for heat transfer

6.4.1 Correlations for passive scalar

Hereafter, we compare the database results with the correlations in the literature for a constant wall temperature. Conjugated heat transfer is not considered here. As for the mean velocity, the wall roughness reduces the mean scalar profile in the streamwise direction. Analogous to the law of the wall for momentum, this reduction may be written from a law of the wall for passive scalar (here Kader [173]) with a defect term:

$$\bar{Z}^+ = \frac{Pr_t}{\kappa}\ln(h^+) + \beta(Pr) - \Delta\bar{Z}^+ \tag{6.17}$$

with

$$\beta(Pr) = (3.85Pr^{1/3} - 1.3)^2 + (Pr_t/\kappa)\ln(Pr_t) \tag{6.18}$$

Here, $\kappa = 0.41$ is the von Kármán constant, Pr is the scalar Prandtl number, Pr_t is the turbulent Prandtl number, and superscript $+$ indicates wall units. The normalization of $\bar{Z}$ is done with the friction scalar $\bar{Z}_\tau = (\nu/(u_\tau Pr))\left.\frac{\partial\bar{Z}}{\partial h}\right|_w$ thus $\bar{Z}^+ = \bar{Z}/\bar{Z}_\tau$. The aim of correlative methods

is to empirically estimate the scalar defect $\Delta\bar{Z}^+$ and use Eqs. 6.17 - 6.18 to evaluate the scalar flux at the wall.

$\bar{Z}$ being a transported scalar, one can think that its behavior and defect should follow those from velocity. However, it has been shown that the roughness affects scalar and momentum fluxes differently [174, 175]. Thus, $\Delta\bar{Z}^+$ must be evaluated with its own correlation. As for ΔU^+, correlations for $\Delta\bar{Z}^+$ may rely on equivalent sand grain roughness k_s (ESGR) or geometrical parameters. Based on Kays and Crawford [176] theory, Peteers and Sandham [175] proposed the following ESGR-based correlation:

$$\Delta\bar{Z}^+ = \frac{Pr_t}{\kappa}\ln(k_s^+) + \beta(Pr) - 7.4 - \frac{5}{4}(k_s^+)^{0.2}Pr^{0.44} \tag{6.19}$$

In the same paper, a correlation based on geometrical parameters is also proposed:

$$\Delta\bar{Z}^+ = \frac{Pr_t}{\kappa}\ln(S_q^+) + \beta(Pr) - 7.4 \tag{6.20}$$

The comparison between the scalar defect measured in the database and Eqs. 6.19 - 6.20 are shown in Fig. 6.27. The corresponding ESGR for our cases is evaluated with the formula from Boyle and Stripf [162]. The advantages and drawbacks of using ESGR or geometrical parameters to characterize surface roughness have been discussed in the previous section.

It is seen that the order of magnitude of the results given by the correlations is consistent with the database references. However, a significant deviation may be remarked, especially for formula 6.20. On the other hand, the lack of data makes it difficult to correctly estimate the correlations' relevance for our cases. The enrichment of the database with more cases, including passive scalar transport, appears here as necessary. Those first results still remain promising for modeling.

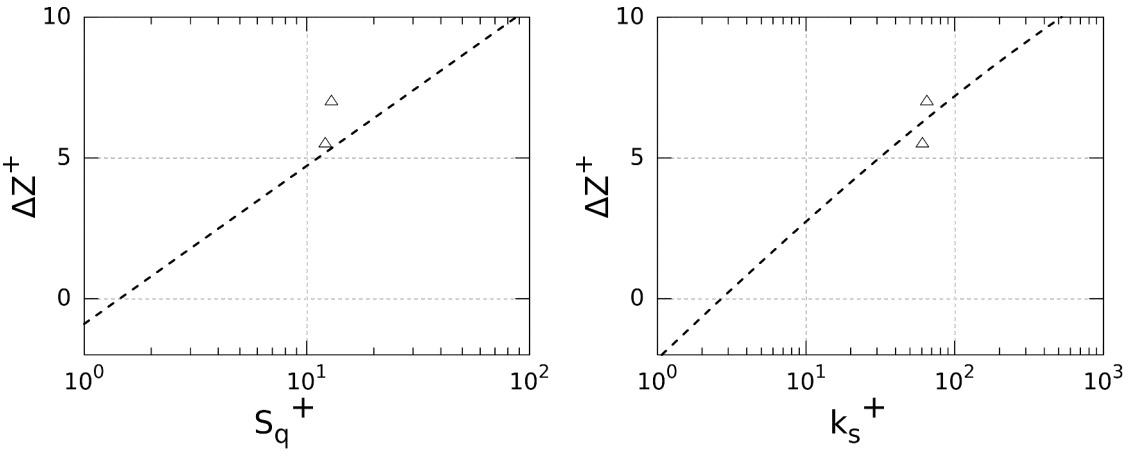

Figure 6.27 – (a) Scalar defect $\Delta\bar{Z}^+$ measured in the database cases as function of S_q^+ compared with the correlation Eq. 6.20 (- - -). Set I: △. Results for set II are identical to set I. (b) Scalar defect $\Delta\bar{Z}^+$ as a function of ESGR k_s^+ compared with correlation Eq. 6.19 (- - -).

6.4.2 Boundary layer modeling

This sub-section presents the boundary layer theory-based modeling strategies for passive scalar proposed in the literature. Our motivation here is to adapt the recent advancements to the numerical framework of our RANS and LES methodologies.

Rough TBLE for passive scalar

Models for passive scalars based on boundary layer theory rely on the same hypotheses and numerical methods described in sub-section 6.3.2 for momentum. In addition to solving the thin boundary layer momentum equations (TBLE) on an embedded near-wall grid, the following simplified transport equation is also considered:

$$\frac{d}{dh}\left[(\nu+\nu_t)\tilde{u}\frac{d\tilde{u}}{dh}+c_p\left(\frac{\nu}{Pr}+\frac{\nu_t}{Pr_t}\right)\frac{d\bar{Z}}{dh}\right]=0 \tag{6.21}$$

with $\tilde{u}$ the wall tangential velocity and c_p the heat capacity. The turbulent eddy viscosity ν_t is modeled by a RANS-type model. The model steps are the following: (i) the near-wall passive scalar values and wall tangential velocities are interpolated on the TBLE grid points at some distance from the wall $h = h_{wm}$, (ii) equation (6.21) is solved with a RANS solver with a no-slip condition for velocity and a Dirichlet condition for scalar at $h = 0$, (iii) the scalar flux evaluated on the second grid at the wall is applied as a Von Neumann condition to close the LES equations. Communication location and overlapping of the two grids are sensitive parameters discussed in Bose and Park [165].

The extension of the TBLE approach by Olmeda *et al.* [167] to rough wall turbulence is also stated for the passive scalar transport. As for the momentum equation, the scalar upper boundary condition of the wall model is modified by writing:

$$\bar{Z}_{TBLE}(h_{wm}) = \bar{Z}_{LES}(h_{wm}) + \bar{Z}_\tau \Delta\bar{Z}^+ \tag{6.22}$$

at the communication grid point. This formulation needs a correlation to know the mean scalar defect $\Delta\bar{Z}^+$.

Duprat wall law

The Duprat wall law has also been extended to passive scalar transport [169]. The normalized scalar is obtained from the scalar difference between the flow and the wall divided by the scalar gradient at the wall:

$$\frac{\bar{Z}^+}{h^+} = \frac{\bar{Z}-\bar{Z}_w}{h}\left.\frac{\partial\bar{Z}}{\partial h}\right|_w \tag{6.23}$$

The normalized scalar gradient is then derived similarly to the velocity gradient:

$$\frac{\partial\bar{Z}^+}{\partial h^+} = \frac{1}{1+(Pr/Pr_t)(\nu/\nu_t)} \tag{6.24}$$

with the eddy viscosity modeled by

$$\frac{\nu_t}{\nu} = \kappa h^+\left[\alpha+h^+(1-\alpha)^{3/2}\right]^{0.78}\left(1-e^{-h^+/(1+17\alpha^3)}\right)^2 \tag{6.25}$$

To close the model, an additional correlation for the turbulent Prandtl number is assumed $Pr_t = 0.85 + 2\nu/(\nu_t Pr)$. In this formulation, the scalar gradient is an explicit function of α. Thus, the scalar model only needs the momentum model to be well-calibrated for rough wall turbulence.

Modified scalar gradient

All the formulations mentioned above commonly rely on pre-existing wall models for passive scalars and momentum. The latter are much more widely used. In the case of a computational code that does not possess any passive scalar wall models (even for a smooth wall) but does for the rough wall momentum, we write here a more straightforward approach. The scalar gradient needed to estimate the scalar wall flux is directly computed by modifying the scalar wall cell center value that follows Eq. 6.22.

This formulation has the advantage of not relying on a near-wall second grid and being very simple to implement. On the other hand, it will not rectify errors in the gradient computation due to a coarse mesh.

6.4.3 Stochastic modeling

This sub-section fits the stochastic LES modeling framework presented in section 6.3.3 for the wall stress. The motivation is to reproduce the rough scalar wall flux statistical behavior and apply it on a flat wall. The statistical analysis of the scalar wall flux from the database results is performed to identify the scenario to be reproduced by the model and is discussed in the first part. The stochastic modeling strategy is then presented.

Statistical analysis

We study the scalar flux at the wall defined as:

$$\phi_w = \frac{\nu}{Pr}\frac{\partial \bar{Z}}{\partial n_{w,i}} \tag{6.26}$$

with $n_{w,i}$ the wall normal vector. We consider the statistics of ϕ_w accumulated for all surface grid points at the statistically stationary state. Angled brackets $\langle\rangle$ denote the average over the surface. Due to the specified boundary conditions for $\bar{Z}$, the mean scalar flux is negative on the upper wall and positive on the lower wall. For the rest of the study, we will only consider the scalar flux on the lower wall. Figure 6.28 shows the probability density function (PDF) of the scalar wall flux for the rough surface $S12$. The results for the other rough surfaces are nearly identical and are not shown here.

We can see that the PDF may be approximated with a classic normal distribution with the presumed mean $\mu = 0$ and standard deviation $\sigma^2 = 1.2$. We point out that those parameters are empirically determined from our present results. For the considered cases, the distribution of ϕ_w seems to be universal. Of course, it would have been of interest to verify this conjecture by enriching the database with more cases, including passive scalar transport. We conclude that for our cases, we can determine the main statistical behavior of the scalar wall flux with its mean value.

Stochastic Rough Modeled Passive Scalar

We model the evolution of the scalar wall flux normalized by its mean value with a normal Ornstein-Uhlenbeck process:

$$d\chi = (\chi - \mu)\frac{dt}{T_w} + \left(\frac{2\sigma^2}{T_w}\right)^{1/2} dW(t) \tag{6.27}$$

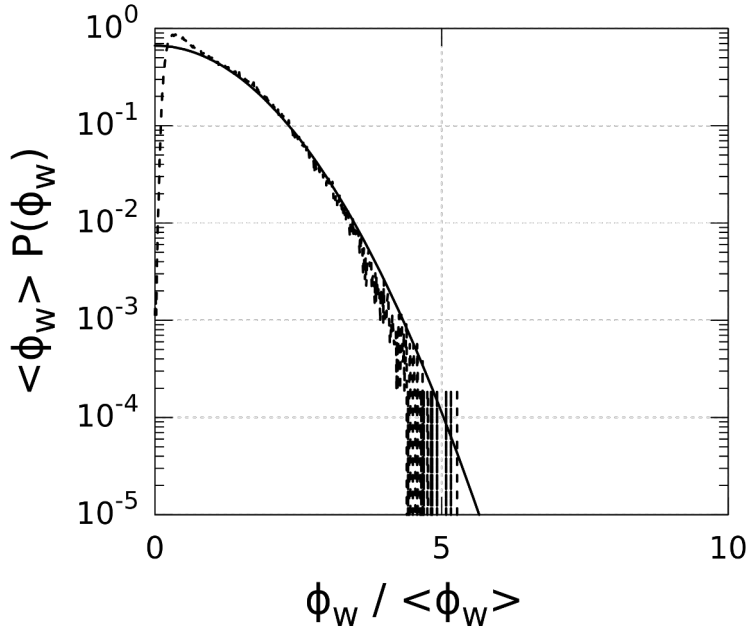

Figure 6.28 – (a) PDF of the scalar wall flux for rough surface $S12$ (- - -) at $Re_b = 8000$ compared to the normal distribution (—) with parameters $\mu = 0$ and $\sigma^2 = 1.2$. PDF is standardized by $\langle\phi_w\rangle$.

where $\chi = \phi_w/\langle\phi_w\rangle$. $dW(t)$ is the increment of a Brownian process ($\langle dW\rangle = 0, \langle dW^2\rangle = dt$) and $T_w = L^*/u_\tau$ the relaxation time. We somehow link the latter to the typical size of recirculation zones turbulent structures with L^* the correlation length of the surface height in the mean flow direction. At each time step, the process loops if the result is not a positive value in order to only obtain the positive part of the normal distribution. Thus, the mean deviation is set to $\sigma^2 = 0.6$ to keep the right distribution shape.

The relaxation value $\langle\phi_w\rangle$ is compulsory to give a dimension to the result and is supposed to be known beforehand. We consider here two different strategies to estimate *a priori* the value of $\langle\phi_w\rangle$. The first method is to use interpolated results from our database or other empirical data. The second option is to use the correlations available in the literature and the modified law of the wall to estimate $\langle\phi_w\rangle$.

The well-calibrated stochastic process is applied at each grid point of the wall surface. The modeled flux is then applied at the wall as a Von Neumann condition to close the scalar transport equation. All processes on grid points tend to have the same mean values, but the random fluctuations are not correlated in space.

6.4.4 Assessment of passive scalar rough modeled LES

Hereafter, we present the assessment of the models. Rough-Modeled LES (RMLES) with a passive scalar $\bar{Z}$ that represents temperature are conducted to reproduce the cases of the Roughness-Resolved LES (RRLES) database. As explained above, only a few cases at bulk Reynolds number $Re_b = 8000$, including passive scalar transport are available in the database.

The models used for evaluation are the Duprat wall law for passive scalar [169] (Duprat), the method in which the computation of the wall scalar gradient is modified with a scalar defect (denoted hereafter as TBLE), and the stochastic model for passive scalar (SRLES). For the latter, the value of $\langle\phi_w\rangle$ needed for calibration is directly taken from the database. For all those cases, the momentum flux is modeled with the Duprat wall law [168] adapted to rough turbulence.

In the Duprat wall law for passive scalar, the prediction of the scalar wall flux is directly dependent on the momentum flux prediction. To evaluate the sensibility of this model to the momentum prediction, we also consider cases in which the momentum is modeled differently. The alternative model combines the rough Duprat model with the stochastic process. The passive scalar is modeled with the scalar Duprat wall law [169]. Those cases are named Duprat-SRLES.

Finally, to estimate the benefit of the passive scalar models, the transport of $\bar{Z}$ is also performed in simulations without a model for the passive scalar. The geometrical correlations from De Marchis *et al.* [163] and Peteers and Sandham [175] are used to calibrate the models. RMLES are performed with the same meshes presented in sub-section 6.3.5.

We first observe the capacity of the model to estimate the scalar transfer in the channel. The Nusselt number

$$Nu = \frac{\partial T}{\partial h}\frac{H}{\bar{Z}_c - \bar{Z}_w} \tag{6.28}$$

obtained with the RMLES is compared with RRLES in Fig. 6.29. H is the channel half-height, $\bar{Z}_c$ the value of $\bar{Z}$ at the channel centerline and $\bar{Z}_w$ the prescribed value of $\bar{Z}$ at the wall. Basically, Nu informs on the capacity of the models to predict the mean value of the scalar wall flux since T_w is imposed and T_c is theoretically known. The main difference between sets I and II is the value of the roughness height skewness Sk. This parameter does not come under consideration for the model's calibration. Thus, results for surfaces from sets I and II are identical.

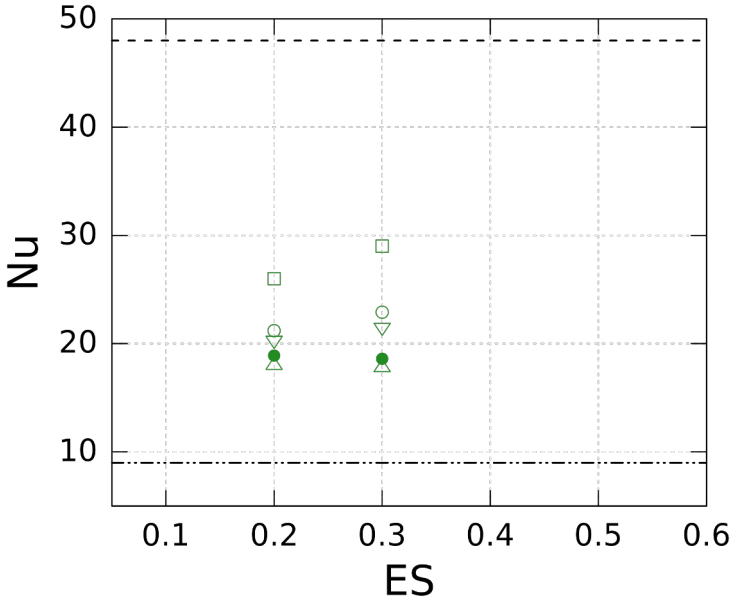

Figure 6.29 – Comparison of the Nusselt number in the $Re_b = 8000$ channel flow between RRLES (•), TBLE (▽), Duprat (○), SRLES (△) and Duprat-SRLES (□) for cases of Set I (—). Lines denote the Nusselt number in the smooth channel for the wall-resolved LES (− − −) and in the rough modeled channel with a model for momentum but not for the passive scalar (− · · −).

We can notice that a significant difference may be seen between the Nusselt number in the smooth and the rough channel. Moreover, all the simulations without a model for the passive scalar give the same Nusselt number, independently of the momentum model. The Nusselt number for

those cases is also largely underestimated. These first observations show the necessity of using a rough model for the passive scalar to correctly predict the transfer at the wall. Concerning the different modeling methods, it is seen that the results for Duprat, TBLE, and SRLES are satisfyingly close to the references.

On the other hand, results given by the Duprat-SRLES method show a significant overestimate of the Nusselt number. Also, the differences between the Duprat and Duprat-SRLES cases are high enough to conclude the high sensitivity of the scalar Duprat model to the momentum model.

A good prediction of the mean scalar wall flux does not guarantee that the transport inside the channel is well reproduced. To evaluate this feature, we perform new simulations in which the exact scalar wall flux $\langle \phi_w \rangle$ extracted from the RRLES is imposed at the boundary condition (MLES for Mean wall flux LES). Then, we compute the mean scalar profile inside the channel. A comparison of the scalar profiles between the different methods is shown in Fig. 6.30. The profile corresponding to the absence of a scalar model is the same, whatever the momentum modeling strategy.

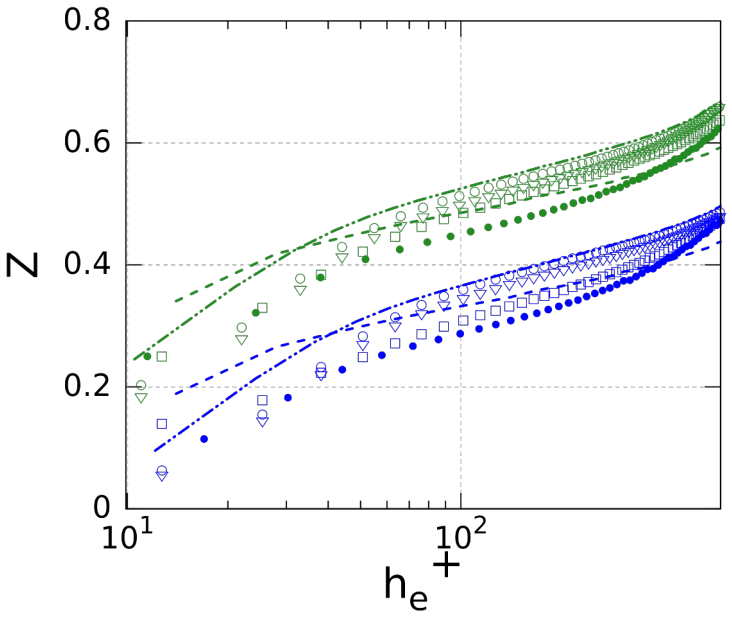

Figure 6.30 – Comparison of the mean scalar profiles in the $Re_b = 8000$ channel flow between RRLES (•), MLES (- - -), TBLE (▽), Duprat (○), Duprat-SRLES (□) and absence of model (— · · —) for cases of Set I ($S12$:—,$S14$:—). See [155] for the definition of h_e^+. Profiles are shifted up for better visibility.

In accordance with previous results, the absence of a model for the passive scalar leads to a wrong prediction of the scalar profile defect inside the channel and emphasizes the need to use a passive scalar model.

As expected, the use of the mean value of the scalar wall flux alone is not enough to predict the right scalar profile. The defect of the profile is in better accordance with the RRLES compared to the absence of the model, but the profile shape exhibits unsatisfying errors. The results of the SRLES are nearly identical to those of the MLES. This suggests that the stochastic fluctuations generated by the model do not bring significant improvements in the scalar wall flux modeling.

As already mentioned for the momentum modeling, the drawback of the previous methods is that the model is not connected to the flow, which is not the case with the TBLE, Duprat,

and Duprat-SRLES approaches. The tendencies and the shape of the profiles predicted by those methods are indeed closer to the references.

Interestingly, despite a lesser good prediction of the Nusselt number, the Duprat-SRLES scalar profiles are the closest to the references.

As explained earlier, results for set I and II are identical due to the models formulation.

6.4.5 Partial conclusions

This section has exposed several strategies to model AM rough wall passive scalar transport without direct representation of the roughness elements at the wall. Unfortunately, only a few cases with transported passive scalar could be performed, and the study needs more data. However, some interesting tendencies have been noticed.

The scalar defect measured in the database has been compared with correlations available in the literature. From the results, we have shown that correlations based on ESGR or geometrical parameters could both predict the scalar defect with acceptable precision.

Then, we have presented the possibility to use the correlations mentioned above to predict the scalar flux at the wall with a standard law of the wall and TBLE methods. Both approaches are compatible with RANS and LES methods.

We have performed a deeper study of the scalar wall flux behavior. The analysis showed that the flux is normally distributed with universal parameters, at least for our cases. The statistical properties observed in the analysis are reproduced with a temporal stochastic process. Input for the model is the mean value of the scalar wall flux only. The latter is estimated from the roughness function correlations.

The assessment of the LES models has also been done. Models have been tested by reproducing representative cases from the RRLES database.

Several modeling strategies were considered for assessment. The first one imposes the exact mean scalar wall flux taken from the RRLES database at the wall. The second strategy evaluates the scalar flux in the framework of TBLE approaches with the scalar Duprat wall law and a correlation-based modification of the scalar wall gradient computation. The last model adds stochastic fluctuations to the mean scalar wall flux. Each of these methods shares the same momentum model. The sensitivity of the scalar Duprat model to the momentum model is also investigated.

First, the capacity of the models to reproduce the scalar wall transfer has been evaluated. All models have shown satisfying performances. We have also shown that the choice of the momentum modeling method could significantly impact the performances of the scalar Duprat model.

Second, we compared the scalar profiles inside the channel with the references. We showed that the use of the mean value of the scalar wall flux alone is not enough to reproduce the mean scalar behavior inside the channel. The results are better predicted if the modeled flux is connected to the flow, like in the TBLE approaches. Contrary to the momentum flux, adding stochastic fluctuations to the scalar flux did not significantly improve the prediction of the mean scalar profiles.

Future work would consist of extending this study to the other cases of the database. Also, the simulated passive scalars in the database shared the same Prandtl number. Confront these conclusions with results having a different Prandtl number would also be an interesting objective.

6.5 Conclusions

The main objective of this chapter was to develop models in the framework of RANS and LES methods that are representative of the flow obtained in additive-manufactured heat exchangers

without explicit representation of the surface details. To this end, a Roughness-Resolved Large Eddy Simulation (RRLES) database of representative channel flows has been built. The most challenging task in building this database is the generation of representative rough surfaces and conformal unstructured meshes.

First, three different configurations of parallel rough plane channels with the same roughness height distribution but different effective slopes have been chosen and modeled. The impact of the effective slope parameter, which is directly linked to the alignment of the wall roughness with the flow, substantially impacts the flow topology, velocity and temperature profiles, as expected. In these cases, the existing empirical correlations find their limits, and new correlations are needed.

Simulations for the database have been conducted for periodic channels. The channel's half height was selected to be close to hydraulic diameters and channel heights encountered for some AM experiments. Blockage effects have then appeared, as expected for such additive-manufactured heat exchangers. The considered Reynolds numbers and surfaces lead RRLES flows to cover both transitionally and fully rough regimes.

From database results, derived strategies for turbulence have been developed in close collaboration with Alexis Barge from the LEGI laboratory. Models have been tested by reproducing representative cases from the RRLES database. Three modeling strategies have been considered for assessment. The first one imposes the exact mean wall stress taken from the RRLES database at the wall. The second model evaluates the wall stress in the framework of TBLE approaches with the Duprat wall law. The last model adds stochastic fluctuations to the wall stress evaluated with the two first approaches.

The capacity of the models to reproduce the value of the friction factor has shown satisfying performances. We have also compared the velocity profiles inside the channel with the references. We showed that using the mean value of the wall stress alone is not enough to reproduce the mean velocity behavior inside the channel. The results are better predicted if the modeled wall stress is connected to the flow, like in the TBLE approach. Adding stochastic fluctuations led to significant improvements in predicting the mean velocity profiles for both methods. The combination of the TBLE method with the stochastic model appears to be promising. However, only a few cases have been conducted with this approach.

Regarding heat transfer, several strategies to model AM rough wall passive scalar transport without directly representing the roughness elements at the wall.

The scalar defect measured in the database has been compared with correlations available in the literature. From the results, we have shown that correlations based on equivalent sand grain roughness (ESGR) or geometrical parameters could both predict the scalar defect with acceptable precision.

We have performed a deeper study of the scalar wall flux behavior. The analysis showed that the flux is normally distributed with universal parameters, at least for our cases. The statistical properties observed in the analysis are reproduced with a temporal stochastic process. Input for the model is the mean value of the scalar wall flux only. The latter is estimated from the roughness function correlations.

Several modeling strategies were considered for assessing the LES models. The first one imposes the exact mean scalar wall flux taken from the RRLES database at the wall. The second strategy evaluates the scalar flux in the framework of TBLE approaches with the scalar Duprat wall law and a correlation-based modification of the scalar wall gradient computation. The last model adds stochastic fluctuations to the mean scalar wall flux. Each of these methods shares the same momentum model. The sensitivity of the scalar Duprat model to the momentum model is also investigated.

All models have shown satisfying performances in reproducing the scalar wall transfer. We

have also demonstrated that the choice of the momentum modeling method could significantly impact the performances of the scalar Duprat model.

Finally, we showed that using the mean value of the scalar wall flux alone is not enough to reproduce the mean scalar behavior inside the channel. The results are better predicted if the modeled flux is connected to the flow, like in the TBLE approaches. Contrary to the momentum flux, adding stochastic fluctuations to the scalar flux did not significantly improve the prediction of the mean scalar profiles.

Future work would consist of extending this study to the other cases of the database. Furthermore, another perspective of this study would be to evaluate the models on other basic cases, such as pipe flows or square channels.

CHAPTER 7

Study of rough heat exchangers

This chapter investigates heat exchanger configurations that exhibit a surface condition similar to that of additive manufacturing. The first configurations studied are square and cylindrical channels, which are commonly found in experimental additive-manufactured heat exchangers. As discussed in Chapter 1, additional surfaces can enhance heat transfer. Therefore the final case examined in this study is a plate with finned tubes.

Contents

7.1 Square and cylindrical channels

7.1.1 Numerical setup

These configurations are widespread among experimental additive-manufacturing heat exchangers (Stimpson *et al.* [23] for instance) and must be studied. In this section, configurations, meshes, and post-processing fields are addressed.

Configurations

In order to compare with previous results, two cases about the effective slope are chosen. The first reason is to ensure consistency of results on the range of the effective slope. The second one is to decrease the CPU cost. Indeed we intended to keep most of the granted CPU hours for the extensive database dedicated to open channel configurations, as presented in Chapter 6.

Selected effective slopes are $ES = 0.2$ and $ES = 0.62$. This corresponds to almost the limits of our previous range, and more importantly, they are the same values as open channel cases previously studied. As the threshold seems to be $ES = 0.3$ for the behavior of roughness function ΔU^+, both regimes are also targeted.

Basically, geometries are generated from rough planes. For square cases, the sides of the channel are linked. Thus, the STL is closed. Dimensions of the computational domain are $8000\ \mu m$ x $3000\ \mu m$ x $3000\ \mu m$ respectively in the streamwise, spanwise, and crosswise directions. Concerning cylindrical channels, the junction is ensured by periodic boundary conditions. Roughness parameters of chosen geometries are exposed in Tab. 7.1.

Geometry	ES	$S_a\ (\mu m)$	$S_q\ (\mu m)$	$S_t\ (\mu m)$	S_k	Ku
Square	0.20	$15.6\ \mu m$	$20.0\ \mu m$	$179.3\ \mu m$	0.23	4.00
	0.62	$38.9\ \mu m$	$50.8\ \mu m$	$447.6\ \mu m$	0.15	3.83
Cylinder	0.20	$15.4\ \mu m$	$20.0\ \mu m$	$163.6\ \mu m$	0.21	3.83
	0.62	$38.9\ \mu m$	$50.0\ \mu m$	$454.4\ \mu m$	0.18	3.92

Table 7.1 – Roughness parameters of chosen geometries

A view of these different configurations is shown in Fig. 7.1. At first glance, one can notice that the roughness is slightly anisotropic with a pattern perpendicular to the flow direction. The latter could be retrieved indeed with additive manufacturing.

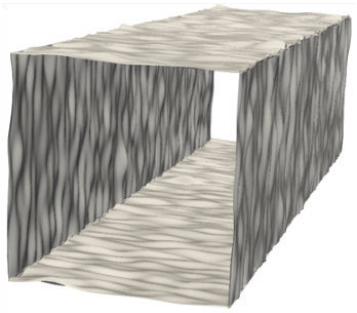

(a) Square rough channel ($ES = 0.20$)

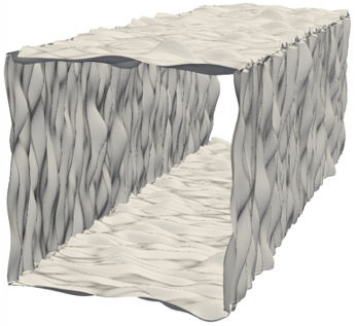

(b) Square rough channel ($ES = 0.62$)

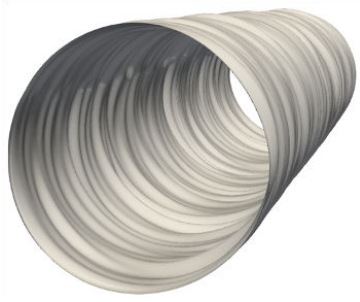

(c) Cylindrical channel ($ES = 0.2$)

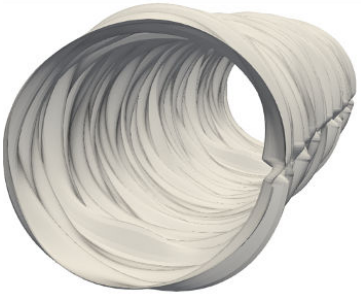

(d) Cylindrical channel ($ES = 0.62$)

Figure 7.1 – Generated geometries for RRLES

7.1.2 Meshes

Square channel

For each case, two meshes are generated in order to verify mesh convergence. The number of cells in each direction for the initial cartesian mesh is chosen as the cell size is equal to 20 μm.

The main difference between both mesh configurations ($M1$ and $M2$) is the cell size on the surface. Indeed for M1, the imposed cell size is 10 μm and 8 μm for M2. Characteristics of meshes for square channel cases are presented in Tab. 7.2. One can notice that the number of elements is relatively large for these configurations as fine cell size is imposed on each side of the channel.

One key point has to be underlined. As the cell size gradient, the cell size on the surface, and the Cartesian grid's cell size are imposed, consistency is required. Thus the outer distance d between the limits of the Cartesian grid and the STL has to be sufficient. This can be easily calculated (see Eq. 7.1), and Fig. 7.2 highlights this constraint. Figure 7.3 presents the mesh M1 for the case $ES = 0.20$, and one can notice the cell gradation from the surface to the center of the channel.

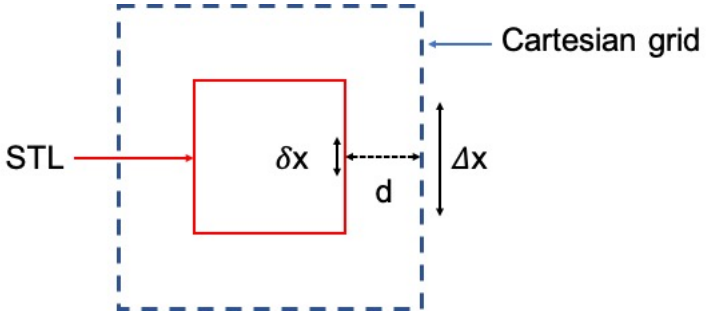

Figure 7.2 – Calculation of required distance between STL and boundaries of Cartesian grid (cross-section view)

$$d = \delta x \sum_{i=1}^{N} (1 + h_{grad})^i = \delta x \left(\frac{(1 + h_{grad})^{N+1} - 1}{h_{grad}} - 1 \right) \tag{7.1}$$

with h_{grad} set by the user. By default, the value is equal to $h_{grad} = 0.1$. The next step is then to calculate the required number of cells N for reaching the cell size Δx, which is imposed for the Cartesian grid. This value is determined via Eq. 7.2:

$$\Delta x = \delta x (1 + h_{grad})^N \tag{7.2}$$

Cases	**Mesh**	**Initial** N_x, N_y, N_z	**Cell size on STL**	**Max cell size gradient**	**Number of elements**
ES 20%	M1	400 ; 200 ; 200	10 μm	0.1	126 M
	M2	400 ; 200 ; 200	8 μm	0.1	171 M
ES 62%	M1	400 ; 200 ; 200	10 μm	0.1	143 M
	M2	400 ; 200 ; 200	8 μm	0.1	198 M

Table 7.2 – Characteristics of meshes for square configurations

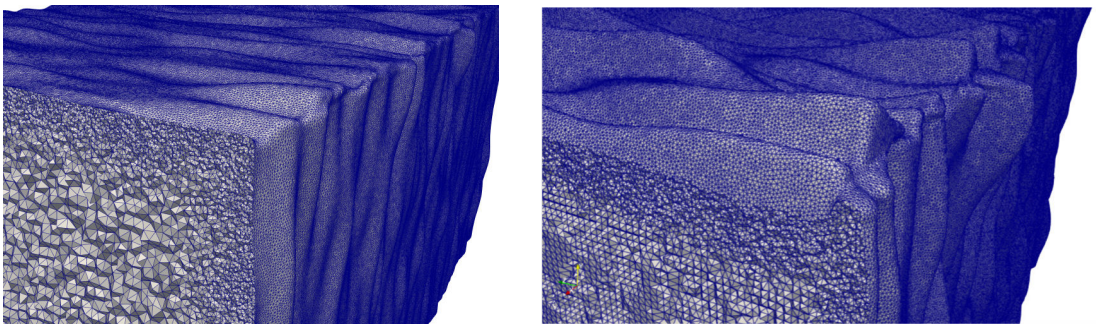

(a) $ES = 0.20$ (b) $ES = 0.62$

Figure 7.3 – Mesh M1 of the computational domain for square cases

Performances of meshing for square cases are assessed in Tab. 7.3.

	ES	Number of cells	Number of CPUs	CPU hours	RAM/CPU
M2	0.20	171 M	1024	4100	1775 Mb
M2	0.62	198 M	1024	7150	2196 Mb

Table 7.3 – Meshing performances for square cases

Cylindrical channel

Concerning the cylinder cases, characteristics of meshes are presented in Tab. 7.4. Since a cylinder could be considered as one rough surface, the number of elements for these cases is reduced compared to square channels.

Cases	**Mesh**	**Initial** N_x, N_y, N_z	**Cell size on STL**	**Max cell size gradient**	**Number of elements**
$ES = 0.20$	M1	400 ; 200 ; 200	10 μm	0.1	52 M
	M2	400 ; 200 ; 200	8 μm	0.1	75 M
$ES = 0.62$	M1	400 ; 200 ; 200	10 μm	0.1	57 M
	M2	400 ; 200 ; 200	8 μm	0.1	84 M

Table 7.4 – Characteristics of meshes for cylindrical channels

A view of obtained meshes is presented in Fig. 7.4. One can remark that the rough surface is well-discretized. Meshing performances are here also given in Tab 7.5.

	ES	Number of cells	Number of CPUs	CPU hours	RAM/CPU
M2	0.20	75 M	1024	6540	1775 Mb
M2	0.62	84 M	1024	7150	2196 Mb

Table 7.5 – Meshing performances for cylindrical cases

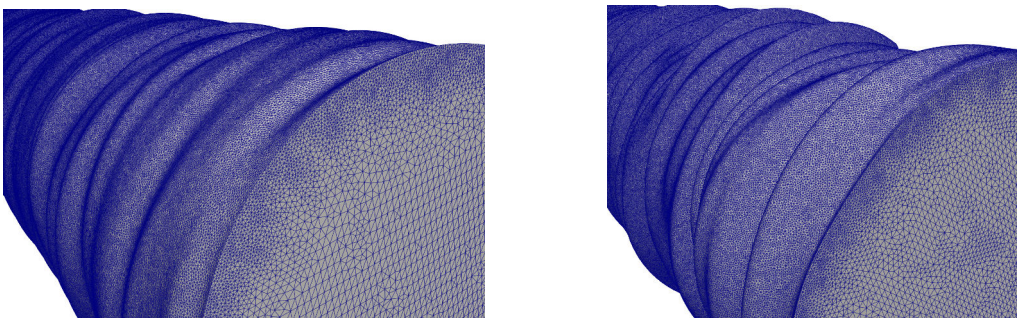

(a) $ES = 0.20$ (b) $ES = 0.62$

Figure 7.4 – Mesh M1 of the computational domain for cylindrical channels

7.1.3 Numerics

Incompressible flow simulations are performed. Like for previous simulations, the chosen target bulk Reynolds number range is the fully developed turbulent flow. This is why, RRLES are performed at $Re = 5\ 000$, $Re = 8\ 000$, $Re = 17\ 000$ and $Re = 25\ 000$. The fluid kinematic viscosity is set to $\nu = 1.517 \times 10^{-5}\ m^2/s$, and the maximal CFL number used equals 0.8. The WALE subgrid-scale model is retained as it is widely used for LES of boundary layer flows [61]. A fourth-order central finite-volume scheme is used, and the four-step fourth-order scheme TFV4A is applied for velocity and scalar transport prediction [66].

7.1.4 Results

Square configurations

A first qualitative analysis can be done by visualizing the velocity inside the computational domain. In Fig. 7.5, the mean velocity field is shown for the case $ES = 0.20$ with a slice selected in the middle of the channel. The white line represents the recycling plane location. The latter is well-located, as the outlet does not influence the mean flow. From this figure, it can be checked that a turbulent Poiseuille flow can be noticed.

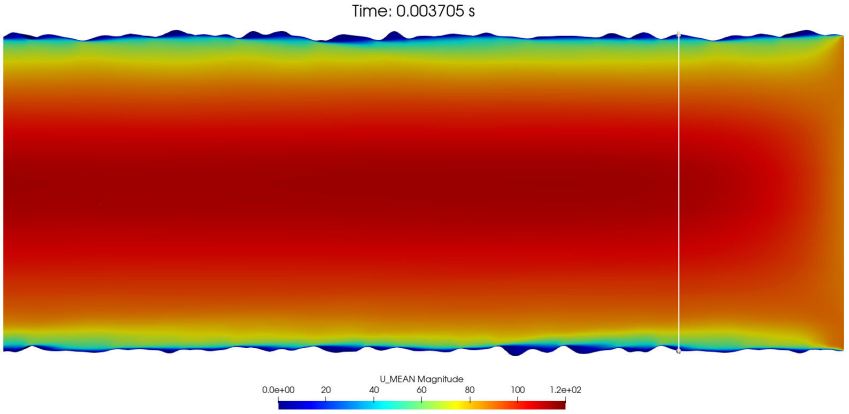

Figure 7.5 – Mean streamwise velocity ($ES = 0.20$ at $Re = 8\ 000$)

About the Fig. 7.6, roughness has an expected impact on the instantaneous velocity field. The boundary layer is clearly modified, especially near the peaks. The wavelengths of velocity

fluctuations close to the wall appear to be close to those of the roughness. With this view though, the influence of the spanwise sides is not visible here.

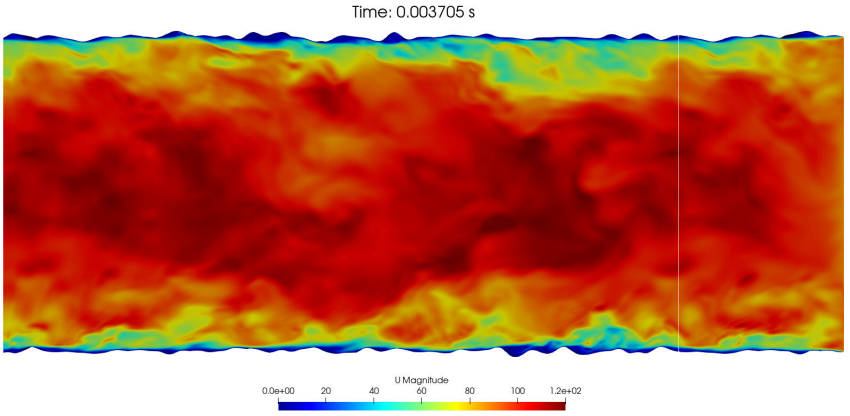

Figure 7.6 – Instantaneous velocity streamwise ($ES = 0.20$ at $Re = 8\,000$)

A crosswise slice selected at the center of the channel is then shown in Fig. 7.7. Concerning the mean velocity, roughness on each wall induces a non-uniform field compared to smooth walls. Interestingly, even with few peaks and valleys at this location in the channel, the velocity is significantly impacted in some regions. This phenomenon is more noticeable in the instantaneous field. Indeed some recirculation zones seem to emerge, particularly on the left wall and at the top right corner.

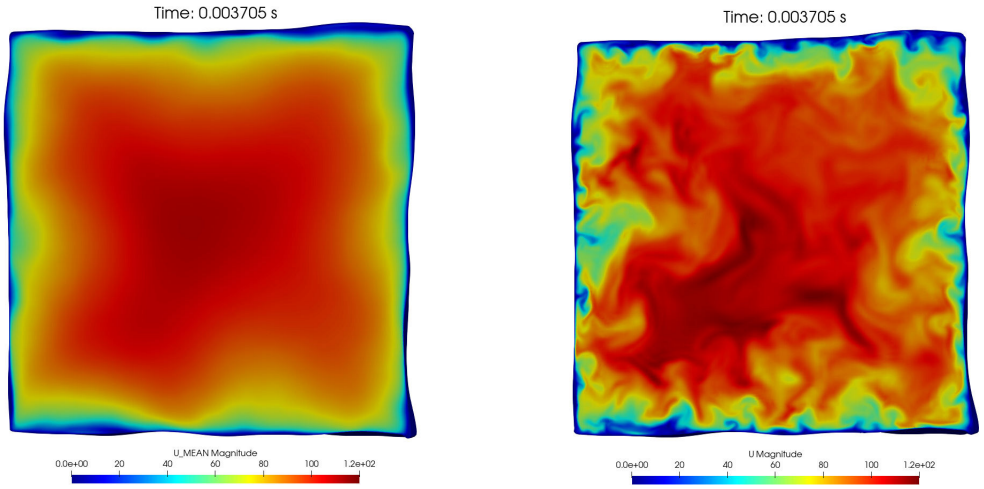

(a) Mean velocity

(b) Instantaneous velocity

Figure 7.7 – Crossview of the velocity field ($ES = 0.20$ at $Re = 8\,000$)

Re	5 000	8 000	17 000	25 000
ES=0.20	1.39×10^{-2}	1.45×10^{-2}	1.42×10^{-2}	1.50×10^{-2}
ES=0.62	4.27×10^{-2}	4.24×10^{-2}	4.24×10^{-2}	4.43×10^{-2}

Table 7.6 – Friction factor values depending on the Reynolds number

For a more quantitative analysis, the friction factor was calculated for both cases and all tested Reynolds numbers. First, values are higher for the $ES = 0.62$ case than for the other as expected. In addition, a ratio of around three between $ES = 0.62$ and $ES = 0.20$ is noticeable. Then the second remark is that the order of values is retrieved compared to previous results with open channel configurations. Thus spanwise sides are not required to get similar results in terms of friction factor. Finally, values remain almost constant with the Reynolds number increase. The latter could be explained by the fact that the plateau on the Moody diagram is reached.

Cylindrical channels

A similar analysis is conducted for cylindrical configurations. Mean and instantaneous velocity fields are presented for $ES = 0.62$ in Fig. 7.8 as this is the case where the roughness has the greatest impact.

In this figure, due to the geometry, one can immediately notice two entanglements in the channel. This is due to a peak in the channel, and the boundary layer modification is therefore more pronounced for cylinders than for open or square channels. Concerning additive manufacturing channels, this phenomenon should then be taken into account when pieces are printed.

Otherwise, as this case is in the dense regime for roughness, recirculation zones between peaks and valleys do almost not exist. Injection of fluid flow in valleys and ejection from the latter is limited.

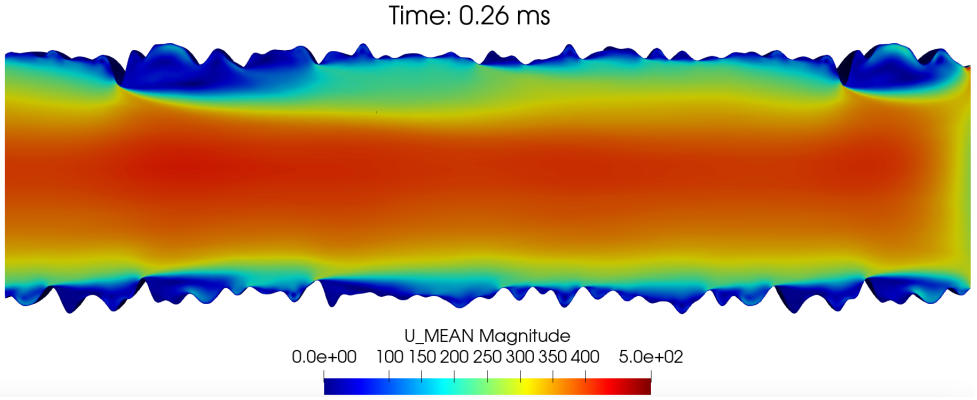

(a) Mean

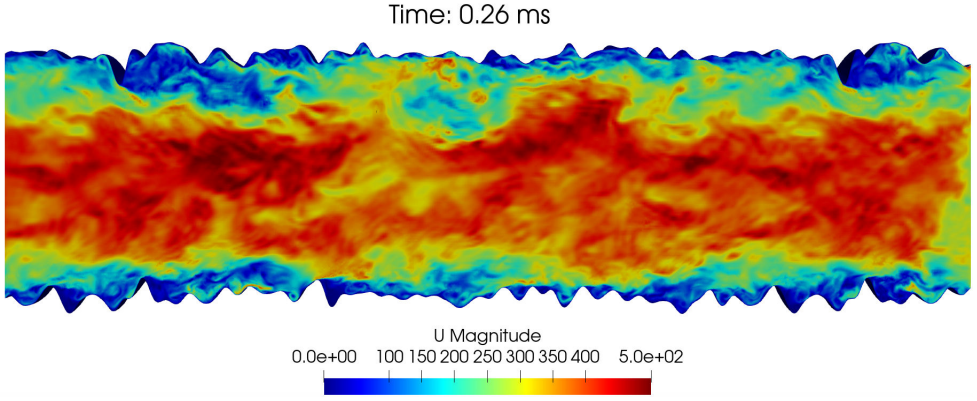

(b) Instantaneous

Figure 7.8 – Velocity fields for cylindrical channels ($ES = 0.62$ at $Re = 8\,000$)

A slice at the channel center is here also presented in Fig. 7.9. The field is clearly non-uniform

and roughness before this location directly impacts the field. Although the roughness at this slice is not such important, some vortices are likely to be created near the wall.

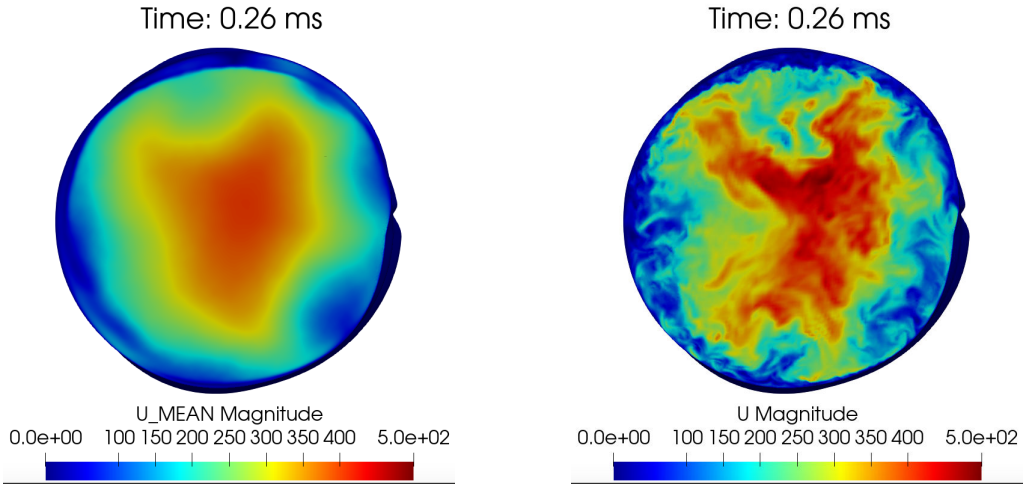

(a) Mean

(b) Instantaneous

Figure 7.9 – Crossview of the velocity magnitude field

Friction factor is summed up in Tab. 7.7. In comparison with square cases, values are clearly higher for cylindrical configurations. Indeed entanglement is more likely to appear and roughness has then a greater impact.

Previous remarks concerning square channels are also valid for these configurations: higher values for higher effective slope, almost a plateau reached with increasing Reynolds number but not for $ES = 0.62$ and a ratio of around three between both cases.

Re	5 000	8 000	17 000	25 000
ES=0.20	5.00×10^{-2}	5.03×10^{-2}	5.05×10^{-2}	5.10×10^{-2}
ES=0.62	15.8×10^{-2}	16.1×10^{-2}	16.6×10^{-2}	16.9×10^{-2}

Table 7.7 – Friction factor values depending on the Reynolds number for cylindrical cases

7.1.5 Conclusions

Roughness-resolved LES have been performed for square and cylindrical channels with the same effective slope values. As expected, results for square channels are close to those obtained with open channels. Therefore for modeling purposes, open channels appear sufficient for this kind of configuration.

For cylinder tubes, roughness seems to have a more pronounced impact on flow topology as well as on the friction factor. Indeed entanglements can be produced when pieces are additive manufactured, and printing direction has then to be taken into account.

7.2 Plate with finned tubes

7.2.1 Context

Fin-and-tube heat exchangers have a wide range of applications, and many investigations have been conducted on such heat exchangers. Early, the heat transfer was found by Zukauskas [177]

to stem in the majority from the pins and not from the endwalls. As illustrated in Fig. 7.10, both in-line and staggered arrangements were considered by this author.

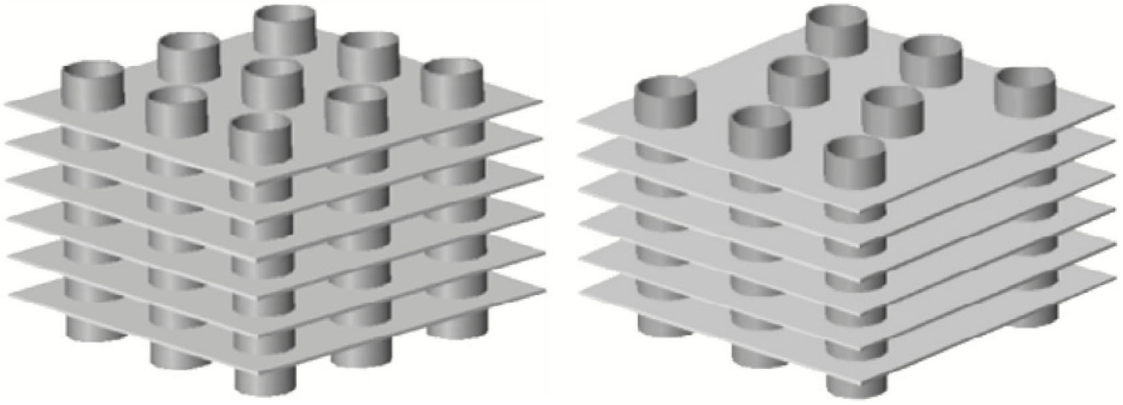

(a) In-line arrangement (b) Staggered configuration

Figure 7.10 – Plate and finned tube heat exchangers [178]

Afterwards, VanFossen [179] has constrained the pin height-to-diameter ratio (F_p/D) between 0.5 and 2. The author found that the magnitude of heat transfer was higher from the endwalls. For a ratio $F_p/D = 1$, Kirsch and Thole [180] studied pin fins made by additive manufacturing. The roughness induced by this manufacturing process was then found to boost heat transfer in comparison to analogous smooth geometries. The impact of the streamwise L_p spacing of pins was evaluated by Metzger *et al.* [181]. A decrease in streamwise spacing with $1.5 < L_p/D < 5$ was found to augment the heat transfer conspicuously.

Numerous investigators have strived to find correlations for heat transfer and the friction factor on such geometries. Gray and Webb [182] proposed such correlations and paid attention to the prediction capability of the friction factor. For plate finned-tube heat exchangers with staggered arrangement, some are available, like ones developed by Kim *et al.* [183] or by Wang *et al.* [184] (2000). One should notice that the latter was developed for tube diameters greater than 6 mm, limiting the range of applicability. Regarding correlations, particularly for the Nusselt number and for pin fins i.e. small tube diameters, Metzger *et al.* [181] developed one based on the streamwise spacing and pin diameter Reynolds number Re_{D_c}.

Some numerical studies have been performed like Bhuiyan *et al.* [178] who conducted RANS simulations for plain fin tube heat exchangers with in-line and staggered arrangements. They found a reasonable agreement with Wang's correlation [185]. In addition, they also investigated multiple characteristic lengths such as fin pitch F_p, longitudinal L_p and transversal T_p tube pitches.

Whereas all previously cited correlations were developed for smooth configurations, such ones for heat transfer with turbulent flow inside rough channels are rare and even rarer with additive-manufactured coupons. Stimpson *et al.* [156] proposed a correlation for the Nusselt number but it was developed for finned plate heat exchangers made by additive manufacturing. More recently, nonetheless, Corbett *et al.* [186] studied several additive-manufactured pin fins configurations and especially tube fins (cf Fig. 7.11 and Fig. 7.12). Metzger's correlation appeared to underestimate Nu_{D_c} for experimental data. This is why they have elaborated a correlation but only for the Nusselt number Nu_{D_c} and not for the friction factor. The latter seems to be adequate for the considered geometry in this report. Kirsch and Thole [180] did not elaborate a correlation but a comparison with their experimental data is possible. Indeed their coupons were made with additive manufacturing and their geometric lengths appear to be close to ours.

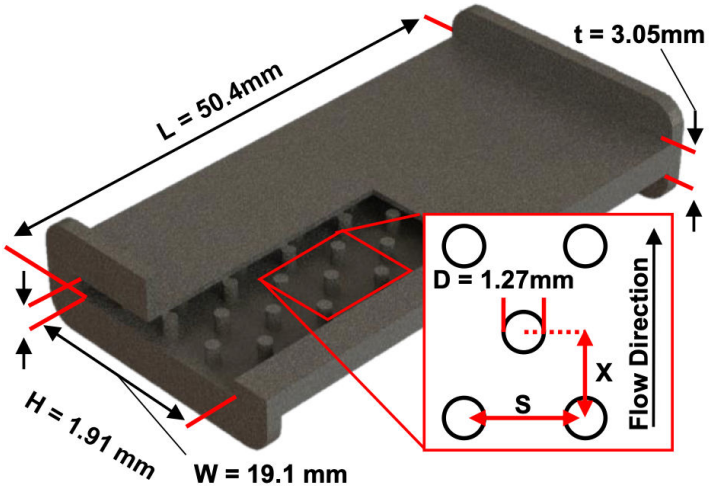

Figure 7.11 – Configuration of test coupons from [186]; corresponding notations in the manuscript $H \rightarrow F_p$, $X \rightarrow L_p$, $S \rightarrow T_p$

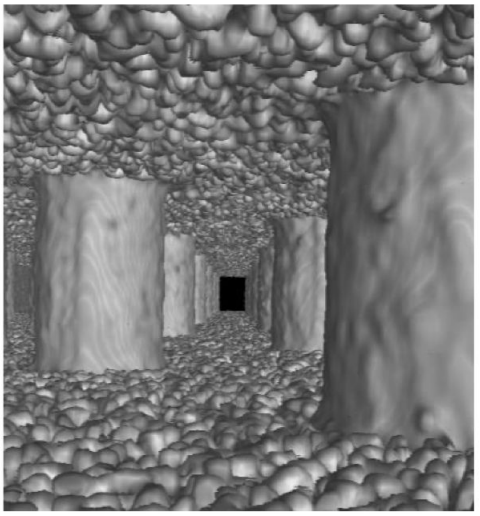

Figure 7.12 – Computed tomography (CT) scan of staggered tube fins heat coupon [186]

7.2.2 Numerical setup

Configuration

In order to compare with RANS results provided by the industrial partner TEMISTh, the chosen geometry is similar. To sum up, different fin types are available for finned tube heat exchangers. In addition, two kinds of arrangement exist for fins, either linear or staggered. The latter was chosen by TEMISTh, hence roughness-resolved LES (RRLES) for this geometry.

Dimensions of the computational domain are set to $6.4\ mm$ x $4.8\ mm$ x $1\ mm$ respectively in the streamwise, spanwise, and crosswise directions. In addition, several geometrical parameters must be prescribed for this configuration: internal and external fin diameters, fin thickness, fin pitch, longitudinal, and transversal tube pitches.

For simplicity, the fin thickness δ_f is considered null. Thus internal and external fin diameters are assumed to be the same. The transversal tube pitch and fin pitch correspond to the domain's

spanwise and crosswise lengths. With the aim of avoiding a tremendous number of cells for the mesh and in order to limit CPU hours consumption, the domain and geometrical sizes have been reduced compared to those fixed with the TEMISTh geometry, particularly fin diameter and pitch. With the developed recycling method shown in Chapter 5, the computational domain size requirements are lower than for RANS simulations that have been performed. These values are summarized in Tab. 7.8 and are illustrated in Fig. 7.13.

Parameter	Value
Streamwise length (L)	6.4 mm
Spanwise length (l)	4.8 mm
Crosswise length (H)	1.0 mm
Fin diameter ($D = D_c$)	1.1 mm
Fin pitch ($F_p = H$)	1.0 mm
Longitudinal tube pitch (L_p)	3.2 mm
Transversal tube pitch (T_p)	4.8 mm

Table 7.8 – Geometrical parameters values

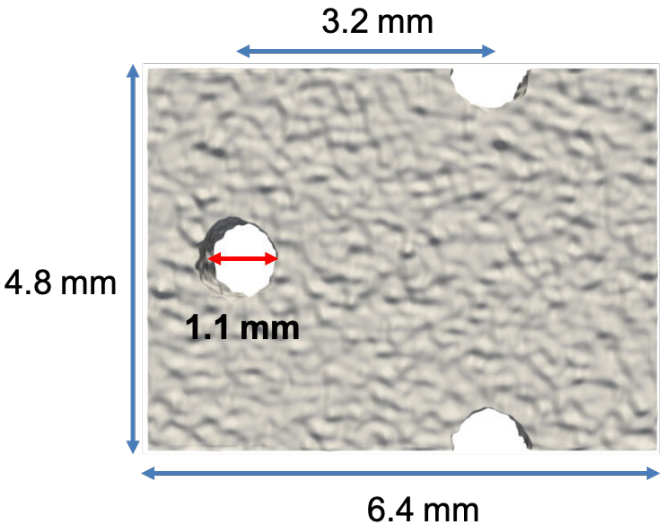

Figure 7.13 – Top view of the computational domain

Due to a fin thickness δ_f considered null, the fin collar outside diameter $D_c = D + 2\delta_f$ is equal to D. Regarding length characteristics, this geometry is likely a pin fin geometry with a staggered arrangement. The hydraulic diameter D_h is equal to $D_h = 1.47\ mm$ and is calculated in the following equations (7.3 - 7.5).

$$D_h = \frac{4A_c.L}{A_0} \tag{7.3}$$

with A_c the minimum cross sectional area (m^2), A_0 the exterior heat transfer area (m) and N the number of tube rows. In our case, N is set to 2.

$$A_c = l \times H - D \times H \tag{7.4}$$

$$A_0 = 2(L \times l) + N\left(\pi D \times H - \left(2\pi\frac{D^2}{4}\right)\right) \tag{7.5}$$

Concerning the roughness, it was chosen to set an additive manufacturing-like isotropic roughness. In addition, the same roughness is applied on planar surfaces and the tube fins. Thus the root-mean-square roughness height, the skewness and the kurtosis are respectively equal to $S_q = 18\ \mu m$, $Sk = 0.2$ and $Ku = 4.0$. With these parameters, the effective slope is then $ES = 0.17$. It should be noted that the total wetted surface A_{tw} is then more significant than A_0 due to the roughness and the ratio is $A_{tw}/A_0 = 1.05$.

All surfaces are generated via the Rough Surface Generator (RSG) presented in detail in Chapter 4. A view of the final geometry is shown in Fig. 7.14.

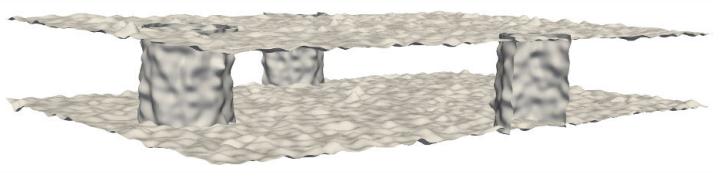

(a) Interior of the computational domain

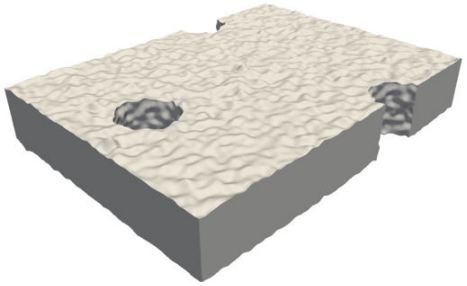

(b) Closed computational domain

Figure 7.14 – Final geometry: plate/tube fins

Even if characteristic lengths have been provided, a calculation of some ratios of these lengths is important for comparison with experimental correlations. Indeed, there are constraints on the applicability domain for these latter correlations. The ratios for our geometry are presented in Tab. 7.9

Parameter	**Value**
T_p/D_c	4.36
L_p/D_c	2.91
F_p/D_c	0.91
T_p/L_p	1.5

Table 7.9 – Geometrical parameters values

7.2.3 Meshes

As for previous configurations, two meshes have been generated. The number of cells in each direction for the initial cartesian mesh is chosen as the cell size is equal to 20 μm.

The main difference between both mesh configurations ($M1$ and $M2$) is the cell size on the surface. Indeed for M1, the imposed cell size is 10 μm and 7 μm for M2. Characteristics of meshes are presented in Tab. 7.10.

A view of the finer mesh is presented in Fig. 7.15. One can remark that the rough surface is well-discretized. Meshing performances are here also given in Tab 7.11.

Mesh	**Initial** N_x, N_y, N_z	**Cell size on STL**	**Max cell size gradient**	**Number of elements**
M1	320 ; 240 ; 200	10 μm	0.3	49 M
M2	320 ; 240 ; 200	7 μm	0.3	66 M

Table 7.10 – Characteristics of the two meshes

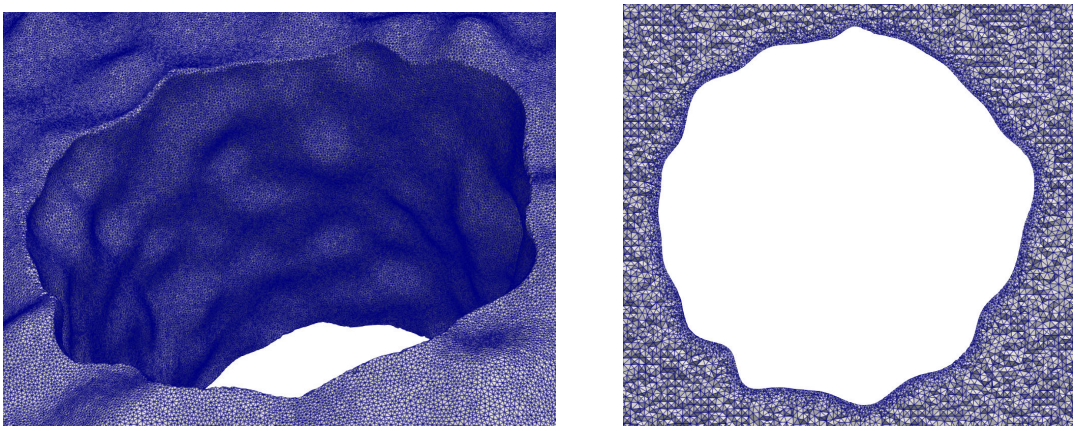

(a) Zoom-in on the full tube

(b) Slice of the full tube

Figure 7.15 – Mesh M2 of the computational domain

Meshing performance are assessed in Tab. 7.11. It should be noticed that the CPU hours are slightly higher than previously observed. Indeed the mesh generator (RRMG), detailed in Chapter 4, was enhanced and is more robust. However, the required CPU hours are moderately increased.

	Number of cells	Number of CPUs	CPU hours	RAM/CPU
M1	49 M	1024	4150	550 Mb
M2	66 M	2560	6050	114 Mb

Table 7.11 – Meshing performance

7.2.4 Correlations and performance index

This section details the different tools used for the subsequent analysis of the RRLES.

Global parameters

As a reminder, for scaling velocity and temperature profiles, a calculated effective distance introduced by Kuwata & Kawaguchi [146] is used. Indeed, due to irregularities of the surface height, this kind of distance is not straightforward to determine as in a smooth-wall case. The effective distance is defined in Eq. 7.6 with h_w the minimal height of the surface. The variable φ corresponds to the x-y plane porosity, which is the ratio between the x-y plane surface occupied by the fluid and the total x-y plane area.

$$h_e = \int_{h_w}^{h} \varphi \, dh \tag{7.6}$$

Computation of the friction velocity u_τ (Eq. 7.7) is based on the difference between average pressure at the inlet and at the recycling plane as exposed in Fig. 7.16. The shear Reynolds number is then calculated as $Re_\tau = \frac{u_\tau H}{\nu}$. and the quantity h_e^+ is defined as $h_e^+ = \frac{h_e u_\tau}{\nu}$.

$$u_\tau = \sqrt{H \frac{\langle p_i \rangle - \langle p_r \rangle}{\rho L}} \tag{7.7}$$

Concerning the friction factor, the Fanning definition $f = 2\left(\frac{u_\tau}{U_b}\right)^2$ is used with U_b the bulk velocity. All these quantities are monitored at each iteration in the LES simulation.

Comparison to experimental data about friction

Basically, there are two definitions of the friction factor, which are Darcy's and Fanning's definitions. The relationship between them is a factor of 4: $f_{Darcy} = 4 f_{Fanning}$. Among all articles and correlations, both are used independently and one has to be aware of which definition is used.

In order to compare friction factor values from these RRLES to experimental data, some correlations are considered. To avoid confusion, the following correlations are detailed and the used definition is given. However, all results will be presented with the Fanning definition.

1. The correlation valid for finned tube heat exchangers taken as reference for RANS simulations by TEMISTh is Wang's one [184]. However, our length characteristics in this report are out of the correlation's applicability domain, notably the tube diameter which should be greater than 6 mm. The friction factor from this correlation is calculated via Eq. 7.8 and Eq. 7.9. Here, the factor is calculated through the Darcy definition. The applicability domain is valid for the following restrictions:

   - $1.19\ mm \leq F_p \leq 8.7\ mm$
   - $6.35\ mm \leq D \leq 12.7\ mm$
   - $1.3\ mm \leq D_h \leq 9.37\ mm$
   - $12.4\ mm \leq L_p \leq 27.5\ mm$
   - $17.7\ mm \leq T_p \leq 31.75\ mm$
   - $1 \leq N \leq 6$ (number of fin rows)

$$f_{Wang} = 0.0267 Re_{D_c}^{F1} \left(\frac{T_p}{L_p}\right)^{F2} \left(\frac{F_p}{D_c}\right)^{F3} \tag{7.8}$$

with

$$\begin{aligned} F1 &= -0.764 + 0.739\frac{T_p}{L_p} + 0.177\frac{F_p}{D_c} - \frac{0.00758}{N} \\ F2 &= -15.689 + \frac{64.021}{\ln(Re_{D_c})} \\ F3 &= 1.696 - \frac{15.695}{\ln(Re_{D_c})} \end{aligned} \tag{7.9}$$

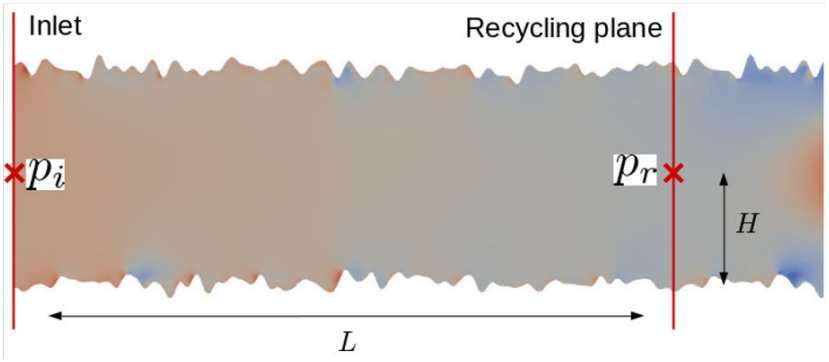

Figure 7.16 – Principle of the calculation of the friction velocity

2. Another one, which was elaborated for smooth fin-and-tube configuration with staggered arrangement, is Kim's one [183]. Additionally, considering the ratio between transversal T_p and longitudinal L_p tube pitches and the ratio between fin pitch F_p and the tube diameter, this correlation relies also on relative endwalls A_w and tube A_t areas to the total wetted surface A_0. The factor corresponds here to the Fanning definition, and the correlation is valid within ± 10 % with the following conditions:

   - $505 \leq Re_{D_c} \leq 19766$
   - $0.857 \leq T_p/L_p \leq 1.654$
   - $1.996 \leq T_p/D_c \leq 2.881$
   - $0.081 \leq F_p/D_c \leq 0.641$

$$f_{Kim} = f_w \frac{A_w}{A_0} + f_t \left(1 - \frac{A_w}{A_0}\right)\left(1 - \frac{\delta_f}{F_p}\right) \tag{7.10}$$

with $A_w = 2(L \times l) - N\left(2\pi \frac{D^2}{4}\right)$ and where

$$f_t = \frac{4}{\pi}\left(0.25 + \frac{0.118}{\left[\frac{T_p}{D_c} - 1\right]^{1.08}} Re_{D_c}^{-0.16}\right)\left[\frac{T_p}{D_c} - 1\right] \tag{7.11}$$

$$f_w = 1.455 Re_{D_c}^{-0.656} \left(\frac{T_p}{L_p}\right)^{-0.347} \left(\frac{F_p}{D_c}\right)^{-0.134} \left(\frac{T_p}{D_c}\right)^{1.23} \tag{7.12}$$

3. Even if no correlation is provided, the friction factor will also be compared to the results from Kirsch and Thole [180]. Geometric characteristics are quite similar to ours, especially the coupon with $L_p/D_c = 2.6$ and $T_p/D_c = 4$. Indeed, for our geometry, $L_p/D_c = 2.91$ and $T_p/D_c = 4.36$. In addition, they studied additive-manufactured coupons. In their article, they used Fanning's definition.

Heat transfer

For the analysis of heat transfer, a normalized passive temperature $\bar{Z}$ is used. This latter can be defined as $\bar{Z} = \frac{\bar{T} - T_p}{T_\infty - T_p}$ with T_p the temperature imposed at a wall and T_∞ the bulk temperature.

This scalar is considered passive and this hypothesis is valid if the temperature difference has no significant impact on the density, which is assumed here. This is why the temperature can be replaced by this dimensionless scalar. The equation for this scalar is the following:

$$\frac{\partial \bar{Z}}{\partial t} + \nabla \cdot (\bar{u}\bar{Z}) = \nabla \cdot (D_z \nabla \bar{Z}) \tag{7.13}$$

The laminar Prandtl number Pr of this scalar is set to $Pr = 0.71$, and the turbulent Prandtl number is equal to unity. The diffusivity D_z includes the molecular and turbulent diffusivities.

For a deeper analysis of thermal behavior, the Colburn factor j is used in addition to the Nusselt number, which is computed. This factor is defined as in Eq. 7.14 and the definition of the Nusselt number is given in Eq. 7.15 with h the convective heat transfer coefficient of the flow and λ the thermal conductivity of the fluid.

$$j = \frac{Nu}{Re_{Dh} Pr^{1/3}} \tag{7.14}$$

$$Nu_{D_h} = \frac{h D_h}{\lambda} \tag{7.15}$$

In our case, the Nusselt number Nu_{D_h} is the total wetted surface averaged and computed through the Eq. 7.16 with $\bar{Z}_{ref} = 0.5$.

$$\begin{aligned} Nu_{LES} &= \frac{|\nabla \bar{Z}|_{wall} D_h}{\bar{Z}_{ref} - \bar{Z}_{wall}} \\ Nu_{D_h} &= \frac{1}{A_0} \int_{\partial\Omega} Nu_{LES} dS \end{aligned} \tag{7.16}$$

Some experimental correlations are obviously taken as a reference for comparison. One should notice that all the empirical correlations, which are presented hereafter, are for a Nusselt number based on the tube diameter (Nu_{D_c}). This is why both Nusselt numbers will be presented.

1. The Wang correlation [184] is computed with the Eq. 7.17

$$j_{Wang} = 0.086 Re_{D_c}^{P3} N^{P4} \left(\frac{F_p}{D_c}\right)^{P5} \left(\frac{F_p}{D_h}\right)^{P6} \left(\frac{F_p}{T_p}\right)^{-0.93} \tag{7.17}$$

where

$$\begin{aligned} P3 =& -0.361 - \frac{0.042N}{\ln(Re_{D_c})} \\ &+ 0.158 \ln\left(N \left(\frac{F_p}{D_c}\right)^{0.41}\right) \\ P4 =& -1.224 - \frac{0.076 \left(\frac{L_p}{D_h}\right)^{1.42}}{\ln(Re_{D_c})} \\ P5 =& -0.083 + \frac{0.058N}{\ln(Re_{D_c})} \\ P6 =& -5.735 + 1.21 \ln\left(\frac{Re_{D_c}}{N}\right) \end{aligned} \tag{7.18}$$

2. Kim's one [183] is valid for $591 \leq Re_{D_c} \leq 14430$ and is described in Eq. 7.19 -7.20. The applicability domain is quite different for the Colburn factor in comparison to the friction factor:

   - $591 \leq Re_{D_c} \leq 14430$
   - $1.154 \leq T_p/L_p \leq 1.654$
   - $2.399 \leq T_p/D_c \leq 2.877$
   - $0.135 \leq F_p/D_c \leq 0.300$

$$\frac{j_{N_{\text{row}}=1,2}}{j_{N_{\text{row}}=3}} = 1.043 \left[Re_{D_c}^{-0.14} \left(\frac{T_p}{L_p}\right)^{-0.564} \left(\frac{F_p}{D_c}\right)^{-0.123} \left(\frac{T_p}{D_c}\right)^{1.17} \right]^{(3-N_{\text{row}})} \tag{7.19}$$

   with

$$j_{N_{\text{row}}=3} = 0.163 Re_{D_c}^{-0.369} \left(\frac{T_p}{L_p}\right)^{0.106} \left(\frac{F_p}{D_c}\right)^{0.0138} \left(\frac{T_p}{D_c}\right)^{0.13} \tag{7.20}$$

   For the two latter correlations, Nusselt numbers will be computed from the result of respective Colburn factors j_{Wang} and j_{Kim}.

3. Metzger's correlation [181]. The range is $1 \leq L_p/D \leq 5$, $T_p/D = 2.5$ and $F_p/D = 1$.

$$Nu_{Metzger} = 0.135 Re_{D_c}^{0.69} \left(\frac{L_p}{D_c}\right)^{-0.34} \tag{7.21}$$

4. Correlation from Corbett *et al.* [186]. Here the range is $2 \leq L_p/D \leq 4$, $3 \leq T_p/D \leq 4$, $F_p/D = 1.5$ and $0.011 \leq S_a/D_h \leq 0.015$.

$$Nu_{Corbett} = 0.127 \left(16.22 \left(\frac{Ra}{D_h}\right)^{0.752} + 1\right) Re_{D_c}^{0.657} \left(\frac{L_p}{D_c}\right)^{-0.066} \left(\frac{T_p}{D_c}\right)^{0.054} \tag{7.22}$$

5. Like for the friction factor, Nusselt numbers will be compared to the ones obtained by Kirsch and Thole [180].

Thermal performance

The condition at which a channel provides as low as possible friction loss along with as high as possible heat transfer rate is an important issue. Consequently, heat transfer from the channel and friction loss must be considered.

This is why a thermal performance index η_{th} is calculated. This index is derived from Gee and Webb [187] and is given via the equation 7.23.

$$\eta_{th} = \frac{Nu_{D_h}/Nu_0}{(f/f_0)^{1/3}} \tag{7.23}$$

There is a global agreement about how to compute the reference friction factor f_0. The Darcy friction factor f_0 is estimated from the Colebrook equation (Eq. 7.24). For additive manufacturing,

Stimpson *et al.* [156] proposed a correlation between the equivalent roughness k_s/D_h with k_s the equivalent sand-grain roughness and the ratio S_a/D_h through the equation 7.25.

$$\frac{1}{\sqrt{f_0}} = -2.0 \log\left(\frac{k_s/D_h}{3.7} + \frac{2.51}{Re_{D_h}\sqrt{f_0}}\right) \tag{7.24}$$

$$\frac{k_s}{D_h} = 18\frac{S_a}{D_h} - 0.05 \tag{7.25}$$

The Colebrook equation Eq. 7.24 is then solved via an iterative procedure described by Praks and Brkic [188].

For the Nusselt number Nu_0, a correlation for a smooth empty duct is used. Nevertheless, there are some differences between articles on which reference correlation is the most appropriate. The most utilized one in articles addressing additive manufacturing is Gnielinski's correlation, described in Eq. 7.26.

$$Nu_{Gnielinski} = \frac{(f/8)(Re_{D_h} - 1000)Pr}{1 + 12.7\sqrt{f/8}(Pr^{2/3} - 1)} \tag{7.26}$$

with f the Darcy friction factor of a smooth duct (cf Eq. 7.24) and Pr the Prandtl number of air ($Pr = 0.71$).

7.2.5 Numerics

Working hypotheses

Incompressible flow simulations are performed, and the chosen target bulk Reynolds number range is the fully developed turbulent flow. Initially, RRLES were supposed to be performed at $Re_{D_h} = 5\,000$, $Re_{D_h} = 8\,000$ and $Re_{D_h} = 17\,000$. To limit the CPU hours, it was chosen not to conduct RRLES at $Re_{D_h} = 25\,000$. However, due to a computation error on the hydraulic diameter, actual values are respectively $Re_{D_h} = 9\,760$, $Re_{D_h} = 15\,610$ and $Re_{D_h} = 33\,170$. A Reynolds number Re_{D_c} based on the tube diameter of the fins is also used in correlations. For our cases, they correspond respectively to $Re_{D_c} = 7\,316$, $Re_{D_c} = 11\,704$ and $Re_{D_c} = 24\,865$.

The fluid kinematic viscosity is set to $\nu = 1.517\ 10^{-5}\ m^2/s$ and the maximal CFL number used is equal to 0.8. The WALE subgrid-scale model is retained as it is widely used for LES of boundary layer flows [61]. A fourth-order central finite-volume scheme is used, and the four-step fourth-order scheme TFV4A is applied for velocity and scalar transport prediction [66].

Initialization of simulations

Before running the simulations, an initialization is applied on the velocity and the dimensionless temperature $\bar{Z}$. A velocity of $128\ m/s$ is set at each node of the fluid domain. About temperature, $\bar{Z} = 1$ is fixed for the upper plate and the tubes, whereas $\bar{Z} = 0$ is applied for the lower plate and the fluid. The initialization is illustrated in Fig. 7.17.

Performance

Simulations are split into two distinct steps. The first one is to flush the transitional flow, and the second step's objective is accumulating the statistics. The times of each step, as well as the number of flow-through times (FTT), are summarized in Tab. 7.12.

A unit value of FTT corresponds to the time one fluid particle goes from the inlet to the outlet along a straight line. For this configuration, it is assumed that tubes do not affect the FTT.

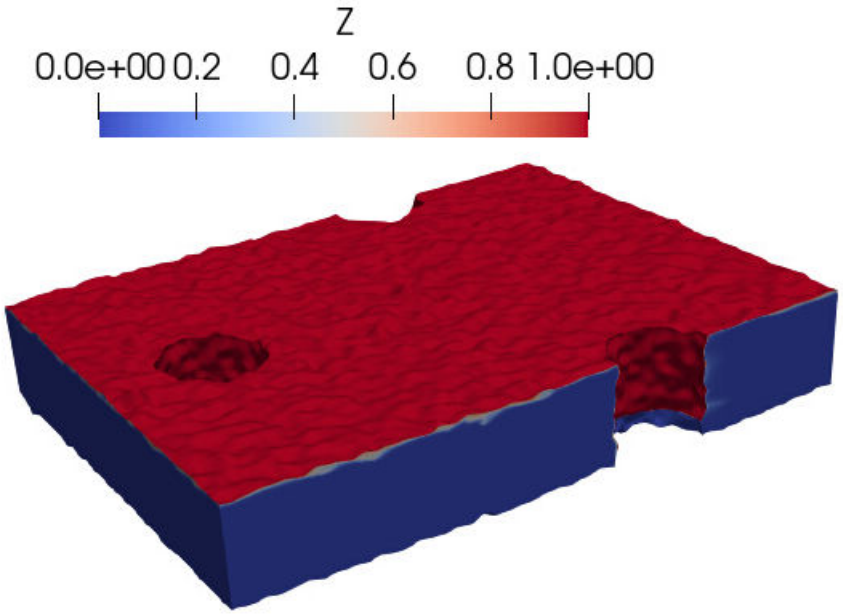

Figure 7.17 – Initialization for the normalized passive temperature $\bar{Z}$

Re_{D_h}	Init [ms]	Init Nbr. of FTT [-]	Stats [ms]	Stats Nbr. of FTT [-]
9 760	0.63	10.0	3.17	50.0
15 610	0.39	10.0	1.98	50.0
33 170	0.18	10.0	0.93	50.0

Table 7.12 – Time accumulation for statistics (Nbr. of FTT: number of flow-through time)

CPU costs for only the resolved-roughness LES are presented in Tab. 7.13. They are globally slightly lower for the mesh M1 than in previous reports as this mesh has fewer cells. However, as the time step between M1 and M2 was divided by around 3, the CPU hours are three times higher for M2 than for M1.

Mesh	Re_{D_h}	Cells	CPUs	CPU hours
M1	9 760	49 M	560	18 800 h
	15 610	49 M	560	18 100 h
	33 170	49 M	560	21 500 h
M2	9 760	66 M	560	60 200 h
	15 610	66 M	560	60 100 h
	33 170	66 M	560	64 000 h

Table 7.13 – Cost of simulations in CPU hours

7.2.6 Qualitative analysis

Results on the flow behavior, the impact on pressure loss through the friction factor, and the thermal impact via the Nusselt number are addressed in hereafter.

Flow visualization

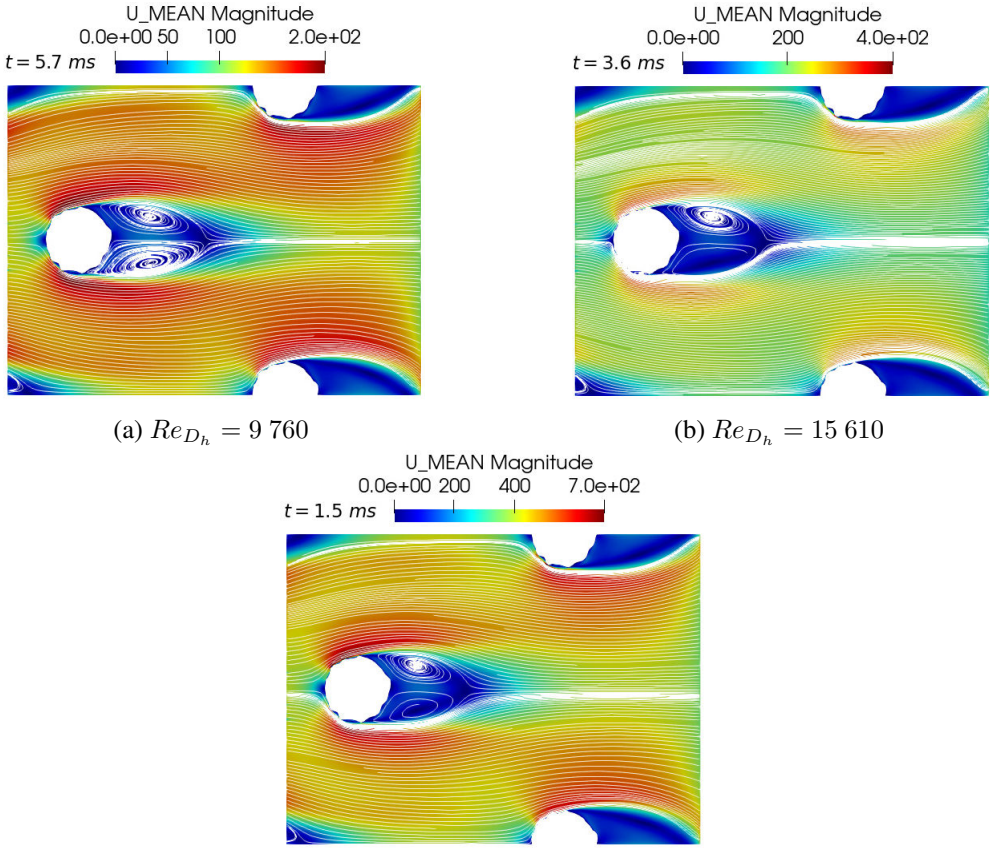

(a) $Re_{D_h} = 9\,760$ (b) $Re_{D_h} = 15\,610$

(c) $Re_{D_h} = 33\,170$

Figure 7.18 – Slices in the x-y plane at mid-height: mean velocity with streamlines (mesh M1)

First of all, the behavior of the flow can be described, and a qualitative analysis has to be made. Slices located in the middle of the channel inside the x-y plane are shown for the mesh M1 in Fig. 7.18. Globally, the flow characteristics of this type of configuration are naturally retrieved, like a stagnation point, acceleration, and weak zones with recirculation of the flow. The main difference between the different Reynolds numbers lies in a higher velocity and not in a variation of the behavior. However, the roughness implies some boundary layer separations and reattachments around tubes, as illustrated in Fig. 7.19.

In Fig. 7.20, the mean velocity field is plotted on slices at different locations along the channel. Fields observed in Fig. 7.18 are then observed along the channel height, acceleration, and weak zones are also significantly noticeable.

Temperature fields

As figures are similar between Reynolds numbers, the temperature fields are shown for $Re_{D_h} = 15\,610$ in Fig. 7.21. One can notice that good mixing is observed along the channel. The presence

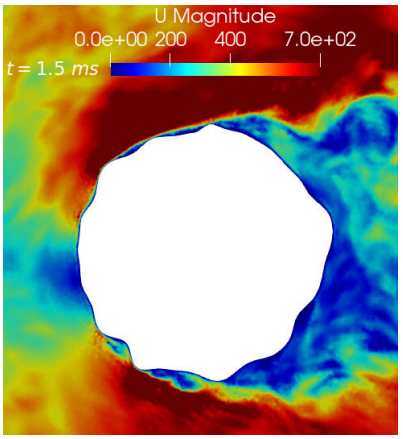

Figure 7.19 – Slice in the x-y plane at mid-height: zoom-in on the mean velocity around a tube, $Re_{D_h} = 33\ 170$ (mesh M1)

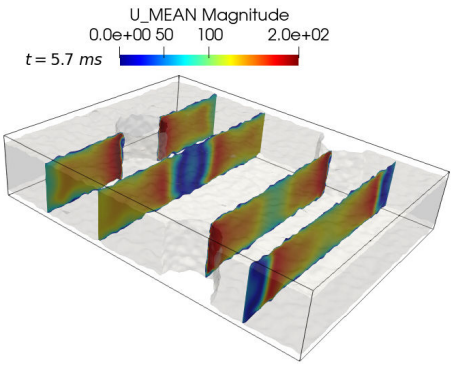

(a) $Re_{D_h} = 9\ 760$

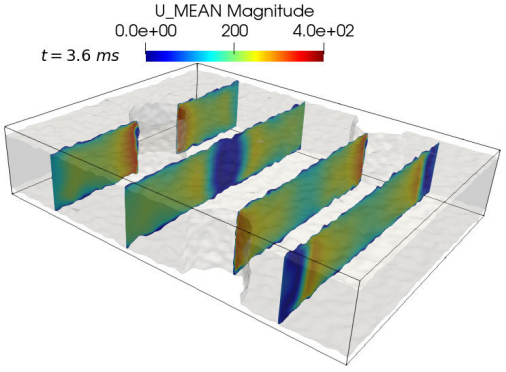

(b) $Re_{D_h} = 15\ 610$

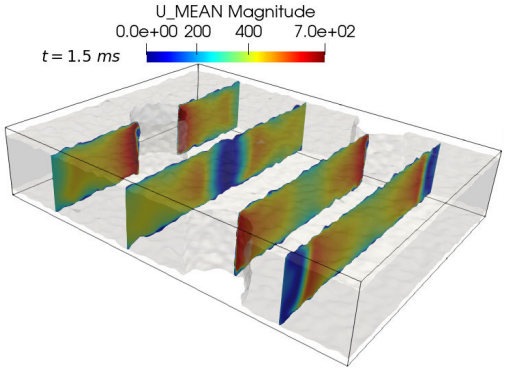

(c) $Re_{D_h} = 33\ 170$

Figure 7.20 – Slices from the top-view of the mean velocity (mesh M1)

of the tube fins helps in accelerating this mixing.

7.2.7 Pressure losses and heat transfer

For clarity and as results are similar between meshes M1 and M2, only the results for M2 are presented.

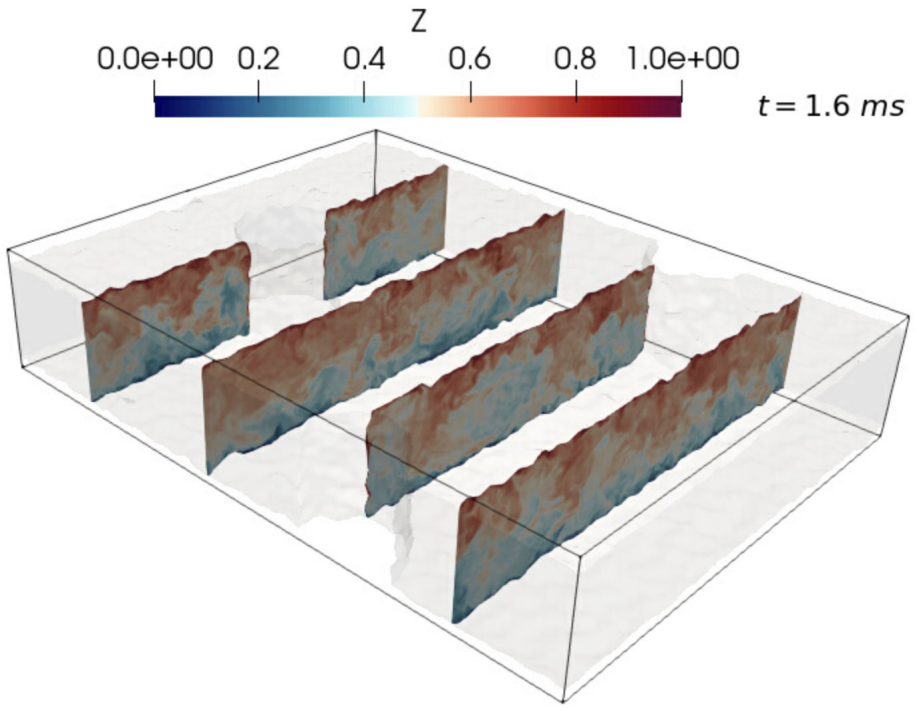

Figure 7.21 – Slices from the top-view of the instantaneous $\bar{Z}$ field at $Re_{D_h} = 15\,610$ (mesh M2)

Pressures losses described by the friction factor

Results are shown hereafter with the Fanning definition.

Re_{D_h}	9 760	15 610	33 170
LES	0.151	0.146	0.142
Wang [184]	1.036	0.918	0.811
Kim [183]	0.138	0.133	0.127

Table 7.14 – Friction factor values with Fanning definition

As expected for Wang's correlation, there is an overprediction for the friction factor. Indeed the characteristic lengths of our case are out of the scope of the applicability domain, and the correlation was elaborated for higher fin diameter.

A comparison with one case from Kirsch and Thole [180] is also done and values are shown in Fig. 7.22. The chosen case from this article is $T_p/D = 4$ and $L_p/D = 2.6$ because our relative lengths are close to these values: $T_p/D = 4.3$ and $L_p/D = 2.9$. However, their relative roughness $S_a/D_h = 0.039$ is higher than ours ($S_a/D_h = 0.01$). Friction factor from the Kim and the Colebrook (cf Eq. 7.24 and Eq. 7.25) correlations are also reported in Fig. 7.22.

First of all, Colebrook underpredicts correct values, as observed in previous reports and studies. Regarding Kim's correlation, the prediction seems to be good for Kirsch's results and our case, even though it is slightly underestimated. Even though the ratios T_p/D_c and F_p/D_c are higher than maximum correlation limits (respectively 2.881 and 0.641) in both cases, this relatively good agreement is observed for experimental results as well.

Then, surprisingly, our values are around 30% higher than the experimental results, although

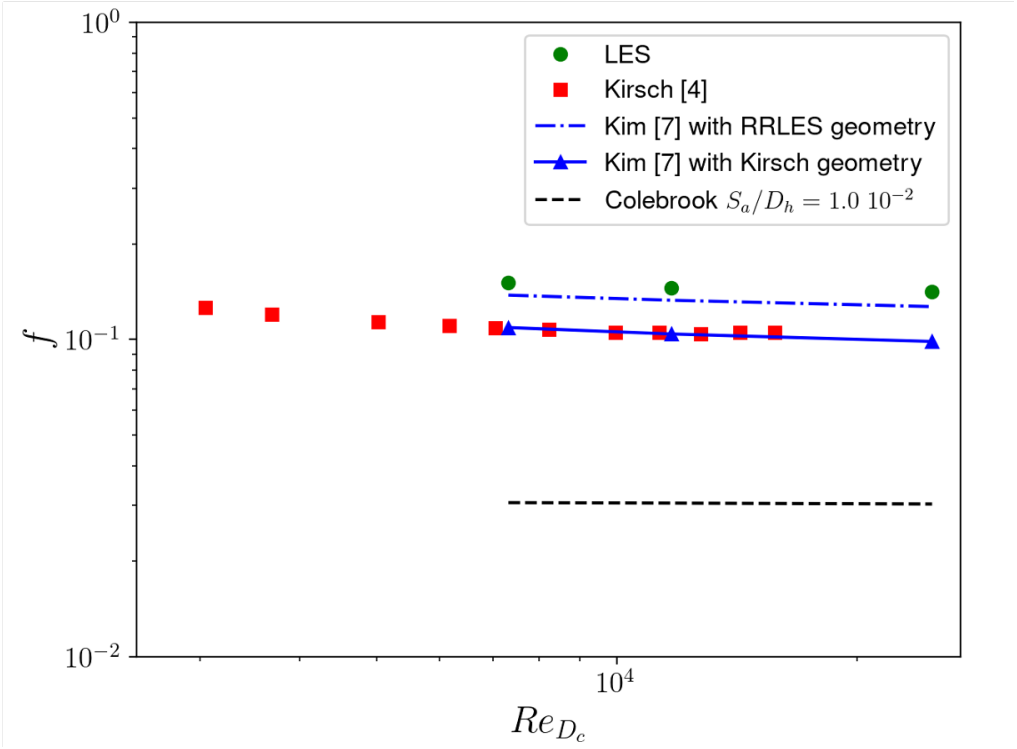

Figure 7.22 – Fanning friction values in comparison with Kirsch and Thole [180] data

our relative roughness is lower. In literature and as highlighted by Metzger *et al.*[189] (1982), at isovalue of L_p/D decreasing T_p/D leads to an increase of the friction factor. Contrariwise, at the isovalue of T_p/D, an increase of L_p/D induces growth of this factor. Compared to the experimental configuration, thus there is a combined effect: an increase of T_p/D_c (decrease of the friction factor) but also an increase of L_p/D_c (augmentation of the friction factor).

Roughness apart, Kim's correlation predicts an overall increase of the pressure losses with our geometrical parameters compared to this correlation used with geometrical lengths of Kirsch and Thole [180]. This leads to the conclusion that friction is more impacted by the configuration than by the roughness itself, at least for these considered cases.

In addition, a close look at the computed tomography scan (CT scan) of a channel, as shown in their article (cf Fig. 7.23), can provide a further explanation. The roughness at the pins is more significant in our case than actually printed by Kirsch and Thole [180]. This higher roughness on fins could also generate an increase in the friction factor and could explain a higher friction factor than predicted by Kim's correlation, hence a coherence between these experimental data and our values.

Impact on heat transfer

For estimating the heat transfer, the Nusselt number Nu_{D_c} is computed like detailed in section 7.2.4. Technically, the direct result from LES is a Nusselt number based on the hydraulic diameter, but for comparison purposes, the latter is rescaled to the tube pins' diameter. Values are given in Tab. 7.15 and plotted in Fig. 7.24.

Like for the friction factor, Wang's correlation is inadequate. For Kim's one, the maximum value for F_p/D_c is much lower than for the friction factor (0.3 instead of 0.641). Then this correlation can not also be taken into consideration.

The difference between what Corbett's correlation predicts and our values is clearly visible. In

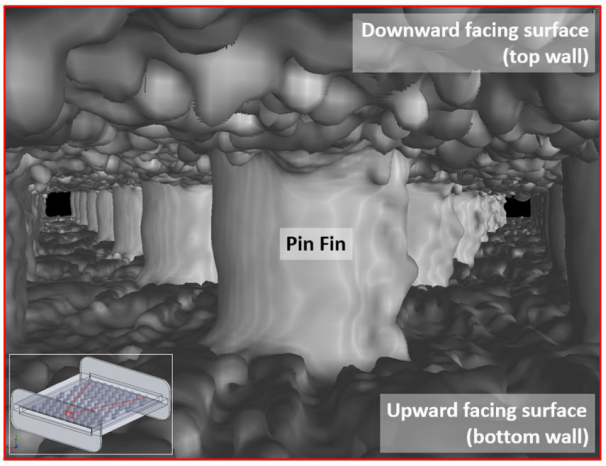

(a) 3D rendering of inside the channel of a case

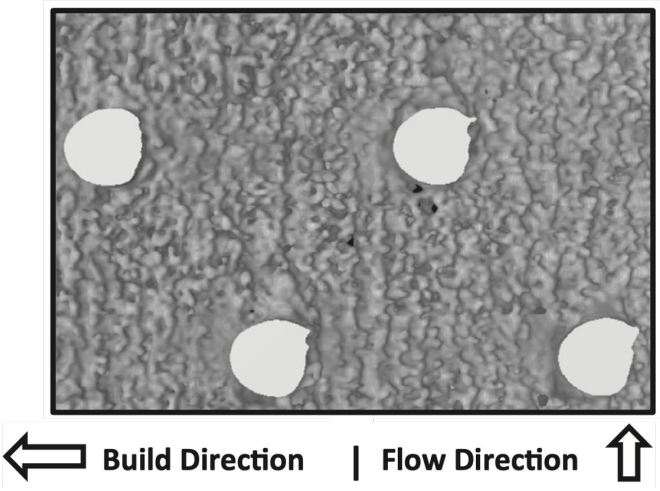

(b) Top down view of the reference case

Figure 7.23 – Computed tomography scans of as-built coupons (from Kirsch and Thole [180])

Re_{D_h}	9 760	15 610	33 170
Nu_{D_h} LES	64.61	86.12	118.69
Nu_{D_c} LES	48.43	64.56	88.97
Metzger [181]	43.55	60.23	101.3
Corbett [186]	67.22	91.53	150.1

Table 7.15 – Nusselt number Nu_{D_c} values from RRLES and from experimental correlations

addition, our results are in relatively good agreement with Metzger's correlation which was established for smooth channels. This suggests that our surfaces need to be rougher in comparison to experimental additive-manufactured coupons. Indeed, the ratio between our rough wetted surface and smooth wetted surface is only 1.05. This ratio seems to be higher for Kirsch and Thole [180] channels hence a heat transfer enhancement.

Whereas geometrical aspects are more significant for friction factor, this is the contrary for the heat transfer. The roughness plays thereby a key role in the latter point.

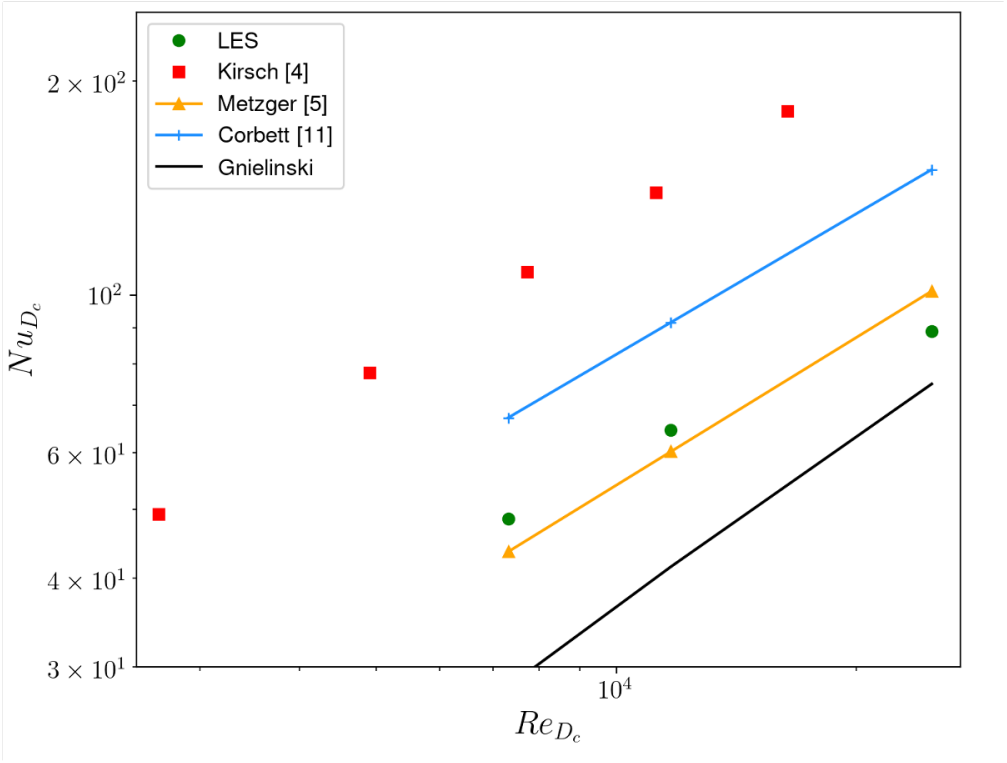

Figure 7.24 – Values of Nu_{D_c} from RRLES and experimental data

Thermal performance

As explained above, the thermal performance is evaluated through the efficiency index η_{th}. Results are given in Tab 7.16 and intermediate values like f_0 and Nu_0 as well. For this configuration and this geometry, these results should indicate that from $Re_{D_h} = 33\,000$, the pressure losses are more important than the gain in terms of heat transfer.

Re_{D_h}	9 760	15 610	33 170
f_0 (Fanning)	0.0306	0.0305	0.0303
f/f_0	4.95	4.78	4.67
Nu_0	28.14	41.48	74.98
Nu_{D_h}/Nu_0	2.30	2.08	1.58
η_{th}	1.35	1.23	0.95

Table 7.16 – Values of the thermal performance η_{th} with f_0 and Nu_0 values

7.2.8 Summary of the last part

The generated geometry and meshes of a plate/finned tube configuration were detailed. Qualitative and quantitative results were yielded and analyzed. Several points have to be underlined.

First, some correlations are available for plates with finned tubes. But few exist with rough surfaces and additive manufacturing coupons. However, some additive manufacturing experimental data are available, and a comparison to those data has been made.

Whereas the flow behavior is similar to smooth geometry and some characteristics are retrieved as expected, the roughness's impact is visually noticeable, particularly around the tube fins. In addition, it was highlighted that the friction factor is coherent with additive manufacturing experimental data, even if some differences were noticed and have been explained.

Concerning heat transfer, our configuration seems to behave like a smooth surface. A comparison to experimental data confirms this point and leads to the conclusion that our surfaces are not rough enough. Finally, exactly reproducing a case from the reference article could help to remove some uncertainties. This implies being very careful about geometrical lengths and mimicking the roughness in this article.

7.3 Conclusions

In this chapter, roughness-resolved Large-Eddy Simulations were conducted for square and cylindrical channels with the same effective slope values. The results obtained for square channels are found to be similar to those obtained with open channels, as expected. Hence, for modeling purposes, open channels appear to be sufficient for this type of configuration.

However, in the case of cylinder tubes, roughness is found to have a more pronounced impact on flow topology and friction factor. This is because entanglements can be produced during the additive manufacturing process, and the printing direction has a significant effect on the performance.

Furthermore, a more complex geometry, such as the plate/finned tube configuration, is studied. Although very few empirical correlations exist for additive-manufactured heat exchangers, some experimental data are available for comparison purposes. Even though the flow behavior is similar to that of a smooth geometry, the influence of the roughness is locally noticeable on the velocity field. However, concerning the friction factor, the geometry characteristics seem to have a more significant impact than the roughness. Conversely, roughness plays a major role in heat transfer.

Finally, due to a general lack of roughness data, precisely replicating the roughness from an experimental reference article is a challenging task.

Conclusions and perspectives

This thesis was motivated by three primary objectives, all aimed at enhancing the modeling of rough walls, particularly for additive-manufactured heat exchangers. The accomplishments pertaining to each objective are summarized below.

Achievements

- **Identification of the key physical parameters and the best methodology to model the turbulence, especially in rough additive manufactured parts**

In chapter 1, several classifications about heat exchangers have been shown owing to numerous types of heat exchangers. Therefore, an insight into the targeted heat exchangers for simulations and modeling in this thesis was provided. One of the classifications is based on compactness, which is defined as the ratio between the heat transfer area and the heat exchanger's volume. A compactness discrimination threshold value is used to distinguish between compact and non-compact heat exchangers.

While conventional manufacturing processes are still widely used, the application of additive manufacturing for heat exchangers has recently gained attention in several research studies and industrial fields. The primary advantages of additive manufacturing include the ability to design complex geometries and achieve high thermal performance in heat exchangers while reducing mass, volume, and cost.

However, additive manufacturing techniques present some drawbacks, particularly the surface condition. Attempts have been made to assess the impact of roughness on conventional geometrical shapes. Only few heat exchanger designs have been proposed so far to fully utilize the potential of additive manufacturing.

Chapter 2 outlined the physics and primary methodologies employed in this thesis. Firstly, it elaborated on the context of turbulent flows and the resolution of the Navier-Stokes equations. Secondly, it introduced the YALES2 CFD platform, from the key tools used in this thesis to the incompressible constant density solver.

Chapter 3 has provided a comprehensive review of previous and current research on roughness characterization and its impact on turbulence modeling of wall flows. The primary goal of such modeling is to accurately predict the roughness velocity function ΔU^+ for scaling the velocity profile and the corresponding skin friction distribution.

Several DNS studies available in the literature have been discussed, including those on transverse ribs, various regular rough surfaces, and anisotropic surfaces. These studies provide rea-

sonable estimates of turbulent statistics, flow structures, and boundary layer characteristics for different roughness densities and surface isotropy.

Two primary strategies exist for surface roughness modeling: the functional and the structural approaches. While the functional approach provides good results under certain boundary layer assumptions, the structural method does not require such assumptions but requires modifications to boundary conditions. However, they are generally not applied for rough surfaces, except for the Kuwata and Kawaguchi model [121]. The chapter also has covered commercial CFD software models that take roughness into account.

Finally, critical parameters and some strategies for rough-wall modeling have been identified. These findings were essential to build a large database of roughness-resolved Large-Eddy Simulations.

- **Automatic generation of numerical rough surfaces and meshes**

Chapter 4 has provided a comprehensive description of the surface and mesh generators and their capabilities. These generators play a crucial role in automatically generating body-fitted meshes that incorporate resolved roughness and customizable parameters.

The rough surface generator (RSG), developed as part of this thesis, has the ability to generate various types of roughness and geometries in the STL format based on roughness parameters. Additionally, it offers an option for periodic boundaries with continuous slope.

The roughness-resolved mesh generator (RRMG) is a fully automatic tool that allows control of the wall cell size. It discretizes both the fluid and the solid domains, resulting in good-quality tetrahedral-based meshes. These tools enable the performance of roughness-resolved Large-Eddy Simulations, facilitating detailed analyses of turbulent flows.

- **Building of a parametric Large-Eddy Simulation database of additive-manufactured heat exchangers**

Numerics used in this thesis and a developed recycling method have been presented in Chapter 5. The latter enables to set a time-varying inlet and to perform periodic channel simulations.

Three different cases have been studied for the methodology's validation purpose. The first one is a periodic smooth channel, and good agreement between tests and references has been found. The recycling boundary condition is then appropriate to perform infinite channel flow simulations.

Simulations with two configurations of packed hemispheres have been performed. For the first configuration, obtained friction factor is in good agreement with the ones obtained with RANS and some empirical correlations. About the second configuration, our LES is consistent with the reference article even if the comparison with literature results obtained with different methods is difficult.

The final test case showcased an irregular rough surface, and the results obtained were found to be in line with the existing literature.

In summary, these cases serve as evidence that the developed tools enable the accurate execution of roughness-resolved Large-Eddy Simulations. As a result, this opens up possibilities for creating a database of RRLES, which could subsequently be used to derive models specifically tailored for additive-manufactured heat exchangers.

The main objective of Chapter 6 was to develop models in the framework of RANS and LES methods that are representative of the flow obtained in additive-manufactured heat exchangers without explicit representation of the surface details. To this end, a Roughness-Resolved Large Eddy Simulation (RRLES) database of representative channel flows has been built. The most

challenging task in building this database is the generation of representative rough surfaces and conformal unstructured meshes.

First, three different configurations of parallel rough plane channels with the same roughness height distribution but different effective slopes have been chosen and modeled. The impact of the effective slope parameter, which is directly linked to the alignment of the wall roughness with the flow, substantially impacts the flow topology, velocity and temperature profiles, as expected. In these cases, the existing empirical correlations find their limits, and new correlations are needed.

Simulations for the database have been conducted for periodic channels. The channel's half height was selected to be close to hydraulic diameters and channel heights encountered for some AM experiments. The considered Reynolds numbers and surfaces lead RRLES flows to cover both transitionally and fully rough regimes.

From database results, derived strategies for turbulence have been developed in close collaboration with Alexis Barge from the LEGI laboratory. Models have been tested by reproducing representative cases from the RRLES database. Three modeling strategies have been considered for assessment. The first one imposes the exact mean wall stress taken from the RRLES database at the wall. The second model evaluates the wall stress in the framework of TBLE approaches with the Duprat wall law. The last model adds stochastic fluctuations to the wall stress evaluated with the two first approaches.

The capacity of the models to reproduce the value of the friction factor has shown satisfying performances. We have also compared the velocity profiles inside the channel with the references. We showed that using the mean value of the wall stress alone is not enough to reproduce the mean velocity behavior inside the channel. The results are better predicted if the modeled wall stress is connected to the flow, like in the TBLE approach. Adding stochastic fluctuations led to significant improvements in predicting the mean velocity profiles for both methods. The combination of the TBLE method with the stochastic model appears to be promising. However, only a few cases have been simulated with this approach.

Regarding heat transfer, several strategies to model AM rough wall passive scalar transport without directly representing the roughness elements at the wall.

The scalar defect measured in the database has been compared with correlations available in the literature. From the results, we have shown that correlations based on equivalent sand grain roughness (ESGR) or geometrical parameters could both predict the scalar defect with acceptable precision.

We have performed a deeper study of the scalar wall flux behavior. The analysis showed that the flux is normally distributed with universal parameters, at least for our cases. The statistical properties observed in the analysis are reproduced with a temporal stochastic process. Input for the model is the mean value of the scalar wall flux only. The latter is estimated from the roughness function correlations.

Several modeling strategies were considered for assessing the LES models. The first one imposes the exact mean scalar wall flux taken from the RRLES database at the wall. The second strategy evaluates the scalar flux in the framework of TBLE approaches with the scalar Duprat wall law and a correlation-based modification of the scalar wall gradient computation. The last model adds stochastic fluctuations to the mean scalar wall flux. Each of these methods shares the same momentum model. The sensitivity of the scalar Duprat model to the momentum model is also investigated.

All models have shown satisfying performances in reproducing the scalar wall transfer. We have also demonstrated that the choice of the momentum modeling method could significantly impact the performances of the scalar Duprat model.

Finally, we showed that using the mean value of the scalar wall flux alone is not enough to

reproduce the mean scalar behavior inside the channel. The results are better predicted if the modeled flux is connected to the flow, like in the TBLE approaches. Contrary to the momentum flux, adding stochastic fluctuations to the scalar flux did not significantly improve the prediction of the mean scalar profiles.

In Chapter 7, roughness-resolved Large-Eddy Simulations were conducted for square and cylindrical channels with the same effective slope values. The results obtained for square channels are found to be similar to those obtained with open channels, as expected. Hence, for modeling purposes, open channels appear sufficient for this configuration type.

However, in the case of cylinder tubes, roughness is found to have a more pronounced impact on flow topology and friction factor. This is because entanglements can be produced during the additive manufacturing process, and the printing direction has a significant effect on the performance.

Furthermore, a more complex geometry, such as the plate/finned tube configuration, was studied. Although very few empirical correlations exist for additive-manufactured heat exchangers, some experimental data are available for comparison purposes. Even though the flow behavior is similar to that of a smooth geometry, the influence of the roughness is locally noticeable on the velocity field. However, concerning the friction factor, the geometry characteristics seem to have a more significant impact than the roughness. Conversely, roughness plays a major role in heat transfer.

Finally, due to a general lack of roughness data, precisely replicating the roughness from an experimental reference article is proved to be a challenging task.

Perspectives

- **Improve numerical rough surfaces generation**

As previously mentioned, achieving an exact replication of additive manufacturing roughness remains a challenging task. Therefore, it is crucial to seek improvements in the rough surface generator. One potential avenue for such enhancements is the utilization of numerous tomography scans. By incorporating this technique, we can gather more comprehensive data and move beyond relying solely on information found in existing literature, which often necessitates making assumptions. However, it should be noted that this approach would require a substantial number of additive-manufactured coupons to effectively capture the diverse range of roughness variations.

- **Extend the roughness-resolved Large-Eddy Simulations database**

Future improvements will involve expanding the existing database to encompass additional cases. Moreover, the current database consists of simulated normalized passive temperatures that share the same Prandtl number. An interesting study would be to compare models for the passive scalar with results obtained using different Prandtl numbers. This comparative analysis would provide valuable insights and contribute to further understanding in this area of study.

- **Evaluate derived models for square channels and curved surfaces**

Another perspective of this thesis would be to evaluate the models on other basic cases, such as pipe flows or square channels. The intrinsic challenge should be to assess presented models for curved surfaces.

- **Perform conjugate heat transfer simulations**

In this thesis, the heat transfer has not been analyzed in the solid domain with simulations performed for the database. With important roughness, peaks and valleys are expected to have different temperatures. The temperature distribution within the solid should then vary. The idea would be to conduct conjugate heat transfer simulations for a deeper analysis of the roughness impact.

- **Toward two-phase flows heat exchangers**

In conclusion, this thesis focused solely on single-phase flows in heat exchangers. However, it would be worthwhile to conduct similar simulations for two-phase flows involving rough walls. Such investigations could lead to the development of rough wall models specifically tailored for heat exchangers operating under two-phase flow conditions.

Nomenclature

Abbreviations

Symbol	Description	Units
AACF	Areal autocorrelation function	
AM	Additive manufacturing	
CAD	Computer-aided design	
CFD	Computational fluid dynamics	
CGDS	Cold gas dynamic spray	
CHX	Compact heat exchanger	
CPU	Central processing unit	
CT	Computed tomography	
CV	Control volume	
DED	Directed energy deposition	
DMLS	Direct metal laser sintering	
DNS	Direct numerical simulation	
EBM	Electron beam melting	
FDM	Fused deposition modeling	
FFF	Fused filament fabrication	
FFT	Fast Fourier transform	
FIR	Finite impulse response	
FTT	Flow-through time	
HX	Heat exchanger	
HVAC	Heat ventilation and air cooling	

IBM	Immersed boundary method
ICS	Incompressible solver
LCM	Lithography-based ceramic manufacturing
LES	Large-eddy simulation
MLES	Mean wall stress Large-Eddy simulation
MPI	Message passing interface
PBF	Powder bed fusion
PDF	Probability density function
PFA	Parametric forcing approach
PHX	Plate heat exchanger
PSD	Power spectral densities
RAM	Random access memory
RANS	Reynolds-averaged Navier-Stokes
RCT	Reduced computing time
REP	Representative elementary plane
RHS	Right hand side
RMLES	Roughness-modeled Large-Eddy simulation
RMS	Root-mean-square
RRLES	Roughness-resolved Large-Eddy simulation
RRMG	Roughness-resolved mesh generator
RSG	Rough surface generator
SBM	Stress-blended method
SGS	Subgrid scale
SLA	Stereolithography
SLM	Selective laser melting
SLS	Selective laser sintering
SRLES	Stochastic roughness Large-Eddy simulation
STL	Standard tessellation language
TBLE	Thin boundary-layer equations
UAM	Ultrasonic additive manufacturing

WALE	Wall-adapting local eddy-viscosity
WCT	Wall clock time
WMLES	Wall-modeled Large-Eddy simulation
WRLES	Wall-resolved Large-Eddy simulation
YALES2	Yet Another LES Solver

Non-dimensional numbers

Symbol	Description	Units
CFL	Courant-Friedrichs-Lewy number	
j	Colburn factor	
Nu	Nusselt number	
Pr	Prandtl number	
Pr_t	Turbulent Prandtl number	
Re	Reynolds number	
Re_η	Reynolds number associated to the Kolmogorov scale	
Re_τ	Shear Reynolds number	
y^+	Distance in wall unit	

Roughness-related symbols

Symbol	Description	Units
ES	Effective slope	$[-]$
k_s	Equivalent sand grain roughness	$[m]$
Ku	Kurtosis	$[-]$
R_a	Arithmetic average height along a line	$[m]$
S_a	Arithmetic average height over a surface	$[m]$
S_q	Root-mean-square roughness	$[m]$
S_t	Maximum roughness height	$[m]$
Sk	Skewness	$[-]$

Latin letters

Symbol	Description	Units
A_c	Minimum cross-sectional area	$[m^2]$
A_{tw}	Total wetted surface	$[m^2]$

A_0	Exterior heat transfer area	$[m^2]$
B	Log-law variable	$[-]$
C_s	Roughness constant	$[-]$
C_{smago}	Smagorinsky constant	$[-]$
C_{wale}	WALE constant	$[-]$
D	Diameter	$[m]$
D_c	Outside diameter of a fin	$[m]$
D_h	Hydraulic diameter	$[m]$
e_i	Unit vector in the direction *i*	$[-]$
E	Total energy	$[J.kg^{-1}.m^{-3}]$
f	Friction factor	$[-]$
F_p	Fin pitch	$[m]$
$\mathcal{G}_\Delta$	Filter associated to the cutoff scale length Δ	$[-]$
h or z	Surface height	$[m]$
h_e	Effective distance	$[m]$
h_{grad}	Refinement ratio	$[-]$
$h(k,l)$	Filter coefficients	$[-]$
H	Half-height channel	$[m]$
$H(w_x, w_y)$	Transfer function coefficients	$[-]$
l_t	Integral length	$[m]$
l_η	Kolmogorov length	$[m]$
L_{out}	Distance between the recycling plane and the outlet of the domain	$[m]$
L_p	Longitudinal tube pitch	$[m]$
L_x	Streamwise length of a surface	$[m]$
L_y	Spanwise length of a surface	$[m]$
M_1	Coarse mesh	
M_2	Fine mesh	
$\boldsymbol{n}$	Outgoing normal unit vector	$[-]$
P	Pressure	$[Pa]$
q	Heat flux	$[W.m^{-2}]$

$\dot{Q}$	Volume heat sources	$[W.m^{-3}]$
$\mathcal{R}$	Universal gas constant	[J.mol^{-1}.K^{-1}]
S_{ij}	Strain rate tensor	$[s^{-1}]$
T	Temperature	$[K]$
T_p	Transversal tube pitch	$[m]$
T_w	Relaxation time	$[s]$
u	Velocity	$[m.s^{-1}]$
u_η	Kolmogorov velocity	$[m.s^{-1}]$
u_τ	Friction velocity	$[m.s^{-1}]$
u^*	Intermediate predicted velocity of incompressible step	$[m.s^{-1}]$
U_b	Bulk velocity	$[m.s^{-1}]$
W	Mixture molar mass	$[mol^{-1}]$
$dW(t)$	Increment of a Brownian process	$[s]$
$\bar{Z}$	Normalized passive temperature	$[-]$
$\bar{Z}_c$	Normalized passive temperature at the center of the channel	$[-]$
$\bar{Z}_w$	Normalized passive temperature at the wall	$[-]$

Greek letters

Symbol	Description	Units
β	Compactness	$[m^2/m^3]$
δ_f	Fin thickness	$[m]$
δ_{ij}	Kronecker symbol	$[-]$
Δt	Simulation time step	$[s]$
Δx	One dimensional mesh size	$[m]$
ϵ	Dissipation rate of turbulent kinetic energy	$[m^2.s^{-3}]$
ϵ_{ijk}	Levi-Civita symbol	$[-]$
η_{th}	Thermal performance index	$[-]$
$\eta(i,j)$	Uncorrelated random numbers having a Gaussian distribution	$[-]$
κ	von Karman constant	$[-]$
λ	Thermal conductivity	$[W.m^{-1}.K^{-1}]$
Λ	Solidity	$[-]$

μ	Dynamic viscosity	$[kg.m^{-1}.s^{-1}]$
ν	Kinematic viscosity	$[m^2.s^{-1}]$
ν_t	Turbulent kinematic viscosity	$[m^2.s^{-1}]$
ρ	Density	$[kg.m^{-3}]$
σ_{ij}	Stress tensor	$[kg.m^{-1}.s^{-2}]$
τ_{ij}	Viscous stress tensor	$[kg.m^{-1}.s^{-2}]$
τ_w	Wall shear stress	$[kg.m^{-1}.s^{-2}]$
τ_x	Correlation lengths of a surface in the streamwise direction	$[m]$
τ_y	Correlation lengths of a surface in the spanwise direction	$[m]$
τ_{ij}^{SGS}	Sub-grid Reynolds stress tensor	$[kg.m^{-1}.s^{-2}]$
ϕ_w	Scalar flux at the wall	$[-]$
φ	Porosity of a plane	$[-]$

Operators

Symbol	Description	Units
$\tilde{f}$	Favre filtering	
$\mid f \mid$	Norm of function f	
$\overline{f}$	Time average	
$\langle f \rangle$	Surface average	
f^+	f expressed in wall units	
f'	Fluctuations of f	
$\frac{D}{Dt}$	Material derivative	
$\boldsymbol{\nabla}$	Gradient operator	
$\boldsymbol{\nabla}\cdot$	Divergence operator	
$\boldsymbol{\Delta}$	Laplacian operator	
$\cdot$	Scalar product	
$\otimes$	Dyadic product	
A^T	Transpose of matrix A	
$\circ$	Stratonovich calculus	

List of Figures

List of Tables

References

[1] CELLCORE (2019) Rocket engine. https://www.etmm-online.com/3d-printing-a-rocket-engine-a-886960/, accessed on 2023-04-10. 1, 191

[2] CAROZZA, A. (2017) Heat exchangers in the aviation engineering. *Heat Exchangers - Advanced Features and Applications* . 2, 7

[3] ARIE, M., SHOOSHTARI, A., DESSIATOUN, S. & OHADI, M. (2016) Performance characterization of an additively manufactured titanium (Ti64) heat exchanger for an air-water cooling application. *Proceedings of the ASME 2016 Heat Transfer Summer Conference* . 2

[4] SALTZMAN, D., BICHNEVICIUS, M., LYNCH, S., SIMPSON, T., REUTZEL, E., DICKMAN, C. & MARTUKANITZ, R. (2018) Design and evaluation of an additively manufactured aircraft heat exchanger. *Appl. Therm. Eng.* **138**, 254–263. 2, 23, 25, 191

[5] SARRAF, K., LAUNAY, S. & TADRIST, L. (2015) Complex 3D-flow analysis and corrugation angle effect in plate heat exchangers. *Int. J. Therm. Sci.* **94**, 126–138. 3, 10, 191

[6] SHAH, R. K. & SEKULIĆ, D. P. (2003) *Fundamentals of heat exchanger design*. 8, 10, 11, 12, 13, 14, 15, 191

[7] NECATI OZIKI, M. (1985) *Heat transfer: A basic approach*. 9

[8] BAHREHMAND, S. & ABBASSI, A. (2016) Heat transfer and performance analysis of nanofluid flow in helically coiled tube heat exchangers. *Chem. Eng. Res. Des.* **109**, 628–637. 9

[9] INCROPERA, F., DEWITT, D., BERGMAN, T. & LAVINE, A. (2011) *Fundamentals of heat and mass transfer*. 11, 12, 191

[10] CHENNU, R. & PATURU, P. (2011) Development of heat transfer coefficient and friction factor correlations for offset fins using CFD. *Int. J. Numer. Methods Heat Fluid Flow* **21**, 935–951. 12, 191

[11] RASTAN, H., ABDI, A., HAMAWANDI, B., IGNATOWICZ, M., MEYER, J. P. & PALM, B. (2020) Heat transfer study of enhanced additively manufactured minichannel heat exchangers. *Int. J. Heat Mass Transf.* **161**, 120271. 14, 191

[12] WONG, M., OWEN, I., SUTCLIFFE, C. & PURI, A. (2009) Convective heat transfer and pressure losses across novel heat sinks fabricated by selective laser melting. *Int. J. Heat Mass Transf.* **52**, 281–288. 14, 17

[13] El Moumen, A., Tarfaoui, M. & Lafdi, K. (2019) Additive manufacturing of polymer composites: Processing and modeling approaches. *Composites Part B: Engineering* **171**, 166–182. 15

[14] Laureijs, R., Roca, J., Narra, S., Montgomery, C., Beuth, J. & Fuchs, E. (2017) Metal additive manufacturing: cost competitive beyond low volumes. *J. Manuf. Sci. Eng.* **139**, 081010. 16, 191

[15] Fera, M., Macchiaroli, R., Fruggiero, F. & Lambiase, A. (2018) A new perspective for production process analysis using additive manufacturing-complexity vs production volume. *Int. J. Adv. Manuf. Technol.* **95**, 673–685. 16

[16] Bauereiss, A., Scharowsky, T. & Körner, C. (2014) Defect generation and propagation mechanism during additive manufacturing by selective beam melting. *J. Mater. Process. Technol.* **214**, 2522–2528. 17

[17] Aqida, S. N., Ghazali, M. I. & Hashim, J. (2004) Effect of porosity on mechanical properties of metal matrix composite: An overview. *Jurnal Teknologi* **40** (1), 17–32. 17

[18] Tapia, G., Elwany, A. H. & Sang, H. (2016) Prediction of porosity in metal-based additive manufacturing using spatial Gaussian process models. *Additive Manufacturing* **12**, 282–290. 17

[19] Zhang, M., Sun, C., Zhang, X., Goh, P., Wei, J., Li, H. & Hardacre, D. (2017) Competing influence of porosity and microstructure on the fatigue property of laser powder bed fusion Stainless Steel 316L. *Solid Freeform Fabrication Symposium* pp. 365–376. 17

[20] Mathur, R. (2016) 3D printing in architecture. *Int. J. Innovat. Sci.* **3**, 583–591. 18, 191

[21] Yan, C., Hao, L., Hussein, A., Bubb, S., Young, P. & Raymont, D. (2014) Evaluation of light-weight AlSi10Mg periodic cellular lattice structures fabricated via direct metal laser sintering. *J. Mater. Process. Technol.* **214**, 856–864. 17

[22] Ventola, L., Robotti, F., Dialameh, M., Calignano, F., Manfredi, D., Chiavazzo, E. & Asinari, P. (2014) Rough surfaces with enhanced heat transfer for electronics cooling by direct metal laser sintering. *Int. J. Heat Mass Transf.* **75**, 58–74. 17, 23, 191

[23] Stimpson, C., Snyder, J., Thole, K. & Mongillo, D. (2017) Scaling roughness effects on pressure loss and heat transfer of additively manufactured channels. *J. Turbomach.* **139** (2), 021003. 17, 23, 24, 153, 191

[24] Kirsch, K. L. & Thole, K. (2017) Pressure loss and heat transfer performance for additively and conventionally manufactured pin fin arrays. *Int. J. Heat Mass Transf.* **108**, 2502–2513. 17

[25] Cormier, Y., Dupuis, P., Farjam, A., Corbeil, A. & Jodoin, B. (2014) Additive manufacturing of pyramidal pin fins: Height and fin density effects under forced convection. *Int. J. Heat Mass Transf.* **75**, 235–244. 18

[26] Dupuis, P., Cormier, Y., Fenech, M. & Jodoin, B. (2016) Heat transfer and flow structure characterization for pin fins produced by cold spray additive manufacturing. *Int. J. Heat Mass Transf.* **98**, 650–661. 18

[27] WU, H., LIU, S., ZANG, Y., LIAO, H., RAOELISON, R. & DENG, S. (2021) New process implementation to enhance cold spray-based additive manufacturing. *J. Therm. Spray Technol.* **30**, 1284–1293. 19, 191

[28] WU, H., LIU, S., ZANG, Y., LIAO, H., RAOELISON, R. & DENG, S. (2015) Solid-state additive manufacturing for heat exchangers. *JOM* **67**, 655–659. 18

[29] GUO, H., BRYANT GINGERICH, M., L.M., H., HAHNLEN, R. & DAPINO, M. (2015) Joining of carbon fiber and aluminum using ultrasonic additive manufacturing (UAM). *Composite Structures* **67**, 655–659. 19, 191

[30] DEISENROTH, D., MORADI, R., SHOOSHTARI, A., SINGER, F., BAR-COHEN, A. & OHADI, M. (2018) Review of heat exchangers enabled by polymer and polymer composite additive manufacturing. *Heat Transf. Eng.* **39**, 1652–1668. 18, 20, 21, 191

[31] AL RASHID, A., AHMED, W., KHALID, M. & KOC, M. (2021) Vat photopolymerization of polymers and polymer composites: Processes and applications. *Additive Manufacturing* **47**, 102279. 20, 191

[32] CEVALLOS, J., BAR-COHEN, A. & DEISENROTH, D. (2016) Thermal performance of a polymer composite webbed-tube heat exchanger. *Int. J. Heat Mass Transf.* **98**, 845–856. 19, 20, 191

[33] LIU, H., TSURU, H., COOPER, A. & PRINZ, F. (2005) Rapid prototyping methods of silicon carbide micro heat exchangers. *Proceedings of the Institution of Mechanical Engineers, Part B: Journal of Engineering Manufacture* **219**, 525–538. 21

[34] SHULMAN, H. & ROSS, N. (2015) Additive manufacturing for cost efficient production of compact ceramic heat exchangers and recuperators. PhD Thesis. 21

[35] ARIE, M., SHOOSHTARI, A., TIWARI, R., DESSIATOUN, S., OHADI, M. & PEARCE, J. (2017) Experimental characterization of heat transfer in an additively manufactured polymer heat exchanger. *Appl. Therm. Eng.* **113**, 575–584. 21

[36] KHAN, T., KHAN, M., CHYU, M.-C. & AYUB, Z. (2010) Experimental investigation of single phase convective heat transfer coefficient in a corrugated plate heat exchanger for multiple plate configurations. *Appl. Therm. Eng.* **30**, 1058–1065. 21

[37] FAIZAL, M. & AHMED, M. (2012) Experimental studies on a corrugated plate heat exchanger for small temperature difference applications. *Exp. Therm. Fluid Sci.* **36**, 242–248. 21, 22, 191

[38] KANDLIKAR, S., JOSHI, S. & TIAN, S. (2003) Effect of surface roughness on heat transfer and fluid flow characteristics at low Reynolds numbers in small diameter tubes. *Heat Transf. Eng.* **24**, 4–16. 21

[39] NILPUENG, K. & WONGWISES, S. (2015) Experimental study of single-phase heat transfer and pressure drop inside a plate heat exchanger with a rough surface. *Exp. Therm. Fluid Sci.* **68**, 268–275. 22

[40] KUMBHAR, N. N. & MULAY, A. V. (2018) Post processing methods used to improve surface finish of products which are manufactured by additive manufacturing technologies: A review. *Journal of The Institution of Engineers (India): Series C* **99**, 481–487. 22

[41] BICHNEVICIUS, M., SALTZMAN, D. & LYNCH, S. (2020) Comparison of additively manufactured louvered plate-fin heat exchangers. *J. Thermal Sci. Eng. Appl.* **12**, 011018. 23

[42] LEEDS, C., WRIGHT, C. & NELLIS, G. (2018) Advanced air-side heat transfer surface geometries enabled by additive manufacturing. *17th International Refrigeration and Air Conditioning Conference* **Paper 1916**. 23, 24, 191

[43] CHEKUROV, S., KAJASTE, J., SAARI, K., KAURANNE, H., PIETOLA, M. & PARTANEN, J. (2019) Additively manufactured high-performance counterflow heat exchanger. *Progress in Additive Manufacturing* **4**, 55–61. 25, 191

[44] SNYDER, J., STIMPSON, C. & THOLE, K. (2016) Build direction effects on additively manufactured channels. *J. Turbomach.* **138** (5), 1–8. 25, 26, 192

[45] POPE, S. (2000) *Turbulent flows*. Cambridge university press. 27, 32

[46] REYNOLDS, O. (1883) An experimental investigation of the circumstances which determine whether the motion of water shall be direct or sinuous, and of the law of resistance in parallel channels. *Proceedings of the Royal Society of London* **35** (224-226), 84–99. 29

[47] RICHARDSON, L. & SHAW, W. (1920) The supply of energy from and to atmospheric eddies. *Proceedings of the Royal Society of London. Series A, Containing Papers of a Mathematical and Physical Character* **97** (686), 354–373. 30

[48] KOLMOGOROV, A. (1991) The local structure of turbulence in incompressible viscous fluid for very large Reynolds numbers. *Proceedings of the Royal Society of London. Series A: Mathematical and Physical Sciences* **434** (1890), 9–13. 30

[49] SPALART, P. (1988) Direct simulation of a turbulent boundary layer up to $R_\theta = 1410$. *J. Fluid Mech.* **187**, 61–98. 31

[50] KLINE, S. & ROBINSON, S. (1990) *Turbulent boundary layer structure: Progress, status, and challenges*. Springer. 31

[51] JEONG, J. & HUSSAIN, F. (1995) On the identification of a vortex. *J. Fluid Mech.* **285**, 69–94. 31

[52] HUNT, J., WRAY, A. & MOIN, P. (1988) Eddies, streams, and convergence zones in turbulent flows. *Studying Turbulence Using Numerical Simulation Databases* **2**, 193–208. 31

[53] BÉNARD, P. (2015) Analyse et amélioration d'une chambre de combustion centimétrique par simulations aux grandes échelles. PhD Thesis, Institut National des Sciences Appliquées de Rouen. 31, 192

[54] SAGAUT, P. (1998) *Introduction a la simulation des grandes échelles pour les écoulements de fluide incompressible. Mathématique & Applications*. Springer Berlin Heidelberg. 32

[55] BÉNARD, P., BALARAC, G., MOUREAU, V., DOBRZYNSKI, C., LARTIGUE, G. & D'ANGELO, Y. (2016) Mesh adaptation for Large-Eddy Simulations in complex geometries. *Int. J. Numer. Methods Fluids* **81** (2), 719–740. 32

[56] BOUSSINESQ, J. (1877) Théorie de l'écoulement tourbillonnant. 33

[57] VASILYEV, O., LUND, T. & MOIN, P. (1998) A general class of commutative filters for LES in complex geometries. *J. Comput. Phys.* **146** (1), 82–104. 33

[58] SMAGORINSKY, J. (1963) General circulation experiments with the primitive equations I. the basic experiment. *Monthly weather review* **91** (3), 99–164. 33

[59] GERMANO, M., PIOMELLI, U., MOIN, P. & CABOT, W. (1991) A dynamic subgrid-scale eddy viscosity model. *Phys. Fluids A, Fluid Dyn.* **3** (7), 1760–1765. 34

[60] LILLY, D. (1992) A proposed modification of the Germano subgrid-scale closure method. *Phys. Fluids A, Fluid Dyn.* **4** (3), 633–635. 34

[61] NICOUD, N. & DUCROS, F. (1976) Subgrid-scale stress modelling based on the square of the velocity gradient tensor. *Flow Turbul. Combust.* **62**, 183–200. 34, 95, 106, 116, 157, 170

[62] MOUREAU, V., DOMINGO, P. & VERVISCH, L. (2011) Design of a massively parallel CFD code for complex geometries. *Comptes Rendus Mécanique* **339** (2-3), 141–148. 34, 36, 37, 192

[63] LEGRAND, N., LARTIGUE, G. & MOUREAU, V. (2017) A multi-grid framework for the extraction of large-scale vortices in Large-Eddy Simulation. *J. Comput. Phys.* **349**, 528–560. 34

[64] JANODET, R., GUILLAMON, C., MOUREAU, V., MERCIER, R., LARTIGUE, G., BÉNARD, P., MÉNARD, T. & BERLEMONT, A. (2022) A massively parallel accurate conservative level set algorithm for simulating turbulent atomization on adaptive unstructured grids. *J. Comput. Phys.* **458**, 111075. 34

[65] DOMINGO-ALVAREZ, P., BÉNARD, P., MOUREAU, V., LARTIGUE, G. & GRISCH, F. (2020) Impact of spray droplet distribution on the performances of a kerosene lean/premixed injector. *Flow Turbul. Combust.* **104** (2), 421–450. 34

[66] KRAUSHAAR, M. (2011) Application of the compressible and low-Mach number approaches to Large-Eddy Simulation of turbulent flows in aero-engines. PhD Thesis, Institut National Polytechnique de Toulouse. 35, 95, 116, 157, 170

[67] CHORIN, A. (1968) Numerical solution of the Navier-Stokes equations. *Math. Comput.* **22**, 745–762. 36, 37

[68] CRANDALL, M. & MAJDA, A. (1980) The method of fractional steps for conservation laws. *Numer. Math.* **34**, 285–314. 36

[69] KARYPIS, G. & KUMAR, V. (1995) METIS – unstructured graph partitioning and sparse matrix ordering system. 36, 85

[70] CHEVALIER, C. & PELLEGRINI, F. (2008) PT-Scotch: A tool for efficient parallel graph ordering. *Parallel Comput.* **34** (6-8), 318–331. 36

[71] MALANDAIN, M., MAHEU, N. & MOUREAU, V. (2013) Optimization of the deflated conjugate gradient algorithm for the solving of elliptic equations on massively parallel machines. *J. Comput. Phys.* **238**, 32–47. 36, 39

[72] KIM, J. & MOIN, P. (1984) Application of a fractional-step method to incompressible Navier-Stokes equations. *J. Comput. Phys.* **59**, 308–323. 37

[73] BELL, J., COLELLA, P. & GLAZ, H. (1989) A second-order projection method for the incompressible Navier-Stokes equations. *J. Comput. Phys.* **85** (2), 257–283. 38

[74] KAASSCHIETER, E. (1988) Preconditioned conjugate gradients for solving singular systems. *J. Comput. Appl. Math.* **24** (1), 265–275. 39

[75] NICOLAIDES, R. (1987) Deflation of conjugate gradients with applications to boundary value problems. *SIAM J. Numer. Anal.* **24** (2), 355–365. 39

[76] VAN DER VORST, H. (1992) Bi-CGSTAB: A fast and smoothly converging variant of Bi-CG for the solution of nonsymmetric linear systems. *SIAM Journal on Scientific & Statistical Computing* **13** (2), 631–644. 39

[77] GADELMAWLA, E., KOURA, M., MAKSOUD, T., ELEWA, I. & SOLIMAN, H. (2002) Roughness parameters. *J. Mater. Process. Technol.* **123**, 133–145. 42, 43, 44, 76, 192

[78] (2012) ISO 25178-2 geometrical product specifications (GPS) - surface texture: Areal - part 2: Terms, definition and surface texture parameters . 42, 77

[79] NIKURADSE, J. (1933) Stromungsgesetze in rauhen rohren. *VDI Forschungsheft No 361* **4** (B), 1–22. 45

[80] COLEBROOK, C. (1939) Turbulent flow in pipes, with particular reference to the transition region between the smooth and rough pipe laws. *Inst. Civil Eng.* **11**, 133–156. 45, 121

[81] MOODY, L. (1944) Friction factors for pipe flow. *Trans. Asme* **66** (8), 671–684. 45, 46, 192

[82] SCHLICHTING, H. (1936) Experimentelle untersuchungen zum rauhigkeitsproblem. *Ing.-Arch.* **7** (1), 1–34. 45

[83] MACDONALD, M., CHAN, L., CHUNG, D., HUTCHINS, N. & OOI, A. (2016) Turbulent flow over transitionally rough surfaces with varying roughness densities. *J. Fluid Dynamics* **804**, 130–161. 47, 50, 52, 54, 55, 62, 192

[84] FLACK, K. & SCHULTZ, M. (2010) Review of hydraulic roughness scales in the fully rough regime. *J. Fluids Eng.* **132** (4), 041203. 45, 46, 47, 192

[85] FOROOGHI, P., STROH, A., MAGAGNATO, F., JAKIRLIC, S. & FROHNAPFEL, B. (2017) Toward a universal roughness correlation. *J. Fluids Eng.* **139** (12), 121201. 46, 62, 66

[86] MIYAKE, Y., TSUJIMOTO, K. & NAKAJI, M. (2001) Direct numerical simulation of rough-wall heat transfer in a turbulent channel flow. *Int. J. Heat Fluid Flow* **22** (3), 237–244. 47, 49, 192

[87] LEONARDI, S., ORLANDI, P., SMALLEY, R., DJENIDI, L. & ANTONIA, R. (2003) Direct numerical simulations of turbulent channel flow with transverse square bars on one wall. *J. Fluid Mech.* **491**, 229–238. 47

[88] IKEDA, T. & DURBIN, P. (2007) Direct simulations of a rough-wall channel flow. *J. Fluid Mech.* **571**, 235–263. 47, 48, 49, 50, 192

[89] JIN, Y., UTH, M. & HERWIG, H. (2015) Structure of a turbulent flow through plane channels with smooth and rough walls: an analysis based on high resolution. *Comput. Fluids* **107**, 77–88. 47

[90] ASHRAFIAN, A., ANDERSSON, H. & MANHART, M. (2004) DNS of turbulent flow in a rod-roughened channel. *Int. J. Heat & Fluid Flow* **25** (3), 373–383. 49, 68

[91] MIYAKE, Y., TSUJIMOTO, K. & AGATA, Y. (2000) A DNS of a turbulent flow in a rough-wall channel using roughness elements model. *JSME Int. J. Series B Fluids Thermal Engrg.* **43** (2), 233–242. 50, 63, 65, 192

[92] BHAGANAGAR, K., KIM, J. & COLEMAN, G. (2004) Effect of roughness on wall-bounded turbulence. *Flow Turbul. Combust.* **72** (2-4), 463–492. 50, 52, 53, 192, 199

[93] ORLANDI, P. & LEONARDI, S. (2008) Direct numerical simulation of three-dimensional turbulent rough channels: parametrization and flow physics. *J. Fluid Mech.* **606**, 399–415. 50, 52

[94] LEE, J., SUNG, H. & KROGSTAD, P.-A. (2011) Direct numerical simulation of the turbulent boundary layer over a cube-roughened wall. *J. Fluid Mech.* **669**, 397–431. 50, 51, 53, 192

[95] CHATZIKYRIAKOU, D., BUONGIORNO, J., CAVIEZEL, D. & LAKEHAL, D. (2015) DNS and LES of turbulent flow in a closed channel featuring a pattern of hemispherical roughness elements. *Int. J. Heat Fluid Flow* **53**, 29–43. 50, 51, 53, 54, 97, 98, 101, 103, 104, 192, 194

[96] KUWATA, Y. & SUGA, K. (2016) Lattice Boltzmann direct numerical simulation of interface turbulence over porous and rough walls. *Int. J. Heat Fluid Flow* **61**, 145–157. 50, 51, 192

[97] NAPOLI, E., ARMENIO, V. & DE MARCHIS, M. (2008) The effect of the slope of irregularly distributed roughness elements on turbulent wall-bounded flow. *J. Fluid Mech.* **613**, 385–394. 55, 56, 77, 192

[98] CARDILLO, J., CHEN, Y., ARAYA, G., NEWMAN, J., JANSEN, K. & CASTILLO, L. (2013) DNS of a turbulent boundary layer with surface roughness. *J. Fluid Mech.* **729**, 603–637. 55, 56, 57, 62, 192, 193

[99] BUSSE, A., LUTZNER, M. & SANDHAM, N. (2015) Direct numerical simulation of turbulent flow over a rough surface based on a surface scan. *Comput. Fluids* **116**, 129–147. 55, 58, 59, 60, 61, 193, 199

[100] YUAN, J. & PIOMELLI, U. (2014) Estimation and prediction of the roughness function on realistic surfaces. *J. Turbul.* **15** (6), 350–365. 55, 62

[101] DE MARCHIS, M., MILICI, B. & NAPOLI, E. (2015) Numerical observations of turbulence structure modification in channel flow over 2D and 3D rough walls. *Int. J. Heat Fluid Flow* **56**, 108–123. 55, 61, 62, 77, 193

[102] CHOI, H. & MOIN, P. (2012) Grid-point requirements for Large-Eddy Simulation: Chapman's estimates revisited. *Phys. Fluids* **24** (1), 011702. 63

[103] BALARAS, E., BENOCCI, C. & PIOMELLI, U. (1996) Two-layer approximate boundary conditions for Large-Eddy Simulation. *AIAA J.* **34**, 1111. 63, 64, 65

[104] PIOMELLI, U. & BALARAS, E. (2002) Wall-layer models for Large-Eddy Simulations. *Annu. Rev. Fluid Mech.* **34**, 349. 64, 193

[105] WANG, M. & MOIN, P. (2002) Dynamic wall modeling for Large-Eddy Simulation of complex turbulent flows. *Phys. Fluids* **14** (7), 2043. 64

[106] MANHART, M., PELLER, N. & BRUN, C. (2008) Near-wall scaling for turbulent boundary-layers with adverse pressure gradient. *Theor. Comput. Fluid Dyn.* **22**, 243–260. 65

[107] DUPRAT, C., BALARAC, G., METAIS, O., CONGEDO, P. M. & BRUGIERE, O. (2011) A wall-layer model for Large-Eddy Simulations of turbulent flows with/out pressure gradient. *Phys. Fluids* **23** (1), 015101. 65, 193

[108] BOSE, S. & PARK, G. (2018) Wall-modeled Large-Eddy Simulation for complex turbulent flows. *Annu. Rev. Fluid Mech.* **50**, 535–561. 65

[109] SCOTTI, A. (2006) Direct numerical simulation of turbulent channel flows with boundary roughened with virtual sandpaper. *Phys. Fluids* **18** (3), 031701. 65

[110] BREUGEM, W., BOERSMA, B. & UITTENBOGAARD, R. (2006) The influence of wall permeability on turbulent channel flow. *J. Fluid Mech.* **562**, 35–62. 65

[111] BUSSE, A. & SANDHAM, N. (2012) Parametric forcing approach to rough-wall turbulent channel flow. *J. Fluid Dynamics* **712**, 169–202. 65

[112] FOROOGHI, P., FROHNAPFEL, B., MAGAGNATO, F. & BUSSE, A. (2018) A modified Parametric Forcing Approach for modelling of roughness. *Int. J. Heat Fluid Flow* **71**, 200–209. 65, 66, 67, 193

[113] KRUMBEIN, B., JAKIRLIC, S. & TROPEA, C. (2019) A unified modeling approach for flow over porous and rough walls in scale-resolving simulation methods. *11th International Symposium on Turbulence and Shear Flow Phenomena* . 65

[114] ALVES PORTELA, F. & SANDHAM, N. (2020) A DNS/URANS approach for simulation rough-wall turbulent flows. *Int. J. Heat Fluid Flow* **85**, 108627. 67

[115] TEMPLETON, J., WANG, M. & MOIN, P. (2008) A predictive wall model for Large-Eddy Simulation based on optimal control techniques. *Phys. Fluids* **20**, 065104. 68

[116] TUCK, E. & KOUZOUBOV, A. (1995) A laminar roughness boundary condition. *Trans. SNAME* **89**, 295–318. 68

[117] JAGER, W. & MIKELIC, A. (2001) On the roughness-induced effective boundary conditions for an incompressible viscous flow. *J. Differ. Eq.* **170** (1), 96–122. 68

[118] FLORES, O. & JIMÉNEZ, J. (2006) Effect of wall-boundary disturbances on turbulent channel flows. *J. Fluid Mech* **566**, 357–376. 68, 193

[119] ORLANDI, P., LEONARDI, S., TUZI, R. & ANTONIA, R. (2003) Direct numerical simulation of turbulent channel flow with wall velocity disturbances. *Phys. Fluids* **15** (12), 3587–3601. 69

[120] BOSE, S. & MOIN, P. (2014) A dynamic slip boundary condition for wall-modeled Large-Eddy Simulation. *Phys. Fluids* **26** (1), 015104. 69, 70, 193, 199

[121] KUWATA, Y. & KAWAGUCHI, Y. (2019) Direct numerical simulation of turbulence over resolved and modeled rough walls with irregularly distributed roughness. *Int. J. Heat Fluid Flow* **77**, 1–18. 71, 72, 74, 180, 193

[122] CHEDEVERGNE, F. & AUPOIX, B. (2017) Accounting for wall roughness effects in turbulence models: a wall function approach. *7th EUCASS Conf.* . 72, 73

[123] PATIR, N. (1978) A numerical procedure for random generation of rough surfaces. *Wear* **47** (2), 263–277. 75

[124] WATSON, W. & SPEDDING, T. (1982) The time series modeling of non-gaussian engineering processes. *Wear* **83** (2), 215–231. 75

[125] WHITEHOUSE, D. (1983) The generation of two dimensional random surfaces having a specified function. *CIRP Annals* **32** (1), 495–498. 75

[126] HU, Y. & TONDER, K. (1992) Simulation of 3-D random rough surface by 2-D digital filter and Fourier analysis. *Int. J. Mach. Tools Manulact.* **32**, 83–90. 75, 77, 78

[127] BAKOLAS, V. (2003) Numerical generation of arbitrarily oriented non-Gaussian three-dimensional rough surfaces. *Wear* **254** (5-6), 546–554. 75, 77

[128] FRANCISCO, A. & BRUNETIERE, N. (2016) A hybrid method for fast and efficient rough surface generation. *Proc IMechE Part J: J. Engineering Tribology* **230** (7), 747–768. 75

[129] MANESH, K., RAMAMOORTHY, B. & SINGAPERUMAL, M. (2010) Numerical generation of anisotropic 3D non-Gaussian engineering surfaces with specified 3D surface roughness parameters. *Wear* **268** (11-12), 1371–1379. 76

[130] LING, F. (1990) Fractals, engineering surfaces and tribology. *Wear* **136** (1), 141–156. 76

[131] THOMAS, T., ROSEN, B. & AMINI, N. (1999) Fractal characterization of the anisotropy of rough surfaces. *Wear* **232** (1), 41–50. 76

[132] TOWNSEND, A., SENIN, N., BLUNT, L., LEACH, R. K. & TAYLOR, J. S. (2016) Surface texture metrology for metal additive manufacturing: a review. *Precis. Eng.* **46**, 34–47. 76, 77

[133] CABANETTES, F., JOUBERT, A., CHARDON, G., DUMAS, J., RECH, J., GROSJEAN, C. & DIMKOVSKI, Z. (2018) Topography of as built surfaces generated in metal additive manufacturing: a multi scale analysis from form to roughness. *Precis. Eng.* **52**, 249–265. 76, 77, 112

[134] DIAZ, A. (2019) Surface texture characterization and optimization of metal additive manufacturing-produced components for aerospace applications. *Additive manufacturing for the aerospace industry* pp. 341–374. 76, 77

[135] GEUZAINE, C. & REMACLE, J.-F. (2009) Gmsh: A 3-D finite element mesh generator with built-in pre- and post-processing facilities. *Int. J. Numer. Methods Eng.* **79** (11), 1309–1331. 76

[136] ITO, Y. & NAKAHASHI, K. (2004) Improvements in the reliability and quality of unstructured hybrid mesh generation. *Int. J. Numer. Meth. Fluids* **45** (1), 79–108. 76

[137] LI, Z., ZHANG, Z., SHI, J. & WU, D. (2019) Prediction of surface roughness in extrusion-based additive manufacturing with machine learning. *Robot. Comput. -Integr.* **57**, 488–495. 77

[138] JOHNSON, N. (1949) Systems of frequency curves generated by methods of translation. *Biometrika* **36**, 149–176. 77, 79

[139] HILL, I., HILL, R. & HOLDER, R. (1976) Fitting Johnson curves by moments. *Appl. Stat.* **25**, 180–189. 79

[140] TUENTER, H. (2001) An algorithm to determine the parameters of SU-curves in the Johnson system of probability distributions by moment matching. *J. Stat. Comput. Simul.* **70**, 325–347. 79

[141] SAVITZKY, A. & GOLAY, M. (1964) Smoothing and differentiation of data by simplified least squares procedures. *Anal. Chem.* **36**, 1627–1639. 79

[142] DAPOGNY, C., DOBRZYNSKI, C. & FREY, P. (2014) Three-dimensional adaptive domain remeshing, implicit domain meshing, and applications to free and moving boundary problems. *J. Comput. Phys.* **262**, 358–378. 85

[143] JANODET, R., VAUDOR, G., LARTIGUE, G., BÉNARD, P., MOUREAU, V. & MERCIER, R. (2019) An unstructured conservative level-set algorithm coupled with dynamic mesh adaptation for the computation of liquid-gas flows. *29th European Conference on Liquid Atomization and Spray Systems* . 87

[144] MEYNET, S., MOUREAU, V., LARTIGUE, G. & HADJADJ, A. (2021) Automatic surface and volume mesh generation for roughness-resolved LES of additive-manufacturing heat exchangers. *ETMM13 Proceedings*. ERCOFTAC, paper number 105. 93

[145] XIAO, F., DIANAT, M. & MCGUIRK, J. (2017) An LES turbulent inflow generator using a recycling and rescaling method. *Flow Turbul. Combust.* **98**, 663–695. 94

[146] KUWATA, Y. & KAWAGUCHI, Y. (2019) Direct numerical simulation of turbulence over systematically varied irregular rough surfaces. *J. Fluid Mech.* **862**, 781–815. 95, 107, 112, 165

[147] KIM, J., MOIN, P. & MOSER, R. (1987) Turbulence statistics in fully developed channel flow at low Reynolds number. *J. Fluid Mech.* **177**, 133–166. 96, 97

[148] TOKI, T., TERAMOTO, S. & OKAMOTO, K. (2019) Velocity and temperature profiles in turbulent channel flow at supercritical pressure. *J. Propuls. Power* **36** (1), 1–11. 105, 194

[149] KUWATA, Y. & NAGURA, R. (2020) Direct numerical simulation on the effects of surface slope and skewness on rough-wall turbulence. *Phys. Fluids* **32** (10), 105113. 108, 194

[150] SALTZMAN, D., BICHNEVICIUS, M., LYNCH, S., SIMPSON, T., REUTZEL, E., DICKMAN, C. & MARTUKANITZ, R. (2018) Design and evaluation of an additively manufactured aircraft heat exchanger. *Appl. Therm. Eng.* **138**, 254–263. 112

[151] VENTOLA, L., ROBOTTI, F., DIALAMEH, M., CALIGNANO, F., MANFREDI, D., CHIAVAZZO, E. & ASINARI, P. (2014) Rough surfaces with enhanced heat transfer for electronics cooling by direct metal laser sintering. *Int. J. Heat Mass Transf.* **75**, 58–74. 112

[152] SIMONELLI, M., TSE, Y. & TUCK, C. (2014) Effect of the build orientation on the mechanical properties and fracture modes of SLM Ti–6Al–4V. *Mater. Sci. Eng. A.* **616**, 1–11. 112

[153] SNYDER, J., STIMPSON, C. & THOLE, K. (2016) Build direction effects on additively manufactured channels. *J. Turbomach.* **138** (5), 051006. 112

[154] STIMPSON, C., SNYDER, J., THOLE, K. & MONGILLO, D. (2017) Scaling roughness effects on pressure loss and heat transfer of additively manufactured channels. *J. Turbomach.* **139** (2), 021003. 112

[155] MEYNET, S., BARGE, A., MOUREAU, V., BALARAC, G., LARTIGUE, G. & HADJADJ, A. (2023) Roughness resolved LES of additive manufacturing-like channel flows. *J. Turbomach.* **145** (8), 081013. 112, 142, 149, 196

[156] STIMPSON, C., SNYDER, J., THOLE, K. & MONGILLO, D. (2016) Roughness effects on flow and heat transfer for additively manufactured channels. *J. Turbomach.* **138** (5), 051008. 112, 161, 170

[157] SHAFI, H. & ANTONIA, R. (1995) Anisotropy of the Reynolds stresses in a turbulent boundary layer on a rough wall. *Exp. Fluid* **18**, 213–215. 119

[158] PIOMELLI, U. (2019) Recent advances in the numerical simulation of rough-wall boundary layers. *Phys. Chem. Earth.* **113**, 63–72. 119

[159] YUAN, J. & PIOMELLI, U. (2014) Roughness effects on the Reynolds stress budgets in near-wall turbulence. *J. Fluid Mech.* **760**, R1. 119

[160] FLACK, K. A. & SCHULTZ, M. P. (2014) Roughness effects on wall-bounded turbulent flows. *Phys. Fluids* **26**, 101305. 130

[161] KADIVAR, M., TORMEY, D. & MCGRANAGAN, G. (2021) A review on turbulent flow over rough surfaces: Fundamentals and theories. *Int. J. Thermofluids* **10**, 100077. 130, 133

[162] BOYLE, R. & STRIPF, M. (2009) Simplified approach to predicting rough surface transition. *J. Turbomach.* **131** (4), 041020. 130, 144

[163] DE MARCHIS, M., SACCONE, D., MILICI, B. & NAPOLI, E. (2020) Large-Eddy Simulations of rough turbulent channel flows bounded by irregular roughness: advances toward a universal roughness correlation. *Flow Turbul. Combust.* **105**, 627–648. 131, 133, 140, 148

[164] KUWATA, Y. & NAGURA, R. (2020) Direct numerical simulation on the effects of surface slope and skewness on rough-wall turbulence. *Phys. Fluids* **32**, 105113. 131, 135

[165] BOSE, S. & PARK, G. (2018) Wall-modeled Large-Eddy Simulation for complex turbulent flows. *Annu. Rev. Fluid Mech.* **50**, 535–561. 132, 145

[166] PARK, G. & MOIN, P. (2014) An improved dynamic non-equilibrium wall-model for Large-Eddy Simulation. *Phys. Fluids* **26**, 015108. 133, 195

[167] OLMEDA, R., DOEHRING, A. & STEMMER, C. (2022) Study and application of wall-roughness models in LES flows. *Int. J. Heat Fluid Flow* **95**, 108948. 133, 134, 145

[168] DUPRAT, C., BALARAC, G., METAIS, O., CONGEDO, P. & BRUGIÈRE, O. (2011) A wall-layer model for Large-Eddy Simulations of turbulent flows with/out pressure gradient. *Phys. Fluids* **23** (1), 015101. 133, 140, 147

[169] MAHEU, N., MOUREAU, V., DOMINGO, P., DUCHAINE, F. & BALARAC, G. (2012) Large-Eddy Simulations of flow and heat transfer around a low-Mach number turbine blade. *CTR: Proceedings of the Summer Program* p. 137. 134, 145, 147, 148

[170] ZAMANSKY, R., VINKOVIC, I. & GOROKHOVSKI, M. (2013) Acceleration in turbulent channel flow: universalities in statistics, subgrid stochastic models and an application. *J. Fluid Mech.* **721**, 627–668. 135

[171] SABELNIKOV, V., BARGE, A. & GOROKHOVSKI, M. (2019) Stochastic modeling of fluid acceleration on residual scales and dynamics of suspended inertial particles in turbulence. *Phys. Rev. Fluids* **4**, 044301. 139

[172] ORLANDI, P., LEONARDI, S., TUZI, R. & ANTONIA, R. (2003) Direct numerical simulation of turbulent channel flow with wall velocity disturbances. *Phys. Fluids* **15**, 3587–3601. 139

[173] KADER, B. (1981) Temperature and concentration profiles in fully turbulent boundary layers. *Int. J. Heat Mass Transf.* **24** (9), 1541–1544. 143

[174] MACDONALD, M., OOI, A., GARCÍA-MAYORAL, R., HUTCHINS, N. & CHUNG, D. (2018) Direct numerical simulation of high aspect ratio spanwise-aligned bars. *J. Fluid Mech.* **843**, 422–432. 144

[175] PETEERS, J. & SANDHAM, N. (2019) Turbulent heat transfer in channels with irregular roughness. *Int. J. Heat Mass Transf.* **138**, 454–467. 144, 148

[176] KAYS, W. & CRAWFORD, M. (1993) *Convective Heat and Mass Transfer*. 144

[177] ZUKAUSKAS, A. (1972) Heat transfer from tubes in crossflow. *Adv. Heat Transf.* **8**, 93–160. 160

[178] BHUIYAN, A., RUHUL AMIN, M. & SADRUL ISLAM, A. K. M. (2013) Three-dimensional performance analysis of plain fin tube heat exchangers in transitional regime. *Appl. Therm. Eng.* **50**, 445–454. 161, 196

[179] VANFOSSEN, G. (1982) Heat-transfer coefficients for staggered arrays of short pin fins. *J. Eng. Power* **104** (2), 268–274. 161

[180] KIRSCH, K. L. & THOLE, K. (2017) Pressure loss and heat transfer performance for additively and conventionally manufactured pin fin arrays. *Int. J. Heat Mass Transf.* **108**, 2502–2513. 161, 167, 169, 174, 175, 176, 197

[181] METZGER, D. E., SHEPARD, W. B. & HALEY, S. W. (1986) Row resolved heat transfer variations in pin-fin arrays including effects of non-uniform arrays and flow convergence. *86-GT-132* . 161, 169, 176

[182] GRAY, D. & WEBB, R. (1986) Heat transfer and friction correlations for plate finned-tube heat exchangers having plain fins. *Proc. 8th. Heat Transfer Conference* **43**, 2745–2750. 161

[183] KIM, N., YOUN, B. & WEBB, R. (1999) Air-side heat transfer and friction correlations for plain fin-and-tube heat exchangers with staggered tube arrangements. *J. Heat Transfer* **121**, 662–667. 161, 167, 169, 174

[184] WANG, C., CHI, K. & CHANG, C. (2000) Heat transfer and friction characteristics of plain fin-and-tube heat exchangers, part II: Correlation. *Int. J. Heat Mass Transf.* **43**, 2693–2700. 161, 166, 168, 174

[185] WANG, C., CHANG, C., HSIEH, Y. & LIN, Y. (1996) Sensible heat and friction characteristics of plate fin-and-tube heat exchangers having plane fins. *Int. J. Refrig.* **19**, 223–230. 161

[186] CORBETT, T., THOLE, K. & BOLLAPRAGADA, S. (2023) Impacts of pin fin shape and spacing on heat transfer and pressure losses. *J. Turbomach.* **145** (5), 051014. 161, 162, 169, 176, 196

[187] GEE, D. & WEBB, R. (1980) Forced convection heat transfer in helically rib-roughened tubes. *Int. J. Heat Mass Transf.* **23** (8), 1127–1136. 169

[188] PRAKS, P. & BRKIC, D. (2018) Advanced iterative procedures for solving the implicit Colebrook equation for fluid flow friction. *Adv. Civ. Eng.* **2018**, 5451034. 170

[189] METZGER, D., BERRY, R. & BRONSON, J. (1982) Developing heat transfer in rectangular ducts with staggered arrays of short pin fins. *J. Heat Transfer* **104** (4), 700–706. 175